

Practical Advances in Microfluidic Electrochemical Energy Conversion

**by
Omar A. Ibrahim**

M.Sc., Mechanical Engineering, Alexandria University, Egypt, 2013

B.Sc., Mechanical Engineering, Alexandria University, Egypt, 2009

Thesis Submitted in Partial Fulfillment of the
Requirements for the Degree of
Doctor of Philosophy

in the
School of Mechatronic Systems Engineering
Faculty of Applied Sciences

© Omar A. Ibrahim
SIMON FRASER UNIVERSITY
Summer 2018

Copyright in this work rests with the author. Please ensure that any reproduction or re-use is done in accordance with the relevant national copyright legislation.

Approval

Name: Omar A. Ibrahim

Degree: Doctor of Philosophy (Engineering)

Title: Practical Advances in Microfluidic Electrochemical Energy Conversion

Examining Committee: **Chair: Mohammad Narimani**
Term Lecturer

Erik Kjeang
Senior Supervisor
Associate Professor

Bonnie Gray
Supervisor
Professor

Hogan Yu
Supervisor
Professor

Woo Soo Kim
Internal Examiner
Associate Professor

Előd Gyenge
External Examiner
Professor
Chemical and Biological Engineering
University of British Columbia

Date Defended/Approved: August 10, 2018

Abstract

Micro-fabrication technologies has enabled the inexpensive production of microchannels which has been utilized in electrochemical flow cells like fuel cells and flow batteries. These offer simplicity and cost benefits as they utilize co-laminar flow for flowing streams separation rather than a physical separator or membrane. This thesis aims to identify practical applications for viable utility of microfluidic flow cells and suggests their potential use for analytical platforms, disposable power sources or combined electrolyte functionalities such as cooling and powering of electronics. All advances reported in this work leverage microfluidic cell architectures with flow-through porous electrodes to achieve competitive performance with simplified, inexpensive device solutions.

A previously reported microfluidic redox battery design is modified to form an analytical cell that is applied throughout this dissertation. The analytical cell designs have two separate cell portions which, when connected in parallel, enable *in-situ* characterization of the dual-pass design, allowing deeper understanding of the reactant conversion and crossover. When the two portions are connected in series, quantifying possible losses in flow cell arrays, such as shunt current, is allowed. The technology is also applied to explore flow cells with non-aqueous electrolytes, which generally enable higher cell voltages but have limited performance from high membrane resistance. The proposed membrane-less cell with non-aqueous electrolytes shows comparable performance with aqueous vanadium electrolytes. Moreover, a chemistry evaluation framework is applied to assess redox reactants and supporting electrolytes selection for biodegradable primary batteries. The selected quinone redox chemistry is demonstrated in a novel 1 V paper-based capillary flow cell, with flow-through porous electrodes, that is proven to be powerful, cheap, scalable and biodegradable and demonstrated to directly substitute a coin cell battery for powering a water quality sensor. This new class of batteries thus holds great promise to radically change the portable battery paradigm; from considering it a harmful waste to a source of biodegradable materials that could even nurture the environment by enriching soil and water beyond its life cycle. Lastly, a scaled co-laminar flow cell is shown for the first time and embedded in a printed circuit board for the application of simultaneous thermal and power management of mounted electronics. This demonstration has advantages in future high-density computers and enables new perspectives for near-term adoption.

Keywords: membraneless; microfluidic fuel cell; microfluidic flow battery; power source; co-laminar flow cell; disposable

إلى والديّ الأعزاء

*Dedicated to my dear parents;
Thanks for your continuous support*

Acknowledgements

I would foremost like to express my extreme appreciation to Dr. Erik Kjeang, for giving me the research opportunity in this area of microfluidic electrochemical energy conversion and offering me the continuous support and guidance during my doctoral studies. I also would like to thank him for allowing the freedom and flexibility in pursuing a variety of ideas, within this project. Funding from Natural Sciences and Engineering Research Council of Canada (NSERC), Canada Foundation for Innovation (CFI) and British Columbia Knowledge Development (BCKDF) is appreciated. I also would like to thank my supervisory committee; Dr. Bonnie Gray and Dr. Hogan Yu, for their considerate advice and comments, which solidified and improved the quality of this outcome.

I would like to thank my predecessor and friend Dr. Marc-Antoni Goulet for his help in the beginning and giving me a head start on the project. I am very grateful for the cooperation and discussions we had. I equally would like to thank our collaborators in the PowerPAD project in Barcelona, Spain; Dr. Juan Pablo Esquivel, Dr. Neus Sabate and Perla Alday, for their influence and foresight and for making this project fun and valuable in many aspects, inside and outside the Lab., and for the amazing outcome and memories. Muchas gracias J-P, Neus e Perla. Funding of the PowerPAD project from the Bill & Melinda Gates Foundation and the Electrochemical Society is appreciated.

I also would like to extend my appreciation and gratitude for Dr. Patrick Ruch and Dr. Bruno Michel at IBM research – Zurich, for offering me the fruitful internship opportunity and hosting me in Switzerland. I would also like to thank the rest of the smart systems integration group and other support staff, for technical and administrative support and valuable conversations, during the internship. Funding of this internship supported by MITACS accelerate international program is highly appreciated.

I also appreciate the technical help provided by many co-ops in our Lab. specially Aronne, Will and Kevin. Thanks! In addition, I would like to extend my thanks to Dr. Caue Martins for his dedication and good vibes while working together in FCReL. Obrigado Caue! Last but not least, I would like to thank my FCReL colleagues and my friends at MSE department for making my stay at SFU during my doctoral studies pleasant.

Table of Contents

Approval.....	ii
Abstract.....	iii
Dedication.....	v
Acknowledgements.....	vi
Table of Contents.....	vii
List of Tables.....	ix
List of Figures.....	x
List of Acronyms.....	xi
Chapter 1. Introduction.....	1
1.1. Background.....	1
1.2. Previous work on CLFCs.....	3
1.3. Motivation.....	7
1.4. Scope and objective.....	10
Chapter 2. Theory.....	13
2.1. Fuel cell performance.....	13
2.2. Fuel cell polarization.....	15
2.2.1. Activation overpotential.....	16
Butler-Volmer equation.....	17
Exchange current density (i_0).....	17
Tafel plot.....	18
2.2.2. Ohmic overpotential.....	18
2.2.3. Concentration overpotential.....	19
2.2.4. Other voltage losses.....	21
2.3. CLFC theory.....	21
Chapter 3. Methodology.....	24
3.1. Cell design and fabrication.....	24
3.1.1. Analytical cell.....	24
3.1.2. RFPCB devices.....	27
3.2. Electrochemical testing.....	29
Chapter 4. Summary of contributions.....	30
4.1. <i>In situ</i> characterization of dual-pass cell architecture.....	30
4.2. Characterization of shunt current in arrays.....	34
4.3. Leveraging CLFCs for non-aqueous systems.....	37
4.4. PowerPAD.....	40
4.4.1. Evaluation of capillary flow-through porous electrodes.....	42
4.4.2. Evaluation of biodegradable redox couples.....	44
4.4.3. A Metal-free biodegradable capillary flow battery.....	48
4.5. Simultaneous power and thermal management of electronics: RFPCB.....	49

Chapter 5. Conclusions and future work	53
5.1. Conclusions.....	53
5.2. Future work	58
References	60
Appendix A. In-situ Characterization of Symmetric Dual-pass Architecture of Microfluidic Co-laminar Flow Cells	71
Appendix B. Microfluidic Electrochemical Cell Array in Series: Effect of Shunt Current	81
Appendix C. Leveraging Co-laminar Flow Cells for Non-aqueous Electrochemical Systems	88
Appendix D. Evaluation of Redox Chemistries for Single-Use Biodegradable Capillary Flow Batteries	118
Appendix E. A Metal-Free and Biotically Degradable Battery for Portable Single-Use Applications	128

List of Tables

Table 1.1.	Some selected key developments in CLFC technology.	6
Table 4.1.	A comparison between reactant chemistries of conventional aqueous VRFB and non-aqueous flow battery based on V_{acac}	38
Table 4.2.	Measured volumetric solvent accessible porosity of Toray carbon paper (TGPH-060) with and without heat treatment.	43
Table 4.3.	Summary of selected organic redox reactants for both half cells.	45
Table 4.4.	A comparison of power and energy densities of different environmentally benign batteries reported in literature.	49
Table 4.5.	Comparison between RFPCB membraneless design results and other similar designs with conventional membranes.	52

List of Figures

Figure 1.1.	Different CLFC key architectures: a) flow-over electrodes, b) flow-by electrodes, c) air breathing electrode, d) array of cylindrical electrodes, e) flow-through porous electrodes, f) dual-pass architecture or MRB design and g) paper based CLFC with capillary-driven flow.....	6
Figure 2.1.	A schematic for a VRFB operation.	14
Figure 2.2.	A typical polarization curve showing the overpotential sources.	15
Figure 2.3.	A sketch of the CLFC fundamental concept utilizing laminar flow to separate reactant streams.....	22
Figure 3.1.	Dual-pass cell designs: a) the original MRB design and b) the modified design to form an analytical cell.	24
Figure 3.2.	Mask for the analytical cell showing geometric dimensions	25
Figure 3.3.	Complete fabrication process flow of the CLFCs using soft lithography..	26
Figure 3.4.	A photograph of a CLFC made in PDMS after full assembly.	27
Figure 3.5.	A schematic showing the components of the membraneless RFPCB design.	28
Figure 3.6.	A photograph of the RFPCB cell after lamination. The cell is connected to a custom designed holder that provides connection of inlet and outlet tubing to their respective ports.	28
Figure 4.1.	The proposed PowerPAD concept	42
Figure 4.2.	Testing Toray-060 carbon paper for capillary flow-through: a) horizontal flow, b) vertical flow against gravity, c) designed setup with hanging electrodes and d) ink reaching the absorbent pad after flowing through the porous electrode.	43
Figure 4.3.	PowerPAD material selection matrix for integrating electronic and fluidic functionalities.	44
Figure 4.4.	Polarization curve and power density curve for membraneless design of RFPCB using rectangular slits.....	51

List of Acronyms

AA	L-Ascorbic acid
AN	Acetonitrile
ASR	Area specific resistance
CAD	Computer aided design
CE	Counter electrode
CLFC	Co-laminar flow cell
CV	Cyclic voltammetry
DMFC	Direct methanol fuel cell
EIS	Electrochemical impedance spectroscopy
GCE	Glassy carbon electrode
GDE	Gas diffusion electrode
H2BQS	Hydroquinone sulfonic acid
ICE	Internal combustion engine
LQ	Leucoquinizarin
MRB	Microfluidic redox battery
NAq	Non-aqueous
OA	Oxalic acid
OCP	Open circuit potential
pBQ	Para-benzoquinone
PCB	Printed circuit board
PDMS	Polydimethylsiloxane
PEM	Polymer electrolyte membrane
RE	Reference electrode
RFB	Redox flow battery
RFPCB	Redox flow cell integrated in a PCB
SCE	Saturated calomel electrode
SOC	State of charge
TEABF ₄	Tetraethylammonium tetrafluoroborate
V _{acac}	Vanadium acetylacetonate
VRFB	Vanadium redox flow battery
WE	Working electrode

Chapter 1.

Introduction

1.1. Background

In order for a full renewable energy dependency to commence and dominate the global energy supply, the fluctuations and intermittency in the input energy sources such as wind or solar have to be addressed by energy storage and supply solutions. These solutions ought to address backup power, load-leveling or peak-shaving. Energy conversion and storage technologies can be divided into four major types: mechanical, electrical, chemical, and electrochemical [1]. Each energy storage technology offers certain advantages and is limited by other drawbacks. For example, pumped hydro power offers storage capacities in the MW and GW scales and offers many advantages in lifetime and safety, yet is constrained to locations with suitable geographical features. Among these technologies, electrochemical energy conversion has increasingly become a favourable choice for a variety of applications towards the transition to sustainable energy as it offers advantages in scalability and flexibility.

Among electrochemical energy technologies, batteries are the primary choice for powering portable applications and for energy storage because of their good energy density and compactness. Recently, both lithium ion (Li-ion) batteries and fuel cells have been commercialized for use in automotive applications, in an effort to limit greenhouse emissions resulting from internal combustion engines (ICEs). Fuel cells rely on the electrochemical conversion of hydrogen and oxygen resulting in the emission of only heat and water vapor. Beside this great advantage, they are thermodynamically open systems; therefore they have much higher theoretical efficiencies than ICEs that are limited by Carnot efficiency [2]. Closed Li-ion cells offer the dominant and most established solution for powering portable applications such as consumer electronics and sensing applications due to their specific energy and compactness. For the energy storage category, Li-ion batteries have moreover emerged in the small household utility scale in the kW order. On the other hand, for grid-scale energy storage in the MW or GW

order, another type of battery has emerged that rely on the continuous recirculation of flowing charged electrolyte solutions, namely the redox flow batteries (RFBs). These RFBs resemble a fuel cell in being a thermodynamically open system and thus have the advantages of decoupled power densities and energy densities over Li-ion systems, since the charge is provided from the flowing electrolytes stored in external tanks [3–5]. While this technology is still in development with efforts to reduce its associated cost per kWh, several pilot projects have been demonstrated and more commercialization activities are being adopted.

In a conventional fuel cell or RFB, electrically insulating physical separators such as polymer electrolyte membranes (PEM) are used to separate the two reactant streams while permitting the ionic conductivity by the transport of cations or anions. These ionomer membranes for example allow selective transport of protons in acidic conditions or hydroxyl ions in alkaline conditions while preventing the undesired crossover of other species [2]. Lots of research efforts are focused on development of those membranes, resulting in reduction in their thicknesses down to scale of tens of micrometers [6]. This is advantageous in terms of reduced ionic resistance and thereby enhanced cell performance. However, it also encounters some technical challenges such as membrane degradation leading to failure as in the case of PEM fuel cells [7] and the increased species crossover due to diffusion and electro-osmotic drag as in the case of direct methanol fuel cells (DMFCs) [2] and RFBs [6,8]. Furthermore, PEMs result in a significant increase in the overall cost of the electrochemical cells besides their durability and crossover issues.

Advances in micro-fabrication technologies have enabled the inexpensive production of microfluidic channels [9,10] which have recently been utilized in electrochemical energy conversion applications such as fuel cells and flow batteries [11]. Among these microfluidic electrochemical cells, some have implemented the concept of co-laminar flow rather than a physical membrane to achieve the required reactant separation [12,13]. In those formerly mentioned co-laminar flow cells (CLFCs), wherein species mixing is mainly governed by diffusion, the diffusional interface provides necessary separation between the two flowing reactant streams whilst permitting ion transport. In general, these cells offer great advantages over their conventional counterparts such as the simplicity of the structure, elimination of the membrane and its cost and hydration issues. These membraneless CLFCs thus hold promises of future

power generation for applications like portable devices and off-grid sensors [11,14] or as an inexpensive and durable alternative for energy storage once an efficient scale-up strategy is established, since membranes are usually a primary source of high cost and performance degradation in fuel cells.

1.2. Previous work on CLFCs

Since their introduction back in 2002, the scientific research of CLFCs field has considerably grown from fuel cells [12,13] to also include flow batteries [15,16] and more recently, electrolyzers [17–20]. Various reviews [14,21–24] and books [11] have highlighted and summarized some of the milestones achieved in device functionality, reactants and architectures, for fuel cells, batteries and electrolyzers. Regarding the chemistry, various reactants have been employed in CLFCs. Many works including the pioneering work relied on vanadium redox electrolytes [12,25]. Others employed various reactants such as hydrogen [26–28], hydrogen peroxide [29–31], borohydride [32], formic acid (HCOOH) [33–35] and alcohols such as methanol, ethanol, ethylene glycol or glycerol [36–39]. Furthermore, CLFCs were also employed for bio-based fuels such as microbial or enzymatic fuel cells [40–44].

Regarding the cell architectures, many innovative designs were reported. The pioneering studies for CLFCs by Ferrigno et al. [12] and Choban et al. [13] used basic Y-shaped microchannel architecture. These first reported architectures used planar electrodes on the bottom or the sides of a microchannel, known as flow-over and flow-by electrodes configurations, respectively, as shown in Figure 1.2a and Figure 1.2b. Jayashree et al. introduced the air breathing electrode architecture, shown in Figure 1.2c [45]. It allowed gaseous oxygen transport from the surroundings and an ion-conducting blank electrolyte maintained the co-laminar interface and prevented the fuel (anolyte) from reaching the cathode [46]. Alternatively, for liquid reactants, Kjeang et al. proposed a simple array of cylindrical electrodes, as shown in Figure 1.2d, to extend the anodic reactive surface area and enhance mass transport [47]. Zhu et al. reported a direct formic acid CLFC that coupled an air breathing cathode with an array of graphite cylinders as the anode [48].

A key advancement in CLFCs was the introduction of flow-through porous electrodes configuration by Kjeang et al. [49,50], shown in Figure 1.2e. The baseline cell design was fed by both reactant streams individually through the porous carbon paper electrodes before meeting in the center manifold for ionic transport. The cell achieved power densities up to 121 mW/cm² and high fuel utilization using vanadium redox species by utilizing the whole three-dimensional area of a porous carbon paper electrode [49]. More recently, the concept of CLFCs expanded beyond fuel cells to include rechargeable flow batteries. The baseline design with flow-through porous electrodes was modified by the introduction of a splitting junction at the outlet for harvesting the reactant streams separately, as seen in Figure 1.2f. This dual-pass architecture permitted both charging and discharging and was thus called the microfluidic redox battery (MRB) for its reversible capability. The cell achieved power densities around 300 mW/cm² and 20% full cycle energy efficiency [15]. Both power density and fuel utilization were enhanced compared to previous cells due to improved mass transport rates in the electrodes facilitated by the dual-pass configuration. The MRB was later analyzed by Goulet and Kjeang [51] demonstrating increased cell performance and complete fuel recirculation and regeneration capabilities, to mimic a conventional redox flow battery. Very recently, Goulet et al. have engineered the geometry of the baseline design to have lower cell resistance and combined that with an innovative dynamic flow deposition of carbon nanoparticles to increase the electrochemical surface area [52,53]. This combination resulted in a low cell resistance and in an enhanced reaction kinetics resulting in a record power density output of 2 W/cm². Moreover, Braff et al. reported a membraneless hydrogen-bromine (H₂ / HBr / Br₂) flow battery, that showed high discharge power density of 795 mW/cm² [16]. They also investigated cell charging and discharging reporting a cycle efficiency of 91%.

In addition, other researchers proposed different configurations. Hayes et al. reported a microfluidic fuel cell with orthogonal flow which acted to move reactants to the electrodes by the convection and served as a pseudo-membrane between the electrodes thus preventing mixed-potentials [54]. Salloum et al. reported a configuration based on sequential convective flow with porous disk electrodes and demonstrated the operation with formic acid and potassium permanganate. Their architecture enabled independent flow rate control for both reactant streams and different electrode areas [55]. Moreover, in another work, they also presented a convective counter flow

configuration wherein sulfuric acid was introduced in a gap between the electrodes and separated the vanadium redox reactant streams by diverting the reactants to opposite and independent outlets [56]. This reduced the reactant stream crossover but also caused a dilution in the outlet streams due to diffusive mixing with sulfuric acid. Huo et al. presented a ladder-shaped microchannel to eliminate the fuel crossover in the CLFC [57]. These ambitious studies however generally achieved only modest power densities advantages despite the demonstrated advantages to reactant crossover. Da Mota et al. nonetheless eliminated conventional membranes with laminar flow combined with porous non-selective convection barrier to separate the reactant streams, while achieving power densities in excess of 250 mW/cm² [32].

In addition, one of the other advantages of CLFCs over their conventional counterparts is the flexibility of tuning the conditions in each half-cell separately. This is known as mixed-media or dual-electrolyte operation. Mixed-media operation is enabled by the membraneless configurations since the conditions are not restricted by the ion selective membranes used in conventional cells [58]. For instance, coupling an alkaline anodic half-cell with an acidic cathodic half-cell has the advantage of a higher thermodynamic cell voltage and thus higher performance. This was demonstrated first by Choban et al. using hydrogen fuel [59] and Cohen et al. in a microfluidic DMFC [60]. Lu et al. reported one of the highest performing CLFCs by employing mixed-media operation of a microfluidic hydrogen fuel cell leading to high cell open circuit potential (OCP) close to 1.9 V and a peak power density of 1.3 W/cm². They also showed the advantages in the reverse electrolytic mode in which the mixed-media operation enabled water electrolysis at reduced cell voltages of 0.6 V by utilizing the thermodynamic advantages of the pH dependency of hydrogen and oxygen evolution reactions [61].

Most of these architectures reported in various works relied mainly on pumps to provide the flow into the cells. While this complicates the system and adds to its overall cost and footprint, it also requires power for actuation which is parasitic to the cell and reduces its overall useful output. Alternatively, researches relied on paper based microfluidics, wherein the flow is solely provided by capillary forces in the paper material [62–65]. Esquivel et al. proposed the utility of self-pumping, using capillarity as an alternative by making the CLFC channels in a paper (Figure 1.2g). They showed peak power density output around 5 mW/cm² using DMFC with an air breathing cathode [62].

They proposed the integration of the concept within lateral flow diagnostic devices. Some selected key technological developments of CLFCs are summarized in Table 1.1.

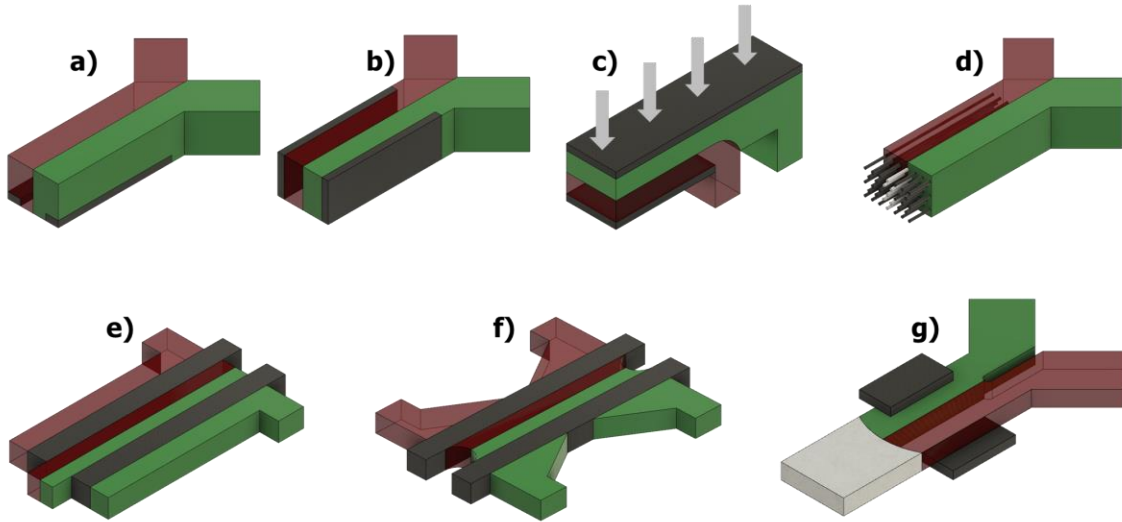


Figure 1.1. Different CLFC key architectures: a) flow-over electrodes, b) flow-by electrodes, c) air breathing electrode, d) array of cylindrical electrodes, e) flow-through porous electrodes, f) dual-pass architecture or MRB design and g) paper based CLFC with capillary-driven flow.

Table 1.1. Some selected key developments in CLFC technology.

Reference	Design	Anode	Cathode	Power density (mW/cm ²)
Ferrigno et al. [12]	Flow-over	V ²⁺ / H ₂ SO ₄	VO ₂ ⁺ / H ₂ SO ₄	38
Choban et al. [13]	Flow-by (dissolved)	HCOOH / H ₂ SO ₄	O ₂ / H ₂ SO ₄	2.4
Jayashree et al. [45]	Air breathing	HCOOH / H ₂ SO ₄	O ₂ / H ₂ SO ₄	26
Choban et al. [59]	Mixed-media (dissolved)	Methanol / KOH	O ₂ / H ₂ SO ₄	12
Cohen et al. [60]	Mixed-media (dissolved)	H ₂ / KOH	O ₂ / H ₂ SO ₄	0.6
Kjeang et al. [49]	Flow-through	V ²⁺ / H ₂ SO ₄	VO ₂ ⁺ / H ₂ SO ₄	121
Da Mota et al. [32]	With porous separator	Borohydride	Cerium	250
Lee et al. [15]	Dual-pass	V ²⁺ / H ₂ SO ₄	VO ₂ ⁺ / H ₂ SO ₄	300
Braff et al. [16]	GDE* & flow-over	H ₂ / HBr	Br ₂ (liq) / HBr	795
Esquivel et al. [62]	Paper-based / Flow-over	Methanol / KOH	O ₂ / KOH	5
Esquivel et al. [66]	Paper-based / GDE	H ₂ / KOH	O ₂ / KOH	103
Lu et al. [61]	Mixed-media (GDE)	H ₂ / KOH	O ₂ / H ₂ SO ₄	1300
Goulet et al. [52]	Flow-through + dynamic deposition	V ²⁺ / H ₂ SO ₄	VO ₂ ⁺ / H ₂ SO ₄	2000

* GDE: Gas diffusion electrode

1.3. Motivation

Despite the numerous advantages of the miniaturization and the membraneless configuration mentioned before, the technology has so far failed to get commercialized, for any potential application. This is likely attributed to the difficulty in the scalability of the technology, which necessitates small microfluidic features in order to maintain laminar flow [14,23]. For an RFB application applied for energy storage, the CLFC technology still shows relatively lower efficiencies compared to conventional counterparts. For example, the dual pass architecture by Lee et al. showed 20% round trip efficiency [15]. This suggests that more analysis and deeper understanding for the reactant conversion and crossover in this configuration is required. On the other hand, the HBr CLFC by Braff et al. reported promising efficiencies of 91% [16]. Nevertheless, the problem of technology scalability will remain questionable and the literature in addition seems to be missing studies on scaling up, stacking combined cells or full system level. For example, the largest CLFC cell to our knowledge had an active area of 1 cm² but suffered from very low performance [67], indicating the scale limitations. Furthermore, it is equally important to consider the whole balance of plant items and the overall system footprint including external components such as pumps and reactant storage. In this regard, Sabaté et al. envisions that the advantages of such considerable simplification in fuel cells structures, such as those offered by CLFCs, are not yet explored commercially because of the need of using such external pumps to keep reactants flowing [68].

On the other hand, it remains unclear whether the use as compact or portable power sources, such as for electronic devices or off-grid sensors, is a promising direction for the technology. The problem of scale also remains valid here despite the high power density levels that have been reached [52]. In addition, the vanadium redox species used in the demonstrations by our group seem not suitable for that, due to reasons of toxicity and high cost. The vanadium redox species is even forecasted to increase more in value and contribute a higher cost proportion than that of membranes in conventional RFBs. Alternative redox species hence requires development and testing. Therefore, this suggests the need for developing power sources that are inexpensive and that are tailored for specific applications. These power sources may thus utilize membraneless configuration and benign materials and therefore be

disposable. Nevertheless, beside the problem of scale, the overall system size including pumps and storage has also to be taken into consideration, as mentioned before.

The CLFC technology in our group and in other groups has however been demonstrated with other benign fuels. For example, formic acid and alcohols such as methanol, ethanol, ethylene glycol and glycerol have been demonstrated with good power density output in the tens/hundreds of milliwatts per square centimeter range. For example, Gurrola et al. showed a coupled formic acid CLFC powering a low-power test board [69]. Nevertheless, the electrochemical oxidation reactions of these fuels generally require precious catalysts such as platinum or palladium. These cells moreover usually utilize an oxygen cathode which often requires platinum catalysts. These precious metals contribute thus to increasing the cost of the power source and require recycling rather than simple disposal to extract these metals. Alternatively, the use of biological catalysts on the other hand has its own disadvantages when it comes to much lower power density levels or enzymes stability [40].

In regard to using alcohols as fuels or other bio-based fuels, a lot of work has been reported with a focus on reporting novel catalysts and their aspects rather than the focus on power density or the CLFC technology or configuration [36,38,70]. Therefore, an opportunity appears to utilize this simplification in fuel cell configuration and cost reduction. CLFCs may hence be used as analytical platforms for quick demonstrations, measurements and/or comparisons for a fuel cell system. These platforms are easily and cheaply fabricated and simply assembled. In addition, CLFCs may be combined with other microfluidic tools to provide useful insights for electrochemical flow systems, such as the analytical three electrode flow cell developed in our group by Goulet et al. and utilized in one of the studies in this thesis [71]. In general, novel catalysts, electrode materials or designs, redox reactants, supporting electrolytes or various operating parameters may therefore be initially tested in such microfluidic platforms. Promising solutions with potential benefits may therefore be simply identified and shortlisted for use in conventional cells.

Instead of using pumps, Esquivel et al. utilized paper-based microfluidics (Figure 1.1g) which allows the reactants flow by capillarity without the need of external pumps [62]. They proposed the potential combination of this inexpensive CLFC technology within in-vitro diagnostic lateral test strips such as those used for pregnancy tests or

blood glucose metering, wherein the CLFC would be activated by the drop wise addition of sample, which may be the same as the liquid added for testing (urine in their case). In this sense, these diagnostic devices already utilize microfluidic paper-based lateral flow, require a sample or an analyte to diagnose and usually have an integrated coin cell battery for powering the devices. This concept is therefore identified as a promising niche application that is matched with CLFC technology, despite using methanol as the initial demonstration, which requires precious catalysts, as mentioned before. In addition, they more recently integrated a hydrogen fuel cell on a paper strip that is designed to perform a diagnostic reaction, which generates hydrogen as a by-product [66]. Therefore, it seems that these types of applications that have combined functionalities may suit the inexpensive CLFC technology that holds promise for substituting the coin cells often used instead. Another advantage is the opportunity to use the same manufacturing methods during mass production of the integrated paper strips.

Overall, new redox materials need to be developed for the context of disposable power sources for application in biomedical diagnostics, environmental monitoring or dipsticks. Those should enable performance outputs much higher than biofuels and comparable to alcohol-based fuel cells whilst eliminating the needs of precious catalysts. With eco-friendly redox alternatives developed and with cheap membrane-less paper-based cells, a fully disposable and sustainable single-use power source may be developed, without the need for catalysts or recycling.

Furthermore, another innovative and promising application that combined different functionalities and proposed utilizing the technology is the combined and simultaneous on-chip powering and cooling of processors [72,73] conceived by IBM Research. They suggested the use of miniaturized flow batteries for the thermal management and power delivery of microprocessors and future electronic chips. However, the power density levels needed for such application is still > 5-10 times higher than for the current state-of-the-art flow battery technology ($\leq 2.5 \text{ W/cm}^2$), whether a membrane is used or not [52,74–76]. Therefore, this application is not currently viable. However, recently they showed high power density output of 1.4 W/cm^2 using an alkaline organic chemistry by introducing a novel 3D printed electrode [74]. The novel electrode enhanced mass transport using herringbones mixing structures [77–79] with multiple reactant passes. They also proposed that the concept of combining functionalities may be extended to similar applications such as lasers or light-emitting diodes which fuses

the power and thermal management functionalities or in other applications for energy storage such as photovoltaic cells, whose performance is affected by temperature and could hence benefit from the cooling capacity of an integrated RFB cell, with or without a membrane.

Therefore, it can be concluded that the CLFC technology may be well-suited for the following promising applications:

- Analytical platforms,
- Disposable or integrated power sources,
- Combined functionalities like thermal and power management of electronics.

1.4. Scope and objective

In our research group, the flow-through porous electrode architecture, shown previously in Figure 1.2e, is the base-line cell architecture for the CLFC research [49]. The previous PhD students that focused on CLFCs have expanded the base-line research advances by tackling performance aspects, with the ultimate goal of increasing the power density output. For example, Dr. Jin Wook Lee used carbon nanofoam material to enhance kinetics [80] and gold current collectors to reduce cell electronic resistance [81]. Dr. Marc-Antoni Goulet conceptualized the dual pass architecture and the MRB as earlier illustrated in the previous section [15,51]. He studied the importance of porous electrodes wetting [82] and also developed a deposition mechanism that enhanced performance, by tackling the reaction kinetics and increasing the electrochemical surface area [83] which resulted in a record breaking performance when combined with the other geometrical optimization strategies that minimized cell area specific resistance (ASR) to as low as $0.12 \Omega\text{cm}^2$ suggesting revisiting the use of liquid electrolytes for separating the two electrodes [52]. Furthermore, Dr. Lee and Dr. Goulet have mainly relied on the vanadium electrolyte for their studies. The scope of this work conversely is likely to be different than performance enhancements and the focus will be on a more broad vision on practicality and viable utility of the technology exploring other reactants. The thesis will thus be focused on the main applications summarized in the previous section, with the ultimate goal of demonstrating a viable and practical outcome that utilizes membraneless electrochemical energy conversion in porous electrodes.

This dissertation will hence focus on practical advances in microfluidic electrochemical energy conversion in membraneless cells with porous electrodes such as CLFCs. The work will aim to apply and leverage the CLFC technology benefits for the applications mentioned previously: analytical platforms, disposable power sources and combined flow cell functionalities such as simultaneous on-chip cooling and powering. Therefore, the objectives of this dissertation, in line and motivated with these applications, are therefore summarized in the list below as:

- Design and development of an analytical CLFC that can be applied in a variety of studies.
- Applying the analytical cell design to investigate the dual-pass architecture.
- Applying the analytical cell design to characterize cells stacking losses.
- Investigating the use of non-aqueous (NAq.) redox electrolytes in CLFC format as an attempt to address the ohmic limitation of the membranes, by testing in the analytical cell design.
- Evaluation of new organic redox chemistries with good kinetics on carbon electrodes for potential use in disposable power sources.
- Co-development of a single-use disposable paper-based power source that is capillary driven and biodegradable.
- Development of a proof-of-concept of a scaled up CLFC for the use in combined powering and cooling of electronics application.

The research project of this thesis started as a continuation on the work of Dr. Goulet on the dual-pass architecture. While the MRB design had potential advantages of high power output, fuel recirculation and in-situ regeneration, the cell design was difficult to optimize because of the convoluting effect of two reactant passes through a single electrode. The first study in this research project presented an analytical cell design for that regard, as presented in Chapter 4.1. The same analytical cell design was utilized in further studies. In Chapter 4.2, it was used to characterize shunt current losses in CLFC arrays, which was limited in the literature, but enabled by this novel analytical cell design. The same analytical cell was also used to evaluate the use of non-aqueous (NAq) electrolytes in CLFC configuration, for the first time. This idea was proposed after the collaborative study which demonstrated minimized cell ASR, as mentioned before, and was thus thought to have potential benefits for NAq flow cells, which have

advantages such as high voltages yet typically suffer from high membrane resistance in NAq solvents. A thorough experimental investigation is conducted in Chapter 4.3 in this regard and a high performance NAq flow cell is shown.

The collaborative development of a portable and disposable power source (PowerPAD) is concluded in Chapter 4.4. The PowerPAD is a biodegradable battery that relies on self-pumping using capillarity in paper based microfluidics, eliminating the need of bulky pumps. Capillary flow-through porous carbon paper is also demonstrated, which unlocks high performance over flow-over designs, previously used in literature. The PowerPAD utilizes novel organic redox species rather than the conventional redox electrolytes. The chemistry requirements are defined and the evaluation of redox chemistry for single-use and biodegradable power sources is reported in section 4.3.2. The same analytical cell design, used previously, aided in the selection and evaluation of benign and environmentally friendly chemistries.

Lastly, in Chapter 4.5, the research related to the integrated thermal management and power delivery functionalities for flow cells is reported. The objective was to design and demonstrate a scaled CLFC for this application, in collaboration with IBM Research – Zurich, during an internship. A scaled membraneless redox flow cell was designed in a printed circuit board (PCB), named RFPCB, as an alternative to utilize the innovative concept of combined thermal and power management functionalities on electronic boards, which alternatively offer a larger footprint than microprocessors mounted on them. This integration has advantages in future high-density high-performing computing microprocessors, such as microservers and data centers [84,85], which would typically rely on pumped water flow for direct cooling and thermal management [84]. The power density requirement is estimated in the order of 0.5 W/cm^2 , which is achievable with current state-of-the-art RFBs, as the whole board area may be utilized [85]. This enables new perspectives for the near-term use of the concept. Hence, a full demonstration of the combined simultaneous functionalities may be performed in a full system level by powering and cooling electronic components mounted on the RFPCB.

Chapter 2.

Theory

2.1. Fuel cell performance

Whether it is a fuel cell or a flow battery, the basic principle of operation is the same. It relies on the conversion of the chemical energy into electric energy [2,86]. These electrochemical cells contain two half-cell compartments each having the electrolyte in contact with their respective electrode while joined externally by electronic wires and internally by the electrolyte in order to close the circuit. During discharge or galvanic operation, the power is generated by oxidizing the fuel or the anolyte at the negative half-cell releasing ions and electrons. The ions travel through the electrolyte phase which promotes ionic conduction while preventing electronic transport. The electrons travel through the external wire and thereby driving an external load. Both the ions and electrons recombine with the oxidant or the catholyte at the positive half-cell to close the circuit. On the other hand, during electrolytic operation, the opposite process takes place leading to charging of the RFB half-cell species or the regeneration of fuel.

Each of these half-cell reactions has a standard reduction potential E^0 relative to a reference. The difference between the E^0 of the two different half-cells define the standard potential of the cell at open circuit. The equilibrium potential E of each reaction however may change significantly from the values of E^0 depending on various operational parameters such as temperature, pressure, reactant concentrations, or the state of charge (SOC) of the RFB. This change is governed by the Nernst equation, given in Eq. 2.1.

$$E = E^0 - \frac{RT}{nF} \ln \left(\frac{a_{ox}^A}{a_{red}^B} \right) \quad (2.1)$$

where $R = 8.31$ J/K mol is the universal gas constant, T is the temperature (K), n is the number of electrons transferred during the reaction per mole, $F = 96485$ C/mol is

Faraday's constant, a is the thermodynamic activity coefficients of the reactants and A and B are the respective mole fractions. When the reactants of each half-cell are in contact with their respective electrode, the OCP of the cell is equal to the difference of the thermodynamic equilibrium potential at the cathode and anode, as given by Eq. 2.2:

$$OCP = E_c - E_a \quad (2.2)$$

For example, a conventional vanadium flow battery (VRFB) [20] is shown in Figure 2.1. Vanadium is widely used for flow battery research while many other half cell chemistries were proposed for cost, energy density, solubility, cell potential or environmental advantages [5,86,87]. In the VRFB shown in the figure, during discharge operation, the V^{2+} is oxidized to V^{3+} at the anode while the VO_2^+ (or V^{5+}) is reduced to VO^{2+} (or V^{4+}) in the cathode [88,89]. The VRFB uses a sulphuric acid based electrolyte and the ion migration relies on proton transport across the electrodes and hence, Nafion® membrane was widely used. The electrochemical equations involved are shown in Eq. 2.3 and Eq. 2.4, for negative and positive half-cells, respectively, showing a combined reversible cell standard potential around 1.25 V. In case of liquid reactants like the VRFB or other reactants presented throughout this thesis, the activity coefficients (a) are proportional to the reactants concentrations (C). Therefore, the Nernst equations for equilibrium potentials for the case of all-vanadium reactants as an example can be described in Eq. 2.5 and Eq. 2.6, respectively.

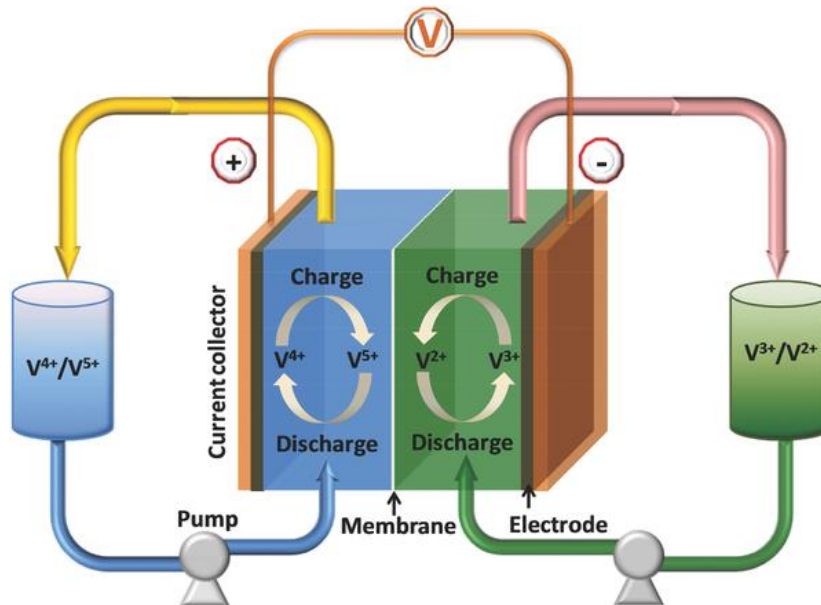


Figure 2.1. A schematic for a VRFB operation.
Reproduced from [90] with permission from John Wiley and Sons.



$$E_a = E_a^0 - \frac{RT}{F} \ln \left(\frac{C_{V^{2+}}}{C_{V^{3+}}} \right) \quad (2.5)$$

$$E_c = E_c^0 - \frac{RT}{F} \ln \left(\frac{C_{VO^{2+}}}{(C_{VO_2^+}) \cdot (C_{H^+})^2} \right) \quad (2.6)$$

2.2. Fuel cell polarization

The OCP of the cell represents the maximum voltage that can be provided to an external circuit in the cell by using those half-cell reactants. If an external voltage higher than this value is supplied to the terminals of the cell, the reverse charging reactions will occur at each electrode (electrolytic operation). On the other hand, if a simple electrical load is connected to the cell terminals, a spontaneous discharge (galvanic) operation will occur at each electrode providing current to the external circuit having that load. The actual discharge current provided by the cell depends on the polarization behaviour of the cell which represents the current-voltage relationship. A typical non-linear polarization curve for a H₂ fuel cell is shown in Figure 2.2, as an example.

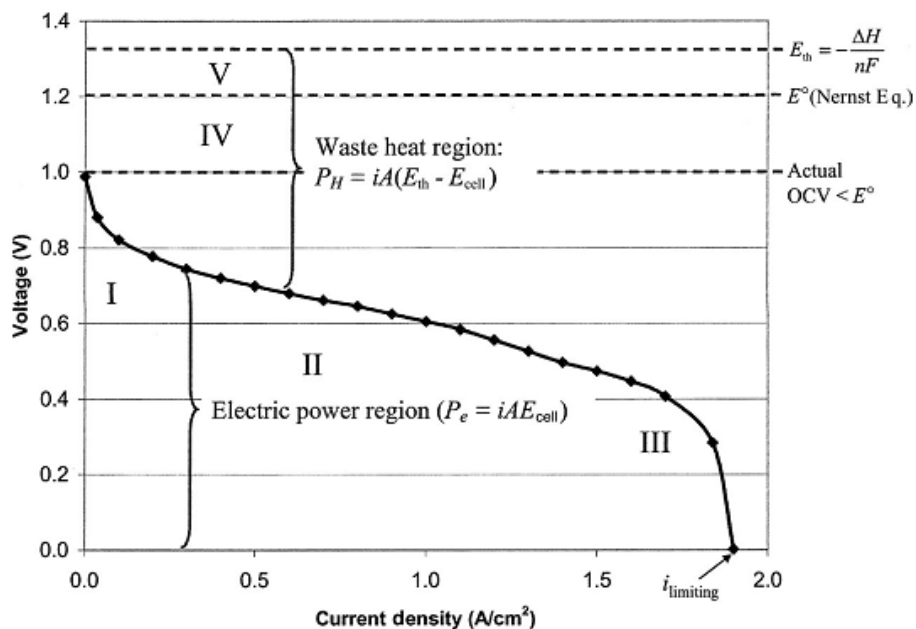


Figure 2.2. A typical polarization curve showing the overpotential sources. Reproduced from [2] with permission from John Wiley and Sons.

Polarization curves describe the performance of fuel cells and flow batteries. Throughout this thesis, polarization curves are used to characterize the performance of the different cells using different reactants. Therefore, in this section, the general relevant polarization behaviour is described. The actual cell voltage obtained during operation is lower than the reversible or equilibrium cell potential due to various voltage losses or overpotentials (η). The general operational cell voltage (E_{cell}) is determined from Eq. 2.7, where the various sources of voltage losses are subtracted from the reversible cell potential. These sources of losses are individually detailed in the following subsections. In general, these subtracted losses correspond to:

- Activation overpotentials due to irreversibility in the kinetics at both electrodes (η_{act} , Region I),
- Total ohmic losses of the cell (η_{Ohmic} , Region II),
- Concentration overpotentials from mass transport limitations at both electrodes (η_{MT} , Region III), and
- Other voltage losses associated with crossover, shorts and mixed-potentials (η_x , Region IV).

$$E_{cell} = OCP - \eta_{act,a} - |\eta_{act,c}| - \eta_{Ohmic} - \eta_{MT,a} - |\eta_{MT,c}| - \eta_x \quad (2.7)$$

2.2.1. Activation overpotential

The first of these major polarization overpotentials is the activation loss, which is distinct in the region of low current of the polarization curve (Region I, Figure 2.2). In this region, the potential is shifted away from the equilibrium potential of the reactants so that, the electrochemical reactions will take place and current will flow between the electronic conducting and ionic conducting phases to reach a new equilibrium between them. This difference in potential defines the activation overpotential (η_{act}), as given in Eq. 2.8. The activation overpotential is thus directly proportional to the increase in current flow and can be represented as given in Eq. 2.9.

$$\eta_{act} = E_{cell} - E \quad (2.8)$$

$$\eta_{act} = \frac{RT}{\alpha n F} \ln \left(\frac{i}{i_0} \right) \quad (2.9)$$

where α is the charge transfer coefficient and i_0 is the exchange current density.

Butler-Volmer equation

The Butler-Volmer equation is commonly used to model the activation overpotential at both electrodes. The Butler-Volmer equation describes the current and overpotential relation at the kinetic region of a half-cell electrochemical reaction, assuming that the surface concentrations of the reactants match the bulk concentrations and thus no concentration gradients present so that the electrochemical reaction is limited by the charge transfer process, as shown in Eq. 2.10.

$$i = i_0 \left[\exp\left(\frac{\alpha_o F}{RT} \eta_{act}\right) - \exp\left(-\frac{\alpha_r F}{RT} \eta_{act}\right) \right] \quad (2.10)$$

where, the subscripts *o* and *r* indicate the oxidation (anodic or forward away from equilibrium) reactions and the reduction (cathodic or reverse away from equilibrium) reactions of the electrochemical half-cell, respectively.

Exchange current density (i_0)

When the overpotential is absent (OCP) and the net current output is zero, then it indicates that the reaction proceeds in both forward direction and reverse direction with no net reaction in any direction or no change in the reactants (equilibrium). The exchange current density (i_0) can be described as the current exchange at the electrode at such equilibrium state and is an important parameter that measures the electrode effectiveness in promoting an electrochemical reaction. For a slow electrochemical reaction, i_0 is small and vice versa. The activation polarization is inversely proportional to the exchange current density and is therefore influenced by the rate of electrochemical reaction and attributed to how sluggish the electrode kinetics is. When i_0 is high, then the activation polarization losses (η_{act}) or overpotential is generally lower for a given current and the reaction is more facile. The exchange current density is however not an intrinsic function the applied catalyst. Nevertheless, it can generally be a function of the applied catalyst, the electrode morphology and purity as well as the operational pressure, temperature and reactant concentration. These factors may effectively result in an increased i_0 and a reduced η_{act} , as shown in Eq. 2.11 for a one-electron electrochemical reaction at reference temperature.

$$i_0 = F k_0 (C_o^{1-\alpha} - C_r^\alpha) \quad (2.11)$$

where, C is the bulk concentration of the reactant and k_0 is the heterogeneous reaction rate constant.

Tafel plot

At sufficient polarization (or overpotential), the Butler-Volmer equation may be treated with a Tafel kinetics approximation, which assumes the domination of either the anodic or the cathodic branches and thus neglecting the other one (similar to Eq. 2.9). The Tafel plot is a plot of the log of the current density versus the overpotential for that given reaction. In such case, Tafel plot may be used to experimentally estimate the exchange current density (i_0) of a given reaction, by reading the intercept of the current on that semilog plot at zero overpotential. This technique was applied in the thesis during studying NAq electrolytes to estimate the exchange current density in flow-through configuration [70], as shown in Chapter 4.3.

In general, during galvanic operation of a fuel cell or flow battery, the reduction current will flow through the cathode whereas the oxidation current will flow through the anode. Due to conservation of current, these currents will be equal, to balance the circuit. However, each electrode will have a different associated overpotential, which will depend on the respective exchange current density of each of the half-cell reactions. The sum of these overpotentials from both electrodes, otherwise known as the activation or kinetic overpotential of the cell, may therefore represent the minimum voltage loss required to produce a given current from the two reactions.

2.2.2. Ohmic overpotential

The ohmic overpotential (Region II in Figure 2.2) results from the resistance to the flow of electrons through the electrodes and the external circuit that has the load. It also results from the resistance to the flow of ions in the electrolyte. The ohmic loss in the electrolyte typically dominates the overall ohmic overpotential, which can thus be

reduced by decreasing the electrode separation (electrolyte thickness) or by modifying the electrolyte properties to enhance its ionic conductivity or adding a supporting electrolyte to the reactants. In any case, both ionic conductivity and electronic conductivity of the various components of the cells are finite and can be generally represented as a linear ohmic resistor. The ohmic overpotential thus depends proportionally on the increase in current drawn from the cell, following Ohm's law (Eq. 2.12), and increases with the entire range of current densities due to the nature of electrochemical cell resistance, as mentioned.

$$\eta_{Ohmic} = I \times R_{cell} \quad or \quad i \times ASR_{cell} \quad (2.12)$$

where, R_{cell} is the combined electrochemical cell resistance in Ω , and ASR_{cell} is the area specific resistance of the cell in $\Omega.cm^2$. R_{cell} can then be estimated as the summation of the series of resistances in the fuel cell encountered in the different phases such as anode and cathode resistances (R_a and R_c , respectively), the contact resistances in both electrodes (R_{con}) and electrolyte resistance (R_{elec}), as given in Eq. 2.13.

$$R_{cell} = R_{c,con} + R_c + R_{elec} + R_a + R_{a,con} \quad (2.13)$$

When the combined cell resistance is constant throughout the entire current density range within an experiment, subtracting the ohmic overpotential from the overall polarization curve is often applied, to show the ohmic independent performance, or to compare other non-ohmic aspects of the performance. This technique is referred to as IR-compensation.

2.2.3. Concentration overpotential

The third source of voltage loss is related to mass transport, which dominates at the high current regime of the polarization curve (Region III in Figure 2.2). While the electrochemical reaction is taking place, the reactants species are consumed at the electrode surface. At high reaction conversion and reactant utilization rate, this leads to the formation of concentration gradients between the reactants at the electrode surface and the bulk of the reactants. This causes a loss in the potential known as the

concentration overpotential or the mass transport overpotential (η_{MT}). The mass transport overpotential can similarly be explained as a result from the depletion of the reactant on the electrode surface and the difficulty of the bulk species to maintain the initial concentration.

The change in potential caused by the mass transport overpotential can thus be described with the help of Fick's law of diffusion, shown in Eq. 2.14. The current density can then be given as shown in Eq. 2.15.

$$j = -D\nabla C \quad (2.14)$$

$$i = \frac{I}{A} = nFD \frac{(C_b - C_s)}{\delta} \quad (2.15)$$

where, j is the molar flux, D is the diffusion coefficient of the species, ∇C is the concentration gradient, I is the current, i is the current density, A is the electrochemical surface area, δ is the boundary layer thickness and the subscripts b and s represent bulk and surface concentrations, respectively.

The molar flux (j) can also be expressed in terms of the mass transfer coefficient (k_m), as shown in Eq. 2.16. The mass transfer coefficient (k_m) depends on the electrode structure and geometry, the physical properties of the reactant species and the velocity of the flow or the hydrodynamic conditions near the surface in general.

$$j = \frac{i}{nF} = k_m (C_b - C_s) \quad (2.16)$$

At maximum consumption or conversion of the reactant species, the surface concentration (C_s) can be assumed to equal zero. The current density in this case is called the limiting current density (i_{lim}), as given in Eq. 2.17. In this case, the rate of supply (mass transfer) of fresh reactants to the surface of the electrodes equals the rate of consumption of the reactant species (reaction kinetics).

$$i_{lim} = \frac{nFDC_b}{\delta} \quad (2.17)$$

2.2.4. Other voltage losses

Region IV in Figure 2.2 represents the last form of overpotential or voltage loss represented by the deviation of the actual cell OCP from the theoretical or expected Nernst potential. This is mainly a result of either crossover of fuel or any electrical short circuits in the fuel cell. The fuel cell electrolyte should ideally be electrically insulating and should allow the selective ion transport across the two half-cells whilst preventing other ions or fuel transport. Practically, this is not possible to achieve. This therefore results in a voltage loss from the waste of fuel passing through the electrolyte or from any electron conduction through the electrolyte.

In a stack in which cells are fluidically connected through the electrolyte, a shunt current may be drawn in an internal parasitic cell which results in a loss in the cells voltage as well as a loss in electrolyte charge [4,91,92]. This is not very common in hydrogen fuel cells but is usually common when using liquid electrolytes such as in flow batteries. These internal shunt currents also belong to this region of the polarization losses and were studied in this dissertation.

In addition, in membraneless cells such as CLFCs, the separation is utilized by means of the co-laminar interface. In this case, the diffusive mixing of the species together with the concentration boundary layers formed on the walls of the microfluidic channels may also result in a crossover voltage drop if the reactants diffuse from one half-cell to the other. This requires careful engineering of such cells and tuning their operational parameters as studied in this dissertation and as will be explained in the next section. While voltage losses may be eliminated by preventing the ions diffusion to reach the opposite half-cell electrode causing the mixed potential losses, a loss in charge may still occur due to the diffusion mixing that occurs along the co-laminar interface.

2.3. CLFC theory

Reynolds number (Re) is a dimensionless group that defines the ratio between the inertial forces to the viscous forces, as given in Eq. 2.18, where, U is the average velocity, L is the characteristic length, and ν is the kinematic viscosity of the fluid. The characteristic length is also often referred to as the hydraulic diameter (d_h), which can be

estimated from the channel cross section area (A_c) and the wetted perimeter (P_w), as shown in Eq. 2.19. In microfluidics, the flow is usually characterized by following laminar flow regime in most conditions with low Reynolds number (< 2000).

$$Re = \frac{U L}{\nu} \quad (2.18)$$

$$d_h = \frac{4A_c}{P_w} \quad (2.19)$$

Peclet number (Pe) is another dimensionless group that represents the ratio of convection to diffusion mass transport, as given in Eq. 2.20, where D is the diffusion coefficient of the species in the fluid.

$$Pe = \frac{U L}{D} \quad (2.20)$$

Therefore, for small Pe , the diffusion transport is fast compared to convection and thus the fluid mixing is governed by diffusion transport, such as in passive mixers. When the flow regime is characterized by low Re and high Pe , such as in microfluidic flow, the fluid mixing is harder because of the slow diffusion transport while the convective transport is negligible [93,94]. When two liquid streams are introduced in a microchannel, a diffusional interface is created between them, as sketched in Figure 2.3. The width of the formed diffusional interface grows in the downstream direction along the microchannel length.

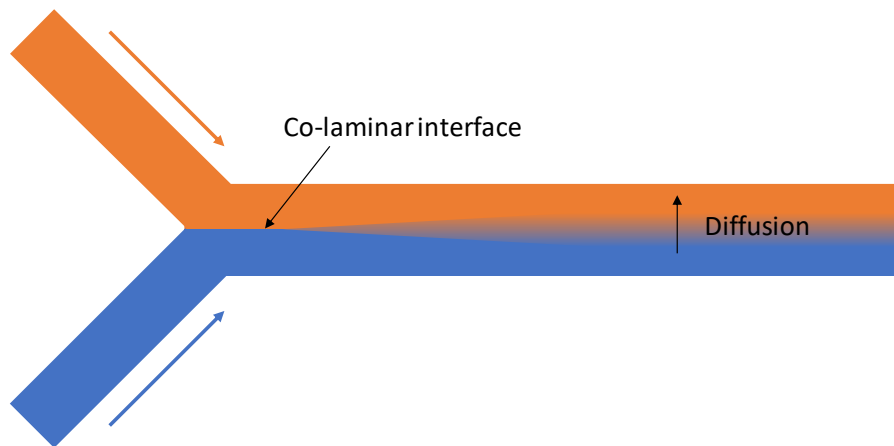


Figure 2.3. A sketch of the CLFC fundamental concept utilizing laminar flow to separate reactant streams.

Hence, by careful engineering of the microfluidic channel geometry and operation parameters, this co-laminar interface can be utilized to provide the necessary separation of the two reactant streams without any physical barrier or membrane whilst permitting the ion transport between the electrodes. This offers great advantages in cost, simplicity and durability, since membranes are a major source of high cost and degradation in fuel cell technology. Thus, as a design rule, the residence time (t_{res}) of the fluid in the microchannel length must be shorter than the diffusion time (t_{diff}) of the species across the microchannel. This is necessary to prevent crossover of any reactant species to the opposite electrode which would result in a mixed-potential, defined previously in section 2.2.4. This rule can be estimated using Einstein's relation for one-dimensional Brownian diffusion, as shown in Eq. 2.21. The equation includes the channel length (L) and channel width (W) as two geometric parameters, the mean velocity (U) as an operational parameter and the diffusion coefficient of the reactant species as a physical property.

$$t_{res} = \frac{L}{U} < \frac{W^2}{2D} = t_{diff} \quad (2.21)$$

In most cases, microfluidic flow is driven by means of pumps, and is therefore considered as pressure-driven flow. Microfluidic liquid flow is typically assumed to follow the continuum hypothesis and the general Navier-Stokes equations [92], because of the macroscopic length scales involved. In other cases, paper or other wicking materials are utilized to provide the flow by capillarity. In paper-based microfluidics, the pumps are eliminated and the overall passive system is cheaper, simpler, more compact and often disposable. The capillary flow occurs because the adhesive forces between the liquid and the solid surface (the paper fibers for example) are stronger than the cohesive forces in the liquid, which results in a driving capillary pressure. In the paper based devices, the pores of the paper substrate act as small capillaries and the capillary flow in these devices thus follows Darcy's law. The capillary flow rate is a function of the capillary pressure, surface energy, liquid viscosity and the permeability and geometry of the paper substrate. Paper-based microfluidics was utilized in this thesis in the PowerPAD project (Chapter 4.4).

Chapter 3.

Methodology

3.1. Cell design and fabrication

Note: The design and fabrication regarding the PowerPAD project (Chapter 4.4) is excluded from the context of this dissertation because it was not a direct contribution and was led by the project collaborators and thus deemed out of the scope of this thesis. Details on the design and fabrication may be found in the attached appendices.

3.1.1. Analytical cell

The geometry of the analytical cell design used throughout the thesis was chosen similar to the original MRB design [15] with dual-pass architecture in order to provide reliable diagnostic data. The original MRB design with dual-pass architecture, shown in Figure 3.1a, is modified by splitting each of the positive and negative electrodes into two separate sections; at the different inlet and outlet passes, as shown in Fig. 3.1b.

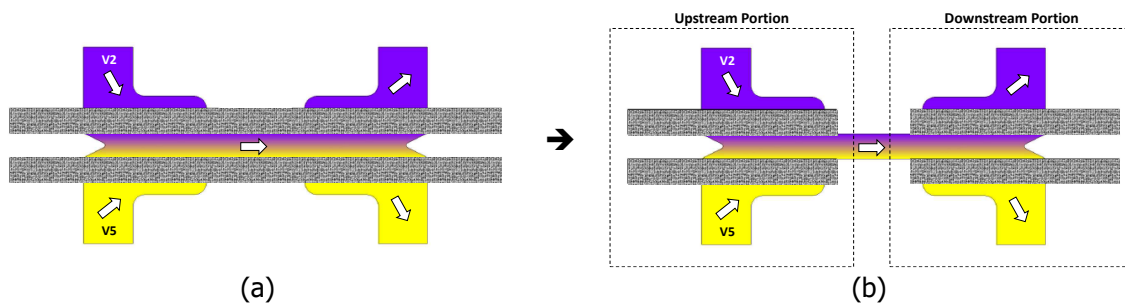


Figure 3.1. Dual-pass cell designs: a) the original MRB design and b) the modified design to form an analytical cell.

Since the geometries are identical, this modification means that the analytical cell design formed features electrodes that are 1 mm wide and separated by a 1 mm wide microchannel. The cell has the same height of 150 μm . The mask design used for the fabrication process is provided in Fig. 3.2, showing the geometric dimensions of the analytical cell design. Each cell portion has an active electrode area (normal to the flow direction and parallel to the co-laminar interface plane) that is 5 mm x 0.15 mm.

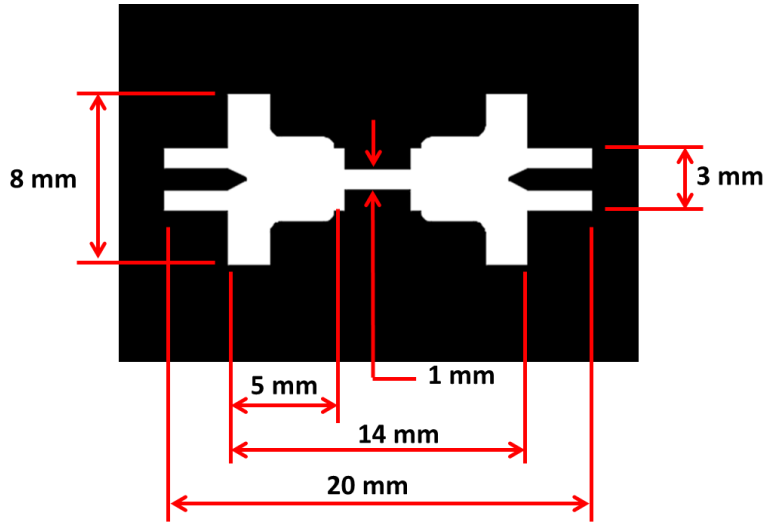


Figure 3.2. Mask for the analytical cell showing geometric dimensions

The CLFCs presented in this dissertation as analytical platforms are typically fabricated using soft lithography microfabrication techniques available in our lab. A base layer of a photoresist (SU-8 2100) is first spin-coated and fully cured to provide support for the secondary layer which contains the master structure for mold replication. The cell is designed using computer aided design (CAD) software (AUTOCAD, 2014) and printed on a transparency mask having the design features of the microfluidic device. The mask (Figure 3.2) is then exposed to UV (15 seconds) on the secondary layer of the photoresist and then hard baked. Next, the master is immersed in the developer solution (Microchem) for 20 minutes and then rinsed with acetone and propanol, respectively, until all residual unexposed SU-8 from the second layer is removed. The height of the SU-8 master is checked by a profilometer to be around the desired value of 150 μm . A 10:1 ratio of polydimethylsiloxane (PDMS) and its hardening agent (Dow Corning) is prepared by rigorously mixing and the mixture is then poured over the master, deaerated by putting under vacuum, and cured for three days or in a few hours by applying heat.

The mold is then peeled off the substrate and cut to shape, and holes are punched for fluidic and electrical connection ports.

Next, rectangular electrode strips for the electrodes of the device are cut from heat treated carbon paper (TGPH-060, Toray) with the desired width around 0.9 mm. The slight difference in height ($\approx 40 \mu\text{m}$) between the electrode thickness and channel depth assures electrode compression and minimizes flow bypass above or below the electrodes. After the electrodes are manually placed inside the PDMS in their respective grooves, a glass lid is bonded permanently to the PDMS by applying a plasma treatment of the two surfaces of glass and PDMS (Electro-Technic Products, BD-20AC). The cell is then left under a weight over night to ensure good and permanent seal. Silver conductive epoxy (MG Chemicals) is used to bond electrical wires to the electrodes. The fabrication process is summarized in Figure 3.1. Tygon tubes (Saint-Gobain) with small diameter (1/32" inner diameter and 3/32" outer diameter) are inserted into the inlets and outlets of the device. A photograph of the final device after assembly and insertion of tubes and electrical wires is shown in Figure 3.2.

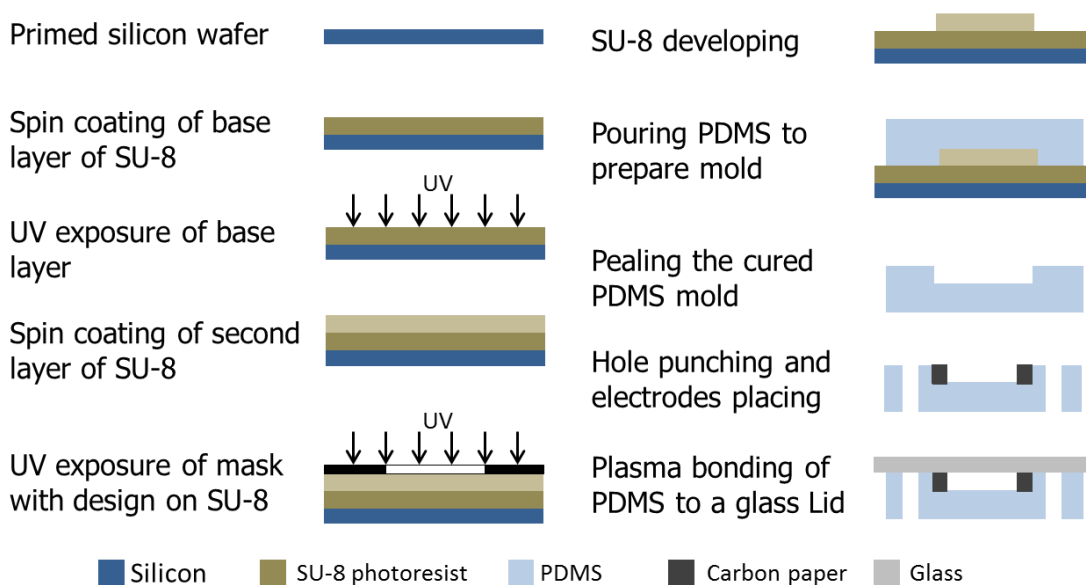


Figure 3.3. Complete fabrication process flow of the CLFCs using soft lithography.

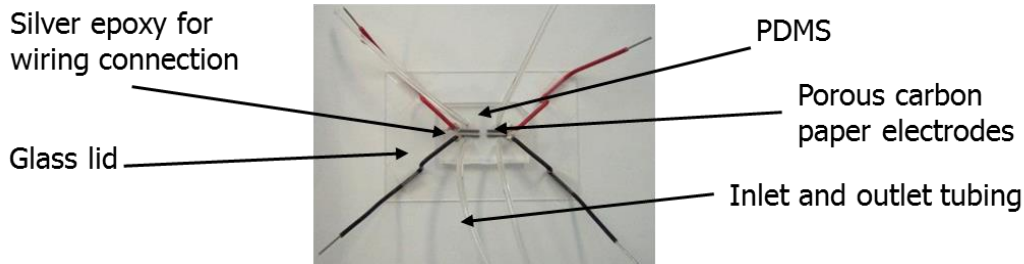


Figure 3.4. A photograph of a CLFC made in PDMS after full assembly.

3.1.2. RFPCB devices

The RFPCB devices used in Chapter 4.5 for the application of combined thermal and power management with IBM Research – Zurich are operated using vanadium redox electrolyte. The devices are fabricated in PCB materials (core, FR4). The different parts are designed by commercial CAD software and sent for fabrication (PCB-pool®, Beta LAYOUT GmbH, Germany). The PCB components serve as supporting materials as well as current collectors. Different flow field designs can be directly made in the PCB materials.

In this dissertation, serpentine flow field is primarily selected because of its foreseen low pressure drop, enhanced mass transport and microchannel liquid cooling benefits, necessary for the present application. The serpentine channels are 1 mm wide and are milled through the whole PCB thickness (0.5 mm deep). Silver and gold are used for the current collection for the negative and positive half-cells, respectively, to be compatible with the respective redox couples; V^{2+}/V^{3+} and VO^{2+}/VO_2^+ , respectively. Fiberglass sheet pre-impregnated with resin (pre-preg) is used to form complementary parts which are designed also using CAD software and sent for water-jet cutting (Qualicut AG, Volketswil, Switzerland). These components serve as electrode housing that, once cured, will form the necessary sealing bond. They also provide the necessary seal for the PCB parts with serpentine flow field. Lastly, for the CLFC studied in this dissertation, three pre-pregs are stacked to create the required co-laminar microchannels, as discussed later in Chapter 4.5. The stacked pre-pregs thus form the co-laminar separator which features six rectangular microchannels with a width of 1 mm and a length of 28 mm. The six channels enable good ionic transport area and thus

reduce the ionic resistance whereas the geometrical dimensions are estimated to maintain the laminar flow conditions. Heat treated carbon paper (Toray, TGPH 060) is used as electrode material ($1.3 \times 2.9 \text{ cm}^2$). Figure 3.5 shows a schematic of the design of the serpentine flow fields made in the PCB material and the pre-preg components, which provide sealing and electrode housing and form the array of six microchannels where the co-laminar separation takes place.

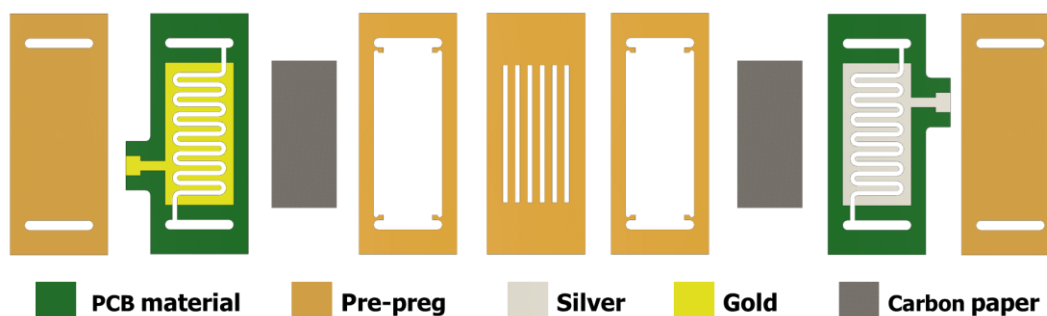


Figure 3.5. A schematic showing the components of the membraneless RFPCB design.

The RFPCBs are fabricated by lamination on a hot plate at a temperature of 170°C and under sufficient pressure using a steel block weight. A photograph is shown in Figure 3.6 for the final RFPCB assembly attached to a custom holder that connects the inlet and outlet tubing from their respective ports on the RFPCB to the pumps.

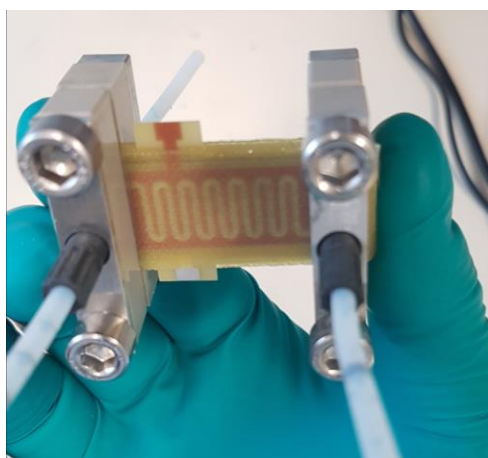


Figure 3.6. A photograph of the RFPCB cell after lamination. The cell is connected to a custom designed holder that provides connection of inlet and outlet tubing to their respective ports.

3.2. Electrochemical testing

The reactant flow into the cell is driven by a dual syringe pump (Harvard Apparatus) within the required flow rate. Fuel cell performance is demonstrated by measuring discharge polarization curves using a potentiostat (Gamry, Reference 3000) by linearly sweeping the voltage and measuring the current with a scan rate that is slow enough to ensure consistency with the steady-state results of potentiostatic measurements. The ohmic resistance of the cells under testing is measured by means of electrochemical impedance spectroscopy (EIS) performed using the same potentiostat by reading the high frequency real-axis intercept of the Nyquist plot, with an AC amplitude of 10 mV rms at OCP, over a frequency range of 1 MHz to 10 Hz. Ex-situ electrochemical analyses such as cyclic voltammetry (CV) are performed in a conventional three electrode beaker cell, using a glassy carbon (GCE) working electrode (WE), a platinum wire counter electrode (CE), and a saturated calomel (SCE) reference electrode (RE), unless otherwise mentioned. Further design, fabrication or electrochemical characterization methods may be found individually for each study in this dissertation.

Chapter 4.

Summary of contributions

As stated before in the introduction in Chapter 1, the scope of this dissertation focuses mainly on practical advances for microfluidic electrochemical energy technology. The dissertation presents several scholarly contributions in this regard, such as the journal articles given in Appendices A-E. Here, in this chapter, these contributions to the state-of-the-art of microfluidic electrochemical energy conversion in flow-through porous electrodes are summarized in the following sections. Rather than chronological organisation, the contributions are arranged according to the different practical utility of the work mentioned in Chapter 1; analytical cells, disposable power sources and simultaneous power and thermal management of electronics.

4.1. *In situ* characterization of dual-pass cell architecture

The first study taken in my PhD studies served as a continuation of prior works conceived by my predecessors from our research group, who developed the microfluidic redox battery (MRB) that relied on symmetric, dual-pass architecture and had reversible charging and discharging capabilities. The original dual-pass architecture offered improvements in performance characteristics and enabled new capabilities for co-laminar flow cells (CLFCs), such as reactant recirculation and in-situ regeneration, which resembled typical redox flow batteries (RFBs) operation. This cell achieved power densities around 300 mW/cm² and 20% full cycle energy efficiency [15].

Despite the benefits shown to the dual-pass architecture, the cell design was generally difficult to optimize because of the convoluting effect of the two reactant passes; inlet and outlet, through the same electrode. The objective of the first study was therefore to develop an analytical cell design with flow-through porous electrodes and dual-pass architecture. The analytical cell design was to be applied to the in-situ

characterization of MRBs with dual-pass architecture. The geometry was therefore chosen similar to the original MRB design [15] with dual-pass architecture in order to provide reliable diagnostic data. The original MRB design with dual-pass architecture was however modified by splitting each of the positive and negative electrodes into two separate sections; at the different inlet and outlet passes, as shown before in Figure 3.1. This configuration could then be applied in order to characterize the formed upstream and downstream cell portions individually. In addition, the two cell portions were connected in parallel in order to resemble the device function of the original MRB whilst permitting detailed analytical characterization of the upstream and downstream cell portions during operation. With this approach, the local current densities at the upstream and downstream cell portions could be measured independently without major alteration of the original MRB architecture. Moreover, the effect of reactant crossover could be readily assessed by comparing the performance of each individual cell portion.

By connecting each portion at open circuit potential (OCP), the crossover of the cell portions was assessed and quantified. For example, the upstream cell OCP was measured at 1.563 V at flow rates of 10 and 100 $\mu\text{L}/\text{min}$, indicating absence of crossover losses. The downstream cell portion however had an OCP of 1.522 V and 1.55 V at flow rates of 10 and 100 $\mu\text{L}/\text{min}$, respectively. In other words, this meant that the downstream cell portion was subject to crossover losses of 41 mV and 13 mV at flow rates of 10 $\mu\text{L}/\text{min}$ and 100 $\mu\text{L}/\text{min}$, respectively. This confirmed that reactant crossover took place due to species diffusion along the channel as well as asymmetric splitting of the reactant streams at the outlet junction before entering the porous electrodes of the downstream portion, as was shown in the results of Goulet and Kjeang [51] on the MRB design. It also confirmed that the reactant crossover decreases at higher flow rates, since the species diffusion was reduced at the higher flow velocity due to a shorter residence time in the co-laminar channel. However, regardless of the flow rate, the downstream cell portion was still exposed to a certain amount of crossover losses due to the aforementioned asymmetric splitting of the two reactant streams at the outlet splitting junction.

When the flow cell discharge operation was investigated, the upstream cell portion achieved a remarkably high room-temperature performance at the high flow rate of 100 $\mu\text{L}/\text{min}$. A peak power output of 5.6 mW was achieved at 7.8 mA. These values corresponded to a power density of 750 mW/cm^2 at a current density of 1.0 A/cm^2 , which

was the highest power density reported at the time for a microfluidic vanadium redox battery. A maximum current density of about 2.0 A/cm^2 was also achieved. The monitored OCP of the unconnected downstream cell portion during the voltage sweep was shown to decrease from 1.550 V at upstream OCP to 1.519 V at the end of the voltage sweep, for the same high flow rate of $100 \mu\text{L/min}$. This 31 mV voltage decrease reflected an estimated 5.6% consumption (conversion) of the vanadium redox reactants in both of the upstream electrodes during the voltage sweep, which resulted in a decreased concentration or SOC and thus a decreased OCP at the downstream portion. At the lower flow rate, the same trends were also observed with a higher downstream OCP drop of 132 mV from 1.522 V to 1.390 V , reflecting a higher $\approx 40\%$ conversion, because of the higher utilization efficiency and longer residence time at the lower flow rates.

When the two cell portions were connected in parallel, the device resembled the original MRB design functionality. At a flow rate of $100 \mu\text{L/min}$, the pair achieved a maximum power output of 9.5 mW at a current of 13.5 mA and cell potential around 0.7 V . The equivalent maximum power density was 630 mW/cm^2 , which was lower than that for an individual portion, because of the lower performance of the downstream cell as it had lower incoming reactant SOC. Despite that, higher fuel utilization efficiency was expected since the unused reactants in the upstream portion were partly consumed downstream. Therefore, the estimated maximum utilization efficiencies at the two flow rates increased from 40% to 52% and from 5.6% to 9.4% , at $10 \mu\text{L/min}$ and $100 \mu\text{L/min}$, respectively. For this reason, the current of the downstream portion was observed to be highly influenced by mass transport losses at the low flow rate, when the two cell portions are connected in parallel, as a consequence of the high fuel utilization at low flow rates. In addition, at this region of mass transport limitations, it was noted that the current output of the downstream portion decreased with the increase of the total current output of the combined parallel cell, which was attributed to a shift in the relative current contributions of the two portions from nearly equal at near-OCP conditions to upstream-dominated current at lower cell potentials. This interesting feature, which was uniquely revealed by the present analytical cell configuration showed the detrimental effect of high reactant conversion in the upstream portion on the performance of the downstream portion. Nevertheless, at the higher flow rate of $100 \mu\text{L/min}$, the mass transport was enhanced and the concentration overpotential was reduced.

Finally, the present analytical device was applied to investigate and diagnose the effectiveness of the two cell portions under relevant conditions of *in situ* regeneration (charging) of the vanadium species, by operating on low SOC (30% VO₂⁺) electrolytes at flow rates of 10 μL/min and 1 μL/min. The initial upstream OCP was 1.359 V while the downstream OCP equalled 1.345 V and 1.279 V at 10 and 1 μL/min, respectively, indicating a significant rate of diffusive crossover. By charging the upstream cell portion at 1.7 V, the downstream OCP increased from 1.345 to 1.376 V, at 10 μL/min, which meant a net voltage gain of 31 mV or 17 mV over the initial inlet upstream OCP. At 1 μL/min, the downstream OCP increased from 1.279 to 1.421 V, which was equivalent to a net gain of 142 mV (62 mV over upstream OCP) and an estimated 27% increase in SOC.

The analysis thus revealed the significant influence of the crossover losses on the charging performance. This was confirmed visually as well from color changes of the electrolytes which indicated a VO₂⁺ dominated electrolyte with high SOC (95%), at flow rate of 1 μL/min, at the outlet of the upstream cell portion, which then encountered diffusive crossover and asymmetric splitting of the two co-laminar streams towards the downstream portion (38% loss). The downstream portion was used to charge the electrolyte by connecting with the upstream portion in parallel to counteract this crossover loss and contribute additional net charge to the reactants. For example, at 10 μL/min, the SOC of the VO₂⁺ electrolyte reached 41% upstream and decreased to 37% due to crossover. During parallel charging, the downstream portion had a calculated reactant conversion of 13%, which corresponded to a theoretical VO₂⁺ outlet SOC of 50% (net cell charging of 20%). The symmetry of the analytical cell was also utilized to demonstrate a charge-discharge cycle test, which showed a charge-discharge cycle efficiency of ~19-21%, which was primarily limited by reactant crossover.

In general, the analytical device provided a straightforward *in situ* method to directly assess the voltage losses in MRBs by simple voltage measurements, and could readily distinguish voltage losses from crossover from voltage changes due to reactant conversion during both discharging and charging operations. The quantitative findings of this analytical study therefore provided a deeper understanding of the reaction conversion and voltage losses during the discharging and charging processes of CLFCs with dual-pass architecture, which would aid further device design and optimization. The study resulted in a full-length journal article [95] in Appendix A.

4.2. Characterization of shunt current in arrays

Various studies including from our group attempted stacking of CLFCs or had studied stacking losses, for multiple cells in parallel or in series [31,96,67,97]. However, none of these studies presented combined serial electrical connection of the cells to increase the voltage output with serial fluidic connection to reuse the partially consumed reactants and thus maximize the fuel utilization. In general, stacking of microfluidic fuel cells and redox batteries might cause internal current losses and reduced performance compared to single cells.

Therefore, the objective of the second study was to experimentally examine and quantify the effect of internal shunt currents on the performance of a microfluidic electrochemical cell array uniquely designed for reutilization of reactants in a single flow manifold. These shunt currents undesirably occur with electrolytic connections during stacking of electrochemical cells. Again, the same analytical cell design that was used in the first study (Section 4.1) was utilized in this characterization. The cell was based on the modified MRB design and featured flow-through porous electrodes and dual pass architecture, with split electrodes. A two cells array was formed by series electronic connection of the two cell portions. This permitted a detailed comparison of upstream and downstream cell performance and also revealed the effects of shunt current due to the shared electrolyte manifold when the cells were connected in series. The two cell portions also had series fluidic connection through the common electrolyte manifold in order to reuse the partially consumed reactants from the first, upstream cell in the second, downstream cell to maximize overall fuel utilization.

It was noted that once the two portions were connected in series, the OCP measured for the upstream portion dropped, despite the absence of any additional crossover losses. For example, at 100 $\mu\text{L}/\text{min}$, the upstream portion OCP dropped to 1.378 V versus 1.556 V when measured individually with absence of series electrical connection with the downstream portion. In addition, visual color changes in the vanadium redox electrolytes were observed, indicating reactant conversion even though the cell array was kept at OCP. A current was also measured confirming reactant discharge through the cross cell, formed from the upstream cell anode and the downstream cell cathode, since it was electrically short circuited and had ionic connection by the electrolyte. This explained the observed color changes and the

upstream and downstream OCP drop, and warranted detailed characterization of the cross cell.

The polarization curve of the cross cell was measured at flow rates of 10 and 100 $\mu\text{l}/\text{min}$ and was found to be highly linear, which indicated that the performance was controlled by ohmic losses. This was also confirmed by the combined ohmic cell resistance of $750\ \Omega$ measured by EIS. This high resistance was more than an order of magnitude higher than for a regular cell which was dominated by the ionic resistance of the electrolyte in the long and narrow microchannel between the two electrodes of the cross cell. The polarization curves also indicated a limiting current around 1.5 mA for both low and high flow rates. During polarization, the OCPs of the upstream and downstream portions were monitored and were shown to decrease with increasing current drawn from the cross cell, but at different rates. The upstream OCP curve experienced a more negative slope than the downstream one. These changes were caused by the electrochemical overpotentials induced by the cross cell polarization in which the anode of the upstream cell had a greater impact than the cathode of the downstream cell due to the slower electrochemical kinetics of the V^{2+} oxidation compared to the VO_2^+ reduction occurring on the cathode. For example, at 100 $\mu\text{l}/\text{min}$, the upstream and downstream OCPs decreased down to 1.386 V and 1.466 V, respectively, at the conditions of maximum cross cell current. These values together with the measured cross cell maximum current were identical to those noted during the serial connection of the upstream and downstream portions, when the pair was at OCP conditions. This was uniquely enabled by direct measurement with the analytical cell design and confirmed the losses in the parasitic cross cell due to the serial electrical connection and ionic electrolytic connection.

The series array was then characterized and gave a maximum power output of 6.5 mW ($434\ \text{mW}/\text{cm}^2$) and 9 mW ($600\ \text{mW}/\text{cm}^2$) and limiting currents of 6 mA ($400\ \text{mA}/\text{cm}^2$) and 13.5 mA ($900\ \text{mA}/\text{cm}^2$) at the two flow rates, respectively. The voltage contributions of the upstream and downstream portions to the serial array as well as the current passing through the serial connection were also recorded during the polarization. At 10 $\mu\text{l}/\text{min}$, the performance of the array was limited by concentration losses. The overall performance of the upstream and downstream cell units was similar at low to medium currents up to 4 mA, where mass transport effects were less prominent. However, at lower array voltage and higher currents, a negative cell voltage was

observed for the downstream portion, which confirmed the starvation of the downstream cell leading to a reversed potential in order to support the total array current. This behaviour was not observed at higher flow rates of 100 $\mu\text{L}/\text{min}$, where more reactant species were available and the fuel utilization was generally less than 5%. This finding was again only revealed by applying the unique analytical cell design.

The current passing through the serial connection was also shown to be higher than the current running through the whole cell array or through the potentiostat. This was because the current running through the serial connection was the sum of the currents from the regular series cell discharging through the connected load during operation and the cross cell discharging at short circuit, formed due to the serial connection. A decreasing trend was noted for the current difference from 1.75 mA at OCP of 2.829 V to only 0.22 mA at the lowest tested voltage condition of 0.1 V, at the flow rate of 100 $\mu\text{L}/\text{min}$. This current difference was therefore demonstrated to be equal to the shunt current that the array experiences internally. The internal shunt current was also shown to be roughly proportional to the operating voltage of the array with the driving force being the electrochemical potential difference of the electrodes of the internal cross cell circuit. The shunt current was discharged through the electrolyte which acted as a resistor for the parasitic internal circuit; hence, increasing the ionic resistance of this pathway would reduce the magnitude of the shunt current. Hence, the maximum shunt current was when the array was held at OCP where the potential difference was greatest.

This internal shunt current was therefore a parasitic reaction from which both cells of the array suffer, primarily in the form of charge loss but also in the form of a slight voltage loss. In order to quantify the effect of the shunt current, the loss in the available state-of-charge of the reactants due to the reactant consumption for the parasitic discharge associated with the shunt current was considered. The drop in coulombic efficiency of the present cell array configuration was determined to be up to 7% at OCP, for the flow rate of 10 $\mu\text{L}/\text{min}$. This result confirmed the significance of the shunt current losses in microfluidic cell arrays and stacks and highlighted the importance of taking it into consideration for array cell design and operation.

In the end, the study provided a novel way of assessing the shunt current losses, which resulted in a full-length journal article [98] in Appendix B. The negative effects of

the shunt current could be mitigated by providing adequate electrolytic charge transfer resistance between adjacent cells, for instance by reducing the cross-sectional dimensions of the electrolyte channel between the cells, although the consequences in terms of reactant crossover and total pressure drop must also be considered. This trade-off was therefore found to be important when designing microfluidic fuel cell arrays and stacks.

4.3. Leveraging CLFCs for non-aqueous systems

The idea of this study started after a collaborative study with my predecessor which resulted in superior power density for a flow cell suggesting revisiting the use of liquid electrolyte for separation [52]. In general, the study reported a cell area specific resistance (ASR) of $0.12 \text{ } \Omega\text{cm}^2$, using conventional vanadium redox electrolyte in a membraneless co-laminar flow cell. It was realized that this membraneless CLFC configuration may offer an alternative solution for non-aqueous (NAq) flow batteries which suffer from relatively high ohmic losses because of the weaker conductivity of the supporting electrolyte and the high membrane resistance when used in non-aqueous solvents. This offers a promising novel alternative to overcome this main bottleneck for NAq flow cells, namely the ohmic limitation and to enable numerous advantages. For example, unlike aqueous flow cells, whose voltages are limited by the water splitting window ($<1.5 \text{ V}$), NAq solvents enable expanded single cell voltage and thus potentially offering much higher energy density as well as wider operating temperature range and faster charging rates.

Therefore, the aim of this study was to leverage the benefits of membraneless CLFC operation with flow-through porous electrodes, for NAq electrolytes for the first time, in order to boost their performance. A model NAq chemistry based on the well-developed vanadium acetylacetonate (V_{acac}) species and tetraethylammonium tetrafluoroborate (TEABF_4) supporting electrolyte in acetonitrile (AN) solvent was selected. Table 4.1 shows the chemistry forming aqueous VRFB and the selected NAq chemistry. Various performance aspects that influence flow cell performance such as kinetics, electrodes wettability, ASR and crossover were experimentally investigated aiming to understand the electrode performance and interaction with the NAq

electrolytes. Finally, the discharge performance in a single CLFC is measured and compared with other NAq systems to assess the power density capabilities offered by using flow-through porous electrodes to enhance kinetics, wetted surface area and mass transport combined with using a membrane-less cell design to reduce the ohmic cell resistance.

Table 4.1. A comparison between reactant chemistries of conventional aqueous VRFB and non-aqueous flow battery based on V_{acac} .

	Aqueous	Non-Aqueous
Solvent	H ₂ O	Acetonitrile (or other)
Supporting electrolyte	H ₂ SO ₄	TEABF ₄ (or other)
Redox reactions	$V^{2+} \Leftrightarrow V^{3+} + e^{-}$ $VO_2^{+} + 2H^{+} + e^{-} \Leftrightarrow VO^{2+} + H_2O$	$V_{acac}^{-} \Leftrightarrow V_{acac} + e^{-}$ $V_{acac}^{+} + e^{-} \Leftrightarrow V_{acac}$
Voltage window	1.26 V	2.2 V

Cyclic voltammetry (CV) measurements used to qualitatively assess the kinetics of the V_{acac} on carbon electrodes, showed two quasi-reversible half cells at -1.43 V and 0.73 V vs. SCE, corresponding to the negative and positive half-cells respectively, which indicated the theoretical voltage window of ca. 2.2 V. The redox reactions of the V_{acac} couples were shown to be generally facile with the peak current density ratios of 0.96 and 1.14 for the positive and negative half-cells, respectively, which indicated faster reactions during charging. The findings were in agreement with literature [99–101].

The reaction kinetics of the positive half-cell V_{acac}/V_{acac}^{+} was also quantified on flow-through porous electrodes using an analytical flow cell technique recently developed in our group by Goulet et al. [71]. The reaction rates were generally found to be similar or faster when compared to aqueous all-vanadium redox couples. The kinetics and mass transport were decoupled at high flow rates above 500 μ L/min, as the Tafel plot showed insignificant variation with the increased flow rate. The exchange current density was estimated to be 1.1 mA/cm² from the Tafel intercept, at this flow rate. This value of exchange current density was on the same order as that of the positive half-cell in aqueous VRFBs (VO^{2+}/VO_2^{+}) and was more than an order of magnitude higher than that of the negative half-cell (V^{2+}/V^{3+}), despite the lower tested concentration conditions. This measurement generally demonstrated that V_{acac} species in AN solvent had good

kinetics on flow-through carbon electrodes, equivalent to the conventional all-vanadium chemistry in aqueous media; hence, the activation overpotential should not pose a major performance limitation for the present NAq model system.

The wetting of the electrode materials was assessed next as it was shown to be important in flow cell applications especially with flow-through porous electrodes [82], so that the electrolytes would access the internal pores of the electrode. The electrodes wetting behaviour in acetonitrile solvent (NAq) was found to be superior to in water (aqueous). This was demonstrated by quantifying the porosity (v/v %) of a Toray (TGP-060) carbon paper sample by using the method of standard porosimetry [102,103] filled with the two solvents which showed 79% for acetonitrile, reflecting high pore lyophilicity. However, it was merely 6.0% in water indicating hydrophobic behaviour in the majority of the pore volume, which usually requires some pre-treatment steps. This behaviour was moreover confirmed visually by observing self-flow by capillarity against gravity in a carbon paper strip in AN demonstrating full electrode wetting which was absent in the case of water and was explained by the differences in the surface tension coefficients.

The CLFC experiments were then performed to investigate ASR, crossover and power density capabilities of such cells for NAq electrochemical systems. The ASR was measured by filling the microfluidic cell with blank TEABF₄ at various concentrations. The ionic conductivity of TEABF₄ was also estimated from the measured cell ASR. For example, at 1 M TEABF₄, the ionic conductivity equalled 53 mS/cm, which was an order of magnitude less than that of 4 M H₂SO₄, typically used in aqueous VRFBs. In addition, when the V_{acac} reactants were added, the ASR slightly increased, as expected. For example, the cell ASR increased from 2.7 Ωcm² to 3.1 Ωcm² for the case of a blank 0.5 M TEABF₄ electrolyte compared to 0.4 M V_{acac} species in 0.5 M TEABF₄. However, the measured cell ASR was generally below the target ASR of 5 Ωcm², defined by techno-economic models for energy storage applications [104,105]. Overall, this showed the potential for the membraneless configuration to enable NAq chemistry based flow cells, when compared to conventional RFBs with membranes which raise the total cell ASR and limit the performance.

Before performance measurement, the species crossover was briefly assessed in a CLFC with flow-through porous electrodes. The cell was fabricated by soft lithography techniques and its design was based on the same cell used in the previous

analytical studies in sections 4.1 and 4.2. The crossover was assessed by measuring the cell OCP and was found to be absent at high flow rates $> 30 \mu\text{L}/\text{min}$, due to the minimized diffusive mixing and low species residence time. The discharge polarization was finally measured and the cell performance was found to be primarily ohmic controlled. At a V_{acac} concentration of 0.4 M in 0.5 M of TEABF_4 , the cell delivered $275 \text{ mW}/\text{cm}^2$ of maximum power density output. At a higher supporting electrolyte concentration of 1 M and V_{acac} concentration of 0.2 M, the cell achieved a high open circuit potential of 2.6 V and delivered a peak power density output of $550 \text{ mW}/\text{cm}^2$. This cell performance level was generally two orders of magnitude higher than other works in the literature that utilized NAq electrolytes and was on the same order of performance as for the conventional all-vanadium aqueous chemistry in a CLFC configuration with the same cell design [95,98], as reported previously in sections 4.1 and 4.2.

While this preliminary investigation only showed the performance enhancements by altering the concentrations, many other modifications might help further boost the performance level. For example, utilizing current collectors, narrower electrode separation and deposition of carbon nanoparticles would further increase power density output [52,81]. Finally, investigating other species with higher reversible potentials such as the 4.5 V chemistry concept introduced by Gong et al. [106] would likely boost the power density output beyond that of aqueous flow cells, since the power density scales with the square of the voltage in ohmic limited cells. Overall, the study demonstrated the utility of flow-through porous electrode configuration to enhance kinetics, wetted surface area and mass transport combined with a membraneless configuration to overcome ohmic limitations and boost performance in NAq flow cells. The CLFC technology demonstrated in the study provided an ideal evaluation platform for such new developments toward high-performance flow cells for electrochemical energy conversion in NAq media.

4.4. PowerPAD

This is a result of an international, multidisciplinary research collaboration. Our group at SFU FCREL was responsible for electrode and cell chemistry development. The device design and overall components integration of the final device and the related experiments was led by the

Institute of Microelectronics in Barcelona, Spain (IMB), by Dr. Juan Pablo Esquivel, Perla Alday and Dr. Neus Sabate. The biodegradation experiments were performed and analyzed by Dr. Belen Fernandez from GIRO Joint Research Unit IRTA-UPC, Barcelona, Spain. All team members have accordingly contributed to the resulting journal articles in Appendices D-E. SFU FCREL led the chemistry evaluation paper (Appendix D) and contributed to the device concept paper (Appendix E), in terms of the chemistry selection and device comparison to other devices in literature with similar environmental features in the different article sections (Methods, Results and Discussion). Other sections in the article, written by the co-authors are not part of the scope of this thesis, but can be found in Appendix E.

During the electrochemical energy and water summit, held during the 226th meeting of the electrochemical society (ECS), in Cancun, Mexico, in Fall 2014, the idea for the “PowerPAD” was proposed as a concept for an eco-friendly, biodegradable, non-toxic portable redox power source made in paper for portable applications such as water monitoring sensors, especially in low resource settings, which lack recycling facilities. The concept arises as an idea to solve the drastically rising global rate of battery waste generation due to increased use and consumption of electronic devices. The idea was awarded funding in the science for solving society’s problems challenge from the Bill & Melinda Gates foundation and the ECS. The concept power source, displayed in Figure 4.1 was based on a microfluidic redox flow cell made on cellulose and carbon materials which would be completely safe and non-toxic, yet inexpensive. The power was generated by flowing organic redox couples through porous electrodes. These organic species would be stored in the paper in a lyophilized state and dissolve upon the addition of any liquid, such as wastewater, seawater, urine. The mass transport would entirely rely on capillary flow through the different porous materials (cellulose paper and carbon paper electrodes). Once the paper became completely wet and the species were discharged, the device could be disposed with no environmental impact, as it would not contain any metals or harmful substances. The PowerPAD acronym thus stands for Power: Portable and Disposable, but was also inspired by the paper material that forms the concept and give it the self-pumping feature and biodegradable nature. The concept leveraged recent advances in microfluidic CLFCs with flow-through porous electrodes from our group at SFU and paper-based fuel cell structures [62] from our collaborators in Autonomous University of Barcelona and University of Washington. SFU FCREL led the

contributions towards the evaluation of porous carbon electrodes and the evaluation of redox chemistries.

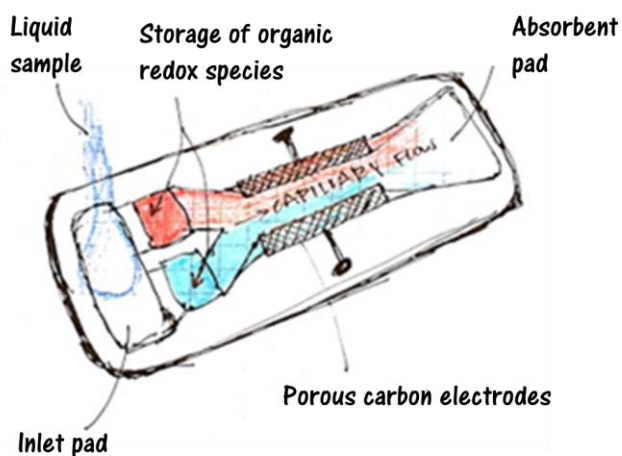


Figure 4.1. The proposed PowerPAD concept

4.4.1. Evaluation of capillary flow-through porous electrodes

The work reported in this section was a collaborative project, for which the work was carried out by me and Dr. Juan Pablo Esquivel in FCR_eL, during a visit from the University of Washington, Seattle.

The objective of this sub-study was to investigate the possible use and integration of porous carbon paper in the paper device to be used in flow-through fashion. For this, Toray carbon paper (TGPH-060) was tested and validated for the potential use as a flow-through electrode in the paper device with self-pumping using capillary effect. Carbon paper generally shows hydrophobic behaviour especially for the inner pores. The hydrophobic porosity of carbon paper was investigated briefly in the previous study, using the method of standard porosimetry (Chapter 4.3), where merely 6% of the pore volume of a carbon paper sample was found to be wetted with water. Details about the method can be found elsewhere [102,103]. Pre-treatments are thus often required to be applied in aqueous systems to enable the important wetting of the carbon paper. Here, pre-treatment techniques applied in aqueous flow cells were leveraged for the carbon paper electrodes, as described in other works by our group [82,95,98,107]. The hydrophilic porosity measured for the heat treated sample equalled 65%, confirming higher wettability, as summarized in Table 4.2.

Table 4.2. Measured volumetric solvent accessible porosity of Toray carbon paper (TGPH-060) with and without heat treatment.

Condition	Porosity (v/v %)
Data sheet	78 - 82 %
Octane	78 %
Water	≈ 6 %
Water with heat treatment	65 %

The carbon paper was then tested initially for the capillary flow of a blue ink, as shown in Figure 4.2. Both lateral flow and vertical (against gravity) flow was observed as the ink was seen to reach the absorbent pad as shown in the figure. Moreover, a setup was customized to confirm the lateral flow as shown in the figure. The setup was made of two lateral strips of paper material similar to the ones that will be used in the final device. The electrode was attached to the strips and ensured to be freely hanging, to confirm capillary flow by the carbon paper pores only. The ink reached the absorbent pad which confirmed the capillary flow-through the carbon paper.

This demonstration of fluidic conduction in an electronically conductive material therefore closed the material selection matrix required for integrating both electronics and fluidics functionalities [108], summarized in Figure 4.3. More characterization work about the fluidics and the flow in either cellulose paper or carbon paper was performed by the project collaborators in Barcelona, Spain and is therefore out of the scope of this thesis.

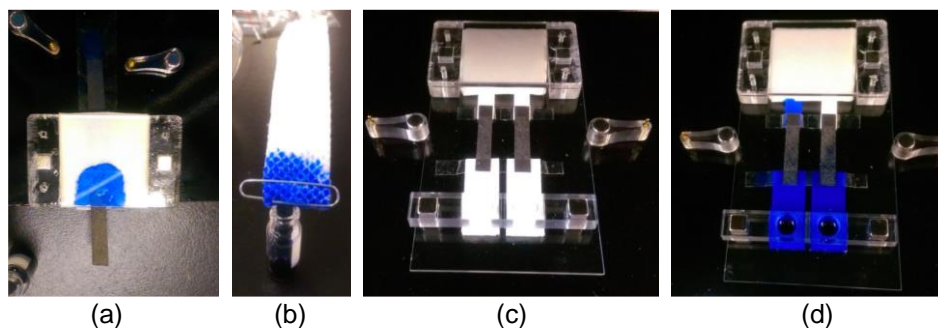


Figure 4.2. Testing Toray-060 carbon paper for capillary flow-through: a) horizontal flow, b) vertical flow against gravity, c) designed setup with hanging electrodes and d) ink reaching the absorbent pad after flowing through the porous electrode.

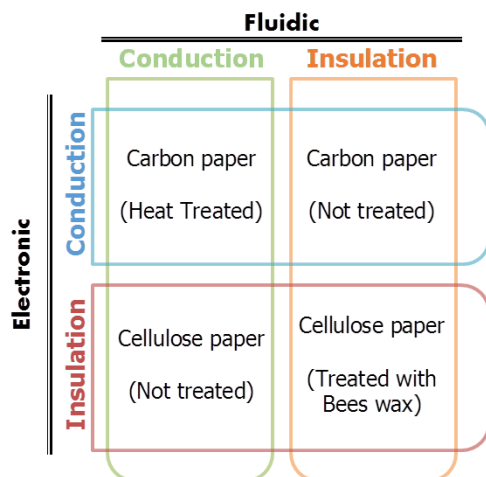


Figure 4.3. PowerPAD material selection matrix for integrating electronic and fluidic functionalities.

4.4.2. Evaluation of biodegradable redox couples

The work reported in this section was a collaborative project. The majority of the work was carried out by me in FCREL. Our collaborators contributed to the design and fabrication of the disposable cell with integrated flow-through electrodes and with on-board stored chemistries. The cell was tested by me, Ms. Perla Alday and Dr. Juan Pablo Esquivel, at the institute of microelectronics in Barcelona, Spain.

The chemistry requirements for PowerPAD were evaluated in a sub-study and resulted in a journal article [58], given in Appendix E. The PowerPAD had unique redox chemistry requirements for both half-cells to achieve a fully biodegradable device with high performance and stability, enabled by the capillary flow. The active redox reactant species therefore were required to:

- be biodegradable, aided by prediction from literature and from EPISUITE™ models, and thus preferably organic.
- exist in the solid phase at ambient conditions, such as powder form, to enable storage on the cell.
- be stored on the cell in the correct redox state required for discharge operation.
- be soluble in water or other desired electrolytes such that they dissolve upon liquid activation of the device, to flow through the porous electrodes.
- have electrochemical reactions compatible with catalyst-free carbon electrodes with fast kinetics, qualitatively assessed by voltammetry techniques.

Quinone compounds that were previously proposed for grid-scale energy storage [109–117] were identified as a potential match for the chemistry requirements except for the storage in the desired redox state. In order to overcome that challenge for direct use in discharge operation, the pH dependence of the redox potential was leveraged by operating in mixed-media conditions in which an alkaline negative electrode and an acidic positive electrode were coupled. The electrochemical reactions for positive and negative half-cells are given in Eq. 4.1 and 4.2, respectively. This enabled higher cell voltages and enabled utilization of a wider range of commercially available species and electrolytes. In addition, the mixed-media operation provided the opportunity for downstream neutralization of the acidic and alkaline streams to form neutral pH conditions for safe disposal, which was important for the disposable cell. A subset of potential organic redox species were accordingly identified to meet the selection criteria of storability, solubility, biodegradability, correct redox state, adequate redox potential and good kinetics. The selection is summarized in Table 4.3.

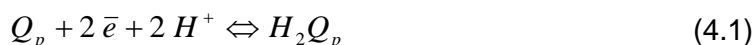
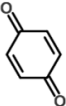
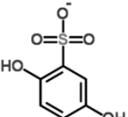
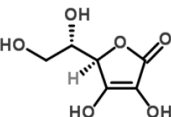
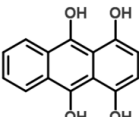


Table 4.3. Summary of selected organic redox reactants for both half cells.

	Positive half-cell		Negative half-cell	
Name	Para-benzoquinone (pBQ)	Hydroquinone sulfonic acid (H ₂ BQS)	L-Ascorbic acid (AA)	Leucoquinizarin (LQ)
Structure (CAS no.)	 (106-51-4)	 (21799-87-1)	 (50-81-7)	 (476-60-8)
Aqueous solubility	0.1 M	0.7 M	1.9 M	poor
Onset potential*	0.52 V	-0.47 V	-0.53 V	-0.80 V

*Measured at 0.1 M concentration in respective supporting electrolyte vs. SCE

The selected chemistries were then assessed experimentally, by ex-situ electrochemical techniques and in situ flow cell discharge measurements. The pBQ was the reactant species with limited aqueous solubility of 0.1 M, while H₂BQS, AA had higher limits of 0.7 M, 1.9 M whereas LQ was dismissed due to hydrophobic behaviour. The half-cell OCPs were measured before cyclic voltammetry experiments and a full cell

voltage window > 1.0 V was expected. Linear sweep voltammetry on a glassy carbon electrode revealed quasi-reversible kinetics for both half-cell species and linear proportionality of the peak current densities with the square root of the scan rate indicating a diffusion controlled process. Therefore the reactant species were deemed adequate for the application with good kinetics on bare carbon electrodes.

The KOH used as supporting electrolyte in the negative half-cell was available in solid form which allowed storing onboard the device. On the other hand, the sulfuric acid used for the positive half-cell could not be dried or stored. Therefore, other supporting electrolytes, mainly acids that were available in solid phase and were soluble in aqueous media, were identified. Oxalic acid (OA) was picked as it was an organic phytochemical and was found to have 1 M aqueous solubility limit. It had inert electrochemical activity around the working potential and the pH of OA was found to be in the range of 0.5 - 1 which indicates only slight reduction in the half-cell OCP of pBQ compared to the sulfuric acid case. However, OA had lower ionic conductivity than sulfuric acid which would affect the ohmic cell resistance and *in situ* discharge performance of the integrated cell.

The discharge performance was then measured in a microfluidic CLFC with flow through porous electrodes, similar to the cell design used in the previous sections 4.1 – 4.3, operated under mixed-media conditions at flow rate of 100 $\mu\text{L}/\text{min}$. The pBQ reactant species identified for the positive electrode was tested against the three negative electrode options of H₂BQS, AA or LQ in 1 M KOH. The reactant species were all tested at a concentration of 0.1 M for both electrodes. First, 1 M H₂SO₄ was used as a supporting electrolyte in the positive electrode to measure the benchmark performance. Although the LQ case displayed high power density of 120 mW/cm^2 as well as an OCP of 1.24 V, which was the highest all-quinone aqueous electrochemical cell OCP reported then, it was excluded due to stability and solubility issues as mentioned before. The AA showed OCP and power density output of 0.92 V and 90 mW/cm^2 , respectively, while for H₂BQS, 0.78 V and 65 mW/cm^2 , were measured, respectively, which met the present application requirements. Next, OA supporting electrolyte was tested at the same concentration of 1 M. The cell OCP for the OA case was slightly lower than the benchmark case with H₂SO₄, which was explained by the lower acidity and higher pH of OA than H₂SO₄. The discharge performance of the AA case dropped from 90 mW/cm^2 measured previously in the benchmark case to 42 mW/cm^2 when OA was used, which was mainly attributed to the overall cell resistance increase from 90 to 170 Ω . This

explained a trade-off between using OA as a supporting electrolyte that could be stored in solid phase while also having relatively lower ionic conductivity than H_2SO_4 . In general, the performance measured with dilute concentrations of active organic redox species on metal-free electrodes was remarkable as the peak power densities achieved were comparable to those of previously reported cells based on organic fuels and precious metal catalysts and was moreover several orders of magnitude higher than other environmentally friendly approaches based on biofuel cells.

Finally, the proposed redox chemistries were integrated and tested in a disposable cell design made in poly(methyl methacrylate), in which the flow was driven in paper by capillarity and all redox species and supporting electrolytes were stored in the solid phase within the device at balanced concentrations for downstream neutralization and electrochemical reaction stoichiometry. The positive half-cell compartment contained 5.4 mg of pBQ and 22.5 mg of OA while the negative half-cell compartment contained 28 mg of KOH and either 11.4 mg of H_2BQS or 8.8 mg of AA. Upon activation of the battery by the addition of 1 mL of deionized water, the OCP of the cell was monitored for one hour. The capillary flow cell could hold the cell OCP of 1.1 V and 0.8 V for both cases of AA and H_2BQS , respectively, for more than one hour. The slow decay in the OCP indicated that mixing of the two half-cell reactants progressed at a very slow pace despite their entry into a common absorbent pad. Cell polarization curves were also measured at different instants after activation and the maximum power output was measured at these different instants during the polarization curve measurements. The cell with AA anode considerably outperformed the respective cell with H_2BQS anode as expected, giving its peak power density of 7.6 mW/cm^2 (1.9 mW) at a current density of 18 mA/cm^2 (4.5 mA) compared to 4.4 mW/cm^2 (1.1 mW) at 12 mA/cm^2 (3 mA) for the latter case, which reflected the previous findings in the microfluidic cell.

The power density outputs measured in the capillary flow cell were generally lower than in the microfluidic cell, which was attributed to the variation in operating flow rates, cell resistance and the transient nature of operation of the capillary flow cell. Nevertheless, a practical performance level was achieved, meeting the requirements of single-use disposable applications and the discharge performance measured was considered sufficient to run small measuring devices or enable a wide range of other electronic components such as microprocessors, communication modules or displays.

The results of this study therefore provided the departing point for a new generation of biodegradable capillary flow cells and sustainable power sources that minimize waste from conception and design.

4.4.3. A Metal-free biodegradable capillary flow battery

Next, it was time to demonstrate a proof-of-concept prototype of the device and prove its functionality. In order to show the outstanding capabilities of this new class of capillary flow batteries, different research and development challenges beside chemistry selection were addressed: device design, battery operation, voltage scalability, practical utility and effective biodegradation. In summary, integrated quinone-based redox chemistry was used to generate electricity, as described in the previous section and this primary capillary flow battery was activated by the addition of a liquid sample, with continuous operation up to 100 min with an output voltage that can be scaled to levels needed of portable electronic devices (1.5 – 3.0 V). Once depleted, the battery can be disposed of without the need for any recycling facility, as its components are nontoxic and shown to be biodegradable in a standardized test (OECD 311). The practical utility of the device was demonstrated by direct substitution of a lithium coin cell battery in an off-the-shelf water quality sensor. The device was fabricated by a cheap bill of materials in the order of tens of cents, at a lab scale, with low-resource fabrication techniques. We also gave recommendation for alternative chemistries and alternative materials for the industrial level scale-up. Further specific details, that were not led by SFU and are thus out of the scope of this thesis, may be found in Appendix E.

The device energy density was also investigated, as an important parameter in battery evaluation. An important advantage of the device configuration, in terms of energy density was the dry, solid state storage of reactants. Compared to conventional RFBs with the same reactant chemistry and concentrations albeit using liquid electrolytes, the energy density was estimated to be ≈ 7 times higher. The operational energy density estimated from discharge curves and normalized by the mass of the stored reactants, was estimated to be 32 Wh/kg, for the all-quinone chemistry which compared favourably to other recently reported biodegradable batteries. Table 4.4 given below summarizes the comparison to other reported batteries with environmentally

benign features with estimated power densities and energy densities based on datasets reported in literature. The power was normalized by the electrode size while the energy was normalized by the active redox reactant species mass.

Table 4.4. A comparison of power and energy densities of different environmentally benign batteries reported in literature.

Reference	Active reactants	Power density mW/cm ²	Energy density (mW h/g)
Lee et al. ^a [118]	Microbial (Bacteria) / O ₂ (on activated carbon)	0.000001	4000
Kim et al. [119]	Na ⁺ / activated carbon / MnO ₂	0.1	0.3
Kim et al. [120]	Na ⁺ / Melanin / MnO ₂	0.283	19
Zhu et al. ^b [121]	Enzymatic (glucose - maltodextrin) / O ₂	0.4	238
Yin et al. ^c [122]	Mg / Mo	0.2	26
Tsang et al. [123]	Mg / Fe	0.15	694
PowerPAD [124]	H ₂ BQS / pBQ	6.8	32

^a Based on theoretical estimations

^b Platinum catalyst based cathode

^c For their four cells stack.

Ultimately, this disposable power source concept holds great promise to radically change the portable battery paradigm; from considering it a harmful waste to a source of materials that nurture the environment, enrich soil, or remove toxins from water, far beyond the traditional life cycle of a battery.

4.5. Simultaneous power and thermal management of electronics: RFPCB

The last study was conducted to demonstrate a scaled CLFC for a real practical application. The CLFC was designed for integration in PCB material to combine the functionalities of thermal and power management, during an internship at IBM Research – Zurich, in the smart systems integration team. The PCB application was chosen in order to utilize the integrated cooling and powering functionalities concept, proposed by IBM for high-density high performance microprocessors, on the whole PCB with much larger footprint than the mounted microprocessors, thus reducing the power density

requirements to levels achievable by current state-of-the-art RFBs. PCBs were used before by O'Hayre et al. to fabricate portable hydrogen fuel cell arrays [125]. However, to our knowledge, this is the first attempt to fabricate RFBs, since RFBs are typically proposed as large-scale energy storage batteries. This concept therefore would have advantages and potential utility in future high density computing servers.

The RFPCB cell was assembled as shown previously in Figure 3.5. Serpentine flow fields were used to better distribute the flow of the electrolyte on a larger area of the electrode and because they would serve as microchannels for liquid cooling of the mounted electronics. Three layers of the pre-pregs with rectangular slits were laminated to form a separating layer with an array of microchannels where the co-laminar flow took place. The total thickness of the separator and the formed microchannel depth equalled ca. 580 μm after compression and curing of the pre-pregs. As mentioned in Chapter 3.1.2, each of the three pre-preg layers forming the co-laminar separator were designed to have six parallel rectangular slits with a width of 1 mm and a length of 28 mm. The slits were designed to ensure laminar flow regime in the microchannels as well as to have sufficient surface area to minimize cell resistance from ionic resistivity of electrolyte.

Figure 4.4 shows the polarization and power curves of the co-laminar RFPCB at flow rates of 5 mL/min and 10 mL/min, using fully charged vanadium electrolyte (V^{2+} & VO_2^+), driven by two syringe pumps. The electrolyte was composed of the same commercial mix (1.7 M vanadium in 4 M H_2SO_4) used in previous studies (section 4.1 and 4.2) and charged using a custom made cell. The RFPCB produced a maximum power of 600 mW at 10 mL/min, which translated to a peak power density of 162 mW/cm^2 , when normalized by the electrode area ($1.3 \times 2.9 \text{ cm}^2$). More importantly, the cell displayed an OCP of 1.55 V in a membraneless fashion and using co-laminar separation. This is believed to be the first demonstration for a scaled up CLFC with such OCP that indicated a minimized mixed-potential from reactants mixing. For example, the RFPCB represented a 75-fold increase in electrode volume and 500-fold increase in active electrode area, parallel to co-laminar interface, when compared to the CLFC design used in Chapter 4.1-4.3.

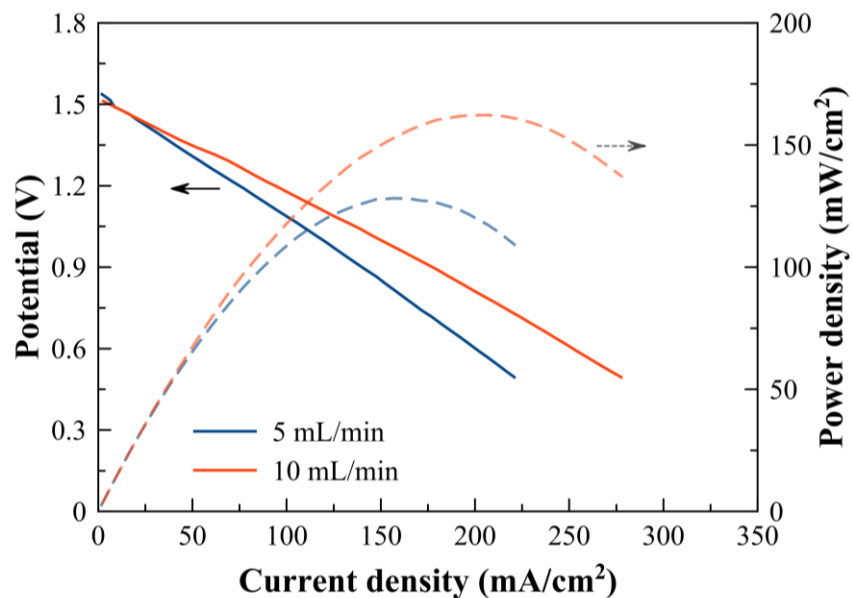


Figure 4.4. Polarization curve and power density curve for membraneless design of RFPCB using rectangular slits.

In order to show the crossover effect on OCP, a comparison is shown in Table 4.5, wherein the results with the CLFC configuration is compared against the RFPCB cells that were assembled using a commercial Nafion® membrane. These cells were tested during the internship but are out of the scope of this thesis. The table shows that the CLFC configuration indicated much better reactant separation than the case when using Nafion® 211 membrane, as shown by the higher OCP measured. The cells with Nafion® 212 however showed absent crossover, as indicated by the high OCP measured that was identical to that measured after reactant charging. Nevertheless, the thicker membrane (Nafion® 212) also had an impact on the overall cell performance, which was attributed to the increased ohmic cell resistance. However, the ohmic resistance measured for the CLFC configuration was the highest among the tested cells, which suggested that further design optimization would be possible.

In general, the power density could be improved by increasing the flow rate, which was limited here by the syringe pump specifications and by optimizing the design, such as minimizing ohmic resistance by reducing separator thickness and slits geometrical parameters or by incorporating a multi-pass architecture. This could be aided by computational modeling and would be recommended as future works, since the purpose of this study was to demonstrate a proof-of-concept, for the first time. The final

PCB design for demonstrating the full combined simultaneous power and cooling functionalities was designed but excluded from the scope of this thesis. The demonstration is currently pending testing by IBM Research - Zurich.

Table 4.5. Comparison between RFPCB membraneless design results and other similar designs with conventional membranes.

Case	Flow field	Separator	OCP (V)	Resistance (Ω)	Maximum power density* (mW/cm ²)
i)	SP	Membraneless	1.55 V	0.63	162
ii)	FT	Nafion® 211	1.35 V	0.21	491
iii)	SP	Nafion® 212	1.61 V	0.30	285
iv)	ID	Nafion® 212	1.58 V	0.46	203

*Measured at 10 mL/min

Chapter 5.

Conclusions and future work

This thesis focused on practical advances in microfluidic electrochemical energy conversion in membraneless cells with porous electrodes such as CLFCs. The work identified potential utility of the CLFC technology as: analytical platforms, disposable power sources and combined flow cell functionalities such as simultaneous on-chip cooling and powering. It is hoped that the results of this research effort would further advance the technology and speed up its adoption within the practical applications defined.

5.1. Conclusions

An analytical cell design was proposed for the first study to characterize CLFCs with dual-pass flow-through porous electrodes and was fabricated in PDMS using soft lithography techniques. The analytical cell design was based on the original dual-pass CLFC architecture and featured split electrodes which divided the cell into separate upstream and downstream portions, which simulated the regular cell operation when connected electrically in parallel. The performance characteristics of the individual portions were simultaneously measured. The crossover losses were estimated by measuring the OCP of the upstream and downstream portions individually at two different flow rates. The downstream cell portion experienced a crossover voltage loss of 41 mV at low flow rate and was decreased to 13 mV at high flow rate due to limited diffusive mixing. A maximum power density of 0.75 W/cm^2 at a current density of 1.0 A/cm^2 was recorded at the upstream cell, which represented the highest power density reported then for a microfluidic vanadium redox cell. The combined performance was measured during parallel connection and the current contribution of both passes of the dual-pass architecture was in-situ characterized. The combined parallel cell achieved a peak power density of 0.63 W/cm^2 which was less than that of the individual upstream

cell due to higher crossover and ohmic losses of the downstream portion as well as the partial reactant conversion upstream. The reactant utilization was calculated for both portions and the contribution of the downstream portion was similar to that of the upstream portion, at both flow rates. However, the downstream portion was found prone to mass transport limitations during the parallel connection. A plateau region at 22% reactant conversion was estimated at the low flow rate, due to the higher upstream reactant conversion. Finally, the charging performance of the dual-pass cell was also investigated by applying a charging voltage to the upstream portion while recording the downstream OCP, which revealed a strong competition between upstream reactant regeneration and downstream crossover losses. This was explained as both reactant conversion and crossover losses increase simultaneously at low flow rates. However, by applying a second stage charging in the downstream portion, the crossover loss could be overcome and a substantial net gain in state of charge could be achieved. Overall, the results of this work confirmed the benefits of the dual-pass architecture which increased discharge performance and enabled reactant recirculation as well as in-situ reactant regeneration by improving mass transport in the flow-through porous electrodes. The analytical cell characterization method could further help device optimization by understanding of the reactant conversion and voltage loss.

In the second study, the same analytical cell was used. An array of two microfluidic electrochemical cells with flow through porous electrodes was formed by series connection and the internal current losses that undesirably occur during stacking of electrochemical cells were experimentally characterized. The two cells had series fluidic connection through the shared electrolyte in order to reuse the partially consumed reactants from the upstream cell in the downstream cell in order to maximize overall fuel utilization. The array produced a maximum power density output of 600 mW/cm^2 and a maximum current density of 900 mA/cm^2 (13.5 mA) at the high flow rate of $100 \text{ }\mu\text{l/min}$. However, internal current losses up to 1.75 mA were indicated at OCP for the same flow rate. This was explained by the parasitic discharge via an internal circuit having both electrolytic and electronic connection, namely the cross cell. The cross cell was formed by opposite electrodes from each individual cell in the array; for example upstream cathode and downstream anode. The parasitic shunt current was measured to be roughly proportional to the operating voltage of the serial array and shown to be driven by the electrochemical potential difference of the electrodes of the cross cell circuit and

the electrolyte resistance. Thus, increasing the ionic resistance of this electrolytic pathway would decrease the magnitude of the shunt current loss. The loss in coulombic efficiency of the serial array was quantified to be up to 7% at OCP, which confirmed the importance of taking shunt current losses into consideration for designing CLFC arrays and stacks. The shunt current can be mitigated by increasing electrolytic resistance between adjacent cells such as by increasing the length or reducing the cross-sectional dimensions of the electrolyte channel between the cells. Nevertheless, the disadvantages of increased pumping power from total pressure drop and increased reactant crossover should be considered.

The third study investigated the performance aspects that are critical for flow cell operation with NAq redox electrolytes using the V_{acac} redox species, TEABF₄ supporting electrolyte and AN solvent as model chemistry with cell voltage window of ca. 2.2 V. The work explored reaction kinetics, electrode wettability, cell resistance and crossover. The reaction kinetics on flow-through porous carbon electrodes were measured using an analytical flow cell and were found to be similar or faster when compared to aqueous all-vanadium redox electrolyte. The electrode wetting behaviour in AN solvent was found to be superior to water as demonstrated by quantifying the electrode porosity filled with the solvent which showed 79% for acetonitrile and merely 6.0% in water, indicating hydrophobic behaviour in the majority of the pore volume. The analytical cell was used to measure the ASR at different TEABF₄ concentrations. The cell ASR was found to be an order of magnitude higher than for the corresponding aqueous cell with moderately concentrated sulfuric acid electrolyte, but less than 5 Ωcm^2 , which meets the targets set by techno-economic models for energy storage applications. Reactant crossover was assessed in the cell similar to the first study and was found to be absent at high flow rates due to the minimized diffusion mixing and low species residence time. Finally, a discharge polarization was measured and the cell achieved a high open circuit potential of 2.6 V and a peak power density output of 550 mW/cm^2 . This power density level is generally two orders of magnitude higher than other works using NAq electrolytes and on the same order as the corresponding aqueous CLFCs using all-vanadium electrolytes, as reported in the first study. Overall, the study demonstrated the utility of flow-through porous electrode configuration to enhance kinetics, wetted surface area and mass transport combined with a membraneless configuration to overcome ohmic limitations and boost performance of NAq flow cells. The CLFC technology

demonstrated in the study provided an ideal evaluation platform for such new developments toward high-performance flow cells for electrochemical energy conversion in NAq media.

In the fourth study, the general chemistry requirements were defined regarding solubility, biodegradability, storability in correct redox state, redox potential and kinetics of the reactant chemistries for the PowerPAD or biodegradable capillary flow batteries for single-use disposable applications. Mixed-media operation was leveraged to allow direct use of commercially available organic compounds by using an alkaline anode and an acidic cathode as well as the added benefit of downstream neutralization for safe disposal. Potential redox chemistries for each half-cell were assessed ex-situ by measuring solubility, redox potential and kinetics and in-situ by cell discharge performance measurements in the same analytical cell developed in the first study. An all-quinone CLFC comprising of LQ and pBQ for anode and cathode, respectively displayed a high OCP of 1.24 V and good power density but was found unsuitable for the application due to stability issues. The most suitable chemistry tested was based on either AA or H₂BQS in KOH and pBQ in oxalic acid at the anode and cathode, respectively. When these two half-cells were coupled, the CLFC displayed an OCP of 0.92 V and a peak power density of 42 mW/cm². Furthermore, the identified half-cell chemistries were demonstrated in the final PowerPAD design forming a disposable capillary flow cell with reactants and supporting electrolytes stored on board in powder form and dissolved upon water activation of the device. The PowerPAD maintained the OCP for more than 1 hour and delivered more than 2 mW peak power (8 mW/cm²), which would power various electronic components like communication or display modules. Finally, the PowerPAD proof-of-concept was developed and shown to be cheap, scalable and biodegradable. The energy density and power density of the device compared well with similar devices with environmental features from literature. The utility of the device was also proven by direct substitution of a lithium coin cell battery in a water quality sensor. The PowerPAD set the departing point for a new generation of biodegradable primary batteries that are sustainable and circular as the waste is minimized from conception.

Lastly, the final study reported an integrated CLFC in PCB for combined thermal management and power delivery functionalities. A scaled CLFC was designed for this application in PCB material. Compared to the CLFC used in the first studies, the

electrode active area, parallel to the co-laminar interface, is scaled 500-fold. A serpentine flow field was used to better distribute the electrolyte over the electrode area and to serve as a microchannel for liquid cooling of mounted electronics. A separation layer was designed having rectangular slits that formed microchannels for the co-laminar reactant separation, and the RFPCB was assembled by lamination and heating. Using conventional vanadium redox electrolytes, the RFPCB displayed a good OCP of 1.55 V indicating acceptable diffusive crossover mixing and produced a peak power density of 162 mW/cm². The CLFC compared well with RFPCBs having a commercial PEM membrane. A final design for demonstrating the full combined simultaneous functionalities with mounted electronics was designed and will be tested by IBM Research - Zurich. Overall, the integration concept of RFPCB has advantages in future high-density high performance computing microprocessors, mounted on the PCB, which would typically require direct liquid cooling. The concept of RFPCB is considered feasible when utilizing the electronic board area since the power density achieved matches target application requirements, which hence enables new perspectives for the near-term use of the concept in high performance servers and data centers.

In summary, this dissertation resulted in some scholarly contributions, for each applications category, as provided below:

I. Analytical platforms:

- Journal articles:
 - OA Ibrahim, E Kjeang, Leveraging Co-laminar Flow Cells for Non-aqueous Electrochemical Systems, Submitted to Journal of Power Sources, 2018
 - OA Ibrahim, MA Goulet, E Kjeang, In-situ characterization of symmetric dual-pass architecture of microfluidic co-laminar flow cells, *Electrochimica Acta*, 187, 277-285, 2016.
 - OA Ibrahim, MA Goulet, E Kjeang, Microfluidic Electrochemical Cell Array in Series: Effect of Shunt Current, *Journal of The Electrochemical Society* 162 (7), F639-F644, 2015.

II. Disposable power sources:

- Patent application:
 - Portable and Disposable Power Source for Measuring and/or Monitoring Solutions, EP15200865.2, Dec. 2015.

- Journal articles:
 - OA Ibrahim, P Alday, N Sabaté, JP Esquivel, E Kjeang, Evaluation of Redox Chemistries for Single-Use Biodegradable Capillary Flow Batteries, Journal of The Electrochemical Society 164 (12), A2448-A2456, 2017.
 - JP Esquivel, P Alday, OA Ibrahim, B Fernández, E Kjeang, N Sabaté, A Metal-Free and Biologically Degradable Battery for Portable Single-Use Applications, Advanced Energy Materials 7 (18), 2017.

III. Combined flow cell functionalities:

- Journal articles:
 - OA Ibrahim, E Kjeang, B Michel and P Ruch, Embedded flow batteries for power distribution and thermal management in high-density and efficient electronics, In preparation, 2018
- Mini-paper in conference proceedings:
 - P Ruch, O Ibrahim, R Heller, S Paredes, E Kjeang, B Michel, Flow battery integration in printed circuit boards, Accepted in Proceedings of the International Flow Battery Forum (IFBF), July 2018, Geneva, Switzerland.

5.2. Future work

This dissertation has broadly proposed various technological advances for CLFC research and development, with focus on practicality and utility of the technology. It is believed that CLFC research will keep growing to include more analytical studies and form essential tools that complement research in electrochemical energy conversion and storage. This can be in the form of two-electrode cells such as the analytical cell in this study or even three-electrode form, to investigate new electrodes, chemistries or catalysts.

To fully unleash the potential of CLFCs for energy storage applications, novel cell architectures are still needed to enable cell cycling with high efficiencies and enable continuous recirculation capabilities with precise pressure control. The absence of pulsations or other inlet or outlet pressure variations is critical in order to maintain a co-laminar interface or even a multitude of interfaces and to maintain a uniform reactant streams splitting at the outlet.

The PowerPAD may further benefit from more chemistry screening. The quinone chemistry can be tailored according to specifications by synthesizing the chemistry and adding functional groups. In general, it is believed that higher cell voltages may be possible under mixed-media operation. A computational study aided by density functional theory can be conducted in that regard, taking into consideration the specific chemistry requirements for the PowerPAD and the reactant species properties that influence the PowerPAD operation such as species solubility, redox potential, reaction kinetics and rate of dissolution.

From the device perspective, the PowerPAD design would also benefit from computational modeling studies. The design in general offers a rich set of parameters such as the absorbent pad design, which influences the cell internal resistance as well as the magnitude and duration of the flow, and thus determines the battery power output and run time. The electrode dimensions are other parameters whose effect may be modeled. Lastly, while the PowerPAD introduced the concept of capillary flow cells, the concept may be extended and the materials forming it may be engineered to add other features such as flexibility for niche applications such as wearable electronics. Other transient ideas are making the concept edible or ingestible and biocompatible for applications of *in vivo* diagnostics.

The last study introduced a proof of concept for the RFPCB using CLFC configuration. This opens doors for further optimization of the device. For example, the power density may be enhanced by optimizing the design such as by adding multi-pass architectures or other geometrical modifications and reducing the cell resistance. The RFPCB may also be stacked vertically which enables higher power outputs to match requirements with a minimized added footprint. In general, the scale up of CLFCs was shown to be possible. Further studies with focus on practical application matching and novel system integration may be conducted. Besides the simultaneous powering and thermal management of electronic boards demonstrated in this dissertation, solar cell performance may also benefit from a liquid cooling solution while integrated RFBs are needed, as an energy storage solution for the intermittency of solar radiation.

References

- [1] B. Dunn, H. Kamath, J.-M. Tarascon, Electrical Energy Storage for the Grid: A Battery of Choices, *Science*. 334 (2011) 928–935. doi:10.1126/science.1212741.
- [2] M.M. Mench, *Fuel Cell Engines*, 2008. doi:10.1002/9780470209769.
- [3] M.L. Perry, A.Z. Weber, Advanced Redox-Flow Batteries: A Perspective, *J. Electrochem. Soc.* 163 (2016) A5064–A5067. doi:10.1149/2.0101601jes.
- [4] A.Z. Weber, M.M. Mench, J.P. Meyers, P.N. Ross, J.T. Gostick, Q. Liu, Redox flow batteries: A review, *J. Appl. Electrochem.* 41 (2011) 1137–1164. doi:10.1007/s10800-011-0348-2.
- [5] G.L. Soloveichik, Flow Batteries: Current Status and Trends, *Chem. Rev.* 115 (2015) 11533–11558. doi:10.1021/cr500720t.
- [6] H. Prifti, A. Parasuraman, S. Winardi, T.M. Lim, M. Skyllas-Kazacos, Membranes for redox flow battery applications, *Membranes (Basel)*. 2 (2012) 275–306. doi:10.3390/membranes2020275.
- [7] R. Borup, J. Meyers, B. Pivovar, Y.S. Kim, R. Mukundan, N. Garland, D. Myers, M. Wilson, F. Garzon, D. Wood, P. Zelenay, K. More, K. Stroh, T. Zawodzinski, J. Boncella, J.E. McGrath, M. Inaba, K. Miyatake, M. Hori, K. Ota, Z. Ogumi, S. Miyata, A. Nishikata, Z. Siroma, Y. Uchimoto, K. Yasuda, K. Kimijima, N. Iwashita, Scientific Aspects of Polymer Electrolyte Fuel Cell Durability and Degradation, *Chem. Rev.* 107 (2007) 3904–3951. doi:10.1021/cr050182l.
- [8] M. Skyllas-Kazacos, M. Kazacos, State of charge monitoring methods for vanadium redox flow battery control, *J. Power Sources*. 196 (2011) 8822–8827. doi:10.1016/j.jpowsour.2011.06.080.
- [9] M. Gad-el-Hak, *The MEMS Handbook*, 2001. doi:10.1201/9781420050905.
- [10] C.M. Ho, Y.C. Tai, Micro-electro-mechanical-systems (MEMS) and fluid flows, *Annu. Rev. Fluid Mech.* 30 (1998) 579–612. doi:10.1146/annurev.fluid.30.1.579.
- [11] E. Kjeang, *Microfluidic fuel cells and batteries*, 2014.
- [12] R. Ferrigno, A.D. Stroock, T.D. Clark, M. Mayer, G.M. Whitesides, Membraneless vanadium redox fuel cell using laminar flow, *J. Am. Chem. Soc.* 124 (2002) 12930–12931. doi:ja020812q [pii].
- [13] E. Choban, Microfluidic fuel cell based on laminar flow, *J. Power Sources*. 128 (2004) 54–60. doi:10.1016/j.jpowsour.2003.11.052.
- [14] M.A. Goulet, E. Kjeang, Co-laminar flow cells for electrochemical energy

- conversion, *J. Power Sources*. 260 (2014) 186–196.
doi:10.1016/j.jpowsour.2014.03.009.
- [15] J.W. Lee, M.-A. Goulet, E. Kjeang, Microfluidic redox battery., *Lab Chip*. 13 (2013) 2504–7. doi:10.1039/c3lc50499a.
- [16] W. a Braff, M.Z. Bazant, C.R. Buie, Membrane-less hydrogen bromine flow battery., *Nat. Commun.* 4 (2013) 2346. doi:10.1038/ncomms3346.
- [17] S.M. H. Hashemi, M.A. Modestino, D. Psaltis, A membrane-less electrolyzer for hydrogen production across the pH scale., *Energy Environ. Sci.* 8 (2015) Ahead of Print. doi:10.1039/C5EE00083A.
- [18] M.A. Modestino, M. Dumortier, S.M. Hosseini Hashemi, S. Haussener, C. Moser, D. Psaltis, Vapor-fed microfluidic hydrogen generator, *Lab Chip*. 15 (2015) 2287–2296. doi:10.1039/C5LC00259A.
- [19] G.D. O’Neil, C.D. Christian, D.E. Brown, D. V. Esposito, Hydrogen Production with a Simple and Scalable Membraneless Electrolyzer, *J. Electrochem. Soc.* 163 (2016) F3012–F3019. doi:10.1149/2.0021611jes.
- [20] M.E. Oruc, A. V. Desai, R.G. Nuzzo, P.J.A. Kenis, Design, fabrication, and characterization of a proposed microchannel water electrolyzer, *J. Power Sources*. 307 (2016) 122–128. doi:10.1016/J.JPOWSOUR.2015.12.062.
- [21] S.A. Mousavi Shaegh, N.T. Nguyen, S.H. Chan, A review on membraneless laminar flow-based fuel cells, *Int. J. Hydrogen Energy*. 36 (2011) 5675–5694. doi:10.1016/j.ijhydene.2011.01.063.
- [22] E. Kjeang, N. Djilali, D. Sinton, Microfluidic fuel cells: A review, *J. Power Sources*. 186 (2009) 353–369. doi:10.1016/j.jpowsour.2008.10.011.
- [23] M.A. Modestino, D. Fernandez Rivas, S.M.H. Hashemi, J.G.E. Gardeniers, D. Psaltis, The potential for microfluidics in electrochemical energy systems, *Energy Environ. Sci.* 9 (2016) 3381–3391. doi:10.1039/C6EE01884J.
- [24] D. V. Esposito, Membraneless Electrolyzers for Low-Cost Hydrogen Production in a Renewable Energy Future, *Joule*. 1 (2017) 651–658. doi:10.1016/j.joule.2017.07.003.
- [25] E. Kjeang, B.T. Proctor, A.G. Brolo, D.A. Harrington, N. Djilali, D. Sinton, High-performance microfluidic vanadium redox fuel cell, *Electrochim. Acta*. 52 (2007) 4942–4946. doi:10.1016/j.electacta.2007.01.062.
- [26] S.M. Mitrovski, R.G. Nuzzo, A passive microfluidic hydrogen-air fuel cell with exceptional stability and high performance., *Lab Chip*. 6 (2006) 353–61. doi:10.1039/b513829a.

- [27] F.R. Brushett, W.-P. Zhou, R.S. Jayashree, P.J.A. Kenis, Alkaline Microfluidic Hydrogen-Oxygen Fuel Cell as a Cathode Characterization Platform, *J. Electrochem. Soc.* 156 (2009) B565–B571. doi:10.1149/1.3083226.
- [28] R.S. Jayashree, M. Mitchell, D. Natarajan, L.J. Markoski, P.J. a Kenis, Microfluidic hydrogen fuel cell with a liquid electrolyte., *Langmuir*. 23 (2007) 6871–6874. doi:10.1021/la063673p.
- [29] E. Kjeang, A.G. Brolo, D. a. Harrington, N. Djilali, D. Sinton, Hydrogen Peroxide as an Oxidant for Microfluidic Fuel Cells, *J. Electrochem. Soc.* 154 (2007) B1220. doi:10.1149/1.2784185.
- [30] A. Déctor, J.P. Esquivel, M.J. González, M. Guerra-Balcázar, J. Ledesma-García, N. Sabaté, L.G. Arriaga, Formic acid microfluidic fuel cell evaluation in different oxidant conditions, *Electrochim. Acta.* 92 (2013) 31–35. doi:10.1016/j.electacta.2012.12.134.
- [31] H. Wang, S. Gu, D.Y.C. Leung, H. Xu, M.K.H. Leung, L. Zhang, J. Xuan, Development and characteristics of a membraneless microfluidic fuel cell array, *Electrochim. Acta.* 135 (2014) 467–477. doi:10.1016/j.electacta.2014.04.165.
- [32] N. Da Mota, D.A. Finkelstein, J.D. Kirtland, C.A. Rodriguez, A.D. Stroock, H.D. Abruña, Membraneless, room-temperature, direct borohydride/cerium fuel cell with power density of over 0.25 W/cm², *J. Am. Chem. Soc.* 134 (2012) 6076–6079. doi:10.1021/ja211751k.
- [33] A. Moreno-Zuria, A. Dector, F.M. Cuevas-Mu??iz, J.P. Esquivel, N. Sabat??, J. Ledesma-Garc??a, L.G. Arriaga, A.U. Ch??vez-Ram??ez, Direct formic acid microfluidic fuel cell design and performance evolution, *J. Power Sources.* 269 (2014) 783–788. doi:10.1016/j.jpowsour.2014.07.049.
- [34] E. Ortiz-Ortega, M.-A. Goulet, J.W. Lee, M. Guerra-Balcázar, N. Arjona, E. Kjeang, J. Ledesma-García, L.G. Arriaga, A nanofluidic direct formic acid fuel cell with a combined flow-through and air-breathing electrode for high performance., *Lab Chip.* 14 (2014) 4596–8. doi:10.1039/c4lc01010h.
- [35] E. Kjeang, R. Michel, D.A. Harrington, D. Sinton, N. Djilali, An alkaline microfluidic fuel cell based on formate and hypochlorite bleach, *Electrochim. Acta.* 54 (2008) 698–705. doi:10.1016/j.electacta.2008.07.009.
- [36] J. Maya-Cornejo, E. Ortiz-Ortega, L. Alvarez-Contreras, N. Arjona, M. Guerra-Balcazar, J. Ledesma-Garcia, L.G. Arriaga, Copper-palladium core-shell as an anode in a multi-fuel membraneless nanofluidic fuel cell: toward a new era of small energy conversion devices, *Chem. Commun.* 51 (2015) 2536–2539. doi:10.1039/c4cc08529a.
- [37] Y. Wang, D.Y.C. Leung, J. Xuan, H. Wang, A vapor feed methanol microfluidic fuel cell with high fuel and energy efficiency, *Appl. Energy.* 147 (2015) 456–465. doi:10.1016/j.apenergy.2015.03.028.

- [38] C.A. López-Rico, J. Galindo-De-La-Rosa, E. Ortiz-Ortega, L. Álvarez-Contreras, J. Ledesma-García, M. Guerra-Balcázar, L.G. Arriaga, N. Arjona, High performance of ethanol co-laminar flow fuel cells based on acrylic, paper and Pd-NiO as anodic catalyst, *Electrochim. Acta.* 207 (2016) 164–176. doi:10.1016/j.electacta.2016.05.002.
- [39] N. Arjona, a Palacios, a Moreno-Zuria, M. Guerra-Balcázar, J. Ledesma-García, L.G. Arriaga, AuPd/polyaniline as the anode in an ethylene glycol microfluidic fuel cell operated at room temperature., *Chem. Commun. (Camb).* 50 (2014) 8151–3. doi:10.1039/c4cc03288h.
- [40] J.W. Lee, E. Kjeang, A perspective on microfluidic biofuel cells, *Biomicrofluidics.* 4 (2010) 041301. doi:10.1063/1.3515523.
- [41] M.J. González-Guerrero, J.P. Esquivel, D. Sánchez-Molas, P. Godignon, F.X. Muñoz, F.J. del Campo, F. Giroud, S.D. Minter, N. Sabaté, Membraneless glucose/O₂ microfluidic enzymatic biofuel cell using pyrolyzed photoresist film electrodes., *Lab Chip.* 13 (2013) 2972–9. doi:10.1039/c3lc50319d.
- [42] A. Zebda, L. Renaud, M. Cretin, F. Pichot, C. Innocent, R. Ferrigno, S. Tingry, A microfluidic glucose biofuel cell to generate micropower from enzymes at ambient temperature, *Electrochem. Commun.* 11 (2009) 592–595. doi:10.1016/j.elecom.2008.12.036.
- [43] Z. Li, Y. Zhang, P.R. Leduc, K.B. Gregory, Microbial electricity generation via microfluidic flow control, *Biotechnol. Bioeng.* 108 (2011) 2061–2069. doi:10.1002/bit.23156.
- [44] A. Fraiwan, D.F. Call, S. Choi, Bacterial growth and respiration in laminar flow microbial fuel cells, *J. Renew. Sustain. Energy.* 6 (2014). doi:10.1063/1.4873399.
- [45] R.S. Jayashree, L. Gancs, E.R. Choban, A. Primak, D. Natarajan, L.J. Markoski, P.J. a Kenis, Air-breathing laminar flow-based microfluidic fuel cell., *J. Am. Chem. Soc.* 127 (2005) 16758–16759. doi:10.1021/ja054599k.
- [46] S.A. Mousavi Shaegh, N.T. Nguyen, S.H. Chan, Air-breathing microfluidic fuel cell with fuel reservoir, *J. Power Sources.* 209 (2012) 312–317. doi:10.1016/j.jpowsour.2012.02.115.
- [47] E. Kjeang, J. McKechnie, D. Sinton, N. Djilali, Planar and three-dimensional microfluidic fuel cell architectures based on graphite rod electrodes, *J. Power Sources.* 168 (2007) 379–390. doi:10.1016/j.jpowsour.2007.02.087.
- [48] X. Zhu, B. Zhang, D.D. Ye, J. Li, Q. Liao, Air-breathing direct formic acid microfluidic fuel cell with an array of cylinder anodes, *J. Power Sources.* 247 (2014) 346–353. doi:10.1016/j.jpowsour.2013.08.119.
- [49] E. Kjeang, R. Michel, D.A. Harrington, N. Djilali, D. Sinton, A microfluidic fuel cell with flow-through porous electrodes, *J. Am. Chem. Soc.* 130 (2008) 4000–4006.

doi:10.1021/ja078248c.

- [50] E. Kjeang, D. Sinton, N. Djilali, Fuel cell with flow-through porous electrodes, US Patent App. 11/869,277, 2009.
- [51] M.A. Goulet, E. Kjeang, Reactant recirculation in electrochemical co-laminar flow cells, *Electrochim. Acta.* 140 (2014) 217–224. doi:10.1016/j.electacta.2014.03.092.
- [52] M.A. Goulet, O.A. Ibrahim, W.H.J. Kim, E. Kjeang, Maximizing the power density of aqueous electrochemical flow cells with in operando deposition, *J. Power Sources.* 339 (2017) 80–85. doi:10.1016/j.jpowsour.2016.11.053.
- [53] M.-A. Goulet, E.A. Kjeang, Process of increasing energy conversion and electrochemical efficiency of a scaffold material using a deposition material, US Patent App. 14/842,812, 2017.
- [54] J.R. Hayes, A.M. Engstrom, C. Friesen, Orthogonal flow membraneless fuel cell, *J. Power Sources.* 183 (2008) 257–259. doi:10.1016/j.jpowsour.2008.04.061.
- [55] K.S. Salloum, J.R. Hayes, C.A. Friesen, J.D. Posner, Sequential flow membraneless microfluidic fuel cell with porous electrodes, *J. Power Sources.* 180 (2008) 243–252. doi:10.1016/j.jpowsour.2007.12.116.
- [56] K.S. Salloum, J.D. Posner, Counter flow membraneless microfluidic fuel cell, *J. Power Sources.* 195 (2010) 6941–6944. doi:10.1016/j.jpowsour.2010.03.096.
- [57] W. Huo, Y. Zhou, H. Zhang, Z. Zou, H. Yang, Microfluidic direct methanol fuel cell with ladder-shaped microchannel for decreased methanol crossover, *Int. J. Electrochem. Sci.* 8 (2013) 4827–4838.
- [58] O.A. Ibrahim, P. Alday, N. Sabaté, J.P. Esquivel, E. Kjeang, Evaluation of Redox Chemistries for Single-Use Biodegradable Capillary Flow Batteries, *J. Electrochem. Soc.* 164 (2017) A2448–A2456. doi:10.1149/2.0971712jes.
- [59] E.R. Choban, J.S. Spendelow, L. Gancs, A. Wieckowski, P.J.A. Kenis, Membraneless laminar flow-based micro fuel cells operating in alkaline, acidic, and acidic/alkaline media, *Electrochim. Acta.* 50 (2005) 5390–5398. doi:10.1016/j.electacta.2005.03.019.
- [60] J.L. Cohen, D.J. Volpe, D.A. Westly, A. Pechenik, H.D. Abruña, A dual electrolyte H₂/O₂ planar membraneless microchannel fuel cell system with open circuit potentials in excess of 1.4 V, *Langmuir.* 21 (2005) 3544–3550. doi:10.1021/la0479307.
- [61] X. Lu, J. Xuan, D.Y.C. Leung, H. Zou, J. Li, H. Wang, H. Wang, A switchable pH-differential unitized regenerative fuel cell with high performance, *J. Power Sources.* 314 (2016) 76–84. doi:10.1016/j.jpowsour.2016.02.092.

- [62] J.P. Esquivel, F.J. Del Campo, J.L. Gómez de la Fuente, S. Rojas, N. Sabaté, Microfluidic fuel cells on paper: meeting the power needs of next generation lateral flow devices, *Energy Environ. Sci.* 7 (2014) 1744. doi:10.1039/c3ee44044c.
- [63] V. Galvan, K. Domalaon, C. Tang, S. Sotez, A. Mendez, M. Jalali-Heravi, K. Purohit, L. Pham, J. Haan, F.A. Gomez, An improved alkaline direct formate paper microfluidic fuel cell, *Electrophoresis.* 37 (2016) 504–510. doi:10.1002/elps.201500360.
- [64] T.S. Copenhaver, K.H. Purohit, K. Domalaon, L. Pham, B.J. Burgess, N. Manorohtkul, V. Galvan, S. Sotez, F.A. Gomez, J.L. Haan, A microfluidic direct formate fuel cell on paper, *Electrophoresis.* 36 (2015) 1825–1829. doi:10.1002/elps.201400554.
- [65] R.K. Arun, S. Halder, N. Chanda, S. Chakraborty, A paper based self-pumping and self-breathing fuel cell using pencil stroked graphite electrodes, *Lab Chip.* 14 (2014) 1661–1664. doi:10.1039/C4LC00029C.
- [66] J.P. Esquivel, J.R. Buser, C.W. Lim, C. Domínguez, S. Rojas, P. Yager, N. Sabatí, Single-use paper-based hydrogen fuel cells for point-of-care diagnostic applications, *J. Power Sources.* 342 (2017) 442–451. doi:10.1016/j.jpowsour.2016.12.085.
- [67] S. Moore, D. Sinton, D. Erickson, A plate-frame flow-through microfluidic fuel cell stack, *J. Power Sources.* 196 (2011) 9481–9487. doi:10.1016/j.jpowsour.2011.07.024.
- [68] J.P. Esquivel, F.J. Del Campo, J.L. Gomez De La Fuente, S. Rojas, N. Sabate, Micro fuel cells: Can we apply them to a successful market?, in: *ECS Trans., The Electrochemical Society*, 2014: pp. 875–880. doi:10.1149/06403.0875ecst.
- [69] M.P. Gurrola, E. Ortiz-Ortega, C. Farias-Zuñiga, A.U. Chávez-Ramírez, J. Ledesma-García, L.G. Arriaga, Evaluation and coupling of a membraneless nanofluidic device for low-power applications, *J. Power Sources.* 307 (2016) 244–250. doi:10.1016/j.jpowsour.2015.12.091.
- [70] D. Morales-Acosta, H. Rodríguez G., L.A. Godinez, L.G. Arriaga, Performance increase of microfluidic formic acid fuel cell using Pd/MWCNTs as catalyst, *J. Power Sources.* 195 (2010) 1862–1865. doi:10.1016/j.jpowsour.2009.10.007.
- [71] M.A. Goulet, M. Eikerling, E. Kjeang, Direct measurement of electrochemical reaction kinetics in flow-through porous electrodes, *Electrochem. Commun.* 57 (2015) 14–17. doi:10.1016/j.elecom.2015.04.019.
- [72] M.M. Sabry, A. Sridhar, D. Atienza, P. Ruch, B. Michel, Integrated microfluidic power generation and cooling for bright silicon MPSoCs, in: *Des. Autom. Test Eur. Conf. Exhib. (DATE)*, 2014, 2014: pp. 1–6. doi:10.7873/DATE.2014.147.
- [73] A. Sridhar, M.M. Sabry, P. Ruch, D. Atienza, B. Michel, PowerCool: Simulation of

integrated microfluidic power generation in bright silicon MPSoCs, in: 2014 IEEE/ACM Int. Conf. Comput. Des., 2014: pp. 527–534. doi:10.1109/ICCAD.2014.7001401.

- [74] J. Marschewski, L. Brenner, N. Ebejer, P. Ruch, B. Michel, D. Poulikakos, X. Li, Y.-B. Zhang, J. Jiang, O.M. Yaghi, E.N. Wang, 3D-printed fluidic networks for high-power-density heat-managing miniaturized redox flow batteries, *Energy Environ. Sci.* 10 (2017) 780–787. doi:10.1039/C6EE03192G.
- [75] A.A. Andreev, A. Sridhar, M.M. Sabry Aly, M. Zapater, P. Ruch, B. Michel, D. Atienza, PowerCool: Simulation of Cooling and Powering of 3D MPSoCs with Integrated Flow Cell Arrays, *IEEE Trans. Comput.* (2017). doi:10.1109/TC.2017.2695179.
- [76] R.A. Elgammal, Z. Tang, C.-N. Sun, J. Lawton, T.A. Zawodzinski, Species Uptake and Mass Transport in Membranes for Vanadium Redox Flow Batteries, *Electrochim. Acta.* 237 (2017) 1–11. doi:10.1016/j.electacta.2017.03.131.
- [77] J. Marschewski, S. Jung, P. Ruch, N. Prasad, S. Mazzotti, B. Michel, D. Poulikakos, Mixing with herringbone-inspired microstructures: overcoming the diffusion limit in co-laminar microfluidic devices, *Lab Chip.* 15 (2015) 1923–1933. doi:10.1039/C5LC00045A.
- [78] J. Marschewski, R. Brechbühler, S. Jung, P. Ruch, B. Michel, D. Poulikakos, Significant heat transfer enhancement in microchannels with herringbone-inspired microstructures, *Int. J. Heat Mass Transf.* 95 (2016) 755–764. doi:10.1016/J.IJHEATMASSTRANSFER.2015.12.039.
- [79] J. Marschewski, P. Ruch, N. Ebejer, O. Huerta Kanan, G. Lhermitte, Q. Cabrol, B. Michel, D. Poulikakos, On the mass transfer performance enhancement of membraneless redox flow cells with mixing promoters, *Int. J. Heat Mass Transf.* 106 (2017) 884–894. doi:10.1016/J.IJHEATMASSTRANSFER.2016.10.030.
- [80] J.W. Lee, E. Kjeang, Nanofluidic fuel cell, *J. Power Sources.* 242 (2013) 472–477. doi:10.1016/j.jpowsour.2013.05.129.
- [81] J.W. Lee, E. Kjeang, Chip-embedded thin film current collector for microfluidic fuel cells, *Int. J. Hydrogen Energy.* 37 (2012) 9359–9367. doi:10.1016/j.ijhydene.2012.02.155.
- [82] M.A. Goulet, M. Skyllas-Kazacos, E. Kjeang, The importance of wetting in carbon paper electrodes for vanadium redox reactions, *Carbon N. Y.* 101 (2016) 390–398. doi:10.1016/j.carbon.2016.02.011.
- [83] M.A. Goulet, A. Habisch, E. Kjeang, In Situ Enhancement of Flow-through Porous Electrodes with Carbon Nanotubes via Flowing Deposition, *Electrochim. Acta.* 206 (2016) 36–44. doi:10.1016/j.electacta.2016.04.147.
- [84] M. Cossale, S. Paredes, R.P. Luitjen, B. Michel, Combined power delivery and

cooling for high density, high efficiency microservers, in: 2015 21st Int. Work. Therm. Investig. ICs Syst., 2015: pp. 1–6.
doi:10.1109/THERMINIC.2015.7389598.

- [85] R.P. Luijten, A. Döring, S. Paredes, T. Engbersen, F. Buining, B. Michel, Objective, innovation and impact of the energy-efficient dome microdatacenter, in: 2017 Int. Conf. Adv. Comput. Commun. Informatics, 2017: pp. 913–921.
doi:10.1109/ICACCI.2017.8125958.
- [86] J. Noack, N. Roznyatovskaya, T. Herr, P. Fischer, The Chemistry of Redox-Flow Batteries, *Angew. Chem. Int. Ed. Engl.* 54 (2015) 9776–809.
doi:10.1002/anie.201410823.
- [87] J. Winsberg, T. Hagemann, T. Janoschka, M.D. Hager, U.S. Schubert, Redox-Flow Batteries: From Metals to Organic Redox-Active Materials, *Angew. Chemie - Int. Ed.* 56 (2017) 686–711. doi:10.1002/anie.201604925.
- [88] M. Rychcik, M. Skyllas-Kazacos, Characteristics of a new all-vanadium redox flow battery, *J. Power Sources.* (1988).
- [89] M. Skyllas-Kazacos, M. Rychcik, R.G. Robins, A.G. Fane, M.A. Green, New All-Vanadium Redox Flow Cell, *J. Electrochem. Soc.* 133 (1986) 1057.
doi:10.1149/1.2108706.
- [90] M. Ulaganathan, V. Aravindan, Q. Yan, S. Madhavi, M. Skyllas-Kazacos, T.M. Lim, Recent Advancements in All-Vanadium Redox Flow Batteries, *Adv. Mater. Interfaces.* (2015) n/a–n/a. doi:10.1002/admi.201500309.
- [91] F. Xing, H. Zhang, X. Ma, Shunt current loss of the vanadium redox flow battery, *J. Power Sources.* (2011).
- [92] A. Tang, J. McCann, J. Bao, M. Skyllas-Kazacos, Investigation of the effect of shunt current on battery efficiency and stack temperature in vanadium redox flow battery, *J. Power Sources.* (2013).
- [93] M. Gad-El-Hak, Gas and liquid transport at the microscale, *Heat Transf. Eng.* 27 (2006) 13–29. doi:Doi 10.1080/01457630500522305.
- [94] N. Nguyen, S. Wereley, Fundamentals and applications of microfluidics, Artech House. (2006) 111. doi:http://doi.wiley.com/10.1002/1521-3773%252820010316%252940%253A6%253C9823%253A%253AAID-ANIE9823%253E3.3.CO%253B2-C.
- [95] O.A. Ibrahim, M.A. Goulet, E. Kjeang, In-situ characterization of symmetric dual-pass architecture of microfluidic co-laminar flow cells, *Electrochim. Acta.* 187 (2016) 277–285. doi:10.1016/j.electacta.2015.11.081.
- [96] B. Ho, E. Kjeang, Planar multiplexing of microfluidic fuel cells, *J. Fluids Eng.*

(2013).

- [97] K.S. Salloum, J.D. Posner, A membraneless microfluidic fuel cell stack, *J. Power Sources*. 196 (2011) 1229–1234. doi:10.1016/j.jpowsour.2010.08.069.
- [98] O.A. Ibrahim, M.-A. Goulet, E. Kjeang, Microfluidic Electrochemical Cell Array in Series: Effect of Shunt Current, *J. Electrochem. Soc.* 162 (2015) F639–F644. doi:10.1149/2.0211507jes.
- [99] Q. Liu, A.E.S. Sleightholme, A.A. Shinkle, Y. Li, L.T. Thompson, Non-aqueous vanadium acetylacetonate electrolyte for redox flow batteries, *Electrochem. Commun.* 11 (2009) 2312–2315. doi:10.1016/j.elecom.2009.10.006.
- [100] M.O. Bamgbopa, N. Pour, Y. Shao-Horn, S. Almheiri, Systematic selection of solvent mixtures for non-aqueous redox flow batteries – vanadium acetylacetonate as a model system, *Electrochim. Acta.* 223 (2017) 115–123. doi:10.1016/j.electacta.2016.12.014.
- [101] T. Herr, J. Noack, P. Fischer, J. Tübke, 1,3-Dioxolane, tetrahydrofuran, acetylacetone and dimethyl sulfoxide as solvents for non-aqueous vanadium acetylacetonate redox-flow-batteries, *Electrochim. Acta.* 113 (2013) 127–133. doi:10.1016/j.electacta.2013.09.055.
- [102] Y.. Volkovich, V.. Bagotzky, V.. Sosenkin, I.. Blinov, The standard contact porosimetry, *Colloids Surfaces A Physicochem. Eng. Asp.* 187-188 (2001) 349–365. doi:10.1016/S0927-7757(01)00650-1.
- [103] J.T. Gostick, M.W. Fowler, M.A. Ioannidis, M.D. Pritzker, Y.M. Volkovich, A. Sakars, Capillary pressure and hydrophilic porosity in gas diffusion layers for polymer electrolyte fuel cells, *J. Power Sources*. 156 (2006) 375–387. doi:10.1016/j.jpowsour.2005.05.086.
- [104] R.M. Darling, K.G. Gallagher, J.A. Kowalski, S. Ha, F.R. Brushett, Pathways to low-cost electrochemical energy storage: a comparison of aqueous and nonaqueous flow batteries, *Energy Environ. Sci.* 7 (2014) 3459–3477. doi:10.1039/C4EE02158D.
- [105] R. Dmello, J.D. Milshtein, F.R. Brushett, K.C. Smith, Cost-driven materials selection criteria for redox flow battery electrolytes, *J. Power Sources*. 330 (2016) 261–272. doi:10.1016/j.jpowsour.2016.08.129.
- [106] K. Gong, Q. Fang, S. Gu, S.F.Y. Li, Y. Yan, Nonaqueous redox-flow batteries: organic solvents, supporting electrolytes, and redox pairs, *Energy Environ. Sci.* (2015) 38–49. doi:10.1039/C5EE02341F.
- [107] J.W. Lee, J.K. Hong, E. Kjeang, Electrochemical characteristics of vanadium redox reactions on porous carbon electrodes for microfluidic fuel cell applications, *Electrochim. Acta.* 83 (2012) 430–438. doi:10.1016/j.electacta.2012.07.104.

- [108] M.M. Hamed, A. Ainla, F. Güder, D.C. Christodouleas, M.T. Fernández-Abedul, G.M. Whitesides, Integrating Electronics and Microfluidics on Paper, *Adv. Mater.* (2016) 5054–5063. doi:10.1002/adma.201505823.
- [109] B. Huskinson, M.P. Marshak, C. Suh, S. Er, M.R. Gerhardt, C.J. Galvin, X. Chen, A. Aspuru-Guzik, R.G. Gordon, M.J. Aziz, A metal-free organic-inorganic aqueous flow battery., *Nature*. 505 (2014) 195–8. doi:10.1038/nature12909.
- [110] K. Lin, Q. Chen, M.R. Gerhardt, L. Tong, S.B. Kim, L. Eisenach, A.W. Valle, D. Hardee, R.G. Gordon, M.J. Aziz, M.P. Marshak, Alkaline quinone flow battery, *Science*. 349 (2015) 1529–1532. doi:10.1126/science.aab3033.
- [111] B. Yang, L. Hooper-Burkhardt, F. Wang, G.K. Surya Prakash, S.R. Narayanan, An Inexpensive Aqueous Flow Battery for Large-Scale Electrical Energy Storage Based on Water-Soluble Organic Redox Couples, *J. Electrochem. Soc.* 161 (2014) A1371–A1380. doi:10.1149/2.1001409jes.
- [112] B. Yang, L. Hooper-Burkhardt, S. Krishnamoorthy, A. Murali, G.K.S. Prakash, S.R. Narayanan, High-Performance Aqueous Organic Flow Battery with Quinone-Based Redox Couples at Both Electrodes, *J. Electrochem. Soc.* 163 (2016) A1442–A1449.
- [113] U. Er, C. Suh, M.P. Marshak, A. Aspuru-Guzik, Computational design of molecules for an all-quinone redox flow battery, *Chem. Sci.* 6 (2015) 845–1592. doi:10.1039/c4sc03030c.
- [114] Y. Ding, Y. Li, G. Yu, Exploring Bio-inspired Quinone-Based Organic Redox Flow Batteries: A Combined Experimental and Computational Study, *Chem.* 1 (2016) 790–801. doi:10.1016/j.chempr.2016.09.004.
- [115] Q. Chen, M.R. Gerhardt, L. Hartle, M.J. Aziz, A Quinone-Bromide Flow Battery with 1 W/cm² Power Density, *J. Electrochem. Soc.* 163 (2015) A5010–A5013. doi:10.1149/2.0021601jes.
- [116] K. Wedege, E. Dražević, D. Konya, A. Bentien, Organic Redox Species in Aqueous Flow Batteries: Redox Potentials, Chemical Stability and Solubility, *Sci. Rep.* 6 (2016) 39101. doi:10.1038/srep39101.
- [117] M.R. Gerhardt, L. Tong, R. Gómez-Bombarelli, Q. Chen, M.P. Marshak, C.J. Galvin, A. Aspuru-Guzik, R.G. Gordon, M.J. Aziz, Anthraquinone Derivatives in Aqueous Flow Batteries, *Adv. Energy Mater.* 7 (2017). doi:10.1002/aenm.201601488.
- [118] H. Lee, S. Choi, An origami paper-based bacteria-powered battery, *Nano Energy*. 15 (2015) 549–557. doi:http://dx.doi.org/10.1016/j.nanoen.2015.05.019.
- [119] Y.J. Kim, S.-E. Chun, J. Whitacre, C.J. Bettinger, Self-deployable current sources fabricated from edible materials, *J. Mater. Chem. B.* 1 (2013) 3781. doi:10.1039/c3tb20183j.

- [120] Y.J. Kim, W. Wu, S.-E. Chun, J.F. Whitacre, C.J. Bettinger, Biologically derived melanin electrodes in aqueous sodium-ion energy storage devices., *Proc. Natl. Acad. Sci. U. S. A.* 110 (2013) 20912–7. doi:10.1073/pnas.1314345110.
- [121] Z. Zhu, T. Kin Tam, F. Sun, C. You, Y.H. Percival Zhang, A high-energy-density sugar biobattery based on a synthetic enzymatic pathway, *Nat. Commun.* 5 (2014). doi:10.1038/ncomms4026.
- [122] L. Yin, X. Huang, H. Xu, Y. Zhang, J. Lam, J. Cheng, J.A. Rogers, Materials, designs, and operational characteristics for fully biodegradable primary batteries, *Adv. Mater.* 26 (2014) 3879–3884. doi:10.1002/adma.201306304.
- [123] M. Tsang, A. Armutlulu, A.W. Martinez, S.A.B. Allen, M.G. Allen, Biodegradable magnesium/iron batteries with polycaprolactone encapsulation: A microfabricated power source for transient implantable devices, *Microsystems Nanoeng.* 1 (2015) 15024. doi:10.1038/micronano.2015.24.
- [124] J.P. Esquivel, P. Alday, O.A. Ibrahim, B. Fernández, E. Kjeang, N. Sabaté, A Metal-Free and Biotically Degradable Battery for Portable Single-Use Applications, *Adv. Energy Mater.* 7 (2017). doi:10.1002/aenm.201700275.
- [125] R. O’Hayre, D. Braithwaite, W. Hermann, S.J. Lee, T. Fabian, S.W. Cha, Y. Saito, F.B. Prinz, Development of portable fuel cell arrays with printed-circuit technology, *J. Power Sources.* 124 (2003) 459–472. doi:10.1016/S0378-7753(03)00802-4.

Appendix A.

In-situ Characterization of Symmetric Dual-pass Architecture of Microfluidic Co-laminar Flow Cells

Reproduced from [94] with permission from Elsevier



In-situ characterization of symmetric dual-pass architecture of microfluidic co-laminar flow cells



Omar A. Ibrahim, Marc-Antoni Goulet¹, Erik Kjeang^{*,1}

Fuel Cell Research Laboratory (FCReL), School of Mechatronic Systems Engineering, Simon Fraser University, Canada

ARTICLE INFO

Article history:

Received 31 July 2015

Received in revised form 14 November 2015

Accepted 15 November 2015

Available online 18 November 2015

Keywords:

microfluidic fuel cell
microfluidic redox battery
co-laminar flow cell
vanadium
dual-pass

ABSTRACT

Microfluidic co-laminar flow cells with dual-pass architecture enable fuel recirculation and in-situ regeneration, and offer improvements in performance characteristics. In this work, a unique analytical cell design is proposed, with two split portions having flow-through porous electrodes. Each cell portion is first tested individually with vanadium redox species and the results are used to quantify the previously unknown crossover losses at the downstream portion of the cell, shown here to be a strong function of the flow rate. Moreover, the upstream cell portion demonstrates impressive room-temperature power density up to 0.75 W cm^{-2} at 1.0 A cm^{-2} , which is the highest performance reported to date for a microfluidic vanadium redox battery. Next, the two cell portions are connected in parallel to resemble a complete cell with dual-pass architecture, thereby enabling novel in-situ diagnostics of the inlet and outlet passes of the cell. For instance, the reactant utilization efficiency of the downstream cell portion is shown to be on the same order as that of the upstream portion at both low and high flow rates. Furthermore, in-situ regeneration is also demonstrated. Overall, the present results provide a deeper understanding of dual-pass reactant conversion and crossover which will be useful for future device optimization.

© 2015 Elsevier Ltd. All rights reserved.

Introduction

Microfluidic fuel cells and redox batteries are a growing area of energy research [1]. In these co-laminar flow cells (CLFCs), the convective mixing of the two reactant fluids flowing at the micro-scale is minimal and thus, the governing mechanism for species mixing is the slow diffusion transport. This is because of the nature of the laminar flow in micro-channels with low Reynolds number and high Peclet number. Therefore, the co-laminar interface formed along the micro-channel provides the required separation of the two reactant streams whilst permitting the necessary ion transport [2,3]. This offers the advantage of simplicity and low cost because of disposing the ion exchange membrane used in conventional fuel cells and redox flow batteries, eliminating the high cost and other issues related to its use. However, as the reactant streams flow along the microchannel, the diffusion zone grows depending on the downstream position, channel geometry,

flow rate, and diffusion coefficient of the reactant species. This causes certain crossover losses and requires careful engineering and design [4].

The pioneering studies for CLFCs by Ferrigno et al. [2] and Chohan et al. used basic Y-shaped micro-channel architecture [3]. Since then, various research developments have been done on device chemistries and architectures, as summarized in recent reviews and books [1,4–6]. The air breathing electrode architecture was introduced by Jayashree et al. [7] wherein an ion-conducting blank electrolyte maintains the co-laminar interface and prevents the anolyte from reaching the cathode [8–11]. Zhu et al. reported an air breathing direct formic acid CLFC with an array of graphite cylinders as the anode [8] to extend the anodic reactive surface area and enhance mass transport, as previously proposed by Kjeang et al. [12]. Esquivel et al. presented a direct methanol microfluidic fuel cell on paper, wherein the fuel and supporting electrolytes were driven by capillary forces without external pumping [11]. A key advancement in CLFC architectures was the introduction of flow-through porous electrodes by Kjeang et al. The baseline cell design fed fuel and oxidant individually through the porous carbon paper electrodes before meeting in the center manifold for ionic transport. The cell achieved power densities up to 121 mW cm^{-2} and high fuel utilization using vanadium redox species [13]. More recently, the concept of CLFCs expanded beyond

* Corresponding author at: School of Mechatronic Systems Engineering, Simon Fraser University, 250-13450 102 Avenue, Surrey, BC V3T 0A3, Canada.

Tel.: +1 778 782 8791; fax: +1 778 782 7514.

E-mail address: ekjeang@sfu.ca (E. Kjeang).

¹ ISE member.

fuel cells to include rechargeable flow batteries. The baseline design with flow-through porous electrodes was modified by the introduction of a junction at the outlet for harvesting the reactant streams separately. This dual-pass architecture permitted both charging and discharging and was thus called the microfluidic redox battery (MRB) for its reversible capability. The cell achieved power densities around 300 mW cm^{-2} and 20% full cycle energy efficiency [14]. Both performance metrics were enhanced compared to previous cells due to the dual-pass cell configuration which facilitated improved mass transport rates in the electrodes. Cell charging and discharging was also investigated by Braff et al. in a hydrogen-bromine flow battery that showed the highest power density of 795 mW cm^{-2} to date with cycle efficiency of 91% [15].

Several analytical studies have been conducted in order to address some of the remaining research challenges associated with CLFCs; e.g., reactant crossover and cell stacking. Reactant crossover to the opposite electrode causes a drop in cell potential due to the presence of a mixed electrode potential. Sprague et al. reported a mathematical model developed to consider the effect of reactant crossover on the performance of a microfluidic fuel cell with various electrode configurations, and concluded that narrow channels suffer from high reactant crossover which reduces the cell performance [16]. A convective counter flow microfluidic fuel cell was presented by Salloum et al. wherein a blank electrolyte was introduced to divert the reactant streams to opposite and independent outlets and thereby minimize diffusive crossover [17]. The same concept was extended to a two-cell array in which the second cell utilized the unconsumed reactant species from the first cell [18]. Ho and Kjeang alternatively doubled the performance of a single cell by supplying fresh reactants to two symmetric bilateral cells connected together in a planar two-cell array [19]. Goulet and Kjeang analyzed the MRB and compared it with other dual-pass architectures to assess the limits of fuel recirculation in CLFCs, as an essential way of minimizing the waste of unused reactant. The crossover losses in the MRB were also identified to be caused by both reactant diffusion and asymmetric splitting at the outlet junction, which was assessed by open circuit voltage (OCV) measurement [20]. More recently, Ibrahim et al. modified the MRB design by splitting the electrodes, forming an array of two symmetric cells with electrical and electrolytic connections in series. This enabled characterizing the shunt current losses associated with serial cell stacks that use a common electrolyte manifold [21].

Although the dual-pass MRB architecture conceived by our group has the potential advantages of high power output, fuel recirculation, and in-situ regeneration, the cell design is difficult to optimize because of the convoluting effect of two reactant passes through a single electrode. The objective of the present work is therefore to develop an analytical cell design with flow-through porous electrodes and dual pass architecture and apply it to in-situ characterization of MRBs. The proposed MRB design is modified by splitting each of the two electrodes into two sections in order to characterize the two upstream and downstream cell portions separately. The geometry is chosen similar to the baseline dual-pass microfluidic cell design from our previous works [14,20] in order to provide reliable diagnostic data. This device layout is similar to that of the previously reported two-cell serial array [21]; but in the present case, the two cell portions are connected in parallel in order to resemble the device function of the original MRB whilst permitting detailed analytical characterization of the upstream and downstream cell portions during operation. With this approach, the local current densities at the upstream and downstream cell portions can be measured independently without major alteration of the original MRB architecture. Moreover, the effect of reactant crossover can be readily assessed by comparing the performance of each individual cell portion. The results of this

work will therefore provide a deeper understanding of reactant conversion and crossover losses in the dual-pass architecture of the MRB, which can aid the design and optimization of dual-pass cells for regular discharge operation as well as for emerging recirculation and recharging applications.

2. Methods

2.1. Cell design and fabrication

A schematic of the proposed analytical cell design and assembly is shown in Fig. 1. Four rectangular carbon paper electrodes are inserted and sealed into a custom-designed microfluidic channel structure and subsequently utilized as flow-through anodes and cathodes of the upstream and downstream cell portions. Each electrode is equipped with a separate electrical connection in order to enable complete in-situ characterization of the two upstream and downstream cell portions. The fabrication of the device is based on UV soft lithography of polydimethylsiloxane (PDMS) from an SU-8 (Microchem) photoresist template on a four-inch silicon wafer. A base layer of SU-8 is first spin-coated to provide support for the secondary layer which contains the master structure for mold replication. A transparency mask having the design features of the microfluidic device is UV-exposed (15 seconds) on the secondary layer of the photoresist. The master is developed (Microchem) for 15 minutes and then rinsed with acetone and propanol, respectively, until all residual SU-8 from the second layer is removed. The height of the SU-8 master is checked by a profilometer to be around the desired value of $150 \mu\text{m}$. A 10:1 mixture of PDMS and hardening agent (Dow Corning) is prepared and poured over the master, deaerated, and cured for three days. The mold is then peeled off the substrate and cut to shape, and holes are punched for fluidic and electrical connection ports. Next, rectangular electrode strips for the four electrodes of the device are cut from heat treated carbon paper (TGPH-060, Toray) with width of 1 mm and thickness of $180 \mu\text{m}$. The slight difference in height ($\approx 30 \mu\text{m}$) between the electrode thickness and channel depth assures electrode compression and minimizes flow bypass. After the electrodes are positioned inside the PDMS mold, a glass lid is bonded permanently to the PDMS by plasma treatment of the two surfaces (Electro-Technic Products, BD-20AC). Silver conductive epoxy (MG Chemicals) is used to bond electrical wires to the electrodes. Four Tygon tubes (Saint-Gobain) with small diameter (1/32 in. I.D; 1/32 in. O.D.) are inserted into the two inlets and two outlets of the device.

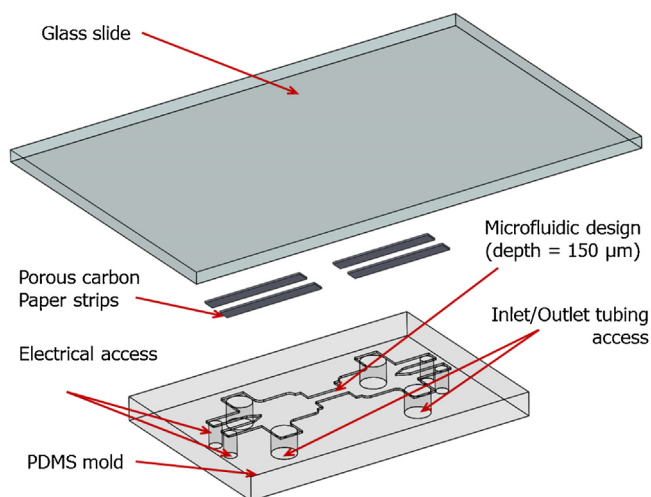
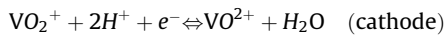
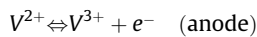


Fig. 1. Exploded view of the analytical cell design and assembly.

2.2. Chemistry

All-vanadium redox species, first developed by Skyllas-Kazacos et al. [22,23], are used for testing the fabricated cell. In this manuscript, V^{2+} , V^{3+} , VO^{2+} , and VO_2^+ will be referred to as V(II), V(III), V(IV), and V(V), respectively, where V(II) is used in the anode and V(V) is used in the cathode during discharge operation of the MRB. A 1.7 M stock commercial grade mixture of V(III)/V(IV) in 4 M sulfuric acid electrolyte is charged to prepare the necessary V(II) anolyte and V(V) catholyte. A saturated calomel electrode (SCE, Fisher Scientific) is used as reference electrode to measure the open circuit potentials of the electrolytes after charging. The potentials are found to be 1.01 V and -0.55 V for the V(V) and V(II) containing electrolytes, which corresponds to an estimated state-of-charge (SOC) of approximately 93% and 87% for V(V) and V(II), respectively. The solutions are then loaded into two separate syringes. The electrochemical discharge reactions for the vanadium redox species are given as:



Redox electrolytes of a lower initial state of charge, representing 'used' electrolyte from discharge operation in the flow cell, are utilized for in-situ regeneration (charging) experiments. In this case, the electrochemical potentials are found to be 0.89 V and -0.46 V for the V(V) and V(II) electrolytes, which indicates approximately 30% and 20% SOC, respectively. Further details about the reactant chemistries and device fabrication can be found elsewhere [21,24–26].

2.3. Experimental setup

The reactant flow through the cell is driven by a dual syringe pump (Harvard Apparatus) from the inlet side. Another unit is used in the withdraw mode from the outlet side to minimize the flow

pulsations and collect the electrolyte in separate syringes for further charging and reusing. Discharge experiments are demonstrated at high and low flow rates of 100 and 10 $\mu\text{L min}^{-1}$, respectively. Cell polarization curves are measured by a potentiostat (Gamry Reference 3000) by linearly sweeping the voltage and measuring the current with a scan rate of 3 mV s^{-1} and 10 mV s^{-1} for the lower and higher flow rates, respectively. During performance measurements of the individual upstream and downstream cell portions, one portion is connected to the potentiostat for the polarization curve measurement while the other portion is connected to a voltmeter (Extech, EX430) to monitor its open circuit voltage (OCV), as shown in Fig. 2a and b. The cell is also characterized when the two portions are connected in parallel to resemble the original MRB, and therefore quantify the contribution of each pass. To form the parallel connection, the anode of the upstream portion is wired to the anode of the downstream portion whereas the cathode of the upstream portion is wired to the cathode of the downstream portion according to Fig. 2c. During the measurement, two ammeters (Extech, EX430) are connected in series to each of the upstream and downstream cell portions to measure the contribution of each portion (I_u and I_d) compared to the total current (I_{pair}) passing through the potentiostat. The measured currents are normalized by the projected area normal to the flow through the electrode (0.0075 cm^2). The ohmic resistances of the two portions and the parallel pair are measured by means of electrochemical impedance spectroscopy (EIS) performed using the same potentiostat by reading the high frequency real axis intercept of the Nyquist plot, with an AC amplitude of 10 mV rms at OCV, over a frequency range of 50 kHz to 10 Hz. In-situ regeneration (charging) experiments are performed using the same physical setup, where the potentiostat is used to apply a constant cell potential of 1.7 V to facilitate the reverse electrochemical reactions. This potential is selected to provide a sufficiently high overpotential for regeneration while avoiding side reactions and hydrogen evolution. Charging experiments are demonstrated at flow rates of 10 $\mu\text{L min}^{-1}$ and 1 $\mu\text{L min}^{-1}$.

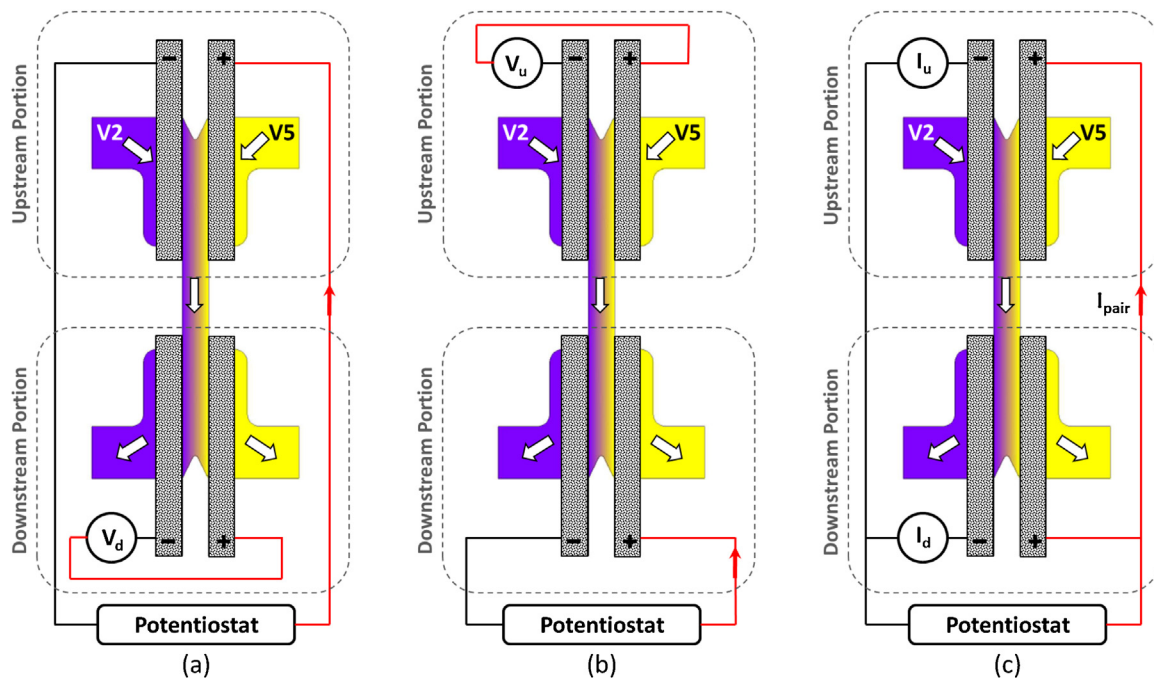


Fig. 2. The experimental electric circuitry for a) individual upstream portion characterization, b) individual downstream portion characterization, and c) parallel electrical connection of both portions.

3. Results and Discussion

3.1. Crossover loss quantification

The proposed device design is fabricated and used as an analytical cell to quantify and analyze the unique performance characteristics and losses due to reactant crossover in the dual-pass MRB. It hence becomes important to understand the individual performance of the upstream and downstream portions in order to assess the crossover losses of the combined cell. First, electrochemical impedance spectroscopy (EIS) is performed for the two portions to measure their ohmic resistances. The measurements show ohmic resistances of 52Ω and 89Ω for the upstream and downstream portions, respectively. Since the two portions are geometrically symmetric, the difference in resistances is attributed to fabrication inconsistencies from the manual cutting and positioning of the electrodes and the manual epoxy filling for the electrical contacts of the electrodes with the wires. The open circuit voltage (OCV) of the two individual portions is also measured. The upstream portion of the cell has an OCV of 1.563 V at a flow rate of $10 \mu\text{L min}^{-1}$, which is similar to the ex-situ measured value using SCE after reactant charging. This demonstrates the absence of a mixed potential due to crossover at the upstream cell because of the favorable incoming flow direction through the porous electrodes into the co-laminar channel where diffusive mixing takes place. At the same flow rate, the OCV of the downstream cell portion is found to be 1.522 V . This difference in the OCV values between the upstream and downstream portions shows that reactant crossover takes place due to species diffusion along the channel as well as asymmetric splitting of the reactant streams at the outlet junction before entering the porous electrodes of the downstream portion. At the higher flow rate of $100 \mu\text{L min}^{-1}$, the OCV of the downstream portion increases to 1.55 V whereas for the upstream portion, the OCV is still 1.563 V , as previously measured at $10 \mu\text{L min}^{-1}$. This means that the downstream cell portion is subject to crossover losses of 41 mV and 13 mV at flow rates of $10 \mu\text{L min}^{-1}$ and $100 \mu\text{L min}^{-1}$, respectively. This is because the reactant crossover decreases at higher flow rates, since the species diffusion is reduced at the higher flow velocity due to a shorter residence time in the co-laminar channel. However, regardless of the flow rate, the downstream cell portion is still exposed to a certain amount of crossover losses due to asymmetric splitting of the two reactant streams at the outlet splitting junction [20].

Next, the discharge performance of each individual cell portion is investigated. Here, one cell portion is connected to the potentiostat load for the discharge experiments while the other portion is connected to a voltmeter to monitor the OCV (Fig. 2a and b). The polarization and power curves for the upstream and downstream cell portions are given in Fig. 3a and b, respectively, for the flow rate of $10 \mu\text{L min}^{-1}$. High power output of about 4.5 mW at a current of 6.5 mA is observed from the upstream cell (Fig. 3a). The performance of the individual downstream portion is found to be lower than for the upstream cell, which is attributed to its higher ohmic resistance and to its slightly lower OCV due to crossover losses. The monitored OCV of the other unconnected cell portion during the voltage sweep is also shown in Fig. 3. When the potentiostat is connected to the upstream portion, the OCV of the downstream cell (OCV_d) decreases from 1.522 V at OCV to 1.390 V at the end of the voltage sweep. The 132 mV voltage decrease, noted here, reflects the overpotential due to the consumption of the vanadium redox species in both of the upstream electrodes during the voltage sweep, which results in a decreased concentration and thus a decreased OCV at the downstream portion. In other words, this decrease in the OCV at the downstream portion, when the upstream portion is connected to the potentiostat, is equivalent

to a 40% decrease in the state of charge (or percentage conversion, % C) at the maximum current output from the upstream cell as estimated according to Eq. (1):

$$\%C = \frac{I_{\max} \times 60 \times 1000}{nFM_0Q} = \frac{11 \times 60 \times 1000}{96485 \times 1.7 \times 10} \cong 40\% \quad (1)$$

where, I_{\max} is the limiting current of the considered cell portion in mA, F is Faraday's constant ($96,485 \text{ C mol}^{-1}$), n is the number of electrons transferred per mole ($n=1$), M_0 is the molar concentration of the fresh vanadium species (1.7 M), and Q is the flow rate in $\mu\text{L min}^{-1}$. This value reflects high percentage conversion for the reactants at low flow rates and is in agreement with previous results in flow through porous electrodes [13]. On the other hand, the OCV of the upstream cell (OCV_u) is constant at 1.563 V throughout the voltage sweep on the downstream cell. This value is identical to the ex-situ measured OCV value of the fully charged electrolytes since the upstream portion is completely isolated from crossover losses, as previously discussed, and the upstream circuit is open such that reactant species are not consumed.

Furthermore, the same measurements are conducted at the higher flow rate of $100 \mu\text{L min}^{-1}$ and the performance data are given in Fig. 4a and b for the upstream and downstream portions,

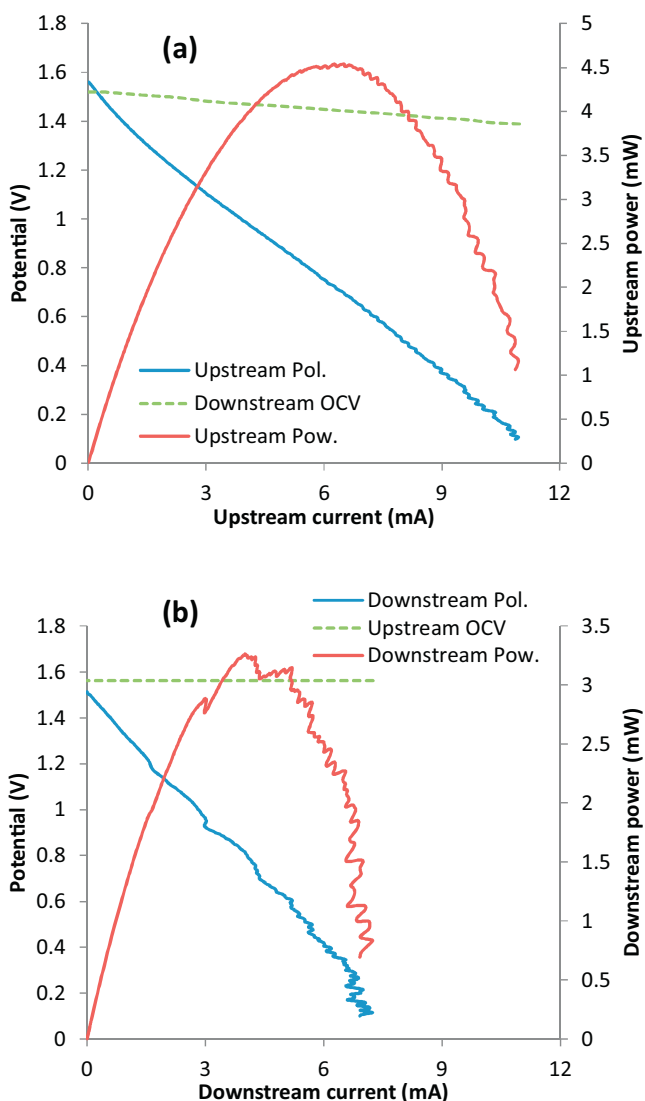


Fig. 3. Polarization and power curves of the two cell portions tested individually at $10 \mu\text{L min}^{-1}$: a) upstream portion and b) downstream portion.

respectively. During the voltage sweep of the upstream portion, OCV_d is observed to decrease from 1.550 V at the upstream OCV condition to 1.519 V at the end of the voltage sweep. This relatively small decrease of 31 mV indicates that the consumption of reactants and fuel utilization at the upstream electrodes are decreased at the higher flow rate, which is in agreement with the theoretical expectation [13,18]. The percentage conversion at the limiting current for the upstream cell portion at the higher flow rate of $100 \mu\text{L min}^{-1}$ is estimated to equal 5.6% (using Eq. (1)), which reflects the smaller OCV drop of the downstream portion (31 mV). The upstream portion achieved a remarkably high room-temperature performance at this flow rate. A peak power output of 5.6 mW is achieved at 7.8 mA, as shown in Fig. 4a. These values correspond to a power density of 750 mW cm^{-2} at a current density of 1.0 A cm^{-2} . To the authors' knowledge, this is the highest power density reported to date for a microfluidic vanadium redox battery. A maximum current density of about 2.0 A cm^{-2} is also achieved. The performance of the downstream portion is also enhanced at the higher flow rate, as deduced from Fig. 4b, because of the higher reactant concentration available and the reduced diffusion crossover. Nevertheless, it is still limited by the relatively high ohmic resistance of this portion. In order to isolate the effect of the difference in cell resistance, the polarization curves of the

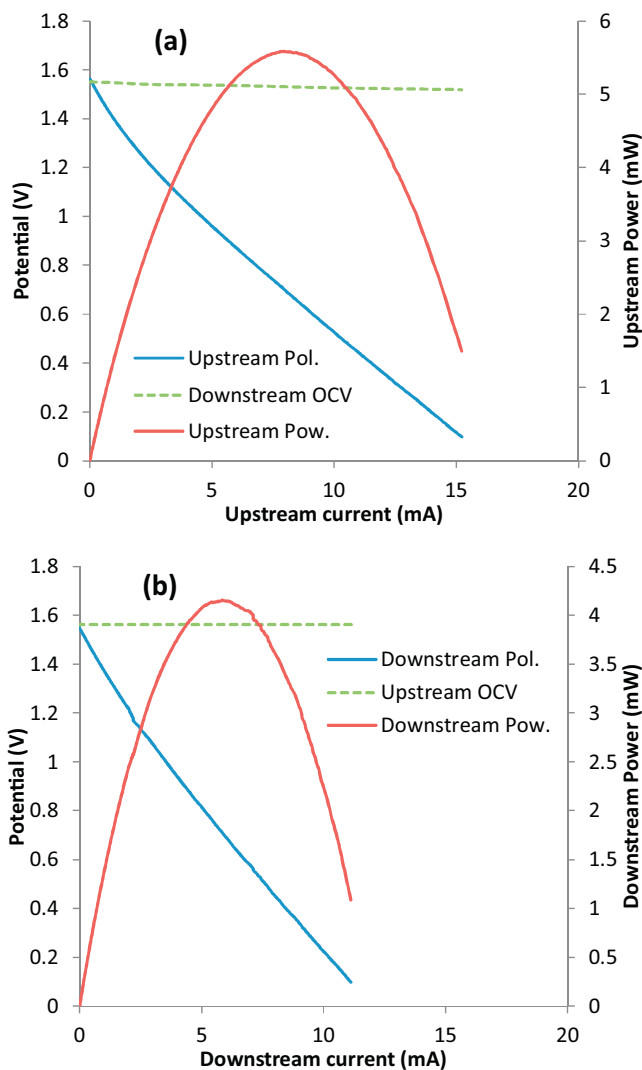


Fig. 4. Polarization and power curves of the two cell portions tested individually at $100 \mu\text{L min}^{-1}$: a) upstream portion and b) downstream portion.

individual upstream and downstream portions are IR-compensated by using the resistance values measured by EIS, as shown in Fig. 5a and b for 10 and $100 \mu\text{L min}^{-1}$, respectively. The figure shows that the slopes of the IR-compensated polarization curves are in good agreement, as expected from the symmetry in the design of the two portions. Noting that crossover losses are small compared to other overpotentials during cell polarization, this indicates that the two symmetric portions perform similarly during discharge when the other portion is held at OCV. This also confirms that the relatively low performance of the downstream cell portion, as stated previously, is mostly attributed to the 70% higher cell resistance.

3.2. Dual-pass characterization

In this section, the contribution of each pass of the dual-pass architecture of the previously published MRB design [14,20] is characterized. The two cell portions are connected in parallel in order to resemble the original MRB design, as shown in Fig. 2c. When the two cell portions are connected in parallel, the OCV value of the parallel pair is in between the OCV values of the upstream and downstream cell portions measured individually and reported in the previous section. The measured OCV of the parallel pair equals 1.536 V and 1.554 V at flow rates of $10 \mu\text{L min}^{-1}$ and $100 \mu\text{L min}^{-1}$, respectively. EIS measurement is performed and the ohmic resistance of the pair is found to be 34Ω . This value is

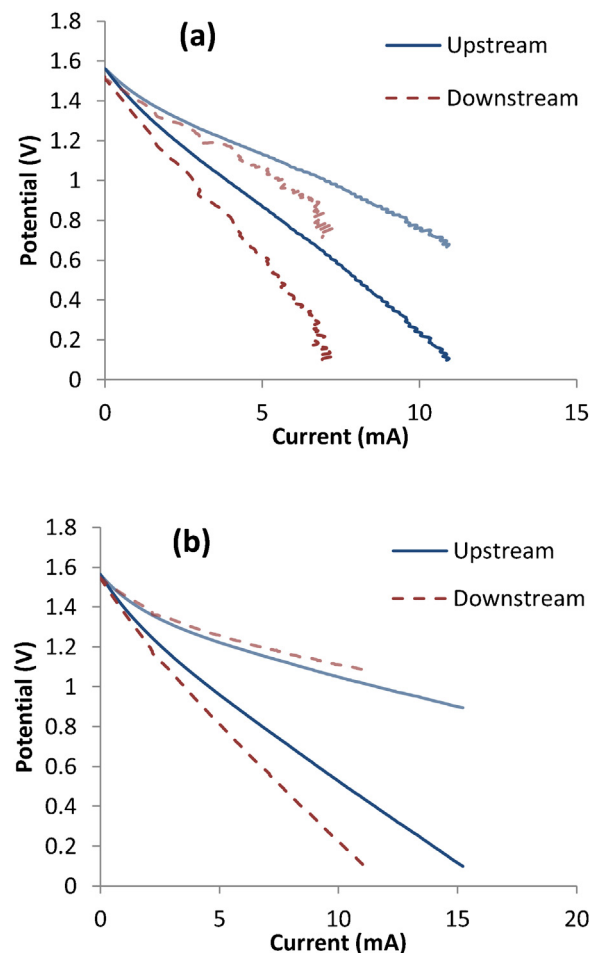


Fig. 5. IR-compensated polarization curves (shown in faded colors) versus regular polarization curves for the upstream and downstream portions when tested individually at: a) $10 \mu\text{L min}^{-1}$ and b) $100 \mu\text{L min}^{-1}$.

comparable to that obtained by a basic equivalent circuit resistance calculation using the resistance values of the two cell portions connected in parallel:

$$\frac{1}{R_{eq}} = \frac{1}{R_u} + \frac{1}{R_d} = \frac{1}{52} + \frac{1}{89} \Rightarrow R_{eq} = 32.8 \Omega \quad (2)$$

The slight difference ($< 2 \Omega$) is likely due to the internal resistance of the ammeters connected in series to each of the two portions.

The parallel pair is then connected to the potentiostat to measure discharge polarization curves at the two flow rates, with results shown in Fig. 6. At a flow rate of $100 \mu\text{L min}^{-1}$, the pair achieves a maximum power output of 9.5 mW at a current of 13.5 mA and cell potential around 0.7 V. The parallel pair also achieves limiting currents up to 25.6 mA. The equivalent maximum power density, which takes into account the electrode areas of both cell portions, is 630 mW cm^{-2} . The reduced maximum power density compared to the upstream portion is attributed to the relatively low performance of the downstream cell due its lower incoming reactant state of charge and higher cell resistance. The difference in the peak power density output between the parallel pair in this study and the original MRB ($\sim 350 \text{ mW cm}^{-2}$ [20]) is mostly attributed to the difference in cell resistances. In the original MRB [14,20], carbon nanofoam was used as the electrode material, which has higher resistivity than the material used in this work [26]. Despite the reduced power density for the parallel pair, compared to the individual upstream portion, higher fuel utilization efficiency is expected since the unused reactants in the upstream portion are now partly consumed downstream, as previously reported by Salloum et al. [18]. For example, the estimated maximum utilization efficiencies using Eq. (1) and the combined current for the parallel pair at the two flow rates of $10 \mu\text{L min}^{-1}$ and $100 \mu\text{L min}^{-1}$ equal 52% and 9.4%, respectively, whereas the utilization efficiencies for the individual upstream portion, at the same flow rates, equal 40% and 5.6%.

Moreover, the currents generated by the upstream and downstream portions of the cell are recorded via two ammeters connected in series with the cell portions, namely I_u and I_d (Fig. 2c). The contribution of each of the upstream and downstream portions is plotted in Fig. 7a and b for the two different operating flow rates of $10 \mu\text{L min}^{-1}$ and $100 \mu\text{L min}^{-1}$, respectively. As expected, the recordings of I_u are in good agreement with the individual upstream cell portion characterization results. However, the downstream contribution (I_d) is different than the individual

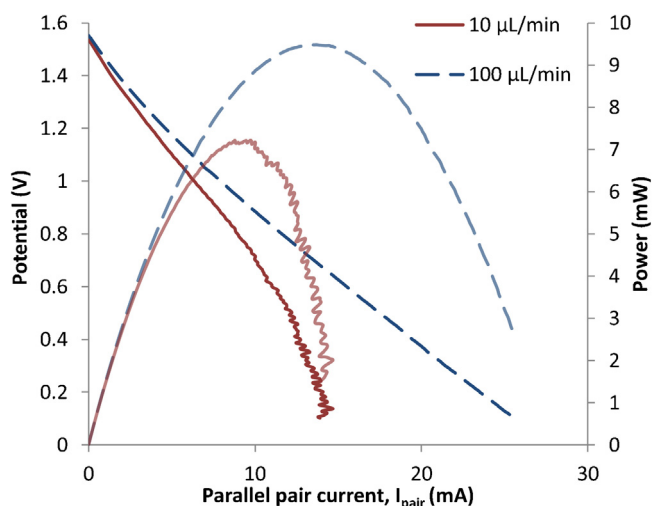


Fig. 6. Performance results of the combined cell with the two portions connected in parallel at flow rates of $10 \mu\text{L min}^{-1}$ and $100 \mu\text{L min}^{-1}$.

downstream portion characterization since upstream reactant conversion occurs during the parallel connection, whereas during the individual downstream cell portion characterization, the upstream portion is kept at OCV. For this reason, the current of the downstream portion is observed to be highly influenced by mass transport losses at the low flow rate, when the two cell portions are connected in parallel. This is a consequence of the high fuel utilization at low flow rates. Moreover, at this region of mass transport limitations, it is noted that the current output of the downstream portion decreases with the increase of the total current output of the combined parallel cell. This is attributed to a shift in the relative current contributions of the two portions from nearly equal at near-OCV conditions to upstream-dominated current at lower cell potentials. This interesting feature, which is uniquely revealed by the present analytical cell configuration, shows the detrimental effect of high reactant conversion in the upstream portion on the performance of the downstream portion. Nevertheless, at the higher flow rate of $100 \mu\text{L min}^{-1}$, the mass transport is enhanced and the concentration overpotential is reduced, as seen in Fig. 7b. In this case, the downstream contribution (I_d) approaches the value obtained by the individual downstream cell portion characterization due to the decreased species conversion upstream ($< 6\%$). As expected, the sum of the two currents from the upstream and downstream portions ($I_u + I_d$) is equal to the total current measured by the potentiostat for all cell voltages of the combined polarization curve of the pair.

The reactant utilization efficiency of the cell can be estimated from the currents produced at different applied loads in order to compare the contributions of the upstream and downstream portions and further analyze the dual-pass architecture. The utilization factor of each portion, when connected in parallel, is

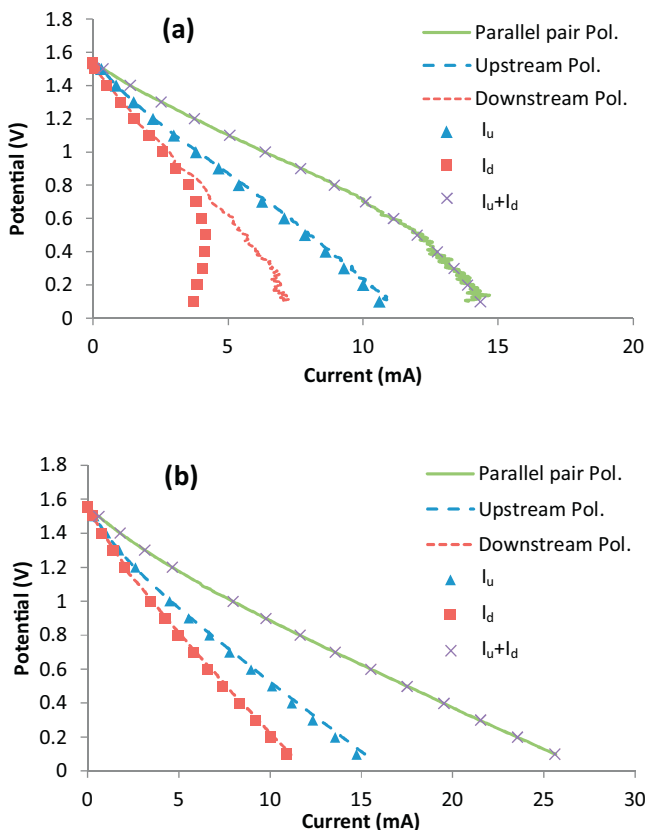


Fig. 7. Polarization curves of the upstream and downstream cell portions when connected in parallel at a) $10 \mu\text{L min}^{-1}$ and b) $100 \mu\text{L min}^{-1}$.

again calculated based on the incoming reactant concentration and current produced at each portion (I_u and I_d). The incoming concentration for the upstream portion is equal to the concentration of the fresh supplied reactant used in the previous calculations. However, for the downstream portion, the incoming concentration is reduced due to the conversion in the upstream portion. The available incoming concentration for the downstream portion is thus estimated by subtracting the upstream conversion, assuming that crossover losses are negligible. The calculations are summarized in Eqs. ((3)-(6)):

$$\Delta C'_{u/d} = \frac{I_{u/d} \times 60}{1000 \times F} \quad (3)$$

$$C'_{u0} = \frac{M_0 \times Q}{1000000} \quad (4)$$

$$C'_{d0} = C'_{u0} - \Delta C'_u \quad (5)$$

$$\%C_{u/d} = \frac{\Delta C'_{u/d}}{C'_{u0/d0}} \quad (6)$$

where $\Delta C'$ represents the rate of reactant conversion (mol min^{-1}), C'_{0i} is the rate of incoming reactant supply (mol min^{-1}), and the subscripts u and d refers to upstream and downstream portions,

respectively. For example, at the low flow rate of $10 \mu\text{L min}^{-1}$ and a cell potential of 0.8 V (close to the peak power output condition), currents of 5.54 and 3.50 mA are produced in the upstream and downstream portions, respectively. These currents correspond to utilization factors of 19.8% and 16.1% .

The obtained reactant utilization efficiency of the upstream and downstream portions is plotted as a function of the cell potential of the parallel pair in Fig. 8a and b at fixed flow rates of $10 \mu\text{L min}^{-1}$ and $100 \mu\text{L min}^{-1}$, respectively. At the low flow rate, a plateau region for the downstream reactant utilization efficiency of about 22% can be noted at potentials below 0.5 V , despite the higher current outputs of the combined cell portions at lower potentials. This further confirms the higher reactant depletion and mass transport limitations for the downstream portion at low flow rates, as previously discussed in Fig. 7a. For the high flow rate of $100 \mu\text{L min}^{-1}$, this region is not observed and the utilization efficiency equals 2.8% and 2.2% for the upstream and downstream portions, respectively, at the condition of peak power output ($\sim 0.7 \text{ V}$). These estimated values of the upstream and downstream utilization efficiencies are thus of the same order. By taking into account the $\sim 70\%$ higher ohmic resistance of the downstream portion, these findings confirm that the downstream section is providing a significant contribution to the performance of dual-pass CLFCs, at both high and low flow rates. However, the effectiveness of the downstream portion in terms of both power density and reactant utilization at various flow rates is an important consideration for these cells.

3.3. In-situ regeneration

Electrolyte recirculation and in-situ regeneration (charging) was previously demonstrated with the baseline dual-pass architecture [14]. The present analytical device could therefore be applied to investigate and diagnose the effectiveness of the two cell portions under relevant conditions of in-situ regeneration of the vanadium species. Here, a new cell is fabricated and operated on low SOC ($20\% \text{ V(II)}$ and $30\% \text{ V(V)}$) electrolytes at $10 \mu\text{L min}^{-1}$ and $1 \mu\text{L min}^{-1}$. Before in-situ charging operations, the individual OCVs of the upstream and downstream portions are measured at both flow rates. OCV_u is found to be 1.359 V for both flow rates, confirming the absence of crossover effects in the upstream portion, while OCV_d equals 1.345 and 1.279 V at 10 and $1 \mu\text{L min}^{-1}$, respectively, indicating a significant rate of diffusive crossover at the lowest flow rate for the downstream portion. Next, the upstream portion is connected to the potentiostat for charging at 1.7 V , while a voltmeter is connected to the downstream portion to record OCV_d . The results are summarized in Fig. 9. At $10 \mu\text{L min}^{-1}$, OCV_d rises from 1.345 to 1.376 V , which is equivalent to a net voltage gain of 31 mV or 17 mV over the initial inlet OCV_u . This demonstrates species regeneration with an estimated 7% increase in SOC based on the Nernst equation and titration curves. The same experiment is repeated at $1 \mu\text{L min}^{-1}$ and the OCV_d is seen to increase from 1.279 to 1.421 V , which is equivalent to a net gain of 142 mV or 62 mV over OCV_u and an estimated 27% increase in SOC.

The crossover loss significantly influences the charging performance. This is confirmed visually during the charging experiments, as shown in Fig. 10. For the high flow rate of $10 \mu\text{L min}^{-1}$, the color changes are marginal (Fig. 10a) due to the rather low net species conversion. However, at the low flow rate of $1 \mu\text{L min}^{-1}$, a deep yellow color is observed at the exit of the positive electrode in the upstream portion (Fig. 10b), which indicates a V(V) dominated electrolyte with high SOC. The effect of diffusive crossover and asymmetric splitting of the two co-laminar streams is then observed by the gradual color changes in the central channel before the split streams enter the electrodes of the downstream portion. In order to diagnose this influence, the estimated SOC

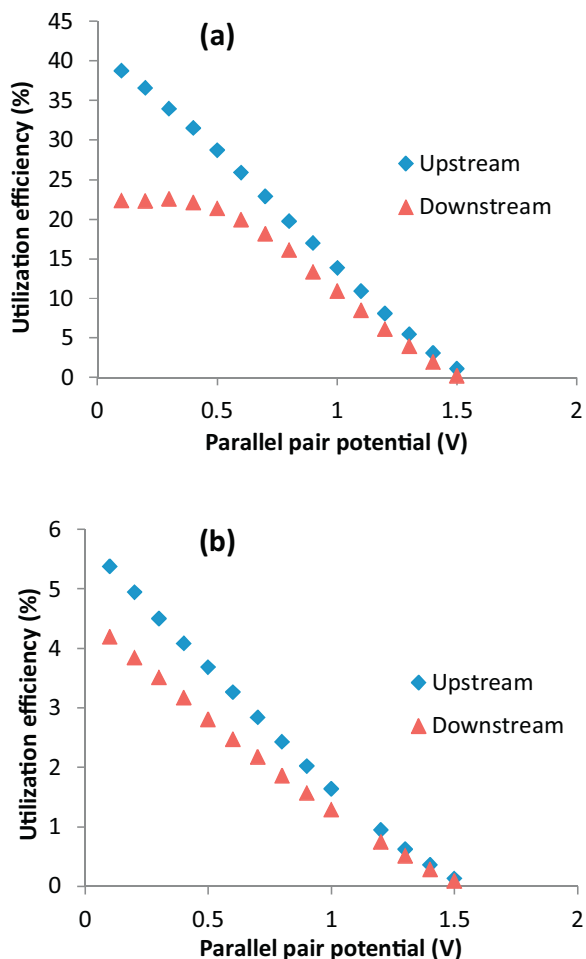


Fig. 8. Reactant utilization efficiency of the upstream and downstream cell portions when connected in parallel at: a) $10 \mu\text{L min}^{-1}$ and b) $100 \mu\text{L min}^{-1}$.

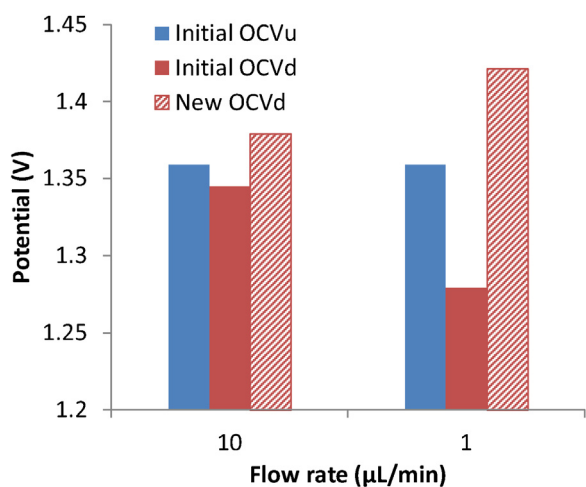


Fig. 9. Steady state results for in-situ regeneration in the upstream portion at $10 \mu\text{L}/\text{min}^{-1}$ and $1 \mu\text{L}/\text{min}^{-1}$ compared to the initial OCV data measured before charging.

from the OCV_d measurement is compared to the theoretical, crossover-free SOC based on the upstream reactant conversion rate calculated from the coulombic charging rate. The measured upstream charging current equals 2.0 mA and 1.3 mA, which is equivalent to reactant conversion of approximately 11% and 65%, at $10 \mu\text{L}/\text{min}^{-1}$ and $1 \mu\text{L}/\text{min}^{-1}$, respectively. The 65% conversion at $1 \mu\text{L}/\text{min}^{-1}$ implies a theoretical upstream SOC of 95% after charging, which confirms the previous observation of a V(V) dominated electrolyte. The condition of high SOC and low flow rate then results in relatively high crossover and partial discharge before entering the downstream portion, hence reducing the downstream SOC to the estimated value of 57% (38% SOC loss). In order to counteract this crossover loss, the downstream portion is also used to charge the species by connecting the two cell portions in parallel. For example, at $10 \mu\text{L}/\text{min}^{-1}$, the SOC of the V(V) electrolyte is estimated to reach 41% upstream and decrease to 37% due to crossover. During parallel charging, the total current recorded is 4.1 mA, comprising of 2.0 mA and 2.1 mA upstream and downstream contributions, respectively. Hence, the downstream

portion has a calculated reactant conversion of 13%, which corresponds to a theoretical V(V) outlet SOC of 50%, representing a net cell charging of 20%. For $1 \mu\text{L}/\text{min}^{-1}$, complete species charging is observed, which results in hydrogen bubble formation in the microfluidic channel and thereby unreliable coulombic data. At both flow rates, downstream reactant charging is found to overcome the crossover loss and contribute additional net charge to the reactants.

Finally, the symmetry of the analytical cell is utilized to demonstrate a charge-discharge cycle test. Here, the upstream cell is charging at 1.7 V, while the downstream cell is discharging at a certain potential. At $10 \mu\text{L}/\text{min}^{-1}$, a potential of 1.262 V is found to discharge the species back to the original 20% SOC (7% conversion). The current output of the downstream portion in this case equals 0.52 mA. Comparing this to the upstream current during charging at 1.7 V (2.0 mA), a charge-discharge cycle efficiency of $\sim 19\%$ is estimated. Similarly, at the low flow rate of $1 \mu\text{L}/\text{min}^{-1}$, the efficiency is estimated to $\sim 21\%$. In both cases the roundtrip efficiency is primarily limited by reactant crossover, which affects the entire amount of reactants, while only a portion of the reactants available is utilized for energy conversion.

In-situ regeneration can theoretically lead to a higher state of charge at lower flow rates due to higher reactant utilization. However, as shown in the previous sections, crossover losses may also increase and therefore negatively affect the charging performance of MRBs, provided that every crossover molecule represents a loss of charge. Although a net positive gain in SOC is observed at both flow rates in the present work, alternate operating conditions could potentially result in a negative outcome of charging (i.e., a lower state of charge than the initial value), in case the crossover voltage loss exceeds the gain due to charging. In general, the analytical device presented in this work provides a straightforward in-situ method to directly assess the voltage losses that occur in MRBs by simple voltage measurements, and can readily distinguish voltage losses from crossover from voltage changes due to reactant conversion during both discharging and charging operations. The quantitative findings of this analytical study therefore provide a method to predict the discharging and charging performance of CLFCs with dual-pass architecture, which can aid further device design and optimization.

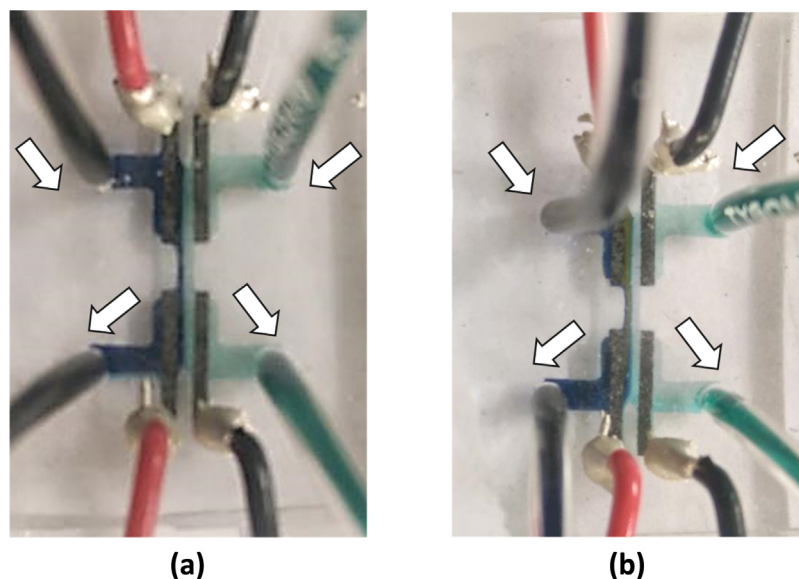


Fig. 10. Annotated images of the analytical device during upstream regeneration at: a) $10 \mu\text{L}/\text{min}^{-1}$ and b) $1 \mu\text{L}/\text{min}^{-1}$. The arrows indicate flow directions at the inlets and outlets.

4. Conclusions

An analytical cell is proposed as a characterization tool for co-laminar flow cells with dual-pass flow-through porous electrodes. The analytical cell design features split electrodes and thus divides the cell into separate upstream and downstream portions that can be connected electrically in parallel to simulate the regular cell operation while the performance characteristics of the individual portions are measured. The crossover losses during discharge operation were assessed by measuring the OCV of the upstream and downstream portions individually at two different flow rates. The crossover loss of the downstream portion was reduced from 41 mV down to 13 mV by increasing the flow rate and thereby limiting diffusive mixing. The upstream cell portion achieved a maximum power density of 0.75 W cm^{-2} at a current density of 1.0 A cm^{-2} , which represents the highest power density reported to date for a microfluidic vanadium redox cell. The performance was also measured with the two cell portions connected in parallel in order to characterize the in-situ current contribution of both passes of the dual-pass architecture. The combined parallel cell produced a peak power density of 0.63 W cm^{-2} which is less than that of the individual upstream cell due to higher crossover and ohmic losses of the downstream portion in addition to the partial reactant conversion upstream. The reactant utilization efficiency was estimated for each of the two portions and the contribution of the downstream portion was found in the same order as that of the upstream, at both flow rates. However, the downstream portion was also observed to be prone to mass transport limitations during the parallel connection and a plateau region at 22% utilization efficiency was estimated at the low flow rate, due to the higher upstream conversion rates. The charging performance of the dual-pass cell was also diagnosed by applying an electrolytic cell voltage to the upstream portion while monitoring the downstream OCV. The results revealed a strong competition between upstream reactant regeneration and downstream crossover losses, as both reactant conversion (current) and crossover increase simultaneously at low flow rates. However, the crossover loss could be overcome by second stage charging in the downstream portion, resulting in substantial net gain in state of charge. Overall, this work confirms the benefits of the outlets design of the dual-pass architecture which enhances discharge performance and enables reactant recirculation and in-situ regeneration by means of improved mass transport in the flow-through porous electrodes. Furthermore, the present results and the analytical cell characterization method are anticipated to aid device optimization by deeper understanding of the reactant conversion and various voltage loss contributions in the cells.

Acknowledgements

The authors highly appreciate the funding for this research provided by the Natural Sciences and Engineering Research

Council of Canada, Western Economic Diversification Canada, Canada Foundation for Innovation, and British Columbia Knowledge Development Fund.

References

- [1] M.-A. Goulet, E. Kjeang, Co-laminar flow cells for electrochemical energy conversion, *J. Power Sources* 260 (2014) 186–196.
- [2] R. Ferrigno, A.D. Stroock, T.D. Clark, M. Mayer, G.M. Whitesides, Membraneless vanadium redox fuel cell using laminar flow, *J. Am. Chem. Soc.* 124 (2002) 12930–12931.
- [3] E.R. Choban, L.J. Markoski, A. Wieckowski, P.J. Kenis, Microfluidic fuel cell based on laminar flow, *J. Power Sources* 128 (2004) 54–60.
- [4] E. Kjeang, N. Djilali, D. Sinton, Microfluidic fuel cells: A review, *J. Power Sources* 186 (2009) 353–369.
- [5] E. Kjeang, *Microfluidic Fuel Cells and Batteries*, Springer, 2014.
- [6] B. Ho, E. Kjeang, Microfluidic fuel cell systems, *Cent. Eur. J. Eng.* 1 (2011) 123–131.
- [7] R.S. Jayashree, L. Gancs, E.R. Choban, A. Primak, D. Natarajan, L.J. Markoski, P.J. Kenis, Air-breathing laminar flow-based microfluidic fuel cell, *J. Am. Chem. Soc.* 127 (2005) 16758–16759.
- [8] X. Zhu, B. Zhang, D.-D. Ye, J. Li, Q. Liao, Air-breathing direct formic acid microfluidic fuel cell with an array of cylinder anodes, *J. Power Sources* 247 (2014) 346–353.
- [9] S.A. Mousavi Shaegh, N.-T. Nguyen, S.H. Chan, Air-breathing microfluidic fuel cell with fuel reservoir, *J. Power Sources* 209 (2012) 312–317.
- [10] E. Ortiz-Ortega, M.-A. Goulet, J.W. Lee, M. Guerra-Balcazar, N. Arjona, E. Kjeang, J. Ledesma-Garcia, L.G. Arriaga, A nanofluidic direct formic acid fuel cell with a combined flow-through and air-breathing electrode for high performance, *Lab chip* 14 (2014) 4596–4598.
- [11] J. Esquivel, F. Del Campo, J.G.m. de la Fuente, S. Rojas, N. Sabate, Microfluidic fuel cells on paper: meeting the power needs of next generation lateral flow devices, *Energy & Environmental Science* 7 (2014) 1744–1749.
- [12] E. Kjeang, J. McKechnie, D. Sinton, N. Djilali, Planar and three-dimensional microfluidic fuel cell architectures based on graphite rod electrodes, *J. Power Sources* 168 (2007) 379–390.
- [13] E. Kjeang, R. Michel, D.A. Harrington, N. Djilali, D. Sinton, A microfluidic fuel cell with flow-through porous electrodes, *J. Am. Chem. Soc.* 130 (2008) 4000–4006.
- [14] J.W. Lee, M.-A. Goulet, E. Kjeang, Microfluidic redox battery, *Lab chip* 13 (2013) 2504–2507.
- [15] W.A. Braff, M.Z. Bazant, C.R. Buie, Membrane-less hydrogen bromine flow battery, *Nat. Commun.* 4 (2013) .
- [16] I.B. Sprague, D. Byun, P. Dutta, Effects of reactant crossover and electrode dimensions on the performance of a microfluidic based laminar flow fuel cell, *Electrochim. Acta* 55 (2010) 8579–8589.
- [17] K.S. Salloum, J.D. Posner, Counter flow membraneless microfluidic fuel cell, *J. Power Sources* 195 (2010) 6941–6944.
- [18] K.S. Salloum, J.D. Posner, A membraneless microfluidic fuel cell stack, *J. Power Sources* 196 (2011) 1229–1234.
- [19] B. Ho, E. Kjeang, Planar Multiplexing of Microfluidic Fuel Cells, *J. Fluids Eng.* 135 (2013) 021304.
- [20] M.-A. Goulet, E. Kjeang, Reactant recirculation in electrochemical co-laminar flow cells, *Electrochim. Acta* 140 (2014) 217–224.
- [21] O.A. Ibrahim, M.-A. Goulet, E. Kjeang, Microfluidic electrochemical cell array in series: effect of shunt current, *J. Electrochem. Soc.* 162 (2015) F639–F644.
- [22] M. Rychcik, M. Skyllas-Kazacos, Characteristics of a new all-vanadium redox flow battery, *J. Power Sources* 22 (1988) 59–67.
- [23] M. Skyllas-Kazacos, M. Rychcik, R.G. Robins, A.G. Fane, M.A. Green, New All-Vanadium Redox Flow Cell, *J. Electrochem. Soc.* 133 (1986) 1057–1058.
- [24] J.W. Lee, E. Kjeang, Chip-embedded thin film current collector for microfluidic fuel cells, *Int. J. Hydrogen Energy* 37 (2012) 9359–9367.
- [25] J.W. Lee, J.K. Hong, E. Kjeang, Electrochemical characteristics of vanadium redox reactions on porous carbon electrodes for microfluidic fuel cell applications, *Electrochim. Acta* 83 (2012) 430–438.
- [26] J.W. Lee, E. Kjeang, Nanofluidic fuel cell, *J. Power Sources* 242 (2013) 472–477.

Appendix B.

Microfluidic Electrochemical Cell Array in Series: Effect of Shunt Current

An open access article [98] reproduced from The Electrochemical Society under creative commons license (CC BY-NC-ND 4.0)



Microfluidic Electrochemical Cell Array in Series: Effect of Shunt Current

Omar A. Ibrahim,* Marc-Antoni Goulet,* and Erik Kjeang**^z

School of Mechatronic Systems Engineering, Simon Fraser University, Surrey, British Columbia V3T0A3, Canada

Stacking of microfluidic fuel cells and redox batteries may cause internal current losses and reduced performance compared to single cells. In the present work, these internal current losses are investigated experimentally for an array of two microfluidic vanadium redox batteries based on flow-through porous electrodes. A unique cell array design is proposed, having two pairs of flow-through electrodes situated in a single co-laminar flow manifold. The two electrochemical cells are connected electrically in series and have series fluidic connection through the electrolyte in order to reuse the partially consumed reactants from the first, upstream cell in the second, downstream cell. The cell array prototype demonstrates a maximum power output of 9 mW and a maximum current of 13.5 mA. However, current losses up to 1.75 mA are observed at open circuit, which is attributed to reactant discharge through a parasitic cross-cell comprising of one electrode from each electrochemical cell in the shared manifold. This current loss, appearing in the form of a shunt current, is shown to be proportional to the cell potential. The drop in coulombic efficiency is calculated to quantify the effect of the shunt current. Recommendations for mitigation of shunt current in microfluidic cell arrays are provided.

© The Author(s) 2015. Published by ECS. This is an open access article distributed under the terms of the Creative Commons Attribution Non-Commercial No Derivatives 4.0 License (CC BY-NC-ND, <http://creativecommons.org/licenses/by-nc-nd/4.0/>), which permits non-commercial reuse, distribution, and reproduction in any medium, provided the original work is not changed in any way and is properly cited. For permission for commercial reuse, please email: oa@electrochem.org. [DOI: 10.1149/2.0211507jes] All rights reserved.

Manuscript submitted January 26, 2015; revised manuscript received March 11, 2015. Published March 27, 2015. This was Paper 27 presented at the Cancun, Mexico, Meeting of the Society, October 5–9, 2014.

Advances in micro-fabrication have enabled the inexpensive production of microfluidic channels which have recently been utilized in electrochemical applications such as fuel cells and flow batteries.¹ Among these microfluidic electrochemical cells, some have implemented the concept of co-laminar flow rather than a physical membrane to achieve reactant separation. In the former mentioned co-laminar flow cells (CLFCs), wherein species mixing is mainly governed by diffusion, the diffusional interface provides separation between the two flowing streams whilst permitting ion transport. In general, these cells offer great advantages over their conventional counterparts such as the simplicity of the structure, elimination of the membrane and its cost and hydration issues. These membraneless CLFCs thus hold promises of future power generation for portable devices and off-grid sensors.^{1,2}

The first CLFC was introduced by Ferrigno et al. in 2002, using vanadium redox species in a Y-shaped channel.³ Since then, several reviews have been published which summarize the fundamental physics of these devices,⁴ and also highlight some of the milestones achieved in device functionality, reactants and architectures,^{2,5} for both fuel cells^{6–10} and batteries.^{11–13} The first architectures reported used planar electrodes on the sides or bottom of a micro-channel.^{3,7} Jayashree et al. introduced the air breathing cathode architecture that allowed gaseous oxygen transport from the surroundings.¹⁴ Kjeang et al. introduced the flow-through electrode architecture that increased both performance characteristics and fuel utilization by utilizing the whole three-dimensional area of a porous carbon electrode.¹⁵ Using a derivative cell architecture with dual pass configuration, Lee et al.¹¹ developed the first microfluidic redox battery (MRB) that was later analyzed by Goulet and Kjeang.¹⁶ This architecture further increased the performance and enabled complete fuel recirculation and regeneration capabilities, to mimic a conventional flow battery.

One of the challenges for these devices is their limited scalability, because their operation is governed by the nature of laminar flow in microfluidic channels. Complementary to upscaling by expansion of single cells, which has fundamental limitations in this case,¹ stacking of multiple cells is an important strategy to meet the power requirements of target applications. However, stacking of fuel cells or flow batteries can lead to other performance drawbacks. One drawback that

is mainly observed in redox flow batteries is the shunt current loss phenomenon that occurs for electrolyte filled paths.¹⁷ These paths not only provide necessary flow connections but may also introduce undesired electrical short connections. The ionic currents generated are driven through these conductive paths and may cause severe energy and performance losses. Codina and Aldaz analyzed the influence of the shunt dependent design parameters on the energy efficiency of a Fe/Cr redox flow battery stack by means of a shunt current calculation model for the stack assembly.¹⁸ Xing et al. presented a stack-level validated model based on circuit analogy to investigate the shunt current loss in vanadium redox batteries.¹⁹ Tang et al. also investigated the effect of the shunt current in vanadium redox cells, with emphasis on the stack efficiency and temperature variation during stand-by periods, since shunt currents can generate heat and cause thermal precipitation of the catholyte.²⁰

Despite the added challenges, several groups have attempted stacking of co-laminar flow cells. Salloum and Posner enhanced the overall fuel utilization of vanadium redox species by reusing the reactants in a downstream cell connected in parallel.²¹ The downstream cell, however, produced less current output due to the reduced species concentration, and a third blank stream of sulfuric acid was required to facilitate the reactant separation between cells. Moore et al. presented a vertical stacking approach for microfluidic fuel cells.²² The output of their two cells stacked in parallel was equivalent to the sum of two single cells with losses attributed to the mal-distribution of reactant flow rates among the two connected cells. Alternatively, Ho and Kjeang addressed the issue of uniform flow distribution with the aid of modeling and experiments, and demonstrated twice the power output by planar multiplexing of two identical cells in series with the symmetric bilateral stack design while supplying fresh reactants to each cell.²³ A very recent study by Wang et al. presented mathematical modeling of microfluidic fuel cell stacks of four cells to analyze shunt current losses.²⁴ The cells had individual serpentine inlet channels with a common distribution port in order to balance the pressures between cells, uniformly distribute the reactants and minimize bypass current. The results showed stacking efficiencies of 93% and 82% for parallel and series electrical connections, respectively, showing the higher significance of shunt currents in series connections. However, none of these studies presented combined serial electrical connection of the cells to increase the voltage output with serial fluidic connection to maximize the fuel utilization.

Therefore, the objective of the present work is to examine the effect of internal shunt currents on the performance of a microfluidic

*Electrochemical Society Student Member.

**Electrochemical Society Active Member.

^zE-mail: ekjeang@sfu.ca

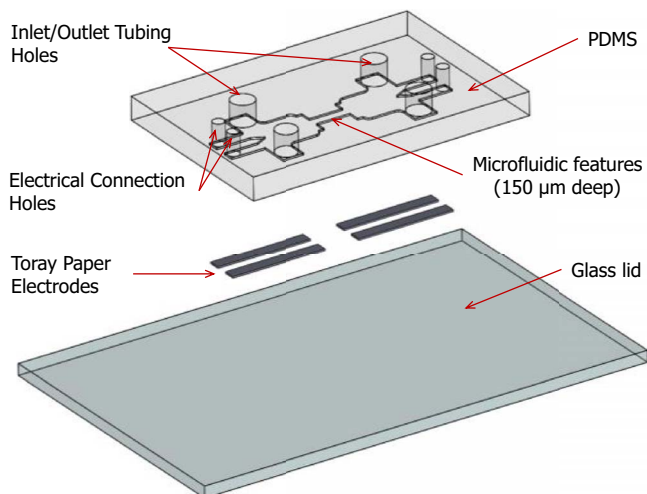


Figure 1. An exploded view of the cell array assembly showing the two cell portions connected by the shared electrolyte microchannel manifold.

electrochemical cell array uniquely designed for reutilization of reactants in a single flow manifold. The cell design is based on the microfluidic redox battery (MRB) previously published by our group,^{11,16} which features flow through porous electrodes and a dual pass architecture. In this case however, the dual pass electrodes have been isolated into separate electrode sections to create a two-cell array and analyze the performance of each cell individually. This permits a detailed comparison of upstream and downstream cell performance and also reveals the effects of shunt current due to the shared electrolyte manifold when the cells are connected in series.

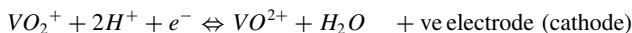
Methodology

Cell design and fabrication.— The new microfluidic electrochemical cell array architecture under consideration is similar to the MRB¹¹ previously discussed with each electrode divided and isolated into two sections with separate electrical routing, as shown in Figure 1. This modification essentially divides the original MRB into two full operating cells; a full upstream portion and a full downstream portion, which have fluidic connection in series via the electrolyte. This would allow utilizing the unconsumed species from the first portion in the second portion. For the purpose of studying shunt currents, the two portions are connected electrically in series.

The fabrication of the presented device is based on soft lithography of polydimethylsiloxane (PDMS) from an SU-8 photo-resist template. An SU-8 (Microchem) master for the design is fabricated on a four-inch silicon wafer and a transparency mask is used for the UV exposure of the features on a secondary layer of SU-8 photoresist. A profilometer is used to measure the height of the SU-8 master to ensure it is $\pm 10 \mu\text{m}$ within the desired value of $150 \mu\text{m}$. Next, a 10:1 mixture of PDMS elastomer (Dow Corning) and its curing agent is used to prepare a mold using the master and is cured for three days under vacuum. The mold is then cut and holes are punched for inlet and outlet ports as well as electrical connections for the electrodes. Heat treated carbon paper (TGPH-060, Toray) is used to cut four rectangular electrode strips for the device electrodes which are manually placed inside the cell before a glass lid is permanently bonded on the cell by plasma treatment of the two surfaces (BD-20AC, Electro-Technic Products). The electrodes have a width of 1 mm and a thickness $>150 \mu\text{m}$ to allow electrode compression and thus minimize flow bypass. Electrical wire connections are bonded to the electrodes using silver conductive epoxy (MG Chemicals). Small diameter (3/32 in. O.D., 1/32 in. I.D.) Tygon tubing (Saint-Gobain) is inserted into the inlet and outlet ports of the cells.

Reactants.— The reactants used for testing the fabricated device are the all-vanadium redox species, first developed by Skyllas-

Kazacos et al.^{25,26} Here, V^{2+} , V^{3+} , VO^{2+} and VO_2^+ will be referred to as V2, V3, V4 and V5, respectively. V2 and V5 are used as anodic and cathodic reactants, respectively, for battery discharge operation. The two half-cell reactions are given as:



V2 and V5 species are prepared by charging a 1.7 M stock commercial mixture of V3/V4 in 4 M sulfuric acid electrolyte using a custom-designed flow cell and a power supply. The potentials at open circuit are measured for both half-cells after charging using a saturated calomel reference electrode (SCE, Fisher Scientific) and found to be -0.545 V and 1.01 V for V2 and V5, respectively. The solutions are loaded into separate syringes. Further details about fabrication and materials are found in previously published articles by our group.^{9,10,16}

Experimental setup.— A dual syringe pump unit (Harvard Apparatus) is used to provide the flow of vanadium redox electrolytes into the cell array. Another unit is used to withdraw the flow from the outlet ports in order to minimize pulsations and collect the electrolyte for further charging and reuse. All experiments are conducted at low and high flow rates of 10 and $100 \mu\text{l}/\text{min}$, respectively. A potentiostat (Gamry Reference 3000) is used to measure discharge polarization curves by linearly sweeping the cell voltage while measuring the current using potentiodynamic mode. Before the dynamic experiments, the open circuit voltage (OCV) of the individual upstream and downstream portions is measured.

To form the serial cell array, the anode of the upstream portion is electrically wired to the cathode of the downstream portion. The performance of the serial array of the two cell portions is also measured by the same method. Two multi-meters (EX430, Extech) are used in voltmeter mode to monitor the voltage across each cell portion during the voltage sweep (V_u and V_d). An extra multimeter is connected in series in ammeter mode between the two wired electrodes from the two different cell portions to measure the current passing through the wire (I_m) and compare it with the total array current (I_{cell}) running through the potentiostat. A detailed circuitry diagram for the serial array is given in Figure 2a.

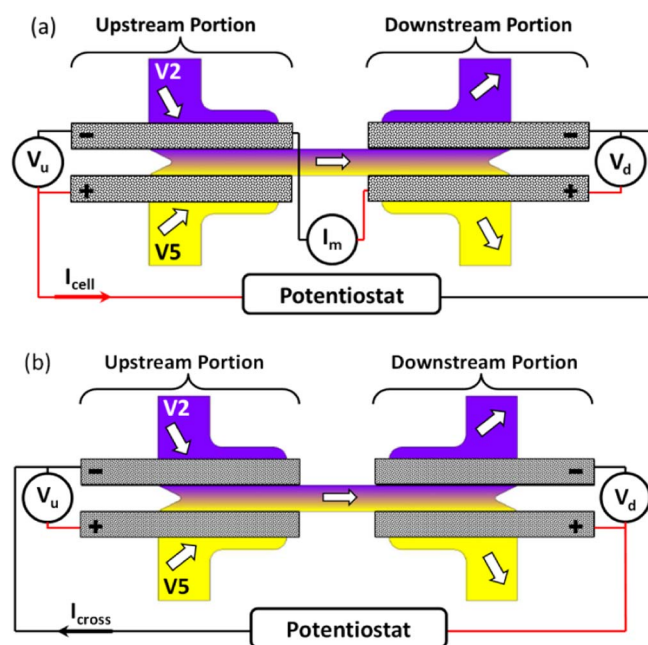


Figure 2. A schematic diagram showing the microfluidic electrochemical cell array design and electrical circuitry for a) serial array connection and b) cross cell connection.

Moreover, the polarization curves of the cell having the upstream anode (V2 side) and the downstream cathode (V5 side) are also measured. This connection will henceforth be referred to as the cross connection. The results of the cross cell are important to consider in any electrochemical cell array that makes use of shared electrolyte manifolds due to the potentially detrimental impact of overall array performance. The OCVs of the two portions are again monitored during the cross cell measurements, as shown in Figure 2b. Finally, the ohmic resistances of the two individual portions, the cross cell and the serial array are also measured by means of electrochemical impedance spectroscopy (EIS) performed using the same potentiostat by reading the real axis value at the high frequency intercept in the Nyquist plot. For the purpose of this study, all the polarization curves are presented in the form of voltage-current plots and are not normalized.

Results and Discussion

Prototypes of the proposed microfluidic electrochemical cell array in series are built and tested experimentally in order to examine the effect of internal shunt currents on the performance and efficiency of the device. Before measuring the performance data of the full cell array, the resistances and open circuit voltages (OCVs) of the individual upstream and downstream portions are measured. The upstream and downstream portions of the array have resistances of 58Ω and 51Ω , respectively, as measured by EIS. The OCV of the upstream cell equals 1.556 V while that of the downstream equals 1.515 V and 1.539 V at flow rates of 10 and $100 \mu\text{l}/\text{min}$, respectively. The differences are mostly due to higher reactant crossover at the downstream portion attributed to inter-diffusion of species along the co-laminar flow interface inside the manifold. Another minor reason is the asymmetric splitting of the reactants toward the outlet ports, as explained in a previous study by our group.¹⁶

Next, the two portions are connected to form the serial array, by wiring the anode of the upstream portion with the cathode of the

downstream portion, as seen in Figure 2a. When the two portions are connected in series, the OCV measured for the upstream portion drops, despite having no additional exposure to reactant crossover. At $100 \mu\text{l}/\text{min}$, the OCV of the upstream portion drops to 1.378 V versus 1.556 V during individual portion characterization. Moreover, color changes for the vanadium electrolytes are observed close to the electrode surfaces, which indicates reactant conversion even though the cell array is held at open circuit condition at zero net current. This indicates that the reactants are being discharged through the cross cell that is both electrically short circuited by the wire and ionically connected via the electrolyte. Furthermore, in these experiments, the serial array is connected with an ammeter (I_m) between the two wired electrodes (Figure 2a), to measure the current passing through the series connection wire. Here, a steady non-zero value for the current I_m is recorded during OCV of the serial array. For example, at $100 \mu\text{l}/\text{min}$, a current of $I_m = 1.75 \text{ mA}$ is recorded, which further confirms the discharge of the cross cell and explains the drop in the OCV in the upstream portion mentioned earlier. It therefore becomes important to characterize the cross cell and this short circuit behavior first before the series data can be properly understood.

Cross cell.— The cross cell is formed from the upstream cell anode and the downstream cell cathode, as shown in Figure 2b. The polarization curve of the cross cell is measured at flow rates of 10 and $100 \mu\text{l}/\text{min}$, and shown in Figure 3a and 3b, respectively. The polarization curve for the cross cell is found to be highly linear, which indicates that the performance is controlled by ohmic losses. This is confirmed by EIS, by which a combined ohmic cell resistance of around 750Ω is measured. This high resistance, which is more than an order of magnitude higher than for a regular cell, is likely dominated by the ionic resistance of the electrolyte in the long and narrow micro-channel between the two electrodes of the cross cell. The curves also indicate a limiting current around 1.5 mA for both low and high flow rates.

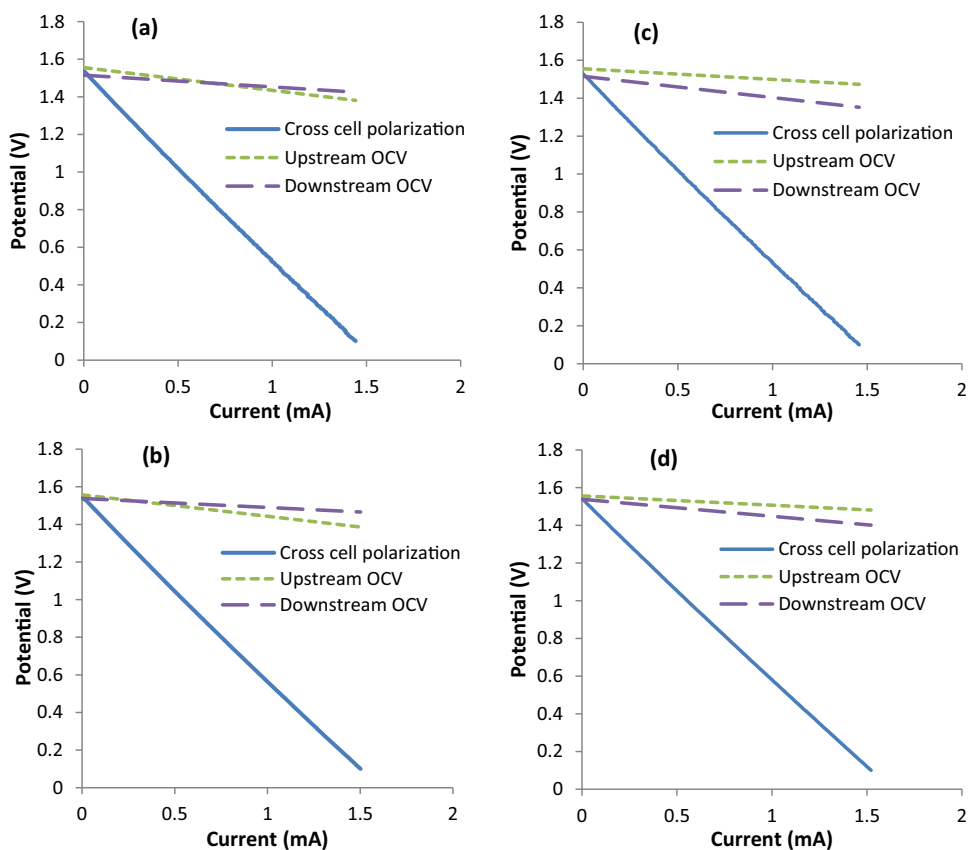


Figure 3. Performance results of the cross cell at a) $10 \mu\text{l}/\text{min}$ and b) $100 \mu\text{l}/\text{min}$. The results for the opposite cross cell configuration at c) $10 \mu\text{l}/\text{min}$ and d) $100 \mu\text{l}/\text{min}$ show the different slopes for the OCV drop of the upstream and downstream cells under the influence of the parasitic cross cell (shunt) current.

Hence, due to the ohmic nature of the cross cell, its current intensity is controlled by the potential difference and the ionic resistance between the two connected electrodes. During the measurements, the OCVs of the upstream and downstream portions (OCV_u and OCV_d) are monitored using voltmeters, V_u and V_d , respectively, as shown in Figure 2b. The results show that the OCVs of both upstream and downstream portions decrease with increasing current drawn from the cross cell, but at different rates. The OCV_u curve has a more negative slope than the OCV_d curve. These changes are caused by the electrochemical overpotentials induced by the cross cell polarization which affect the anode of the upstream cell and the cathode of the downstream cell. The impact on OCV is greater for the anode due to the slower electrochemical kinetics of the V2 oxidation compared to the V5 reduction occurring on the cathode.²⁷ The Nernstian effect of the changes in the respective reactant concentrations appears to be less significant, as it would have a more severe impact on the downstream cell (reductions in both anode and cathode concentrations) than on the upstream cell (reduction in anode concentration only). For example, at 100 $\mu\text{l}/\text{min}$, OCV_u and OCV_d decreased down to 1.386 V and 1.466 V, respectively, at the conditions of maximum (limiting) cross cell current.

Recalling the previously measured OCV results of the serial array, it is noteworthy that the OCV recordings of the two serial array cells are identical under the maximum current condition for the cross cell. To clarify, at a flow rate of 100 $\mu\text{l}/\text{min}$, the OCVs of the upstream and downstream portions equal 1.378 V and 1.461 V, respectively, while the current I_m is around 1.75 mA. These values are almost equal to the OCV values and the maximum current values measured for the cross cell connection (Figure 3b), which further confirms our observation. The slight differences between the data are attributed to the fact that the cross cell polarization voltage is swept down to 0.1 V only and not to the actual short circuit condition of zero potential difference that occurs in the series connection.

The same cross cell experiments are repeated for the opposite cross cell configuration, which has the cathode from the upstream portion and the anode from the downstream portion. The results of the resistance and limiting currents are found to be consistent with the previous results. The OCV drops for the upstream and downstream portions are different, however, because of the V5 reduction in the upstream portion and the V2 oxidation in the downstream portion. The OCV_d curve has a more negative slope than the OCV_u curve and therefore the OCV_u is higher than the OCV_d for all cross cell currents, as seen in Figure 3c and 3d.

Series cells.— Once the characteristics of the cross cell are known, a more detailed analysis of the two cells in series is possible. In these experiments, the two-cell array is connected with an ammeter between the cells (Figure 2a) and externally to the potentiostat. As expected, the ohmic resistance of 108 Ω for the two cells in series measured via EIS is equivalent to the sum of the individual cells.

The polarization and power curves for the array are shown in Figure 4, for the flow rates of 10 and 100 $\mu\text{l}/\text{min}$. This figure also shows the maximum attainable ohmic loss slope, based on the array resistance measured by EIS and the array OCV measured at 100 $\mu\text{l}/\text{min}$. A maximum power output from the serial array of around 6.5 mW and 9 mW at the two different flow rates, respectively, is obtained. Limiting currents of 6 mA and 13.5 mA, respectively, can also be noted. At 10 $\mu\text{l}/\text{min}$, the performance of the array is limited by concentration losses, as can be seen in Figure 4. This is due to the higher fuel utilization at low flow rates. The individual cell voltages are monitored by the two voltmeters, V_u and V_d connected with the upstream and downstream portions, respectively (Figure 2a), and the corresponding cell polarization curves at 10 $\mu\text{l}/\text{min}$ are shown in Figure 5a. The overall performance of the upstream and downstream cell units is similar at low to medium currents up to ~ 4 mA, where mass transport effects are less prominent. However, at low array voltage and high currents, a negative cell voltage is observed for the downstream portion, as shown in Figure 5a. This observation confirms the starvation of the downstream cell, which leads to a reversed

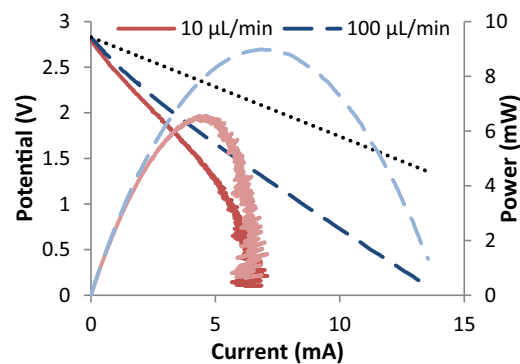


Figure 4. Polarization curves of the series array at 10 $\mu\text{l}/\text{min}$ (—) and 100 $\mu\text{l}/\text{min}$ (---) (left vertical axis). The lighter color lines represent the power curves at the same flow rates (right vertical axis). The maximum attainable ohmic loss slope is also shown (••).

potential in order to support the total array current. This behavior is not observed at higher flow rates of 100 $\mu\text{l}/\text{min}$ (Figure 5b), because at higher flow rates, more reactant species are available and the fuel utilization is generally less than 5%,¹⁵ which means that the downstream cell would still have sufficient reactant species. Overall, it is recommended to avoid array operation in the low-voltage regime as undesirable side reactions may occur at negative downstream cell potentials.

Ideally, the current passing through the ammeter (I_m) should equal the current running through the whole array. However, the current measured through I_m is found to be higher than the array cell current

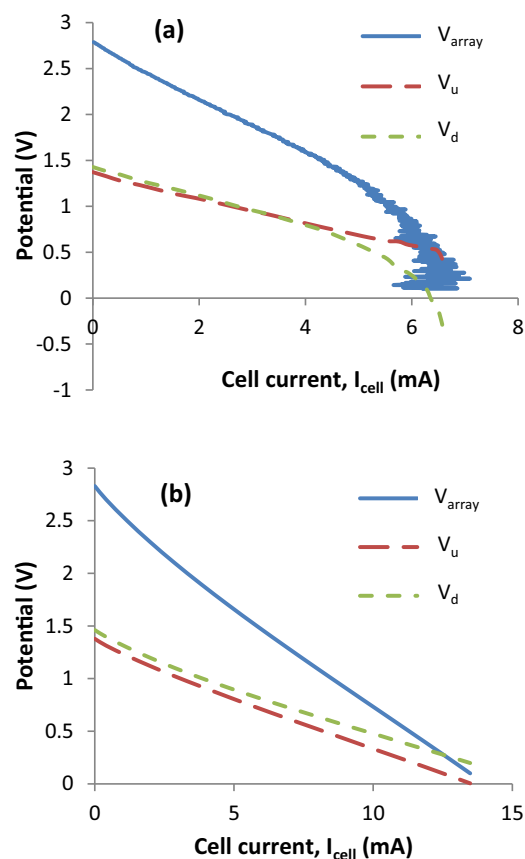


Figure 5. Polarization curves of the upstream and downstream cells measured by multimeters V_u and V_d during serial array measurements at a) 10 $\mu\text{l}/\text{min}$ and b) 100 $\mu\text{l}/\text{min}$. Reversed potentials are noted for the downstream cell at low flow rate and high array current.

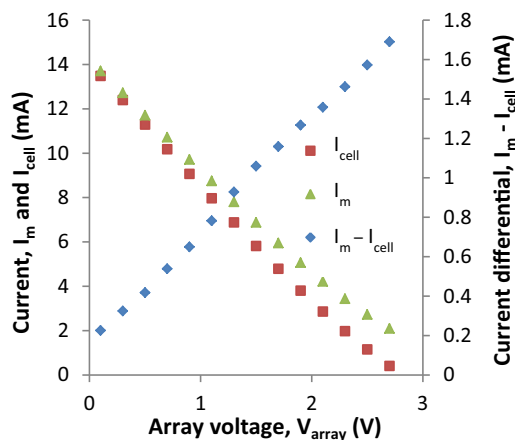


Figure 6. Comparison of the current in the wire between the two cell portions (I_m) and the cell current of the array (I_{cell}) at different array voltages (V_{array}) during series cell connection at a flow rate of 100 $\mu\text{l}/\text{min}$. The current differential ($I_m - I_{cell}$) represents the internal shunt current of the array.

(I_{cell}) running through the potentiostat. This is because the current running through I_m is the sum of the currents from the regular series cell discharging through the connected load during practical operations (I_{cell}) and the cross cell discharging at short circuit. Figure 6 shows the currents I_m and I_{cell} against different array voltages (V_{array}), for the flow rate of 100 $\mu\text{l}/\text{min}$. The difference between the current values, $I_m - I_{cell}$, is also shown in the same figure for different array voltages. The figure shows a decreasing trend for the current differential from 1.75 mA at OCV of 2.829 V to only 0.22 mA at the lowest tested voltage condition of 0.1 V. The current differential is therefore demonstrated to be equal to the shunt current that the array experiences internally. This internal shunt current is shown to be roughly proportional to the array voltage and thereby acts similar to the electrical current through a resistor. The shunt current passing through the electrically shorted cross cell under the influence of the overarching discharge of the two regular cells in the array is ‘discharged’ through the electrolyte between the upstream anode and the downstream cathode, acting as an ionic load for the cross cell. The electrochemical potential difference of the cross cell electrodes (upstream anode and downstream cathode) provides the driving force for this internal circuit. Hence, the maximum shunt current is obtained when the array is held at OCV where the potential difference is greatest, and decreases as the array current is drawn due to the electrochemical overpotentials formed on each electrode. In the present cell array, the electrochemical potential difference between the upstream cathode and the downstream anode is approximately equal to the cell voltage of each cell in the array, which explains why the shunt current is effectively proportional to the array voltage. To further verify the driving forces of the shunt current, the shunt current can also be compared to a current from Ohm’s law as given by: $I = V / R$, with the electrochemical potential difference as a cell voltage and the combined ohmic cell resistance of the cross cell (measured by EIS) as a resistor. A current of ~ 2 mA is estimated by the simple Ohm’s law calculation at OCV, which is comparable to the measured current of 1.75 mA.

This internal shunt current is therefore a parasitic reaction from which both cells of the array suffer, primarily in the form of charge loss but also in the form of a slight voltage loss. Therefore, the most useful approach to describe these losses is to consider the loss in the available state-of-charge of the reactants due to the reactant consumption for the parasitic discharge associated with the shunt current. Hence, the effect of that phenomenon on the coulombic efficiency can be quantified by Eq. 1, where ϵ_c is the drop in the coulombic efficiency of the array, C_0 is the initial concentration (1.7 M \times 87% SOC), Q is the flow rate, F is Faraday’s constant and n is the electron stoichiometry.

$$\epsilon_c = \frac{(I_m - I_{cell})}{C_0 \times Q \times F \times n} \quad [1]$$

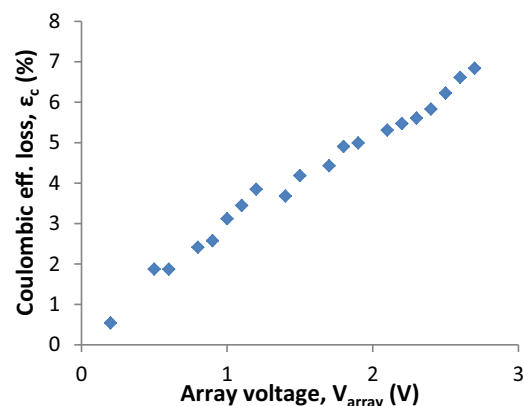


Figure 7. The drop in the coulombic efficiency (ϵ_c) due to shunt current at 10 $\mu\text{l}/\text{min}$ at different operating voltages of the array (V_{array}).

The drop in the coulombic efficiency is plotted as a function of the array voltage (V_{array}) in Figure 7, at 10 $\mu\text{l}/\text{min}$. The results again show a roughly proportional trend up to 7% drop in the coulombic efficiency at OCV, which further confirms the significance of the internal shunt current losses and highlights the importance of taking it into consideration for array cell design and operation.

In electrochemical cell arrays, series stacking of two identical cells would ideally have negligible shunt current and generate twice the OCV and power output of a single cell, such as in the study by Ho and Kjeang.²³ This is likely because the cells employed common distribution ports, which means that they had parallel fluidic connection. The electrolyte path length between the two cells was long enough to create ionic resistance that would make the internal shunt current and associated performance losses negligible. In addition, by the parallel fluidic connection, the two cells were supplied with highly concentrated, unconsumed charged reactants. The symmetry of the bilateral design additionally enabled even flow distribution among both cells, resulting in identical performance. However, if the cells are to have series fluidic connection in order to reuse the unconsumed fuel and increase the overall fuel utilization, the cells should be carefully designed and engineered, because there is a tradeoff between the shunt current losses and other factors such as the pressure drop.¹⁷ In summary, increasing the length of the fluidic connection between the cells and decreasing the microchannel cross sectional area would increase the ionic resistance and decrease the shunt current but may also have drawbacks in the form of increased reactant crossover and pressure drop.

Conclusions

A unique design for an array of two microfluidic electrochemical cells with flow through porous electrodes was fabricated in PDMS using soft lithography techniques and tested in order to experimentally characterize the internal current losses that undesirably occur during stacking of electrochemical cells. The two cells were connected electrically in series as a stacking approach and had series fluidic connection through the common electrolyte manifold in order to reuse the partially consumed reactants from the first, upstream cell in the second, downstream cell to maximize overall fuel utilization. The series array gave a maximum power output of 9 mW and a maximum current of 13.5 mA at a flow rate of 100 $\mu\text{l}/\text{min}$. However, the measurements showed internal current losses up to 1.75 mA at open circuit condition for the same flow rate. This was attributed to the reactant discharge through a parasitic internal circuit having both electronic and electrolytic connection, namely the cross cell formed from opposite half-cells from each individual cell in the array. The internal shunt current was shown to be roughly proportional to the operating voltage of the array with the driving force being the electrochemical potential difference of the electrodes of the internal cross cell circuit. The

shunt current was discharged through the electrolyte which acted as a resistor for the parasitic internal circuit; hence, increasing the ionic resistance of this pathway would reduce the magnitude of the shunt current. The drop in coulombic efficiency of the present cell array configuration was determined to be up to 7% at OCV, which confirmed the significance of the shunt current losses and highlighted the importance of taking it into consideration for design of microfluidic cell arrays and stacks. The negative effects of the shunt current can be mitigated by providing adequate electrolytic charge transfer resistance between adjacent cells, for instance by reducing the cross-sectional dimensions of the electrolyte channel between the cells, although the consequences in terms of reactant crossover and total pressure drop must also be considered.

Acknowledgments

Funding for this research provided by the Natural Sciences and Engineering Research Council of Canada (NSERC), Western Economic Diversification Canada, Canada Foundation for Innovation (CFI), British Columbia Knowledge Development Fund, and Simon Fraser University (SFU) is highly appreciated.

References

1. E. Kjeang, *Microfluidic Fuel Cells and Batteries*, Springer (2014).
2. M.-A. Goulet and E. Kjeang, *J. Power Sources*, **260** 186 (2014).
3. R. Ferrigno, A. D. Stroock, T. D. Clark, M. Mayer, and G. M. Whitesides, *J. Am. Chem. Soc.*, **124**(44), 12930 (2002).
4. E. Kjeang, N. Djilali, and D. Sinton, *J. Power Sources*, **186** (2), 353 (2009).
5. B. Ho and E. Kjeang, *Cent. Eur. J. Eng.*, **1**(2), 123 (2011).
6. E. R. Choban, J. Spendelov, L. Gancs, A. Wieckowski, and P. Kenis, *Electrochim. Acta*, **50**(27), 5390 (2005).
7. E. R. Choban, L. J. Markoski, A. Wieckowski, and P. J. Kenis, *J. Power Sources*, **128**(1), 54 (2004).
8. S. M. Mitrovski and R. G. Nuzzo, *Lab chip*, **6**(3), 353 (2006).
9. J. W. Lee and E. Kjeang, *J. Power Sources*, **242** 472 (2013).
10. J. W. Lee and E. Kjeang, *Int. J. Hydrogen Energy*, **37**(11), 9359 (2012).
11. J. Wook Lee, M.-A. Goulet, and E. Kjeang, *Lab chip*, **13**(13), 2504 (2013).
12. W. A. Braff, M. Z. Bazant, and C. R. Buie, *Nat. Commun.*, **4** (2013).
13. W. A. Braff, C. R. Buie, and M. Z. Bazant, *J. Electrochem. Soc.*, **160**(11), A2056 (2013).
14. R. S. Jayashree, L. Gancs, E. R. Choban, A. Primak, D. Natarajan, L. J. Markoski, and P. J. Kenis, *J. Am. Chem. Soc.*, **127**(48), 16758 (2005).
15. E. Kjeang, R. Michel, D. A. Harrington, N. Djilali, and D. Sinton, *J. Am. Chem. Soc.*, **130**(12), 4000 (2008).
16. M.-A. Goulet and E. Kjeang, *Electrochim. Acta*, **140** 217 (2014).
17. A. Z. Weber, M. M. Mench, J. P. Meyers, P. N. Ross, J. T. Gostick, and Q. Liu, *J. Appl. Electrochem.*, **41**(10), 1137 (2011).
18. G. Codina and A. Aldaz, *J. Appl. Electrochem.*, **22**(7), 668 (1992).
19. F. Xing, H. Zhang, and X. Ma, *J. Power Sources*, **196**(24), 10753 (2011).
20. A. Tang, J. McCann, J. Bao, and M. Skyllas-Kazacos, *J. Power Sources*, **242** 349 (2013).
21. K. S. Salloum and J. D. Posner, *J. Power Sources*, **196**(3), 1229 (2011).
22. S. Moore, D. Sinton, and D. Erickson, *J. Power Sources*, **196**(22), 9481 (2011).
23. B. Ho and E. Kjeang, *J. Fluids Eng.*, **135**(2), 021304 (2013).
24. H. Wang, S. Gu, D. Y. Leung, H. Xu, M. K. Leung, L. Zhang, and J. Xuan, *Electrochim. Acta*, **135** 467 (2014).
25. M. Skyllas-Kazacos, M. Rychcik, R. G. Robins, A. G. Fane, and M. A. Green, *J. Electrochem. Soc.*, **133**(5), 1057 (1986).
26. M. Rychcik and M. Skyllas-Kazacos, *J. Power Sources*, **22**(1), 59 (1988).
27. J. W. Lee, J. K. Hong, and E. Kjeang, *Electrochim. Acta*, **83** 430 (2012).

Appendix C.

Leveraging Co-laminar Flow Cells for Non-aqueous Electrochemical Systems

Leveraging Co-laminar Flow Cells for Non-aqueous Electrochemical Systems

Omar A. Ibrahim^a and Erik Kjeang^{a*}

^a Fuel Cell Research Lab (FCReL), School of Mechatronic Systems Engineering, Simon Fraser University, Canada

*Corresponding Author Information:

Dr. Erik Kjeang,

Address: School of Mechatronic Systems Engineering, Simon Fraser University, 250-13450
102 Avenue, Surrey, BC, V3T0A3, Canada

Email: ekjeang@sfu.ca

Tel: +1 (778) 782-8791, Fax: +1 (778) 782-7514

Abstract:

Non-aqueous flow cells offer expanded electrochemical potential windows, which is desirable for energy storage. The performance of such electrochemical systems is however constrained by high cell resistance due to the low ionic conductivity of electrolytes and membranes in non-aqueous media. In this work, we apply membrane-less cell configurations with flow-through porous electrodes to address the ohmic losses and boost the performance of non-aqueous flow cells. Vanadium acetylacetonate redox chemistry is used as a model system and various performance aspects such as reaction kinetics, electrode wettability, cell resistance and crossover are investigated. The kinetics, measured in flow-through mode, is found competitive due to the enhanced mass transport and surface area utilization in the flow-through porous electrode. The electrode porosity is measured to be 79% and only 6.0% in acetonitrile and water, respectively, indicating superior wettability behaviour for non-aqueous electrolytes. A fully integrated co-laminar flow cell demonstrates negligible crossover and a combined ohmic cell resistance that meets techno-economic targets. Its discharge power density of 550 mW cm^{-2} is two orders of magnitude higher than for other non-aqueous flow cells, demonstrating that membrane-less cell designs with flow-through porous electrodes are favourable in order to overcome performance limitations in non-aqueous electrochemical systems.

Keywords:

co-laminar flow cell; non-aqueous; vanadium acetylacetonate; microfluidic; membrane-less; energy storage

1. Introduction

Redox flow batteries (RFBs) are a promising technology for grid-scale energy storage as they offer a scalable and decoupled solution for power and energy density, since the charge is stored in the flowing electrolytes [1,2]. Various metal based reactant electrolytes have been investigated since their conception such as the iron chromium and all-vanadium chemistries. Many novel reactant chemistries are additionally being developed and investigated by various research groups including organic based reactants, which enable new advantages such as low cost and eco-friendliness [3–9]. Historically, RFB reactant chemistries have relied on aqueous media [10]. However, conventional aqueous electrochemical flow cells have a limited cell potential window (< 1.5 V), constrained by decomposition of the supporting electrolyte which limits their energy density and charging voltages. Consequently, non-aqueous (NAq) RFB systems were recently introduced which, instead of water, rely on organic solvents that offer an expanded electrochemical potential stability window [11]. The key advantages of NAq redox electrolytes in this application include a higher cell voltage, a wider range of working temperatures and faster charging rates, thus potentially offering much higher energy density [12–14]. A variety of redox chemistries have been demonstrated for NAq cells to date, most commonly using transition metal organic complexes based on ruthenium [15,16], vanadium [17,18], manganese [19], chromium [12,20], copper [21] and cobalt [22–24]. Among the various acetylacetonate metal complexes, vanadium acetylacetonate (V_{acac}) has been widely used in various organic solvents or solvents mixtures [25–30]. Shinkle et al. studied the kinetics of the V_{acac} couples on carbon, gold and platinum electrodes [25]. Bamgbopa et al. employed various solvent mixtures for the V_{acac} system, optimizing species solubility, conductivity and reaction rates [26,27]. All-organic reactants have also been reported [9,31–33]. For example, Wei et al. introduced a NAq RFB using a TEMPO based catholyte with an energy density of 126

Wh L⁻¹ [33]. Recently, a NAq RFB proof of concept was proposed with an open circuit potential (OCP) of 4.5 V and species solubility up to 3 M, suggesting an unprecedented energy density [13].

The majority of works however have generally focused on developing NAq redox chemistries and electrochemical proof of concepts and only a few works focused on cell design and performance investigations in actual flow cells. The major drawback that hinders the performance of NAq RFBs compared to their aqueous counterparts is their relatively high ohmic resistance, due to much lower ionic conductivity of the electrolytes as well as the conventional membrane separators when used in NAq conditions [34,35]. Therefore, techno-economic studies for RFB systems and electrolytes [36,37] have set a target area specific resistance (ASR) below 5 Ω cm² for feasible NAq RFBs. Escalante-Garcia et al. assessed the cycling performance of a V_{acac} RFB with ion exchange membranes and porous separators [38]. Milshtein et al. reported cycling at relatively high current densities of 100 mA cm⁻² at 0.4 V and scalable cell performance both enabled by low cell ASR [32]. They also reported a modified vanadium flow cell architecture for compatibility with NAq electrolytes achieving ASR around 1.7 Ω cm² using ferrocene based couples [39]. Recently, Sun et al. compared the performance of an all-vanadium RFB with a simulated performance of a NAq flow cell assuming thin separator and electrolyte conductivity of 10 mS cm⁻¹ [40]. Their work concluded the impracticality of NAq flow cells under the present circumstances while other works have suggested that new membranes are required for realizing competitive NAq RFBs [35].

On the other hand, another type of cells, namely the co-laminar flow cell (CLFC), has emerged that eliminates the need of using a physical separator or membrane [41,42]. These

membrane-less cells utilize internal laminar flow to provide the necessary separation between the reactant streams whilst allowing the necessary ion transport. CLFCs generally offer significant advantages in simplicity, cost, durability and performance as well as the flexibility in choosing the reactant stream media individually [43,44]. These features are also advantageous for the use of CLFCs as analytical cell platforms for evaluation of new catalysts, electrodes and electrolytes for use in electrochemical flow cells, provided that the flow rates and mass transport conditions can be accurately controlled. The physical scale of CLFCs is however constrained by the requirement for laminar flow in the space between the electrodes. Braff et al. addressed crossover issues in hydrogen-bromine RFBs by using a membrane-less CLFC design [45]. Kjeang et al. integrated flow through porous electrodes within a CLFC architecture which led to ground-breaking cell performance for the all-vanadium electrolyte system, primarily attributed to improved mass transport within the electrodes [46]. This cell design was further developed by Goulet et al. who reported a record peak power density output of 2.0 W cm^{-2} by incorporating a dynamic deposition technique in addition to optimizing the cell for low ASR, suggesting that the use of liquid electrolyte separation should be revisited in lieu of physical separators [47]. The CLFC technology has been demonstrated for a variety of fuel cells, liquid flow batteries and hybrid flow cells. However, to the authors' knowledge, it has not yet been applied to NAq chemistries, despite its potential ohmic benefits.

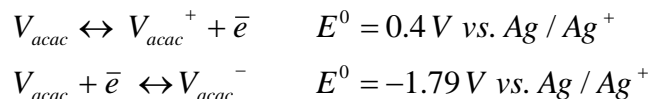
Therefore, the aim of this work is to leverage the benefits offered by membrane-less operation and flow-through porous electrodes for NAq redox flow cells. V_{acac} redox species and tetraethylammonium tetrafluoroborate supporting electrolyte in acetonitrile solvent are used as a model system for the investigation. Various performance aspects of flow cells such as kinetics, electrodes wettability, ASR and crossover are investigated in order to understand the electrode

performance and its interaction with the NAq electrolytes as well as the power density capabilities. Finally, the discharge performance of a fully integrated CLFC is measured and compared with other NAq flow cells to assess the opportunity offered by using flow-through porous electrodes to enhance kinetics, wetted surface area and mass transport combined with using a membrane-less cell design to reduce the ohmic cell resistance and thereby boost overall cell performance.

2. Experimental

2.1 Materials and reactions

Acetonitrile (AN) is used as the NAq solvent for the redox flow reactants. Tetraethylammonium tetrafluoroborate (TEABF₄) is used as the supporting electrolyte. Vanadium acetylacetonate (V_{acac}) is used as the redox active species. All chemicals are purchased from Sigma-Aldrich (Oakville, ON, Canada), unless otherwise stated. The selection is well established in literature [17,25–29] and the electrochemical reactions of the positive and negative half cells are given by [48]:



2.2 Measurement procedures

Kinetics

The kinetics of the electrochemical reactions is first assessed qualitatively by means of cyclic voltammetry (CV) techniques. A solution of V_{acac} species (0.01 M) and TEABF₄ (0.1 M)

supporting electrolyte is prepared in AN. The CVs are performed in a classical three electrode cell with glassy carbon (0.07 cm^2), platinum wire and saturated calomel (SCE) as working, counter and reference electrodes, respectively (CH instruments Inc, TX, USA). The preparation of solutions and CV experiments are performed inside a glove bag (Spilfyter®, NPS Corp, WI, USA) filled with dry nitrogen gas to minimize any instability issues encountered due to exposure to moisture or ambient air. The measurements are performed using a potentiostat (Gamry, Reference 3000), at a scan rate of 10 mV s^{-1} .

In addition, the kinetics in flow-through porous electrodes is in-situ assessed in an analytical flow cell, as shown in Fig. 1a, by extracting the exchange current from the measured Tafel plots. The measurement technique was recently developed by our group and previously applied for conventional all-vanadium aqueous reactants, as detailed elsewhere [49,50]. In short, the cell directly measures the kinetics of redox reactions on flow-through porous electrodes. The reactants are supplied to the cell by means of a syringe pump (Harvard apparatus) at stepwise increasing flow rates. A Tafel plot is recorded at each flow rate until negligible variation in the Tafel slopes is observed, which indicates that the mass transport and reaction kinetics are decoupled. The Tafel plots are recorded with the same potentiostat at a scan rate of 10 mV s^{-1} . The cell features a 3 mm wide microfluidic channel and is fabricated by soft-lithography techniques in polydimethylsiloxane (PDMS) from a SU-8 photoresist master (ca. $150 \mu\text{m}$ high). Carbon paper (Toray, TGP-060) electrodes are placed in the PDMS cell and compressed and sealed with a glass slide. The working electrode has an active volume of $0.75 \text{ mm} \times 3.0 \text{ mm} \times 0.15 \text{ mm}$ exposed to the flow, which is equivalent to an electrochemical surface area of 6.08 cm^2 . A larger carbon paper electrode (5.0 mm long) is used downstream as a counter electrode and a

platinum foil (0.025 mm thick, Sigma-Aldrich, Oakville, ON, Canada) is used upstream as a pseudo-reference electrode, as shown in Fig. 1a.

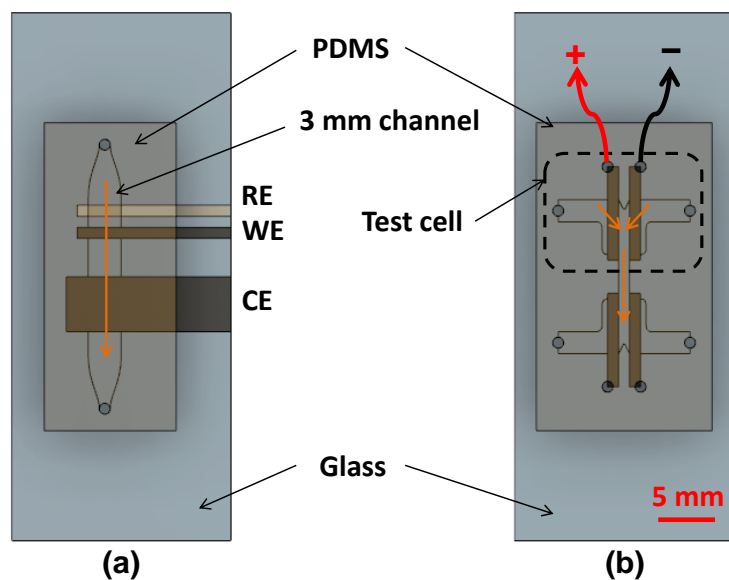


Fig. 1. Schematics of: a) the three electrode analytical flow cell for direct measurement of kinetics on flow-through porous electrodes (3 mm wide), having an upstream platinum pseudo-reference electrode (RE) and carbon paper working electrode (WE) and a downstream counter electrode (CE); and b) the integrated two electrode membrane-less CLFC in which the V_{acac}^+ and V_{acac}^- are pumped from their respective half-cell inlet port into the flow-through porous electrodes and the microfluidic channel (1 mm wide) wherein they are separated by a co-laminar interface.

Wetting

The wetting of the carbon paper electrode materials is assessed in both cases of aqueous and non-aqueous solvents. Representative electrode strips (Toray, TGP-060) are first immersed into the solvents and the wetting behaviour is visually inspected. The wetting effect is then quantified by the change in the measured porosity of the carbon paper using different working solvents. The technique is well established and used in the method of standard porosimetry

(MSP). Stacks of six layers of carbon paper are cut and dried in a furnace at 150⁰C under vacuum. The pore volume is estimated from the difference of dry and wet sample masses and the density of the working liquid ($n = 3$). Here, octane is initially used as a standard working liquid for the technique as it can wet all pores and thus gives the actual porosity of the carbon paper that matches the material datasheet or porosity measurements by other techniques [51]. Next, other stacks of carbon paper are tested in both water and AN and the dry and wet masses are similarly measured to reflect the amount of pore volume exposed to the working solvent (hydrophilic or lyophilic porosity). Further details about the MSP technique can be found elsewhere [51,52].

Area specific resistance

The ASR is quantified by measuring the combined ohmic cell resistance ($n = 3$) of a microfluidic cell filled with the supporting electrolyte (TEABF₄) solution at concentrations ranging from 0.25 to 1.5 M in AN. The same technique and cell were used previously by our group in other works to study cell ASR for aqueous all-vanadium reactants [47]. Here, the cell resistance reflects mainly the change in the ionic resistance of the electrolyte with concentration at a fixed electrodes spacing. In summary, the cell is similarly fabricated by soft lithography techniques in PDMS and has 150 μm deep microfluidic features where the carbon paper electrodes are placed. The electrodes (Toray, TGP-060) are 1 mm wide and are separated by a 1 mm microchannel. The active electrode length is 10 mm, which translates to an active area of 0.015 cm^2 , which is multiplied by the measured resistance. To minimize contact resistance, toothless alligator clips are used for the electrodes electrical connection with the same potentiostat and the resistance of the cell is measured by means of electrochemical impedance

spectroscopy (EIS) by reading the high frequency real axis intercept value of the Nyquist plot, with an AC amplitude of 10 mV rms at cell OCP.

Cell polarization

The microfluidic cell, shown in Fig. 1b, is utilized as a co-laminar flow cell with flow-through porous electrodes for the polarization measurements. The cell is similarly fabricated by soft lithography techniques in PDMS with 150 μm deep microfluidic features. The two electrodes, which are 1 mm wide and have 5 mm active length, are compressed and sealed against a glass slide. The electrodes thus have an active area (normal to the flow direction) of 0.0075 cm^2 , which is used to normalize the measured current and power output. The microchannel separating the two electrodes is also 1 mm wide. Further details about the design and fabrication of this cell are available in prior reports [53–55]. Electrical wires are bonded permanently with the electrodes using silver conductive epoxy (MG Chemicals). The reactants are supplied to the cell by the same syringe pump (in dual mode operation). Before polarization, the cell OCP is initially measured at various flow rates from 1 to 300 $\mu\text{L min}^{-1}$ to investigate the flow rate effect and the mixed potential losses due to diffusive crossover between the two electrodes in the CLFC, as demonstrated in other works [56]. Finally, the cell polarization performance is measured at two high flow rates of 100 and 300 $\mu\text{L min}^{-1}$, where diffusive crossover is typically absent, by sweeping the voltage from OCP to 0.1 V at a scan rate of 10 mV s^{-1} .

3. Results and Discussion

In order to investigate the prospective use of NAq redox chemistries in membrane-less cell architectures with flow-through porous electrodes, various aspects that influence flow cell performance are first assessed. These performance-related aspects include reaction kinetics, electrode wettability, cell resistance and crossover. Next, the discharge performance in an integrated, membrane-less CLFC structure is analyzed. TEABF₄ and AN are chosen as the supporting electrolyte and solvent for the V_{acac} model system, respectively, for both half-cells. The selection is based on other literature works showing good solubility and ionic conductivity for the scope of this work [13,29]. The performance results are compared against conventional RFB systems in NAq media in order to assess the advantages and limitations of using CLFCs with flow-through porous electrodes for NAq flow cells. The results are also compared to the case of an aqueous all-vanadium CLFC using commercial electrolyte mix.

3.1 Kinetics

Cyclic voltammetry (CV) measurements are first used to qualitatively assess the kinetics of the V_{acac} model system on regular glassy carbon electrodes. TEABF₄ is used as supporting electrolyte and AN is used as solvent. The IR-compensated voltammogram for the two V_{acac} half-cells of interest is shown in Fig. 2. Two reversible peaks corresponding to the negative and positive half-cells are identified at -1.43 V and 0.73 V vs. SCE, respectively, which indicates a theoretical cell voltage window of ca. 2.2 V for this redox system, in accordance with other works [17,28]. The figure shows that the redox reactions of the V_{acac} couples are generally facile and that the activation over-potential is expected to be low in AN solvent. The positive half-cell shows a peak current density ratio (i_{pc}/i_{pa}) of 0.96 while for the negative half-cell, the ratio equals 1.14, which indicates quasi-reversible or irreversible kinetics and that the electrochemical conversion of charging V_{acac} into V_{acac}⁺ and V_{acac}⁻ is likely faster than the electrochemical

discharge reactions of either V_{acac}^+ or V_{acac}^- into V_{acac} , which is in general agreement with Bamgbopa et al. [26]. The two half-cells are also shown to exhibit a similar peak separation of 150 mV.

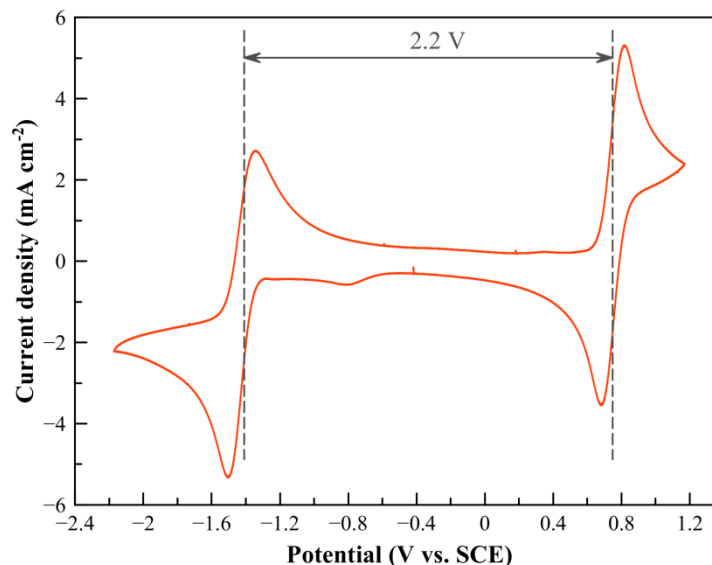


Fig. 2. Cyclic voltammogram at a scan rate of 10 mV s^{-1} for the V_{acac} redox system (0.01 M) in TEABF_4 supporting electrolyte (0.1 M) and AN solvent, showing the theoretical reversible cell voltage window.

To further assess the electrochemical kinetics while operating in flow-through porous electrode configuration, the analytical flow cell technique is utilized [49]. Tafel plots are recorded for the $V_{\text{acac}}/V_{\text{acac}}^+$ couple at different flow rates as shown in Fig. 3. For the oxidation branch, the flow rate of $300 \mu\text{L min}^{-1}$ displays a significant variation in the Tafel curve slope over the initial $100 \mu\text{L min}^{-1}$ flow rate, indicating the presence of a mass transport effect. However, at the higher flow rate of $500 \mu\text{L min}^{-1}$, the Tafel plot shows insignificant variation when compared to the $300 \mu\text{L min}^{-1}$ case. This indicates that the kinetics and mass transport are decoupled at such flow rate, which allows extraction of kinetic data in flow-through mode. The

Tafel intercept at the flow rate of $500 \mu\text{L min}^{-1}$ gives an exchange current in the few milliampere range ($\approx 7 \text{ mA}$), which when normalized by the active electrochemical surface area of the working electrode shows an exchange current density generally on the order of 1.1 mA cm^{-2} . It is also observed that the oxidation and reduction branches are not fully symmetric in the Tafel plot, which indicates different charge transfer characteristics in each polarization direction and confirms the relatively faster kinetics of the electro-oxidation reaction (charging V_{acac} into V_{acac}^+) than the electrochemical reduction reaction (discharging V_{acac}^+ into V_{acac}), as previously discussed in the CV measurement in Fig. 2 ($i_{\text{pc}} < i_{\text{pa}}$) and other works [26].

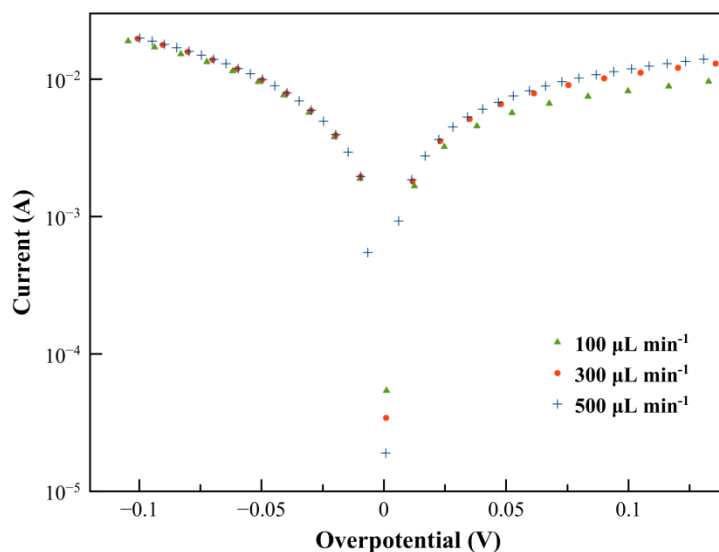


Fig. 3. Tafel plots measured with the analytical flow cell with flow-through porous electrodes for the $\text{V}_{\text{acac}}^+/\text{V}_{\text{acac}}$ redox couple at different flow rates.

While the exchange current density measured for the positive NAq half cell ($\text{V}_{\text{acac}}/\text{V}_{\text{acac}}^+$) is lower than that of the aqueous all-vanadium positive half cell ($\text{VO}^{2+}/\text{VO}_2^+ - 3.0 \text{ mA cm}^{-2}$) reported in previous work using the same technique [49], it still demonstrates rapid kinetics in flow-through porous carbon electrodes and is more than an order of magnitude higher than the value measured for the $\text{V}^{2+}/\text{V}^{3+}$ couple used in the negative half-cell in aqueous media. It is also

worth noting that the aqueous all-vanadium measurements used a commercial electrolyte with a reactant concentration of 1.7 M, which is higher than the concentration used for the V_{acac} electrolyte. For the negative half-cell of V_{acac}^-/V_{acac} , it is experimentally challenging to measure the exchange current density using the same technique and to prepare a 50:50 mix of V_{acac}^-/V_{acac} due to significant instability and degradation of the charged species (V_{acac}^-), as observed by immediate color change and half-cell OCP rise, which is attributed to partial exposure to moisture and ambient air, as reported by Shinkle et al. [57]. Nevertheless, it was shown in other works that the negative half-cell of the V_{acac} reactant chemistry generally exhibits higher reaction kinetics than the positive half-cell [26], and is thus not the limiting reaction. Overall, the measured results show that V_{acac} redox couples undergo electrochemical reactions on porous carbon electrodes in NAq media with facile kinetics equivalent to the conventional all-vanadium chemistry in aqueous media; hence, the activation over-potential should not pose a major performance limitation for the present NAq model system.

3.2 Wetting

Next, the solvent wetting of the electrode is assessed for the NAq case of the V_{acac} redox chemistry used in this work and compared with the aqueous all-vanadium case. The wetting of the electrode materials have been shown to be important in flow cell applications, especially when relying on flow-through porous electrodes [58]. Here, only the solvents used in both NAq and aqueous cases are compared; namely AN and water. The wetting effect of both solvents on the carbon paper electrode material is quantified by estimating the pore volume of carbon paper samples when filled with the working solvent. Fig. 4 shows the different porosity (Vol./Vol. %) values measured for the Toray carbon paper samples in the different working solvents. Octane is used as the benchmark standard solvent for the MSP equipment as it facilitates complete wetting

of the carbon surface [51,52]. Therefore, the porosity measured in octane ($80.1 \pm 1.1 \%$) is in agreement with the standard value reported in the manufacturer data sheet for this material (78%). Similarly, the sample measured in AN gives a comparable porosity of $78.8 \pm 0.6 \%$, reflecting high pore lyophilicity for this solvent. Conversely, when the sample is measured in water, the hydrophilic porosity is merely 6%. This means that even if the pore volume of the electrode is ca. 80% as measured in octane, only 6% of the sample volume is wetted in water, while the rest of the pore volume is hydrophobic. This hydrophobicity of the pores thus usually requires pre-treatment methods for use in aqueous flow cells, such as thermal baking or annealing, chemical etching, or electrochemical treatment steps to enhance the electrode wetting [58,59].

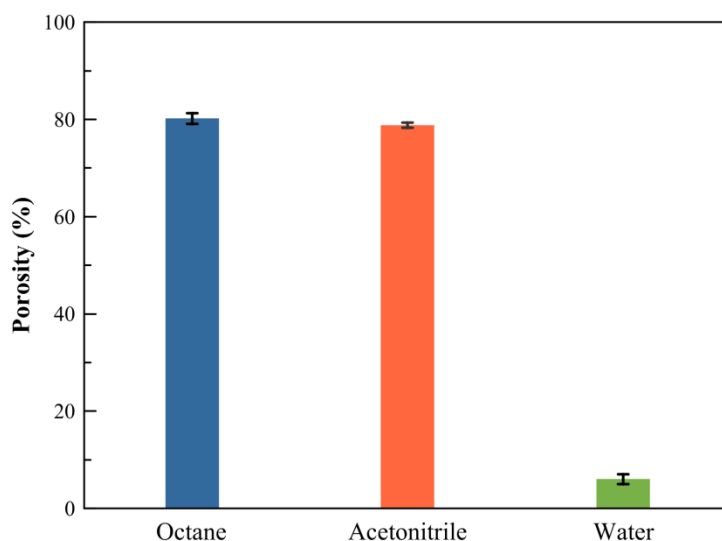


Fig. 4. Porosity of the Toray carbon paper electrode measured in different working solvents of octane, acetonitrile and water.

To further show the difference in the wettability behaviour visually, the video attached to Fig. 5 is captured when two strips of the Toray carbon paper are dipped in AN and water, respectively. The video clearly shows the difference in the wetting behaviour for the same sample material in the two different solvents. The video also shows the presence of self-flow

against gravity by means of capillarity in the AN case, demonstrating full electrode wetting. In the case of water, the hydrophobicity of the carbon paper pores can be also noted. This behaviour might be explained by the difference in the surface tension coefficients of AN and water. Since AN has a smaller surface tension coefficient, it can easily flow-through the pores of the carbon paper, without requiring any pre-treatment steps. In general, the electrode wettability for the NAq electrolytes thus shows superior behaviour when compared to the aqueous conventional all-vanadium electrolytes and can thus readily utilize all the actual pore space as well as the associated internal surface area of the electrode.

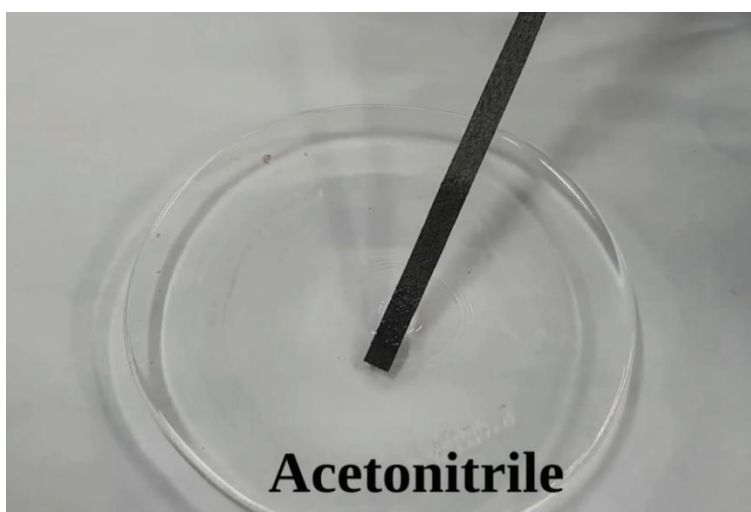


Fig. 5. Video of the wetting behaviour of a Toray carbon paper strip in acetonitrile and water. Self-flow by capillary action is observed in the case of acetonitrile solvent which reflects high wettability.

3.3 Cell area specific resistance

The cell resistance is measured using a technique similar to that of Goulet et al. [47] by filling the microfluidic cell solely with the supporting electrolyte at various concentrations. The cell electrodes are 10 mm long and have a fixed separation of 1 mm, which is filled with the electrolyte. The area specific resistance (ASR) is then estimated from the combined ohmic resistance, obtained from EIS, at the various concentrations of the TEABF₄ supporting

electrolyte in AN. The measured ASR values are displayed in Fig. 6. The measurements show that even at low concentrations of TEABF₄, the cell ASR values in a membrane-less cell design are below 5 Ω cm², which satisfies the recommendation given by techno-economic models [37]. This shows the potential of membrane-less cell configurations to enable the NAq technology when compared to conventional cells with membranes that further raise the total cell ASR and hinder the performance. The figure also shows the cell ASR for species concentration of 0.4 M of V_{acac} dissolved in 0.5 M TEABF₄. In this case, the cell ASR increases slightly from 2.7 Ω cm² without V_{acac} to 3.1 Ω cm² in the presence of V_{acac} in the supporting electrolyte, which is in agreement with the findings of Shinkle et al. who reported weaker dual-solute effects on the magnitude of the electrolyte conductivity [29] since the conductivity is dominated by the supporting electrolyte (TEABF₄).

The ionic conductivity of the electrolyte is also estimated by back calculation from the measured cell ASR and the electrode separation of 1 mm in the membrane-less cell. The obtained ionic conductivity is displayed in Fig. 6 as a function of the TEABF₄ concentration. For example, at 1 M TEABF₄, the ionic conductivity is estimated to equal 53 mS cm⁻¹, which is in agreement with literature values for the 1 M TEABF₄ ionic liquid in AN solvent [38,60], and is an order of magnitude less than that of 4 M H₂SO₄ typically used in aqueous all-vanadium RFBs [47].

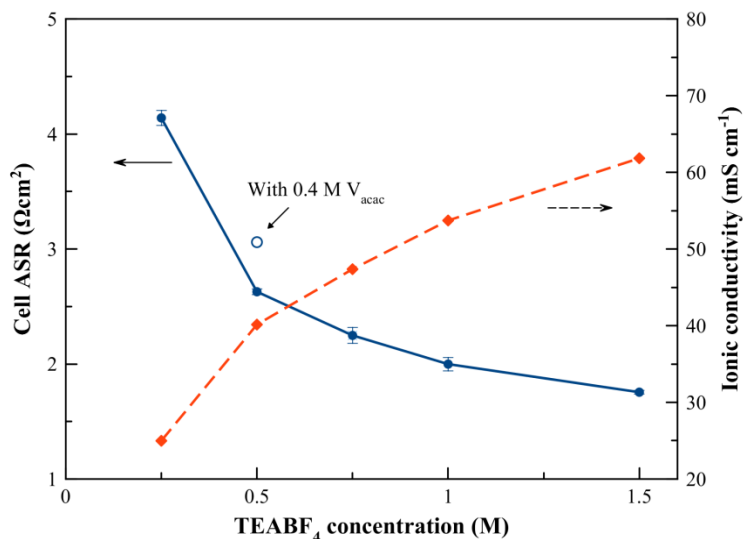


Fig. 6. Area specific resistance (ASR) of the membrane-less cell and estimated corresponding ionic conductivity of the AN electrolyte at different TEABF₄ concentrations.

3.4 Flow cell discharge performance

The V_{acac} electrolyte is prepared and charged in a custom charging cell [53,54] into V_{acac}^+ and V_{acac}^- for discharge performance testing in an integrated, co-laminar flow cell with flow-through porous electrodes, wherein the two charged species are pumped into the two inlets of the cell. The cell is initially tested with 0.4 M active V_{acac} species in 0.5 M supporting electrolyte (TEABF₄) in order to provide moderate species concentration and electrolyte conductivity, in accordance with previous findings (Fig. 6) and literature [29]. At various flow rates, the reactant species crossover is investigated by studying the cell OCP. Generally, at low flow rates, the species have long residence time inside the channel which promotes diffusive mixing and results in cell voltage loss due to mixed potential. The effect of varying the operating flow rate on the cell OCP is shown in Fig. 7. The results show that at flow rates $> 30 \mu\text{L min}^{-1}$, crossover losses are minimized which is seen by the constant OCP of $\approx 2.41 \text{ V}$ reached and insignificant drift ($< 2 \text{ mV}$) with further increase in the flow rate. It is worth noting that, at a different species

concentration, the concentration gradient across the electrodes will be altered, resulting in a different rate of crossover.

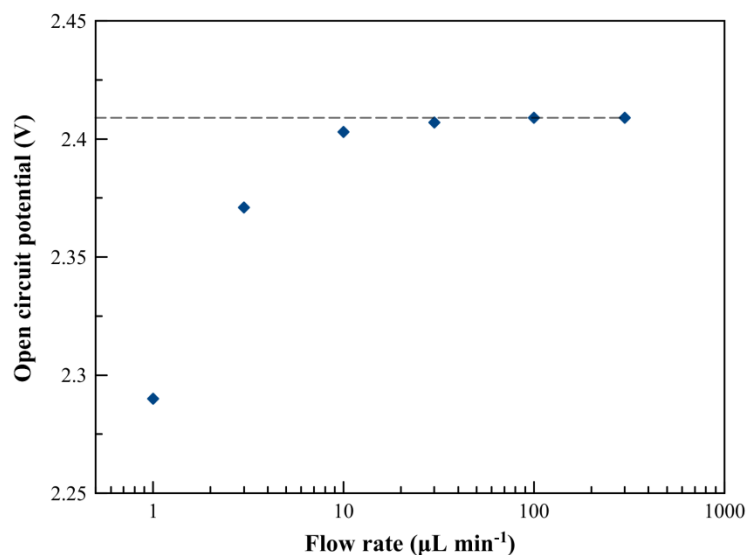


Fig. 7. Open circuit potential (OCP) of the CLFC operated with 0.4 M V_{acac} and 0.5 M TEABF_4 in AN solvent at various flow rates.

The measured cell polarization curves are shown in Fig. 8a at high flow rates of 100 and 300 $\mu\text{L min}^{-1}$, where mass transport is enhanced and crossover losses are absent. The figure shows that the discharge performance only differs marginally between the two flow rates, with a slight rise in performance at the higher flow rate due to increased mass transport, thus indicating ohmic control. In this case, the cell outputs a peak power density of 235 mW cm^{-2} and a maximum current density of 275 mA cm^{-2} at both flow rates. The ohmic cell resistance is measured by means of EIS and translates to an ASR of 3.8 $\Omega \text{ cm}^2$. The maximum attainable ohmic loss slope is also given in the same figure which is a linear polarization curve approximation based on the measured cell ASR and OCP ($\approx 2.4 \text{ V}$) at high flow rates (100 – 300 $\mu\text{L min}^{-1}$). The slope indicates moderate impact of reaction kinetics on the performance but also indicates a major ohmic over-potential in excess of 1 V at the maximum current density. The

relatively high ASR of this cell compared to the one shown previously in Fig. 6 is attributed to the presence of the active redox species in the electrolyte solution as well as the added contact resistance from connecting the electrical leads to the electrodes via silver conductive epoxy. However, as mentioned before, this value satisfies the targets given by the techno-economic analyses [37].

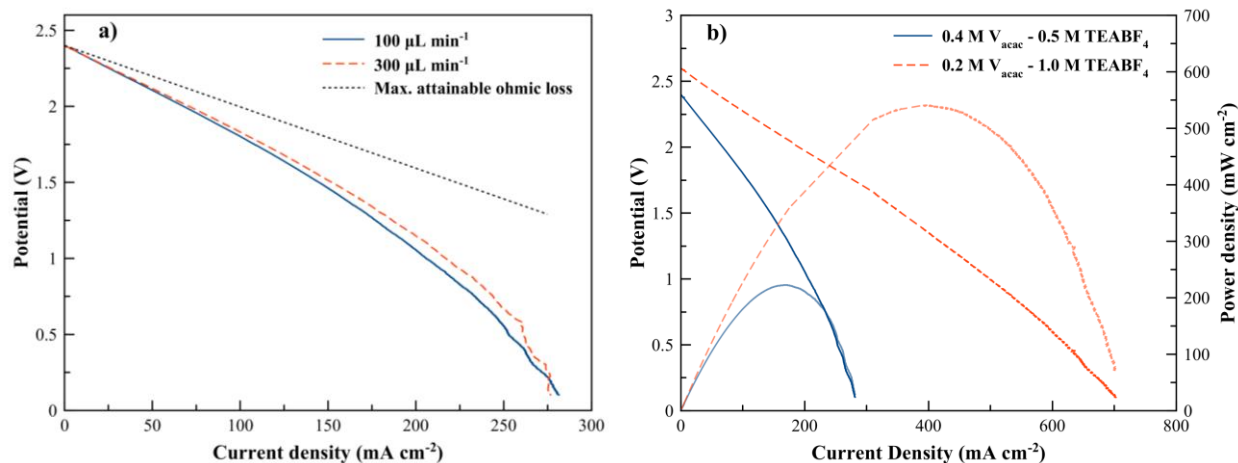


Fig 8. a) CLFC polarization curves at flow rates of 100 and 300 $\mu\text{L min}^{-1}$. The maximum attainable ohmic loss slope ($OCP - i \times ASR$) is also shown. b) CLFC polarization and power density curves at different concentrations of V_{acac} redox species and $TEABF_4$ supporting electrolyte, at a flow rate of 100 $\mu\text{L min}^{-1}$.

The flow cell is then operated at a higher supporting electrolyte concentration of 1 M in order to increase the ionic conductivity. Due to the dual-solute effects on the solubility of both V_{acac} and $TEABF_4$ in AN, previously shown by Shinkle et al. [29], the concentration of the V_{acac} active redox species is reduced to 0.2 M, which is the observed saturation limit of the V_{acac} species in AN solvent in the presence of $TEABF_4$ at the new concentration of 1 M [29]. The cell resistance is again measured and the ASR for this case drops to $2.1 \Omega \text{ cm}^2$. This represents a reduction of $\approx 45\%$ in the cell ASR from the initial concentration case of 0.4 M V_{acac} in 0.5 M $TEABF_4$, which is expected due to the increase in the ionic conductivity of the $TEABF_4$ at higher concentration, as estimated in Fig. 6. The polarization and power density curves are shown in

Fig. 8b for the two concentration cases operated at a flow rate of $100 \mu\text{L min}^{-1}$. The cell operated with $0.2 \text{ M V}_{\text{acac}}$ in 1 M TEABF_4 shows an initial OCP of $\approx 2.6 \text{ V}$, which is $\approx 190 \text{ mV}$ higher than the initial concentration case of $0.4 \text{ M V}_{\text{acac}}$ in 0.5 M TEABF_4 . The cell also gives a peak power density output of 550 mW cm^{-2} , which is roughly twice the power density output measured before at the initial concentration case. Only a few studies have reported cell performance power densities for NAq redox systems to date in H-cells or flow cells, which were however in the range of only a few milliwatts per square centimeter. For example, Herr et al. reported maximum power densities in the range of 0.08 mW cm^{-2} [28] and 0.25 mW cm^{-2} [30] for the V_{acac} system in a conventional RFB cell with graphite felt flow-through electrodes and anion exchange membrane with ASR of $\approx 2400 \Omega \text{ cm}^2$. Bamgbopa reported a peak power density output of 2.6 mW cm^{-2} for a NAq iron-chromium acetylacetonate flow cell with carbon paper electrodes and treated Nafion membrane showing an ASR of $15 \Omega \text{ cm}^2$ [12]. Chakrabati et al. recorded $1.4\text{-}7.2 \text{ mW cm}^{-2}$ for a NAq ruthenium-based undivided RFB with graphite felt porous electrodes and polypropylene mesh separator [15] while Ding et al. reported 5.7 mW cm^{-2} power density output from their lithium-quinone hybrid flow cell [61]. Hence, the range of power density output reported in the present work is comparably two orders of magnitude higher and is shown for the first time for NAq flow cells. In order to further compare with the case of the conventional vanadium redox system in aqueous media, using the same membrane-less CLFC design as in the present work with a commercial electrolyte of 1.7 M vanadium redox species in 4 M sulfuric acid [53,54], resulted in a peak power density of 700 mW cm^{-2} which is on the same order as the present NAq case. The discharge performance demonstrated in the present work thus shows the potential of NAq electrolytes and the levels of power density that can be achieved when the ohmic limitation is tackled combined with flow-through porous

electrodes configuration. In addition, the membrane-less cell also yields higher voltage efficiencies because of the lower cell ASR. For example, Escalante-Garcia et al. reported voltage efficiencies of 87.9% and 91.9% at 10 mA cm^{-2} for a V_{acac} flow cell using Nafion membrane and Daramic microporous separator, respectively [38]. At the same current density, the membrane-less cell presented in this work displays considerably higher voltage efficiency of 98.7% and 97.6% for the two concentration cases shown in Fig. 8b.

In general, we only showed the performance enhancements by altering the concentrations. However, various other modifications may help optimize the performance level further. For example, using narrower electrode separation and current collectors would be beneficial [47]. Similarly, NAq electrolytes with higher ionic conductivity and solubility [30,48] would benefit the performance of ohmic controlled cells. Another strategy is to investigate alternative redox couples with higher reversible cell potentials such as the 4.5 V chemistry concept introduced by Gong et al. [13] which would potentially boost the power densities to levels that may likely exceed the aqueous flow cells, since the power density scales with the square of the voltage in ohmic limited cells. The CLFC technology demonstrated in the present work provides an ideal platform for evaluation of such new developments toward performance flow cells for electrochemical energy conversion in NAq media.

4. Conclusions

This work proposed the opportunity offered by membrane-less operation and flow-through porous electrodes for electrochemical flow cells with non-aqueous redox electrolytes by exploring the various performance aspects that are critical for design and operation, using the

vanadium acetylacetonate chemistry, tetraethylammonium tetrafluoroborate supporting electrolyte and acetonitrile solvent as a representative model system. The work investigated reaction kinetics, electrode wettability, cell resistance and crossover. The reaction kinetics on flow-through porous carbon electrodes were measured using an analytical flow cell and were found to be similar or faster when compared to aqueous flow cells with all-vanadium redox electrolytes. The electrode wetting behaviour in acetonitrile solvent was found to be superior to aqueous media. This was demonstrated by quantifying the electrode porosity filled with the solvent which showed 79% for acetonitrile and merely 6.0% in water indicating hydrophobic behaviour in the majority of the pore volume. The area specific resistance was measured in a microfluidic cell to be an order of magnitude higher than for the corresponding aqueous cell but was consistently below $5 \Omega \text{ cm}^2$, which meets the targets set by techno-economic models for energy storage applications. Redox species crossover was assessed in a co-laminar flow cell with flow-through porous electrodes and found to be absent at high flow rates due to the minimized diffusive mixing and low species residence time in the co-laminar channel. Finally, the discharge polarization was measured in the same cell, indicating ohmic controlled cell performance, as expected. The highest cell performance was achieved by increasing the supporting electrolyte concentration and reducing the active redox species concentration, arriving at an open circuit potential of 2.6 V and a peak power density output of 550 mW cm^{-2} . This power density level is generally two orders of magnitude higher than for other NAq flow cells reported to date and on the same order as an all-vanadium aqueous co-laminar flow cell with the same design. In short, this demonstrates the utility of flow-through porous electrodes to enhance kinetics, wetted surface area and mass transport combined with using membrane-less cell designs to overcome

ohmic limitations from conventional membranes, when used in non-aqueous electrolytes, and thereby boost overall cell performance.

Acknowledgements

The funding for this research provided by Natural Sciences and Engineering Research Council of Canada (NSERC), Canada Foundation for Innovation (CFI) and British Columbia Knowledge Development Fund (BCKDF) is appreciated. This research was undertaken, in part, thanks to funding from the Canada Research Chairs program.

References

- [1] A.Z. Weber, M.M. Mench, J.P. Meyers, P.N. Ross, J.T. Gostick, Q. Liu, Redox flow batteries: A review, *J. Appl. Electrochem.* 41 (2011) 1137–1164. doi:10.1007/s10800-011-0348-2.
- [2] G.L. Soloveichik, Flow Batteries: Current Status and Trends, *Chem. Rev.* 115 (2015) 11533–11558. doi:10.1021/cr500720t.
- [3] B. Huskinson, M.P. Marshak, C. Suh, S. Er, M.R. Gerhardt, C.J. Galvin, X. Chen, A. Aspuru-Guzik, R.G. Gordon, M.J. Aziz, A metal-free organic-inorganic aqueous flow battery., *Nature.* 505 (2014) 195–8. doi:10.1038/nature12909.
- [4] K. Lin, Q. Chen, M.R. Gerhardt, L. Tong, S.B. Kim, L. Eisenach, A.W. Valle, D. Hardee, R.G. Gordon, M.J. Aziz, M.P. Marshak, Alkaline quinone flow battery, *Science.* 349 (2015) 1529–1532. doi:10.1126/science.aab3033.
- [5] E.S. Beh, D. De Porcellinis, R. Gracia, K. Xia, R.G. Gordon, M. Aziz, A Neutral pH Aqueous Organic/Organometallic Redox Flow Battery with Extremely High Capacity Retention, *ACS Energy Lett.* (2017) acsenergylett.7b00019. doi:10.1021/acenergylett.7b00019.
- [6] B. Yang, L. Hooper-Burkhardt, F. Wang, G.K. Surya Prakash, S.R. Narayanan, An Inexpensive Aqueous Flow Battery for Large-Scale Electrical Energy Storage Based on Water-Soluble Organic Redox Couples, *J. Electrochem. Soc.* 161 (2014) A1371–A1380. doi:10.1149/2.1001409jes.

- [7] T. Janoschka, N. Martin, M.D. Hager, U.S. Schubert, An Aqueous Redox-Flow Battery with High Capacity and Power: The TEMPTMA/MV System, *Angew. Chemie - Int. Ed.* 55 (2016) 14427–14430. doi:10.1002/anie.201606472.
- [8] T. Janoschka, N. Martin, U. Martin, C. Friebe, S. Morgenstern, H. Hiller, M.D. Hager, U.S. Schubert, An aqueous, polymer-based redox-flow battery using non-corrosive, safe, and low-cost materials, *Nature*. 527 (2015) 78–81. doi:10.1038/nature15746.
- [9] P. Leung, A.A. Shah, L. Sanz, C. Flox, J.R. Morante, Q. Xu, M.R. Mohamed, C. Ponce de León, F.C. Walsh, Recent developments in organic redox flow batteries: A critical review, *J. Power Sources*. 360 (2017) 243–283. doi:10.1016/j.jpowsour.2017.05.057.
- [10] W. Wang, Q. Luo, B. Li, X. Wei, L. Li, Z. Yang, Recent progress in redox flow battery research and development, *Adv. Funct. Mater.* 23 (2013) 970–986. doi:10.1002/adfm.201200694.
- [11] S.-H. Shin, S.-H. Yun, S.-H. Moon, A review of current developments in non-aqueous redox flow batteries: characterization of their membranes for design perspective, *RSC Adv.* 3 (2013) 9095. doi:10.1039/c3ra00115f.
- [12] M.O. Bamgbopa, Y. Shao-Horn, S. Almheiri, The potential of non-aqueous redox flow batteries as fast-charging capable energy storage solutions: demonstration with an iron–chromium acetylacetonate chemistry, *J. Mater. Chem. A*. 5 (2017) 13457–13468. doi:10.1039/C7TA02022H.
- [13] K. Gong, Q. Fang, S. Gu, S.F.Y. Li, Y. Yan, Nonaqueous redox-flow batteries: organic solvents, supporting electrolytes, and redox pairs, *Energy Environ. Sci.* (2015) 38–49. doi:10.1039/C5EE02341F.
- [14] Y. Huang, S. Gu, Y. Yan, S.F.Y. Li, Nonaqueous redox-flow batteries: Features, challenges, and prospects, *Curr. Opin. Chem. Eng.* 8 (2015) 105–113. doi:10.1016/j.coche.2015.04.001.
- [15] M.H. Chakrabarti, E.P.L. Roberts, C. Bae, M. Saleem, Ruthenium based redox flow battery for solar energy storage, *Energy Convers. Manag.* 52 (2011) 2501–2508. doi:10.1016/j.enconman.2011.01.012.
- [16] Y. Matsuda, K. Tanaka, M. Okada, Y. Takasu, M. Morita, T. Matsumura-Inoue, A rechargeable redox battery utilizing ruthenium complexes with non-aqueous organic electrolyte, *J. Appl. Electrochem.* 18 (1988) 909–914. doi:10.1007/BF01016050.
- [17] Q. Liu, A.E.S. Sleightholme, A.A. Shinkle, Y. Li, L.T. Thompson, Non-aqueous vanadium acetylacetonate electrolyte for redox flow batteries, *Electrochem. Commun.* 11 (2009) 2312–2315. doi:10.1016/j.elecom.2009.10.006.
- [18] J.A. Suttill, J.F. Kucharyson, I.L. Escalante-Garcia, P.J. Cabrera, B.R. James, R.F. Savinell, M.S. Sanford, L.T. Thompson, Metal acetylacetonate complexes for high energy density non-aqueous redox flow batteries, *J. Mater. Chem. A*. 3 (2015) 7929–7938. doi:10.1039/C4TA06622G.

- [19] A.E.S. Sleightholme, A.A. Shinkle, Q. Liu, Y. Li, C.W. Monroe, L.T. Thompson, Non-aqueous manganese acetylacetonate electrolyte for redox flow batteries, *J. Power Sources*. 196 (2011) 5742–5745. doi:10.1016/j.jpowsour.2011.02.020.
- [20] Q. Liu, A.A. Shinkle, Y. Li, C.W. Monroe, L.T. Thompson, A.E.S. Sleightholme, Non-aqueous chromium acetylacetonate electrolyte for redox flow batteries, *Electrochem. Commun.* 12 (2010) 1634–1637. doi:10.1016/j.elecom.2010.09.013.
- [21] Y. Li, J. Sniekers, J. Malaquias, X. Li, S. Schaltin, L. Stappers, K. Binnemans, J. Fransaer, I.F.J. Vankelecom, A non-aqueous all-copper redox flow battery with highly soluble active species, *Electrochim. Acta*. 236 (2017) 116–121. doi:10.1016/j.electacta.2017.03.039.
- [22] X. Xing, Y. Zhao, Y. Li, A non-aqueous redox flow battery based on tris(1,10-phenanthroline) complexes of iron(II) and cobalt(II), *J. Power Sources*. 293 (2015) 778–783. doi:10.1016/j.jpowsour.2015.06.016.
- [23] B. Hwang, M.S. Park, K. Kim, Ferrocene and cobaltocene derivatives for non-aqueous redox flow batteries, *ChemSusChem*. 8 (2015) 310–314. doi:10.1002/cssc.201403021.
- [24] Y. Ding, Y. Zhao, Y. Li, J.B. Goodenough, G. Yu, A high-performance all-metallocene-based, non-aqueous redox flow battery, *Energy Environ. Sci.* 10 (2017) 491–497. doi:10.1039/C6EE02057G.
- [25] A.A. Shinkle, A.E.S. Sleightholme, L.T. Thompson, C.W. Monroe, Electrode kinetics in non-aqueous vanadium acetylacetonate redox flow batteries, *J. Appl. Electrochem.* 41 (2011) 1191–1199. doi:10.1007/s10800-011-0314-z.
- [26] M.O. Bamgbopa, N. Pour, Y. Shao-Horn, S. Almheiri, Systematic selection of solvent mixtures for non-aqueous redox flow batteries – vanadium acetylacetonate as a model system, *Electrochim. Acta*. 223 (2017) 115–123. doi:10.1016/j.electacta.2016.12.014.
- [27] M.O. Bamgbopa, S. Almheiri, Influence of solvents on species crossover and capacity decay in non-aqueous vanadium redox flow batteries: Characterization of acetonitrile and 1, 3 dioxolane solvent mixture, *J. Power Sources*. 342 (2017) 371–381. doi:10.1016/j.jpowsour.2016.12.050.
- [28] T. Herr, J. Noack, P. Fischer, J. Tübke, 1,3-Dioxolane, tetrahydrofuran, acetylacetone and dimethyl sulfoxide as solvents for non-aqueous vanadium acetylacetonate redox-flow-batteries, *Electrochim. Acta*. 113 (2013) 127–133. doi:10.1016/j.electacta.2013.09.055.
- [29] A.A. Shinkle, T.J. Pomaville, A.E.S. Sleightholme, L.T. Thompson, C.W. Monroe, Solvents and supporting electrolytes for vanadium acetylacetonate flow batteries, *J. Power Sources*. 248 (2014) 1299–1305. doi:10.1016/j.jpowsour.2013.10.034.
- [30] T. Herr, P. Fischer, J. Tübke, K. Pinkwart, P. Elsner, Increasing the energy density of the non-aqueous vanadium redox flow battery with the acetonitrile-1,3-dioxolane-dimethyl sulfoxide solvent mixture, *J. Power Sources*. 265 (2014) 317–324. doi:10.1016/j.jpowsour.2014.04.141.

- [31] J.A. Kowalski, L. Su, J.D. Milshtein, F.R. Brushett, Recent advances in molecular engineering of redox active organic molecules for nonaqueous flow batteries, *Curr. Opin. Chem. Eng.* 13 (2016) 45–52. doi:10.1016/j.coche.2016.08.002.
- [32] J.D. Milshtein, A.P. Kaur, M.D. Casselman, J.A. Kowalski, S. Modekrutti, P.L. Zhang, N. Harsha Attanayake, C.F. Elliott, S.R. Parkin, C. Risko, F.R. Brushett, S.A. Odom, High current density, long duration cycling of soluble organic active species for non-aqueous redox flow batteries, *Energy Environ. Sci.* 9 (2016) 3531–3543. doi:10.1039/C6EE02027E.
- [33] X. Wei, W. Xu, M. Vijayakumar, L. Cosimbescu, T. Liu, V. Sprenkle, W. Wang, TEMPO-based catholyte for high-energy density nonaqueous redox flow batteries, *Adv. Mater.* 26 (2014) 7649–7653. doi:10.1002/adma.201403746.
- [34] M. Doyle, M.E. Lewittes, M.G. Roelofs, S.A. Perusich, R.E. Lowrey, Relationship between ionic conductivity of perfluorinated ionomeric membranes and nonaqueous solvent properties, *J. Memb. Sci.* 184 (2001) 257–273. doi:10.1016/S0376-7388(00)00642-6.
- [35] L. Su, R.M. Darling, K.G. Gallagher, W. Xie, J.L. Thelen, A.F. Badel, J.L. Barton, K.J. Cheng, N.P. Balsara, J.S. Moore, F.R. Brushett, An Investigation of the Ionic Conductivity and Species Crossover of Lithiated Nafion 117 in Nonaqueous Electrolytes, *J. Electrochem. Soc.* 163 (2016) A5253–A5262. doi:10.1149/2.03211601jes.
- [36] R. Dmello, J.D. Milshtein, F.R. Brushett, K.C. Smith, Cost-driven materials selection criteria for redox flow battery electrolytes, *J. Power Sources.* 330 (2016) 261–272. doi:10.1016/j.jpowsour.2016.08.129.
- [37] R.M. Darling, K.G. Gallagher, J.A. Kowalski, S. Ha, F.R. Brushett, Pathways to low-cost electrochemical energy storage: a comparison of aqueous and nonaqueous flow batteries, *Energy Environ. Sci.* 7 (2014) 3459–3477. doi:10.1039/C4EE02158D.
- [38] I.L. Escalante-Garcia, J.S. Wainright, L.T. Thompson, R.F. Savinell, Performance of a Non-Aqueous Vanadium Acetylacetonate Prototype Redox Flow Battery: Examination of Separators and Capacity Decay, *J. Electrochem. Soc.* 162 (2014) A363–A372. doi:10.1149/2.0471503jes.
- [39] J.D. Milshtein, J.L. Barton, T.J. Carney, J.A. Kowalski, R.M. Darling, F.R. Brushett, Towards Low Resistance Nonaqueous Redox Flow Batteries, *J. Electrochem. Soc.* 164 (2017) A2487–A2499. doi:10.1149/2.0741712jes.
- [40] C.-N. Sun, M.M. Mench, T.A. Zawodzinski, High Performance Redox Flow Batteries: An Analysis of the Upper Performance Limits of Flow Batteries Using Non-aqueous Solvents, *Electrochim. Acta.* 237 (2017) 199–206. doi:10.1016/j.electacta.2017.03.132.
- [41] R. Ferrigno, A.D. Stroock, T.D. Clark, M. Mayer, G.M. Whitesides, Membraneless vanadium redox fuel cell using laminar flow, *J. Am. Chem. Soc.* 124 (2002) 12930–12931. doi:10.1021/ja020812q.

- [42] E.R. Choban, L.J. Markoski, A. Wieckowski, P.J.A. Kenis, Microfluidic fuel cell based on laminar flow, *J. Power Sources*. 128 (2004) 54–60. doi:DOI 10.1016/j.jpowsour.2003.11.052.
- [43] E. Kjeang, N. Djilali, D. Sinton, Microfluidic fuel cells: A review, *J. Power Sources*. 186 (2009) 353–369. doi:10.1016/j.jpowsour.2008.10.011.
- [44] M.A. Goulet, E. Kjeang, Co-laminar flow cells for electrochemical energy conversion, *J. Power Sources*. 260 (2014) 186–196. doi:10.1016/j.jpowsour.2014.03.009.
- [45] W. a Braff, M.Z. Bazant, C.R. Buie, Membrane-less hydrogen bromine flow battery., *Nat. Commun.* 4 (2013) 2346. doi:10.1038/ncomms3346.
- [46] E. Kjeang, R. Michel, D.A. Harrington, N. Djilali, D. Sinton, A microfluidic fuel cell with flow-through porous electrodes, *J. Am. Chem. Soc.* 130 (2008) 4000–4006. doi:10.1021/ja078248c.
- [47] M.A. Goulet, O.A. Ibrahim, W.H.J. Kim, E. Kjeang, Maximizing the power density of aqueous electrochemical flow cells with in operando deposition, *J. Power Sources*. 339 (2017) 80–85. doi:10.1016/j.jpowsour.2016.11.053.
- [48] J.F. Kucharyson, L. Cheng, S.O. Tung, L.A. Curtiss, L.T. Thompson, Predicting the potentials, solubilities and stabilities of metal-acetylacetonates for non-aqueous redox flow batteries using density functional theory calculations, *J. Mater. Chem. A*. 5 (2017) 13700–13709. doi:10.1039/C7TA01285C.
- [49] M.-A. Goulet, M. Eikerling, E. Kjeang, Direct measurement of electrochemical reaction kinetics in flow-through porous electrodes, *Electrochem. Commun.* 57 (2015) 14–17. doi:10.1016/j.elecom.2015.04.019.
- [50] M.A. Goulet, A. Habisch, E. Kjeang, In Situ Enhancement of Flow-through Porous Electrodes with Carbon Nanotubes via Flowing Deposition, *Electrochim. Acta*. 206 (2016) 36–44. doi:10.1016/j.electacta.2016.04.147.
- [51] Y.. Volfkovich, V.. Bagotzky, V.. Sosenkin, I.. Blinov, The standard contact porosimetry, *Colloids Surfaces A Physicochem. Eng. Asp.* 187-188 (2001) 349–365. doi:10.1016/S0927-7757(01)00650-1.
- [52] J.T. Gostick, M.W. Fowler, M.A. Ioannidis, M.D. Pritzker, Y.M. Volfkovich, A. Sakars, Capillary pressure and hydrophilic porosity in gas diffusion layers for polymer electrolyte fuel cells, *J. Power Sources*. 156 (2006) 375–387. doi:10.1016/j.jpowsour.2005.05.086.
- [53] O.A. Ibrahim, M.-A. Goulet, E. Kjeang, Microfluidic Electrochemical Cell Array in Series: Effect of Shunt Current, *J. Electrochem. Soc.* 162 (2015) F639–F644. doi:10.1149/2.0211507jes.
- [54] O.A. Ibrahim, M.A. Goulet, E. Kjeang, In-situ characterization of symmetric dual-pass architecture of microfluidic co-laminar flow cells, *Electrochim. Acta*. 187 (2016) 277–285. doi:10.1016/j.electacta.2015.11.081.

- [55] O.A. Ibrahim, P. Alday, N. Sabaté, J.P. Esquivel, E. Kjeang, Evaluation of Redox Chemistries for Single-Use Biodegradable Capillary Flow Batteries, *J. Electrochem. Soc.* 164 (2017) A2448–A2456. doi:10.1149/2.0971712jes.
- [56] M.A. Goulet, E. Kjeang, Reactant recirculation in electrochemical co-laminar flow cells, *Electrochim. Acta.* 140 (2014) 217–224. doi:10.1016/j.electacta.2014.03.092.
- [57] A.A. Shinkle, A.E.S. Sleightholme, L.D. Griffith, L.T. Thompson, C.W. Monroe, Degradation mechanisms in the non-aqueous vanadium acetylacetonate redox flow battery, in: *J. Power Sources*, 2012: pp. 490–496. doi:10.1016/j.jpowsour.2010.12.096.
- [58] M.A. Goulet, M. Skyllas-Kazacos, E. Kjeang, The importance of wetting in carbon paper electrodes for vanadium redox reactions, *Carbon N. Y.* 101 (2016) 390–398. doi:10.1016/j.carbon.2016.02.011.
- [59] J.P. Esquivel, P. Alday, O.A. Ibrahim, B. Fernandez, E. Kjeang, N. Sabaté, A metal-free and biotically degradable battery for portable single-use applications, *Adv. Energy Mater.* Accepted (2017) 1700275. doi:10.1002/aenm.201700275.
- [60] T. Devarajan, S. Higashiya, C. Dangler, M. Rane-Fondacaro, J. Snyder, P. Haldar, Novel ionic liquid electrolyte for electrochemical double layer capacitors, *Electrochem. Commun.* 11 (2009) 680–683. doi:10.1016/j.elecom.2009.01.013.
- [61] Y. Ding, Y. Li, G. Yu, Exploring Bio-inspired Quinone-Based Organic Redox Flow Batteries: A Combined Experimental and Computational Study, *Chem.* 1 (2016) 790–801. doi:10.1016/j.chempr.2016.09.004.

Appendix D.

Evaluation of Redox Chemistries for Single-Use Biodegradable Capillary Flow Batteries

An open access article [58] reproduced from The Electrochemical Society under creative commons license (CC BY-NC-ND 4.0)



Evaluation of Redox Chemistries for Single-Use Biodegradable Capillary Flow Batteries

Omar A. Ibrahim,^a Perla Alday,^b Neus Sabaté,^{b,c} Juan Pablo Esquivel,^{b,d} and Erik Kjeang^{a,*}

^aFuel Cell Research Laboratory (FCReL), School of Mechatronic Systems Engineering, Simon Fraser University, Vancouver, Canada

^bInstituto de Microelectrónica de Barcelona, IMB-CNM (CSIC), Campus UAB, Barcelona, Spain

^cInstitució Catalana de Recerca i Estudis Avançats (ICREA), Barcelona, Spain

^dDepartment of Bioengineering, University of Washington, Seattle, Washington 98105, USA

The rate of battery waste generation is rising dramatically worldwide due to increased use and consumption of electronic devices. A new class of portable and biodegradable capillary flow batteries was recently introduced as a solution for single-use disposable applications. The concept utilizes stored organic redox species and supporting electrolytes inside a dormant capillary flow cell which is activated by the dropwise addition of aqueous liquid. Herein, various organic redox species are systematically evaluated for prospective use in disposable capillary flow cells with regards to their electrochemical characteristics, solubility, storability and biodegradability. Qualitative ex-situ techniques are first applied to assess half-cell solubility, redox potential and kinetics, followed by quantitative in-situ measurements of discharge performance of selected redox chemistries in a microfluidic cell with flow-through porous electrodes. Para-benzoquinone in oxalic acid and either hydroquinone sulfonic acid or ascorbic acid in potassium hydroxide are identified for the positive and negative half-cells, respectively, yielding a maximum discharge power density of 50 mW/cm². A prototype capillary flow battery using the same redox chemistries demonstrates robust cell voltages above 1.0 V and maximum discharge power of 1.9 mW. These results show that practical primary battery performance can be achieved with biodegradable chemistries in a disposable device.

© The Author(s) 2017. Published by ECS. This is an open access article distributed under the terms of the Creative Commons Attribution Non-Commercial No Derivatives 4.0 License (CC BY-NC-ND, <http://creativecommons.org/licenses/by-nc-nd/4.0/>), which permits non-commercial reuse, distribution, and reproduction in any medium, provided the original work is not changed in any way and is properly cited. For permission for commercial reuse, please email: oa@electrochem.org. [DOI: 10.1149/2.0971712jes] All rights reserved.



Manuscript submitted June 21, 2017; revised manuscript received August 4, 2017. Published August 18, 2017. This was Paper 80 presented at the San Diego, California, Meeting of the Society, May 29- June 2, 2016.

The market demand for small-size single-use electronic devices such as portable sensors and diagnostic devices has been rising drastically in recent years. The power needs of such devices have so far been met by Li-ion batteries and other primary battery technologies, resulting in a consequent rise in their consumption. These batteries often contain heavy metals and strong electrolytes which make them one of the most hazardous components of electronic waste.¹ In addition, the majority of the primary Li batteries used globally are not recycled nor properly disposed of, thus ending up in landfills without regulations.² In applications that do not require long discharge times and have modest capacity requirements such as medical devices, these batteries are not even fully discharged before being disposed of. This requires further resources for re-extracting the materials if not recovered, which is not sustainable and raises concerns about the abundance of these resources. The end-of-life fate of these batteries and their life cycle assessment therefore only justifies the use in rechargeable applications beyond hundreds of cycles.^{3,4} These issues trigger a worrying concern about associated future environmental hazards from the battery waste generation and urgently call for novel alternatives, tightened environmental policies and switching the linear consumption habit of “take-make-dispose” for these primary batteries into a circular economy model. This approach utilizes novel concepts such as green electronics and cradle-to-cradle design to eliminate waste from the conception of new devices as a top priority considering the waste hierarchy.^{5,6}

A few prototypes have been reported to date for batteries that align with the philosophy of green electronics. However, most of these prototypes were designed for transient implantable or edible applications and were generally based on benign metals that will dissolve upon use in a short time. Kim et al. utilized melanin and activated carbon in water activated sodium ion batteries that are edible.⁷ Yin et al. discussed the use of biodegradable metals such as Mg, Fe, W or Mo as electrode materials for ingestible applications.⁸ Tsang et al. reported the design, fabrication and testing of a biodegradable battery based on Mg and

Fe with power output of 30 μ W that satisfies the lower range required for implantable applications.⁹ Recently, Nadeau et al. demonstrated an ingestible battery based on Zn and Cu that is activated by gastric fluid.¹⁰ Aside from the implantable applications, a biodegradable super capacitor was recently reported as an environmentally friendly energy storage solution.¹¹

Various other electrochemical power source concepts have been proposed as sustainable alternatives for portable applications, with limited attention to their end of life disposal. Within the fuel cells category, different organic liquid fuels were used as benign fuel, such as methanol, formic acid, ethanol or ethylene glycol.¹²⁻¹⁵ For example, Esquivel et al. presented a paper-based direct methanol fuel cell that can be integrated within lateral flow test strips.¹⁵ However, the electrochemical reactions involving these organic liquid fuels often require precious metal catalysts such as platinum or palladium that are scarce and thus not readily disposable. Other works reported the use of biological fuels, such as glucose.¹⁶⁻¹⁹ However, despite the high energy density associated with biofuels,¹⁸ their power output is generally much lower than the target application requirements and the biocatalysts often have limited stability.²⁰ Moreover, ion exchange membranes associated with conventional fuel cells are typically not suitable for disposable applications, due to their cost and composition. This dictates the use of membrane-less cell designs such as those recently developed based on co-laminar flow, wherein the mixing of reactants is governed by slow, cross-stream diffusion in lieu of a physical barrier or membrane otherwise used to separate the reactants.^{21,22} These membrane-less devices thus offer advantages in cost, simplicity, performance and durability.²³ In addition, membrane-less cells have the flexibility of tuning the specific conditions in each half-cell (mixed-media operation) since the conditions are not restricted by the ion selective membranes required in conventional cells.²⁴ Kjeang et al. applied flow through porous electrodes in co-laminar flow cells, which eliminated mass transport limitations and enabled full utilization of the three dimensional electrode area for increased reactant conversion and high discharge power density.²⁵ These porous electrodes were recently engineered together with the device dimensions to offer unprecedented power densities of 2.0 W/cm², which is the highest performance reported to date for aqueous electrochemical flow cells.²⁶

*Electrochemical Society Member.

^zE-mail: ekjeang@sfu.ca

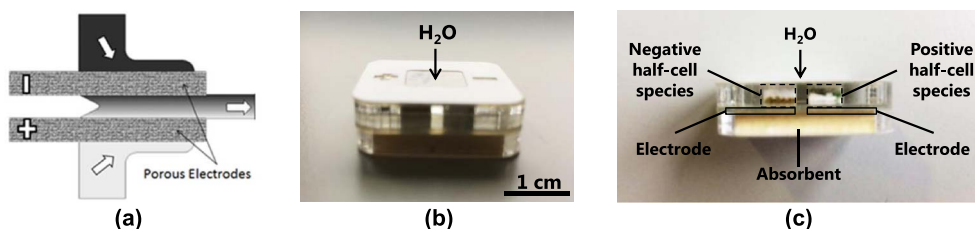


Figure 1. a) Microfluidic co-laminar flow cell with flow-through porous electrodes used for measuring discharge performance. b) Side view and c) cross-sectional view of the disposable capillary flow cell used for final demonstration of reactant chemistries in an integrated device.

Nevertheless, the vanadium redox electrolyte used in that case is not adequate for single-use applications, due to associated toxicity and cost.

Many paper-based electrochemical cells have been reported owing to various advantages such as self-pumping using capillarity, simplicity, disposability enabled by low-cost and ease of integration within devices for low-resource environments.^{27,28} In the case of co-laminar flow cells, the capillary action in paper-based cells can eliminate the need for a pump to drive the flow.¹⁵ Some paper-based devices relied on the use of metals such as Cu, Al, Mg or Ag to form a microfluidic galvanic cell,^{29,30} with open circuit voltages up to 2.2 V.³¹ Others have developed biological and microbial fuel cells in paper.^{32,33} Choi et al. presented various bio-fuel cells in a paper platform as an alternative power source based on benign fuel alternatives that can be harvested.^{34–36} Lee and Choi presented an origami paper based bacterial battery with a power output of 48 nW.³⁷ Other researchers utilized Li-ion origami-inspired paper batteries for both transient and rechargeable uses.^{38–40}

Recently, a new concept of single-use capillary flow batteries was introduced, which can be disposed of by the biotic degradative process.⁴¹ This allows the battery to close its life cycle to nature at its end-of-life, which complies well with the circular economy and the concepts of green electronics as the associated waste is minimized from the device conception. The concept leverages advances in paper-based fuel cells which enable self-pumping and microfluidic fuel cells with flow-through porous electrodes which enable high power densities. The battery is made exclusively of environmentally benign, biotically degradable materials such as cellulose and beeswax. The electrochemical energy conversion utilizes organic redox reactants which are stored on the device in solid phase in a dedicated compartment. Upon activation by the dropwise addition of liquid, the stored reactants and electrolytes dissolve and flow by capillarity through the pore network of the electrodes where the power is generated.

In this work, various organic redox species are systematically analyzed and evaluated for prospective use in disposable capillary flow cells. The chemistry requirements for this class of batteries are reviewed with regards to their electrochemical characteristics, solubility, storability and biodegradability, and the results for the evaluation of redox reactants and electrolytes, suitable for the operation of the disposable device, are presented. The investigation includes half-cell assessment of the redox reactants and electrolytes regarding their redox potential and kinetics as well as cell level assessment to measure their discharge performance. Finally, the identified chemistries are demonstrated in an integrated capillary flow cell.

Experimental

Sulfuric acid (H_2SO_4 , 95%) from Caledon Laboratories Ltd (Georgetown, ON, Canada) is diluted to the desired concentrations (0.5–1 M). Leucoquinizarin (LQ) is purchased from TCI America (Portland, OR, USA) and used as received. All other species and electrolytes are purchased from Sigma Aldrich (Oakville, ON, Canada), and used as received, unless otherwise stated.

The redox chemistry screening is based on identifying suitable redox species and supporting electrolytes that are commercially available, aided by literature. Solutions are prepared by dissolving each

combination of supporting electrolyte and redox species, consecutively, in deionized water (DI- H_2O , Millipore) to the desired concentrations. The solubility of the species is assessed in water and/or desired electrolytes based on literature and on visual absence of solid precipitation at the desired concentrations. The soluble redox chemistry options are then characterized ex-situ using voltammetry techniques to measure the open circuit potential (OCP) and to qualitatively assess the electrochemical reaction kinetics for the different redox species and electrolytes. The measurements are performed in a conventional three-electrode electrochemical cell bubbled with nitrogen to minimize solution oxidation due to dissolved oxygen or ambient air. Glassy carbon electrode (0.07 cm^2), platinum wire electrode and saturated calomel electrode (SCE) (CH instruments Inc, TX, USA) are used as working electrode, counter electrode and reference electrode, respectively, and the cell is operated by a frequency response analysis compatible potentiostat (Gamry, Reference 3000). Prior to scanning, the OCP of each half-cell is measured at zero applied current. Cyclic voltammetry (CV) is then recorded at a scan rate (ω) of 50 mV/s followed by linear sweep voltammetry (LSV) measurements in the voltage sweep direction of the respective discharge reaction of interest at various scan rates of 5, 10, 25, 50 and 100 mV/s. The cell ohmic resistance is measured by means of electrochemical impedance spectroscopy (EIS) performed using the same potentiostat from 1 MHz to 1 Hz with an AC amplitude of 10 mV rms at the OCP, by reading the high frequency real axis intercept value of the Nyquist plot. The resistance value obtained is used to perform post-measurement IR-compensation of the measured voltammograms.

Next, the discharge performance of the selected redox chemistries is measured in-situ in a microfluidic co-laminar flow cell.²³ A microfluidic cell design with flow through porous electrodes²⁵ is used as an analytical platform for the in-situ discharge performance analysis, as shown in Fig. 1a. The cell design was previously used in other analytical studies and shown to enable high discharge performance and minimal cross over losses.⁴² The device is fabricated by UV soft lithography of polydimethylsiloxane (PDMS) (Dow Corning) from an SU-8 (Microchem) photoresist master with 150 μm height then bonded to a glass slide. Rectangular strips of carbon paper (TGPH-060, Toray), with 1 mm width, are heat treated and placed to form both cell electrodes. Further details about the device design and fabrication can be found elsewhere.⁴³ The pre-mixed solutions of redox reactants and supporting electrolytes are prepared at required concentrations and pumped into the cell by means of a dual syringe pump (Harvard apparatus) at a flow rate of 10 or 100 $\mu\text{L}/\text{min}$. This flow rate is chosen in order to minimize influences from mass transport losses on the cell performance, as demonstrated in other works utilizing the same analytical cell.⁴² The measurements are performed by the same potentiostat in potentiodynamic mode at a scan rate that is slow enough to match steady state measurements (10 mV/s) from OCP to 0.1 V. The performance is normalized to the active cross sectional area normal to the flow ($0.5 \times 0.015 \text{ cm}^2$). The cell ohmic resistance is measured by EIS performed at OCP using the same potentiostat and same frequency range as in the ex-situ measurements.

Finally, the identified suitable redox species and supporting electrolytes are tested in a disposable capillary flow cell featuring the same design as the biodegradable battery recently reported,⁴¹ wherein the reactant and electrolyte species are stored on the device in solid form,

Table I. Structure, standard potential and theoretical capacity of basic quinone compounds.

Quinone (CAS no.)	1,4-Benzoquinone (106-51-4)	1,2-Benzoquinone (583-63-1)	1,4-Naphthoquinone (130-15-4)	9,10-Anthraquinone (84-65-1)
Structure				
Abbreviation	pBQ	oBQ	NQ	AQ
Standard potential (vs. SHE)	0.69 V	0.78 V	0.48 V	0.15 V
Theoretical capacity (mAh/g)	496	496	339	257

as shown in Fig. 1b and Fig. 1c. In this case, the device enclosure is made of PET-based pressure sensitive adhesives (PSA) (Adhesives Research, Glen Rock, PA, USA) and poly (methyl methacrylate) (PMMA) layers, for rapid prototyping using CO₂ laser micromachining (Mini 24, Epilog Laser, Golden, CO, USA). Cellulose paper (Ahlstrom, Helsinki, Finland) is laser cut and used for absorbent pads to provide the capillary flow. Porous carbon paper strips (TGPH-120, Toray) are heat treated and used as electrodes with an active area of 0.25 cm². Further details about the device fabrication and structure can be found elsewhere.⁴¹ The device is activated by adding 1 mL of DI-H₂O and the OCP is monitored for 1 hour. During this measurement period, a cell polarization curve is measured and recorded every 5 minutes in potentiodynamic mode from OCP to zero volts.

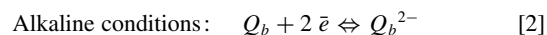
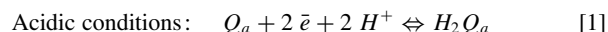
Reactant Chemistry Requirements and Selection

A disposable capillary flow battery resembles a redox flow battery albeit of a primary battery type designed for single-use discharge operation. This new class of batteries features unique requirements for the redox chemistries used in the positive and negative half-cells. The opportunity enabled by the capillary flow cell design is to achieve a fully biodegradable device with high performance and stability. The active redox species used as reactants are therefore required to exist in the solid phase at ambient conditions, for instance in powder form, to enable 'dormant' storage on the cell with useful shelf life. They should moreover be soluble in water or other desired electrolytes such that they dissolve upon liquid activation of the device and are carried into the flow-through porous electrodes for the electrochemical energy conversion. They are also required to be biodegradable and thus preferably organic. The species should also be stored on the cell in the correct redox state required for discharge operation with net current generation at an adequate cell voltage. Furthermore, their electrochemical reactions should be compatible with catalyst-free carbon electrodes with fast kinetics.

The use of organic active redox species is an emerging alternative for redox flow battery development⁴⁴⁻⁴⁶ and has recently captured the interest of the energy storage research community.⁴⁷⁻⁵⁰ Huskinson et al. introduced a novel flow battery system for energy storage, in which they coupled a quinone redox species with a bromine positive half-cell. Their metal-free cell showed high power density during discharge and high cycling efficiency.⁴⁷ Yang et al. substituted the toxic bromine with another, high-reduction potential quinone, to create an ecofriendly, water-based all-quinone system and named it the organic redox battery (ORBAT).⁴⁸ Quinones are inexpensive and can be extracted from natural organic compounds present in plants, which makes them eco-friendly. Moreover, quinone redox species generally have rapid kinetics on catalyst-free carbon electrodes.

Quinone compounds can generally be defined as a class of cyclic organic compounds that contain two carbonyl groups (C = O). This class includes for example benzoquinones, naphthoquinones and anthraquinones, as the basic forms shown in Table I. By the addition of more rings to the structure, the aqueous solubility and standard reduction potential are expected to decrease,⁵¹ as shown in Table I. Therefore, benzoquinones (BQ) will have the highest solubility and highest standard potential while anthraquinones (AQ) will have the

least solubility and the lowest standard potential. Alternatively, naphthoquinones (NQ) are expected to have moderate solubility and standard reduction potential between BQ and AQ and may therefore also be considered. These quinone compounds can moreover be tuned for their standard reduction potentials as well as their solubility by adding different functional groups to the structure.^{50,52} When quinones are reduced reversibly to their respective hydroquinones, the two carbonyl groups change to two hydroxyl groups (C–OH). Their electrochemical reactions involve two electrons in either acidic^{47,48} or alkaline conditions,^{45,49} as shown in Eqs. 1–2, respectively.



In addition, quinones have high probability of fast biodegradation as predicted by the biodegradation models (BIOWIN) in EPISuite and other works.^{53,54} The quinone species are therefore considered to satisfy the majority of the disposable battery criteria. A preliminary discharge experiment in a microfluidic cell is therefore conducted to establish a proof-of-concept for the all-quinone chemistry. The reactants in this example are adopted from the ORBAT⁴⁸ and includes using sodium salts of anthraquinone-2-sulfonic acid (AQS, Fig. 2a) and 1,2-dihydroxybenzene 3,5-disulfonic acid (H₂BQDS, Fig. 2b) as negative and positive half-cells, respectively, in 1 M sulfuric acid (H₂SO₄). While H₂BQDS has relatively high solubility due to the hydroxyl (–OH) and sulfonic acid (–SO₃[–]) groups, the solubility of the sodium salt of AQS is merely ~0.05 M. Therefore, solutions of H₂BQDS and AQS are prepared and tested at a concentration of 0.05 M in 1 M H₂SO₄. In order to perform in-situ battery discharge performance measurements, the solutions are first electrolytically charged to the forms required for discharge in a separate, custom made flow cell at 1.0 V applied voltage. After charging, the AQS is reduced into

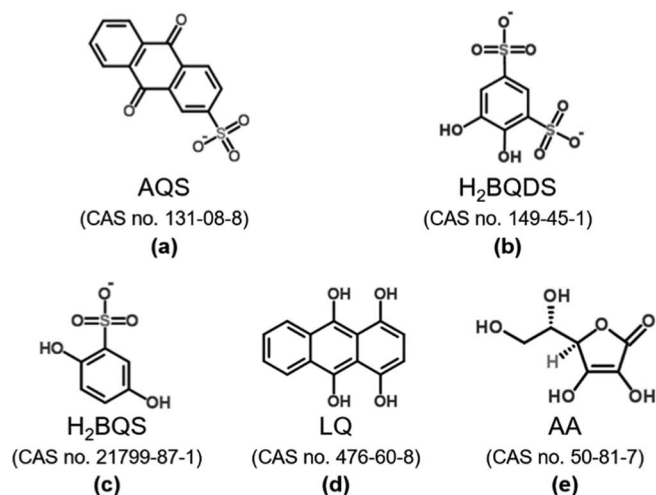


Figure 2. Structures of quinones used in ORBAT⁴⁸ (a, b) and this work (c, d, e).

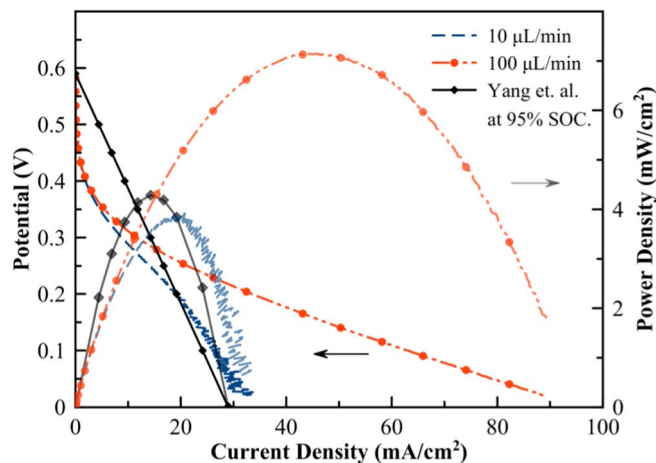


Figure 3. Discharge results in a microfluidic co-laminar flow cell for the all-quinone battery chemistry with H₂BQDS and AQS based on ORBAT compared with discharge data at 95% SOC from literature.⁴⁸

H₂AQS and the H₂BQDS is oxidized into BQDS, both of which are suitable for discharge experiments in the microfluidic cell. This is confirmed by the change of color from light yellow to dark green in the case of AQS/H₂AQS and from a colorless solution to light brown in case of H₂BQDS/BQDS, which is consistent with literature.^{55,56} The results of the discharge experiments in the microfluidic cell operated at flow rates of 10 and 100 µL/min are shown in Fig. 3. The cell is found to have an OCP of 0.59 V and a peak power density of 3.9 mW/cm² at 10 µL/min, which is in good agreement when compared with a linear approximation of the discharge data reported for the ORBAT at 95% state-of-charge (SOC).⁴⁸ At the high flow rate of 100 µL/min, the cell output is increased to 7.2 mW/cm² because of the enhanced mass transport at higher flow rates.

The limited solubility of AQS can be improved by applying a sodium ion exchange step, and thus higher associated discharge performance outputs can be anticipated, as shown in other works.⁵⁷ Nonetheless, the commercially available forms of these quinone compounds are generally in a redox state that cannot be directly used for discharge, as an initial charging step would be required. To elaborate this challenge on the demonstrated example above, the high potential quinone intended for the positive half-cell is available commercially in its reduced form (e.g., Tiron or H₂BQDS) while the low potential quinone intended for the negative half-cell is available in the oxidized form (AQS). In order to store the species on the disposable cell in a redox state ready for discharge, the positive half-cell requires a high potential species in an oxidized/quinone form (= O), while the negative half-cell requires a low potential species in a reduced/hydroquinone form (-OH).

In order to overcome the challenge of the desired redox state of the quinone compounds for direct use in discharge operation, the pH dependence of the standard redox potential of quinones can be leveraged in the present application.^{58,59} This is facilitated by mixed-media operating conditions in which an alkaline negative electrode and an acidic positive electrode are employed. This enables higher electrochemical cell voltages during discharge operation and hence the available reduced quinones (-OH) can be used under alkaline conditions at the negative electrode for direct discharge operation. This mixed-media feature is uniquely enabled by membrane-less cells such as the microfluidic co-laminar flow cells where the diffusion interface is used to separate the reactant streams instead of a physical barrier such as ion exchange membranes which dictate the choice of the reactant media. For the present application, the mixed-media condition not only enables higher cell voltage but also enables utilization of a wider range of commercially available species and electrolytes. Furthermore, mixed-media operation offers an opportunity for the acidic and alkaline electrolytes to neutralize downstream by means

of diffusive mixing to form neutral or near neutral pH conditions that allow safe disposal, which is an essential requirement for the disposable cell.

A subset of potential organic redox species are identified to theoretically meet all the aforementioned selection criteria of storability, solubility, biodegradability, correct redox state, adequate redox potential and good kinetics. For the oxidized quinone to be used in the positive electrode, para-benzoquinone (pBQ), shown earlier in Table I is identified and selected. pBQ is the most basic form of quinone compounds and is therefore soluble in aqueous media and readily biodegradable. pBQ is also commercially available in solid form in its oxidized state which enables direct use for electrochemical reduction in the positive half-cell of the battery. The choice of pBQ is favored over other oxidized quinones such as NQ and AQ (Table I) since both NQ and AQ have lower solubility and standard reduction potential and are thus considered inadequate for the current application. While the ortho-benzoquinone (oBQ) has higher reduction potential than pBQ, it is not found commercially available in the oxidized form and only the reduced form (Catechol) is available. On the other hand, for the reduced hydroquinones to be used at the negative electrode, hydroquinone sulfonic acid (H₂BQS, Fig. 2c), is an example identified as a potential benzoquinone available in the reduced form. Beside benzoquinones, anthraquinones are known to have relatively low standard potential and are thus considered suitable for use in the negative electrode of the current approach, by facilitating a sufficiently negative electrode potential when used in alkaline media for a targeted cell potential on the order of ~1 V. The reduced forms of anthraquinones available commercially are limited however, and the most suitable option for the negative half-cell is deemed to be 1,4,9,10-Tetrahydroxyanthracene or leucoquinizarin (LQ, Fig. 2d). In addition to the quinone based species, organic acids with anti-oxidant characteristics can also be considered as biodegradable options for the negative half-cell. For example, ascorbic acid (AA, Fig. 2e), also known as vitamin C, is deemed to be a theoretically viable candidate for the negative half-cell as it is a soluble phytochemical and commonly used antioxidant with a suitably negative standard potential for oxidation.

Results and Discussion

The reactant chemistry options that passed the preliminary screening described in the previous section are experimentally assessed for prospective use in disposable capillary flow batteries according to the aforementioned criteria. The solubility of the species is first assessed in water and/or desired electrolytes. The species are then evaluated ex-situ by measuring their half-cell open circuit potentials (OCPs) and electrochemical kinetics by using cyclic voltammetry (CV) and linear sweep voltammetry (LSV) techniques. Next, the discharge performance is measured in-situ in a microfluidic co-laminar flow cell with flow-through porous carbon electrodes, aiming for a power density output in the range of tens of mW/cm². The most promising reactant chemistries are finally demonstrated in a capillary flow cell device.

Ex-situ assessment of viable half-cells.—For the positive half-cell, para-Benzoquinone (pBQ) is first selected for evaluation. It undergoes a two electron, two proton transfer in acidic media, following Eq. 1, with a standard reduction potential of 0.69 V vs. SHE.⁶⁰ Here, pBQ is found to have an aqueous solubility limit of 0.1 M at room temperature and is thus dissolved to this saturation concentration in 1 M sulfuric acid (H₂SO₄) as a benchmark acidic supporting electrolyte. The measured half-cell OCP equals 0.52 V vs. SCE, which is in reasonable agreement with the standard potential given the more acidic condition and fully oxidized form used here. The IR-compensated CV of 0.1 M pBQ is shown in Fig. 4a at a scan rate of 50 mV/s. The figure shows a peak current density ratio (i_{pa}/i_{pc}) close to unity but with a relatively wide peak separation ($E_{pa} - E_{pc}$) of 445 mV, which is much greater than the 59 mV per electron expected for a reversible process. While quinones are generally known to be electrochemically reversible in aqueous media, this behavior of pBQ is in

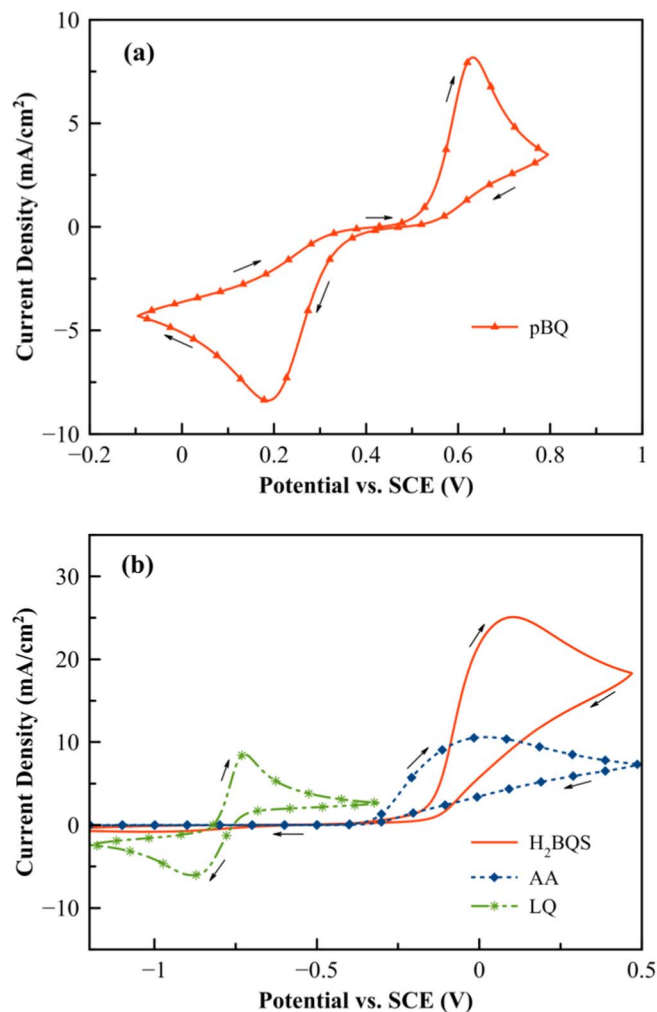


Figure 4. IR-compensated cyclic voltammograms at a scan rate of 50 mV/s for a) 0.1 M pBQ in 1 M H₂SO₄ and b) 0.1 M H₂BQS, AA and LQ in 1 M KOH.

agreement with literature studies where the peak separation is observed to increase in buffered media, indicating an overall process with relatively slow kinetics.^{58,59,61} IR-compensated LSVs are shown in Fig. 5a at various scan rates for the respective electrochemical reduction of pBQ of concern to this study. The cathodic peak current densities (i_{pc}) are shown to have approximately linear proportionality with the square root of the scan rate ($\omega^{0.5}$), as shown in the figure inset, indicating a process that is diffusion controlled. The i_{pc} values in this case are higher than for the CV data (Fig. 4a) due to the decrease in cathodic current after each cycle in the CV as it approaches a steady result. The figure also shows that the cathodic peak potential (E_c) varies slightly with the scan rate and that the difference between cathodic peak potential and potential at half peak current ($|E_{pc} - E_{pc/2}|$) decreases with reduced scan rate, which confirm a quasi-reversible process. Overall, pBQ shows good kinetics on the carbon electrode and is deemed an adequate reactant species for the positive half-cell of the present application.

For the negative half-cell, H₂BQS; a hydroquinone, AA; a commonly used antioxidant present in nature and LQ; a reduced anthraquinone are identified for potential use, as they exist in the reduced redox state, and are thus evaluated in 1 M potassium hydroxide (KOH) to establish the desired alkaline conditions for this electrode. The electrochemical reaction for the quinones (H₂BQS and LQ) involves transfer of two electrons after deprotonation in alkaline conditions,⁴⁹ following Eq. 2. For the AA case, the electrochemical reaction in highly alkaline media also follows Eq. 2 and involves a two electron oxidation of ascorbate,^{62,63} since deprotonation of the acid occurs by reaction with KOH. The solubility in aqueous media is found to be much higher for H₂BQS and AA than for the pBQ previously assessed for the positive half-cell. H₂BQS is soluble up to 0.7 M while AA is soluble up to 1.9 M in water. However, LQ is found to be poorly soluble in water and to have a hydrophobic behavior, which may impose a limitation for the present application. The solubility limit for the three compounds is expected to be particularly high in KOH solution due to the deprotonation that provides solubility and higher electron donation capabilities.⁴⁹ The three compounds are however further evaluated at a concentration of only 0.1 M in 1 M KOH in order to match the concentration of the corresponding pBQ in the other half-cell and thereby balance the overall cell chemistry. Next, the three redox species are characterized ex-situ using the voltammetry techniques, while nitrogen is bubbled into the cell to minimize solution partial oxidation⁵⁶ by dissolved oxygen or ambient air and enhance stability. Before the potential sweep, the

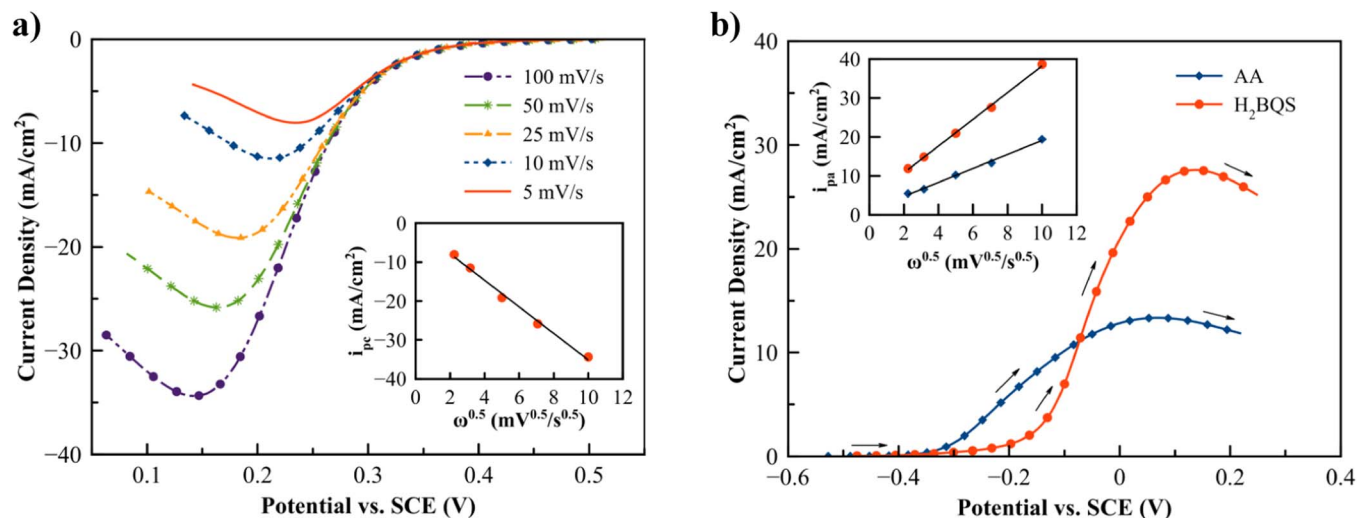


Figure 5. IR-compensated linear sweep voltammograms representing the a) electrochemical reduction of 0.1 M pBQ in 1 M H₂SO₄ at various scan rates and b) electrochemical oxidation of 0.1 M H₂BQS and AA in 1 M KOH at a scan rate of 50 mV/s. The figure insets show the peak current densities (i_p) versus the square root of the scan rates ($\omega^{0.5}$).

half-cell OCPs are measured to be -0.47 V, -0.53 V and -0.80 V vs. SCE for the H_2BQS , AA and LQ, respectively, which suggests a prospective full cell potential window of > 1.0 V when paired with pBQ. IR-compensated CVs for the three redox species are shown in Fig. 4b at a scan rate of 50 mV/s. The LQ active species shows a reversible electrochemical process, which was also observed in other works for anthraquinone compounds in alkaline media.^{45,49} The CV shows a peak current density ratio (i_{pa}/i_{pc}) of around 1.15 and a peak separation ($E_{pa} - E_{pc}$) of 159 mV. Nevertheless, the LQ is found to be rather unstable and its oxidized form has limited solubility in KOH causing visually observed precipitation which challenges its prospective use in capillary flow cells due to possible clogging of the porous media. Recalling that the active species and supporting electrolytes are intended to be stored in solid form and simultaneously dissolve in water, the LQ is hence deemed unsuitable because of its aqueous solubility limitations and is excluded from operation of the final device.

In contrast to the LQ case, the reverse (cathodic) peak is absent in both cases of AA and H_2BQS . The absence of the reverse peak is likely attributed to the instability of the electro-oxidation produced species in alkaline conditions, as also observed in other works.^{61,64-66} Post CV, the half-cell OCP for both species drops below -0.6 V vs. SCE, which suggests the formation and presence of a new species in the solution. Despite these indications that both H_2BQS and AA may not be reversible under alkaline conditions and hence unsuitable for a conventional flow battery application in alkaline conditions, both are still deemed adequate for the primary battery approach presented in this work, since only the electro-oxidation portion of the cycle is of interest. Despite the more positive half-cell OCP of H_2BQS compared to AA which results in a slightly lower cell voltage, the CV results also show that H_2BQS has a higher peak current density than AA which may reflect higher species diffusivity and faster kinetics.

For the anodic (oxidation) peak of interest to the primary battery approach, IR-compensated LSVs for 0.1 M redox active species (AA and H_2BQS) in 1 M KOH are shown in Fig. 5b, at a scan rate of 50 mV/s. Both species exhibit an anodic peak potential (E_{pa}) that varies slightly with the scan rate. Similar to the CV results, the electro-oxidation of H_2BQS has a higher anodic peak current density (i_{pa}) compared to AA, which indicates a higher diffusion rate and faster kinetics. The difference in kinetics of the electro-oxidation can also be observed from the difference of the peak potential and the potential at half peak current density ($E_{pa} - E_{pa/2}$) in each case. For example, at 50 mV/s, this difference equals 193 and 252 mV for H_2BQS and AA, respectively, indicating that H_2BQS has faster kinetics. The anodic peak current densities (i_{pa}) are shown to be approximately proportional to the square root of the scan rate (inset of Fig. 5b), wherein H_2BQS has a higher slope than AA, again reflecting the higher diffusion and faster kinetics. It is thus concluded that both AA and H_2BQS are suitable for the final device application, with AA having a more negative half-cell OCP advantage and H_2BQS having a higher diffusion rate and faster kinetics.

Ex-situ assessment of compatible supporting electrolytes.—In order to satisfy the functional requirements of disposable capillary flow cells, both active species and supporting electrolytes need to be stored in the solid phase onboard the device, for instance in powder form, and then activated by addition of liquid when used for battery discharge. The active redox species selected in the previous section achieve these requirements in full. For the supporting electrolytes, the KOH used as a supporting electrolyte at the negative electrode exists in solid form and thus can also be stored and dissolved on the final device to fulfill the requirements. However, while H_2SO_4 shows high performance when initially used as a benchmark supporting electrolyte at the positive electrode, it cannot be dried or stored in the solid phase on the final device. Therefore, it needs to be replaced with a suitable supporting electrolyte that is available in solid phase and soluble in aqueous media. Various organic or inorganic acids or salts could be considered for this purpose; however, the resulting supporting electrolyte must also be stable with inert chemical and electrochemical

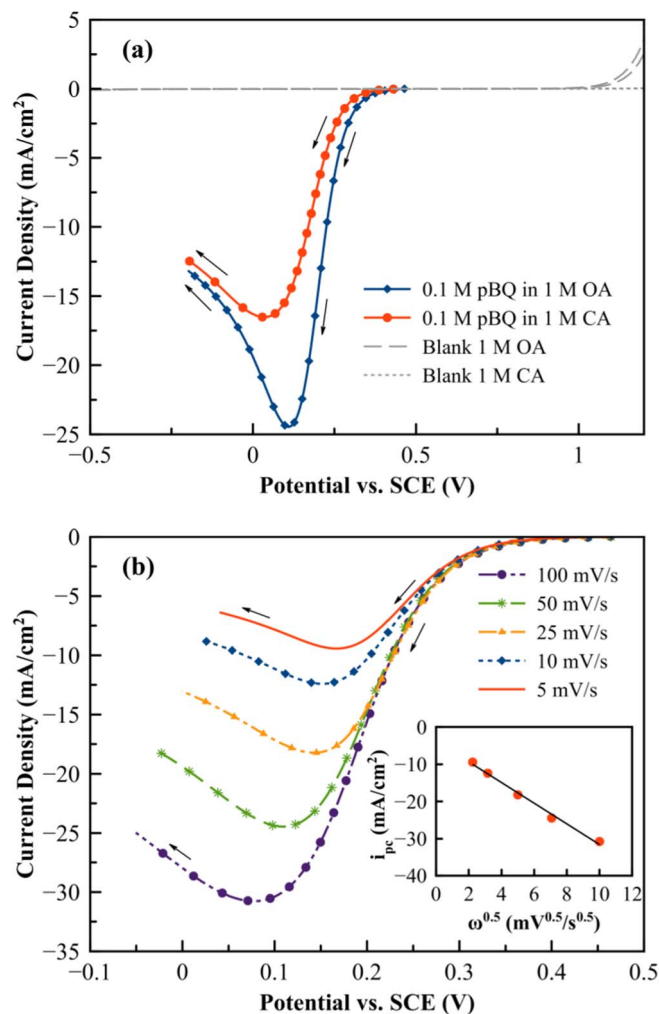


Figure 6. IR-compensated linear sweep voltammograms representing the electrochemical reduction of a) 0.1 M pBQ in 1 M OA and 1 M CA at 50 mV/s with a background CV presenting inert activity for blank supporting electrolytes and b) 0.1 M pBQ in 1 M OA at various scan rates with an inset showing the cathodic peak current density (i_{pc}) versus the square root of the scan rates ($\omega^{0.5}$).

activity, acidic at low pH in order to maintain the mixed-media benefits and have high ionic conductivity in order to retain the good discharge performance. For example, oxalic acid (OA) is identified as a strong organic acid with low measured pH and aqueous solubility up to 1 M. Moreover, citric acid (CA) is also identified as another organic acid with a much higher solubility limit. Both OA and CA are phytochemicals that are present in nature and are both predicted to have fast biodegradation probability by EPISuite from the US Environmental Protection Agency.⁵⁴ At a concentration of 1 M, the pH is measured to be in the range of 0.5 – 1 and 1.5 – 2 for OA and CA, respectively (pH test paper, Fisher Scientific, ON, Canada). The OCP of 0.1 M pBQ in 1 M OA and in 1 M CA is measured to equal 0.47 and 0.42 vs. SCE, respectively. The relatively low (less positive) half-cell OCP in case of CA supporting electrolyte is likely attributed to the higher pH which results in lower Nernstian potential due to the pH dependence of pBQ standard potential. Moreover, impedance measurements indicate that CA has an order of magnitude higher solution resistance, presumably due to lower dissociation of the acid. The IR-compensated LSVs measured for both cases are shown in Fig. 6a, at a scan rate of 50 mV/s. The data show a lower cathodic peak current density (i_{pc}) for pBQ reduction in CA supporting electrolyte compared to the corresponding result for OA, which is consistent with the previous results and

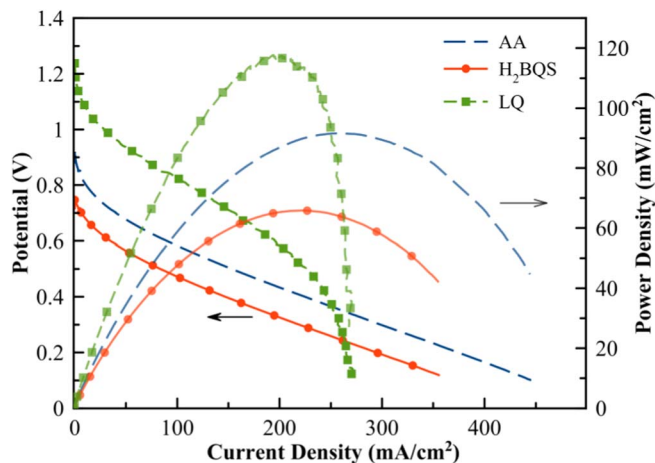


Figure 7. Polarization results of in-situ measurements in a microfluidic co-laminar flow cell operated on 0.1 pBQ in 1 M H₂SO₄ at the positive electrode and 0.1 M AA, H₂BQS and LQ in 1 M KOH at the negative electrode.

likely due to the lower availability of protons for the pBQ reduction.⁶⁴ Blank supporting electrolyte CVs at 50 mV/s are also shown in the background of Fig. 6a, wherein the electro-oxidation of electrolyte species is not expected to occur in the potential range of interest at the catalyst-free electrode materials and conditions of this study,⁶⁷ which confirms the inert activity of both CA and OA as supporting electrolytes. Nevertheless, despite the much higher solubility of the CA supporting electrolyte than OA, the latter option is likely preferred due to the more positive potential, faster kinetics and higher ionic conductivity, which are likely to positively impact the cell performance. IR-compensated LSVs for the 1 M OA supporting electrolyte case are shown in Fig. 6b, again representing the electrochemical reduction of 0.1 M pBQ at various scan rates. The results suggest quasi-reversible kinetics in this case, considering the variation of the cathodic peak potential (E_{pc}) and increase of $|E_{pc} - E_{pc/2}|$ with increased scan rates. The linearity of the peak cathodic current density (i_{pc}) with the square root of the scan rates ($\omega^{0.5}$) is also shown in the same figure inset. The result suggests similar reduction kinetics for the OA case when compared to the H₂SO₄ benchmark electrolyte case. For example, at 50 mV/s, the cathodic peak current densities i_{pc} equal -24.5 and -25.8 mA/cm², while the measured $|E_{pc} - E_{pc/2}|$ values equal 103 and 83.6 mV, for the OA and H₂SO₄ cases, respectively. However, the OA cell resistance is found to be higher than the H₂SO₄ case due to the lower ionic conductivity⁶⁰ which may hence suggest a reduced in-situ discharge performance.

In-situ microfluidic co-laminar flow cell discharge performance.—Next, the in-situ discharge performance is measured, using the resulting positive and negative half-cells together in mixed media operation inside the microfluidic cell with flow-through porous electrodes. A solution of 0.1 M pBQ in 1 M H₂SO₄ is initially used at the positive electrode of the cell and measured against the three negative half-cell options of 0.1 M H₂BQS, AA and LQ in 1 M KOH at the negative electrode. The polarization curves and power density curves for the three cases are shown in Fig. 7, at the flow rate of 100 μ L/min. The AA at the negative electrode shows a cell OCP of 0.92 V whereas for H₂BQS, the OCP equals 0.78 V. The EIS measurements show similar cell resistance values around 90 Ω for both cases, a value which is dominated by the ionic resistance of the electrolytes. This is also reflected by the similar slopes in the ohmic region of the polarization curves. The cell achieved peak power densities of 90 and 65 mW/cm² for AA and H₂BQS, respectively, which meets and exceeds the present application requirements in both cases. In addition, the result when using LQ is also shown on the same figure wherein the cell achieved a higher OCP of 1.24 V, which to the authors' knowledge represents the highest all-quinone

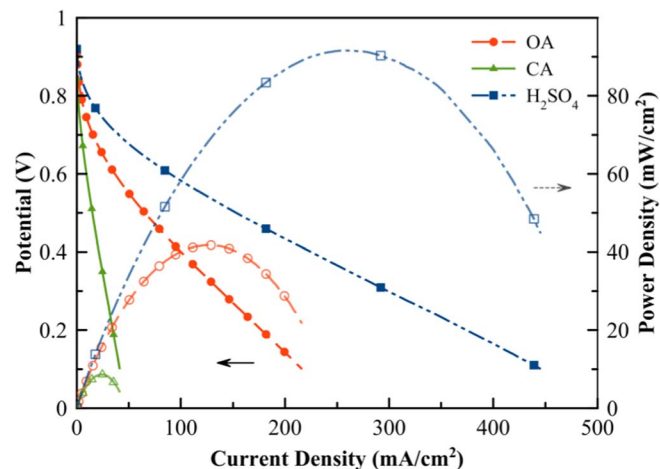


Figure 8. Polarization and power density discharge curves in a microfluidic co-laminar flow cell using 0.1 M AA in 1 M KOH at the negative electrode and 0.1 M pBQ in 1 M H₂SO₄, OA and CA at the positive electrode.

aqueous electrochemical cell potential reported to date. Although a higher power density of 120 mW/cm² is measured for the LQ case, higher mass transport limitations are also observed, despite the low reactant utilization at these flow rates. This further confirms the limited stability of LQ and the limited solubility of its oxidation product, as previously indicated in the ex-situ analysis section, which results in potential electrode clogging and limits the prospective use of LQ in the present application. In general, the performance obtained in the microfluidic cell with dilute concentrations of active organic redox species on metal-free electrodes is remarkable. The peak power density achieved is comparable to that of previously reported cell designs based on concentrated liquid organic fuels and precious metal catalysts^{13,14} and is several orders of magnitude higher than other environmentally friendly approaches based on biofuel cells.^{18,37}

Then, the effect of the supporting electrolytes on the full cell discharge performance is assessed in-situ in the microfluidic co-laminar flow cell, and compared to the H₂SO₄ benchmark case. Fig. 8 presents the polarization curves and power density curves for 0.1 M pBQ in 1 M of the supporting electrolytes of OA and CA coupled with 0.1 M AA in 1 M KOH at the negative electrode. The AA case is chosen here as it showed higher performance than H₂BQS (Fig. 7). The discharge performance for the H₂SO₄ benchmark case is also shown in the same figure for comparison. It is shown that the peak power density with CA is 10 mW/cm², which is merely 11% of the discharge power density obtained with H₂SO₄ and further confirms the performance trade-offs of CA observed in the ex-situ study. The cell OCP for the OA case is slightly lower than the benchmark case with H₂SO₄, which is explained by the lower acidity (higher pKa) of OA and higher pH than H₂SO₄. More importantly, however, a peak power density of 42 mW/cm² is obtained with OA as supporting electrolyte, which is considered to meet the cell performance requirement of the target portable applications. The combined ohmic cell resistances are measured by means of EIS and are found to be 90, 170 and 1200 Ω for the cases of H₂SO₄, OA and CA, respectively, which explains the much stronger performance in case of OA than that of CA. The result also suggests an ohmic limited cell performance which explains the trade-off of using OA supporting electrolyte when compared to H₂SO₄. While OA allows the possibility of solid phase storage on the final device, it has relatively low ionic conductivity compared to H₂SO₄,⁶⁰ which results in increased ohmic cell resistance from 90 to 170 Ω and the consequent reduction in peak power density from 90 to 42 mW/cm².

Demonstration in a capillary flow cell.—Finally, the proposed redox chemistries are integrated and tested in a disposable cell design in which the flow is solely provided by capillarity and all redox

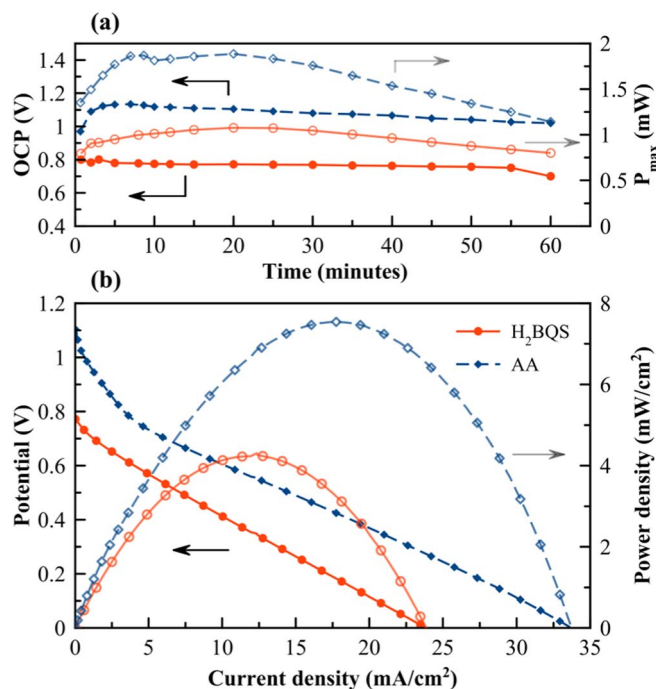


Figure 9. Discharge results for a disposable capillary flow cell device using the selected biodegradable reactant chemistries: a) open circuit potential and maximum power output measured over the range of one hour; and b) normalized cell polarization and power density curves measured at the time of peak power output.

species and supporting electrolytes are stored in the solid phase within the device. The concentration of OA is adjusted to 0.5 M in order to match the downstream neutralization requirement of the supporting electrolytes, since OA is a diprotic acid that can donate two protons per molecule. Therefore, 1 M KOH and 0.5 M OA can neutralize into neutral or near neutral conditions downstream after operation, and allow safe disposal. In this case, the cell contains 5.4 mg of pBQ and 22.5 mg of OA in the positive electrode compartment and 28 mg of KOH and either 11.4 mg of H₂BQS or 8.8 mg of AA in the negative electrode compartment. These masses are chosen to match the molar concentrations of active species and supporting electrolytes used in the previous section, for a total 1 mL of liquid (0.5 mL for each electrode), and are balanced for both downstream neutralization and the overall electrochemical reaction stoichiometry. Upon activation by the addition of 1 mL of DI-H₂O, the OCP of the cell is monitored for one hour as shown in Fig. 9a. It is shown that in the two cases of AA and H₂BQS, the capillary flow cell can hold the open circuit cell voltages of 1.1 V and 0.8 V respectively for more than one hour. This represents the functional time window of the device during which power can be generated and demonstrates that mixing of the two half-cell reactants progresses at a very slow pace despite their entry into a common absorbent pad. The initial progressive rise in the measured cell OCP curves is likely due to the transient nature of the device operation wherein the concentrations are not controlled and are based on the rates of species dissolution from the solid phase. Similarly, the slow decay in OCP after this initial period indicates the rate of reactant mixing in the device. The operational time of the battery is however expected to be reduced if the cell is continuously connected to an external load and will generate current until the redox species are fully discharged. Cell polarization curves are also measured at different instants during the functional time of the device. The maximum power output measured at different instants during the polarization curve measurements is shown in Fig. 9a, where it is seen that the cell with AA in the negative half-cell can provide a maximum power output of 1.9 mW (7.6 mW/cm²) compared to 1.1 mW for the H₂BQS case. The full polarization and power density curves

after 20 minutes of water activation, corresponding to the instant of maximum power, are given in Fig. 9b for both H₂BQS and AA cases. At the low current density range (< 4 mA/cm²), the AA case shows higher activation over-potential when compared to the H₂BQS case, which confirms the slower kinetics in agreement with the findings in the previous sections. Despite this limitation, the cell with AA anode considerably outperforms the respective cell with H₂BQS anode at medium to high discharge current densities, reaching its peak power density of 7.6 mW/cm² at a current density of 18 mA/cm² (4.5 mA) compared to 4.4 mW/cm² at 12 mA/cm² (3 mA) for the latter case, which reflects the previous findings with the microfluidic cell. This discharge performance is considered sufficient to run a small measuring device or enable a wide range of other electronic components such as microprocessors, communication modules or displays.

While the data obtained with the microfluidic analytical cell show potential for higher power density outputs, the lower performance level obtained with the capillary flow cell can be attributed to the variation in the operating flow rates, internal cell resistance and the transient nature of reactant dissolution and transport. The present capillary flow cell prototype has not yet been optimized and further improvements are possible for the design and fluidics of the absorbent pads. Nonetheless, it is important to stress that a practical performance level has been achieved, meeting the requirements of single-use disposable applications. The results of this study thus provide the departing point for a new generation of biodegradable and sustainable power sources that minimize waste from conception and design. While the present work focuses on suitable organic species available off-the-shelf, the battery concept is not restricted to the use of these species. For example, many other suitable quinone species are commercially available and many more are under development by various groups. Custom species with tailored characteristics of solubility, redox state, redox potential and rate of dissolution can be synthesized by functionalizing quinone compounds.⁵² This approach can enable higher cell voltages, power outputs and energy densities. While the present work demonstrated the use of oxalic acid and citric acid as organic supporting electrolytes, other inorganic acids may also be utilized such as phosphoric acid which exists as a solid powder in its pure form. This makes it suitable for storage and would ultimately form benign phosphate salts after device neutralization which are used as food additives or fertilizers. The present work also demonstrated the use of other organic redox compounds such as ascorbic acid. Various inorganic salts could also be used for this concept, which may enable high solubility as well as other environmental benefits. For example, Fe³⁺ is abundant and has a standard potential slightly higher than the pBQ used in this work (0.77 V vs. SHE)⁶⁰ and a relatively high aqueous solubility. Therefore, ferric salts of nitrates, sulfates or phosphates, that are known to enrich soils, may lead to a battery that could even add value to the soil or water in which it is disposed of.

Conclusions

This study reviewed the general requirements regarding solubility, biodegradability, storability in correct redox state, redox potential and kinetics of the reactant chemistries for biodegradable capillary flow batteries for single-use disposable applications. Mixed-media operation suitable for membrane-less cells was leveraged to allow direct use of commercially available organic compounds such as quinones by using an alkaline negative half-cell and an acidic positive half-cell with the added benefit of downstream neutralization for safe disposal. Prospective redox chemistries for each half-cell were systematically assessed by ex-situ measurements of solubility, redox potential and kinetics and in-situ discharge performance in a microfluidic co-laminar flow cell with flow through porous electrodes. An all-quinone cell comprising of LQ and pBQ for the negative and positive half-cells, respectively was shown to have a high open circuit potential of 1.24 V but was deemed unsuitable for disposable cells due to stability issues. The overall most effective chemistry identified for disposable cells was based on either ascorbic acid or H₂BQS in KOH and pBQ in oxalic acid at the negative and positive electrodes, respectively.

The coupling of these two half-cells in a microfluidic cell resulted in an open circuit cell voltage of 0.92 V and a peak power density of 42 mW/cm². Finally, the selected half-cell chemistries were demonstrated in a disposable capillary flow cell with all redox reactant and supporting electrolyte species stored in the solid phase on the device and dissolved upon water activation. The cell was shown to maintain high open circuit voltage for more than 1 hour and to achieve more than 2 mW peak power output at 4.5 mA which would be sufficient to power a wide variety of portable electronic components such as small signal processors, communication modules or displays. The results provide the departing point for a new generation of biodegradable and sustainable primary batteries that minimize waste from conception and design.

Acknowledgments

The funding for this research provided by the Electrochemical Society (ECS) and the Bill & Melinda Gates Foundation, as part of the Science for Solving Society's Problems Challenge (S³P), is highly appreciated. Additional funding from Natural Sciences and Engineering Research Council of Canada (NSERC), Canada Foundation for Innovation (CFI) and British Columbia Knowledge Development Fund (BCKDF) is appreciated. J.P.E. thanks support from Marie Curie International Outgoing Fellowship (APPOCS) within the 7th European Community Framework. N. S. thank financial support received from ERC Consolidator grant (SUPERCCELL). E.K. acknowledges support from the Canada Research Chairs program.

References

- D. Lisbona and T. Snee, *Process Saf. Environ. Prot.*, **89**, 434 (2011).
- L. Moreno-Merino, M. E. Jiménez-Hernández, A. de la Losa, and V. Huerta-Muñoz, *Sci. Total Environ.*, **526**, 187 (2015).
- T. C. Wanger, *Conserv. Lett.*, **4**, 202 (2011).
- D. Larcher and J. -M. Tarascon, *Nat. Chem.*, **7**, 19 (2015).
- M. Sun, X. Yang, D. Huisingh, R. Wang, and Y. Wang, *J. Clean. Prod.*, **107**, 775 (2015).
- W. McDonough and M. Braungart, *Cradle to cradle: Remaking the way we make things*, (2002).
- Y. J. Kim, W. Wu, S. -E. Chun, J. F. Whitacre, and C. J. Bettinger, *Proc. Natl. Acad. Sci. U. S. A.*, **110**, 20912 (2013).
- L. Yin, X. Huang, H. Xu, Y. Zhang, J. Lam, J. Cheng, and J. A. Rogers, *Adv. Mater.*, **26**, 3879 (2014).
- M. Tsang, A. Armutlulu, A. W. Martinez, S. A. B. Allen, and M. G. Allen, *Microsystems Nanoeng.*, **1**, 15024 (2015).
- P. Nadeau, D. El-Damak, D. Gletting, Y. L. Kong, S. Mo, C. Cleveland, L. Booth, N. Roxhed, R. Langer, A. P. Chandrakasan, and G. Traverso, *Nat. Biomed. Eng.*, **1**, 0022 (2017).
- C. Chen, Y. Zhang, Y. Li, J. Dai, J. Song, Y. Yao, Y. Gong, I. Kierzewski, J. Xie, and L. Hu, *Energy Environ. Sci.*, **10**, 538 (2017).
- J. Maya-Cornejo, E. Ortiz-Ortega, L. Alvarez-Contreras, N. Arjona, M. Guerra-Balcázar, J. Ledesma-García, and L. G. Arriaga, *Chem. Commun.*, **51**, 2536 (2015).
- C. A. López-Rico, J. Galindo-De-La-Rosa, E. Ortiz-Ortega, L. Álvarez-Contreras, J. Ledesma-García, M. Guerra-Balcázar, L. G. Arriaga, and N. Arjona, *Electrochim. Acta*, **207**, 164 (2016).
- E. Ortiz-Ortega, M. -A. Goulet, J. W. Lee, M. Guerra-Balcázar, N. Arjona, E. Kjeang, J. Ledesma-García, and L. G. Arriaga, *Lab Chip*, **14**, 4596 (2014).
- J. P. Esquivel, F. J. Del Campo, J. L. Gómez de la Fuente, S. Rojas, and N. Sabaté, *Energy Environ. Sci.*, **7**, 1744 (2014).
- S. O. García, Y. V. Ulyanova, R. Figueroa-Teran, K. H. Bhatt, S. Singhal, and P. Atanassov, *ECS J. Solid State Sci. Technol.*, **5**, M3075 (2016).
- M. J. González-Guerrero, J. P. Esquivel, D. Sánchez-Molas, P. Godignon, F. X. Muñoz, F. J. del Campo, F. Giroud, S. D. Minter, and N. Sabaté, *Lab Chip*, **13**, 2972 (2013).
- Z. Zhu, T. Kin Tam, F. Sun, C. You, and Y. -H. Percival Zhang, *Nat. Commun.*, **5**, 877 (2014).
- M. J. González-Guerrero, F. J. del Campo, J. P. Esquivel, D. Leech, and N. Sabaté, *Biosens. Bioelectron.*, **90**, 475 (2017).
- J. W. Lee and E. Kjeang, *Biomicrofluidics*, **4**, 041301 (2010).
- R. Ferrigno, A. D. Stroock, T. D. Clark, M. Mayer, and G. M. Whitesides, *J. Am. Chem. Soc.*, **124**, 12930 (2002).
- E. R. Choban, L. J. Markoski, A. Wiecekowsky, and P. J. A. Kenis, *J. Power Sources*, **128**, 54 (2004).
- M. A. Goulet and E. Kjeang, *J. Power Sources*, **260**, 186 (2014).
- X. Lu, J. Xuan, D. Y. C. Leung, H. Zou, J. Li, H. Wang, and H. Wang, *J. Power Sources*, **314**, 76 (2016).
- E. Kjeang, R. Michel, D. A. Harrington, N. Djilali, and D. Sinton, *J. Am. Chem. Soc.*, **130**, 4000 (2008).
- M. -A. Goulet, O. A. Ibrahim, W. H. J. Kim, and E. Kjeang, *J. Power Sources*, **339**, 80 (2017).
- T. H. Nguyen, A. Fraiwan, and S. Choi, *Biosens. Bioelectron.*, **54**, 640 (2014).
- S. Choi, *Biotechnol. Adv.*, **34**, 321 (2016).
- N. K. Thom, K. Yeung, M. B. Pillion, and S. T. Phillips, *Lab Chip*, **12**, 1768 (2012).
- S. -S. Chen, C. -W. Hu, I. -F. Yu, Y. -C. Liao, and J. -T. Yang, *Lab Chip*, **14**, 2124 (2014).
- Y. Koo, J. Sankar, and Y. Yun, *Biomicrofluidics*, **8**, 054104 (2014).
- A. Zebda, L. Renaud, M. Cretin, F. Pichot, C. Innocent, R. Ferrigno, and S. Tingry, *Electrochim. Commun.*, **11**, 592 (2009).
- M. J. González-Guerrero, F. J. del Campo, J. P. Esquivel, F. Giroud, S. D. Minter, and N. Sabaté, *J. Power Sources*, **326**, 410 (2016).
- A. Fraiwan, H. Lee, and S. Choi, *IEEE Sens. J.*, **14**, 3385 (2014).
- A. Fraiwan and S. Choi, *Phys. Chem. Chem. Phys.*, **16**, 26288 (2014).
- C. Fischer, A. Fraiwan, and S. Choi, *Biosens. Bioelectron.*, **79**, 193 (2016).
- H. Lee and S. Choi, *Nano Energy*, **15**, 549 (2015).
- Z. Song, T. Ma, R. Tang, Q. Cheng, X. Wang, D. Krishnaraju, R. Panat, C. K. Chan, H. Yu, and H. Jiang, *Nat. Commun.*, **5**, 273 (2014).
- Z. Song, X. Wang, C. Lv, Y. An, M. Liang, T. Ma, D. He, Y. -J. Zheng, S. -Q. Huang, H. Yu, and H. Jiang, *Sci. Rep.*, **5**, 10988 (2015).
- K. K. Fu, Z. Wang, C. Yan, Z. Liu, Y. Yao, J. Dai, E. Hitz, Y. Wang, W. Luo, Y. Chen, M. Kim, and L. Hu, *Adv. Energy Mater.*, **6**, 1502496 (2016).
- J. P. Esquivel, P. Alday, O. A. Ibrahim, B. Fernandez, E. Kjeang, and N. Sabaté, *Adv. Energy Mater.*, **Accepted**, 1700275 (2017).
- O. A. Ibrahim, M. A. Goulet, and E. Kjeang, *Electrochim. Acta*, **187**, 277 (2016).
- O. A. Ibrahim, M. -A. Goulet, and E. Kjeang, *J. Electrochem. Soc.*, **162**, F639 (2015).
- G. L. Soloveichik, *Chem. Rev.*, **115**, 11533 (2015).
- J. Marschewski, L. Brenner, N. Ebejer, P. Ruch, B. Michel, D. Poulidakos, X. Li, Y. -B. Zhang, J. Jiang, O. M. Yaghi, and E. N. Wang, *Energy Environ. Sci.*, **10**, 780 (2017).
- J. Winsberg, T. Hagemann, T. Janoschka, M. D. Hager, and U. S. Schubert, *Angew. Chemie - Int. Ed.*, **56**, 686 (2016).
- B. Huskinson, M. P. Marshak, C. Suh, S. Er, M. R. Gerhardt, C. J. Galvin, X. Chen, A. Aspuru-Guzik, R. G. Gordon, and M. J. Aziz, *Nature*, **505**, 195 (2014).
- B. Yang, L. Hooper-Burkhardt, F. Wang, G. K. Surya Prakash, and S. R. Narayanan, *J. Electrochem. Soc.*, **161**, A1371 (2014).
- K. Lin, Q. Chen, M. R. Gerhardt, L. Tong, S. B. Kim, L. Eisenach, A. W. Valle, D. Hardee, R. G. Gordon, M. J. Aziz, and M. P. Marshak, *Science*, **349**, 1529 (2015).
- K. Wedege, E. Dražević, D. Konya, and A. Bentien, *Sci. Rep.*, **6**, 39101 (2016).
- J. B. Conant and L. F. Fieser, *J. Am. Chem. Soc.*, **46**, 1858 (1924).
- S. Er, C. Suh, M. P. Marshak, and A. Aspuru-Guzik, *Chem. Sci.*, **6**, 845 (2015).
- F. J. Enguita and A. L. Leitão, *Biomed Res. Int.*, **2013**, 1 (2013).
- US EPA, *Estim. Programs Interface Suite Microsoft Wind. (EPISuite)*, v 4.11 (2016).
- Y. Xu, Y. H. Wen, J. Cheng, G. P. Cao, and Y. S. Yang, *Electrochim. Acta*, **55**, 715 (2010).
- G. Atkinson and W. McBryde, *Can. J. Chem.*, **35**, 477 (1957).
- B. Yang, L. Hooper-Burkhardt, S. Krishnamoorthy, A. Murali, G. K. S. Prakash, and S. R. Narayanan, *J. Electrochem. Soc.*, **163**, A1442 (2016).
- P. S. Guin, S. Das, and P. C. Mandal, *Int. J. Electrochem.*, **2011**, 1 (2011).
- M. Quan, D. Sanchez, M. F. Wasylikiw, and D. K. Smith, *J. Am. Chem. Soc.*, **129**, 12847 (2007).
- W. M. Haynes, *CRC Handbook of Chemistry and Physics*, 94th Edition, (2013).
- M. Rafiee and D. Nematollahi, *Electroanalysis*, **19**, 1382 (2007).
- J. Du, J. J. Cullen, and G. R. Buettner, *Biochim. Biophys. Acta - Rev. Cancer*, **1826**, 443 (2012).
- N. Fujiwara, S. Yamazaki, Z. Siroma, T. Ioroi, and K. Yasuda, *J. Power Sources*, **167**, 32 (2007).
- C. Giacomelli, K. Kless, D. Galato, F. S. Miranda, and A. Spinelli, *J. Braz. Chem. Soc.*, **13**, 332 (2002).
- S. I. Bailey and I. M. Ritchie, *Electrochim. Acta*, **30**, 3 (1985).
- R. Gulaboski, I. Bogeski, V. Mirčeski, S. Saul, B. Pasička, H. H. Haeri, M. Stefova, J. P. Stanoeva, S. Mitrev, M. Hoth, and R. Kappl, *Sci. Rep.*, **3**, 2841 (2013).
- C. A. Martínez-Huitle, S. Ferro, and A. De Battisti, *Electrochim. Acta*, **49**, 4027 (2004).

Appendix E.

A Metal-Free and Biotically Degradable Battery for Portable Single-Use Applications

An open access article [125] reproduced with permission from Wiley and Sons

A Metal-Free and Biotically Degradable Battery for Portable Single-Use Applications

Juan Pablo Esquivel,* Perla Alday, Omar A. Ibrahim, Belén Fernández, Erik Kjeang, and Neus Sabaté

This article presents a new approach for environmentally benign, low-cost batteries intended for single-use applications. The proposed battery is designed and fabricated using exclusively organic materials such as cellulose, carbon, and wax and features an integrated quinone-based redox chemistry to generate electricity within a compact form factor. This primary capillary flow battery is activated by the addition of a liquid sample and has shown continuous operation up to 100 min with an output voltage that can be conveniently scaled to match the voltage needs of portable electronic devices (1.5–3.0 V). Once depleted, the battery can be disposed of without the need for any recycling facility, as its components are nontoxic and shown to be biotically degradable in a standardized test. The practical utility of the battery is demonstrated by direct substitution of a lithium ion coin cell in a diagnostic application.

waste electrical and electronic equipment (WEEE) generated after their disposal. The large quantities of WEEE and the wide variety of materials they often contain (ferrous metals, nonferrous metals, noble-metal, chemicals, glass, and plastics) have raised a serious alarm on their potential adverse health and environmental consequences when incorrectly disposed of. Moreover, this waste can be regarded as a resource of valuable materials (e.g., Au, Pt, Li) that if not recovered, has to be extracted again, resulting in natural resource depletion and environmental degradation. Recovering these metals and satisfying the demand for cheap second-hand equipment has become profitable

1. Introduction

The use of electronic devices has experienced a tremendous rise in the past three decades and consequently, so has the rate of

business in emerging economies, which has turned Asia (in particular, China and India) and Africa into recipients of 90% of globally exported WEEE.^[1] However, dismantling procedures are often carried out in inappropriate infrastructures with discarded components being openly incinerated and disposed of in unlined landfills that lack monitoring of leachate recovery systems of any kind. Due to their content of heavy metals, batteries are one of the most hazardous components of e-waste. For this reason, many Organization of Economic Cooperation and Development (OECD) countries have established regulations on the maximum permitted content of certain metals such as mercury or cadmium and the mandatory recycling of spent batteries.^[2]

Dr. J. P. Esquivel, P. Alday, Prof. N. Sabaté
Instituto de Microelectrónica de Barcelona
IMB-CNM (CSIC)
C/ del Tíllers, Campus Universitat Autònoma de Barcelona (UAB)
08193 Bellaterra, Barcelona, Spain
E-mail: juanpablo.esquivel@csic.es


Dr. J. P. Esquivel
Department of Bioengineering
University of Washington
Seattle, WA 98195, USA

O. A. Ibrahim, Prof. E. Kjeang
Fuel Cell Research Lab (FCReL)
School of Mechatronic Systems Engineering
Simon Fraser University
Surrey BC V3T 0A3, Canada

Dr. B. Fernández
GIRO Joint Research Unit IRTA-UPC
Torre Marimon
08140 Caldes de Montbui, Barcelona, Spain

Prof. N. Sabaté
Catalan Institution for Research and Advanced Studies (ICREA)
Passeig Lluís Companys 23, 08010 Barcelona, Spain

This is an open access article under the terms of the Creative Commons Attribution-NonCommercial License, which permits use, distribution and reproduction in any medium, provided the original work is properly cited and is not used for commercial purposes.

 The ORCID identification number(s) for the author(s) of this article can be found under <http://dx.doi.org/10.1002/aenm.201700275>.

DOI: 10.1002/aenm.201700275

Lithium-ion batteries are today the most predominant energy sources in portable applications because of their high energy density, low sensitivity to temperature variations, and no memory effect when recharging.^[3] However, they are starting to raise important concerns related to the relatively low abundance of lithium metal—which is likely to increase the environmental impact of its extraction methods—and the large amount of CO₂ generated during battery manufacturing. In fact, its life cycle assessment determines that the use of lithium is only justified in rechargeable applications beyond hundreds of cycles, which clearly prohibits its use as primary batteries.^[3,4] Despite all these worrying facts, battery recycling is far from meeting the goals set in developed regions (less than 30% of sold batteries are collected for proper recycling) and it is practically inexistent in low resource settings.^[5] The most alarming issue is that consumption of batteries is expected to rise significantly in the following years due to the growth of small-sized portable appliances in the Information and Communications Technology

(ICT) sector. Generally, these devices are powered by primary cells that are to be disposed of after depletion. This means a future rise in the number of batteries that will be discarded in an uncontrolled way—and almost fully charged in case of applications with short duration such as single use point-of-care devices. In view of this perspective, tightened environmental laws and increased provisions for recycling infrastructure (primary battery collection and processing) are urgently needed. However, this approach is not conducive in the short-term in developing economies due to the high cost and complexity of implementation. Indeed, this may not be environmentally sustainable even for developed economies; building up costly and energy-consuming recycling plants to take care of the batteries generated along the linear “take–make–dispose” path followed traditionally since the early days of industrialization entails a huge waste of natural resources, energy, and labor. In this sense, the approach of the circular economy—which aims to minimize, track, and eliminate the use of toxic chemicals and waste through careful device design and conception—appears to be a promising way to meet the technological needs of current society without compromising future generations.

In this regard, green electronics is an emerging area of research aimed at creating new methods and processes for the production of environmentally friendly electronics. This area is completely aligned with the circular economy principles as it specifically targets components that do not cause exhaustion of natural elements, do not require large amounts of energy to be produced, do not produce toxic by-products during their manufacture, and feature biodegradability in mild degradation conditions at the end of their life cycle. Such components would thus bypass the need for complex recycling structures and associated investments.^[6]

Despite their key role in electronic devices, very few battery prototypes able to meet the requirements of green electronics have been developed to date. For *in vivo* applications, relevant innovative concepts have been presented, e.g., Kim et al. reported an edible water activated sodium battery based on melanin^[7] and Yin et al. showed the abiotic degradation of a polymer encapsulated battery that uses metals like Mg, Fe, W, and Mo as electrodes.^[8] These batteries are developed for implantable or edible applications and thus designed to be innocuous to the human body when decomposed in their primary elements in a short time after having been implanted or eaten. The rationale behind these devices is to make use of different nontoxic materials (both organic and inorganic) that once dissolved in the body, do not exceed the recommended dietary allowance. Other promising transient battery approaches for *ex vivo* applications have been recently reported. For example, Ding and Yu support the use of hydroquinone as metal-free, inexpensive redox-active organic materials for environmental-friendly, cost effective sustainable energy storage. Nevertheless, the reported battery still relies on an anode reaction based on the intercalation and deintercalation process of Li ions in graphite and a NASICON type Li-ion-conducting solid membrane LATP as separation membrane.^[9] Fu et al. reports another example of transient battery with high power density, which contains a lithium anode, a vanadium oxide cathode, and indium tin oxide as conducting material. Although these materials may present toxicity concerns for environment and human health, the article completely

neglects what would be the impact of the battery after its degradation in water under unregulated conditions (i.e., rivers, lakes, landfills, etc.).^[10] Recent works on paper fuel cells based on biocatalysts such as microbes and enzymes have opened a new alternative to sustainable power sources. However, there are still many challenges to overcome regarding their reproducibility, signal stability, and power density to meet energy requirements of portable electronics.^[11] The field of supercapacitors has also experienced relevant activity toward the use of environmentally benign fabrication processes and materials, such as cellulose and carbon.^[12] A recent article by Chen et al. reports an asymmetric supercapacitor based on wood carbon anode, a wood separation membrane, and a MnO₂/wood carbon cathode. The article shows noteworthy results as an energy storage device with high energy and power density where most of its components could be biodegraded.^[13] These examples evidence the diverse efforts in portable energy storage research toward more environmentally respectful solutions.

The present work introduces a new concept of single-use primary battery specifically made to power small electronic devices that when disposed of, breaks down into simple compounds as a result of the biotic degradative processes of microorganisms present in soils and natural water bodies. This means that unlike the previous examples of transient batteries where only some components were dissolvable in saline solutions or degraded due to self-corrosion processes, this battery has the potential to undergo complete mineralization of its chemicals to CO₂, CH₄, H₂O, and N₂, which allows the battery to effortlessly close its cycle back to nature.

The presented battery is completely built upon organic materials made of cellulose, carbon paper, beeswax, and organic redox species and can be fabricated by affordable methods with low energy consumption. Once activated, the battery is set to operate for a certain amount of time—up to 2 h—and then be disposed of in an organic waste container or even discarded in the field, where it will biotically degrade by bacteria with a minimal environmental impact.

In order to show its outstanding capabilities, six different research challenges pertaining to battery development are addressed in this work: device design, chemistry selection, battery operation, voltage scalability, practical application, and effective biotic degradation. Proposed solutions to each of these six challenges are outlined in the following sections.

2. Results

2.1. Device Design

We hereby introduce the PowerPAD (Power: Portable And Disposable), a fully organic and completely biodegradable battery concept inspired by the sustainability principles of green electronics. As illustrated schematically in **Figure 1**, the PowerPAD concept^[14] represents a new class of batteries designed to operate for relatively short periods of time (from minutes to 1–2 h) to fulfill the power needs of portable applications while not requiring any specific recycling facility for its disposal. The PowerPAD design, as well as its acronym, is inspired from a traditional notepad made from a stack of paper sheets, i.e.,

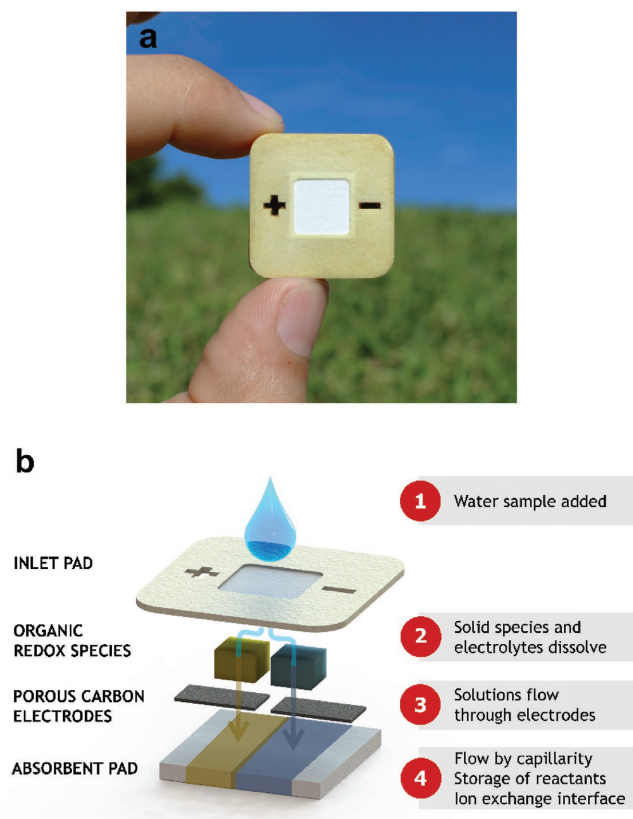


Figure 1. PowerPAD biodegradable battery: a) actual photograph and b) conceptual schematic of relevant components and working principle.

layered organic materials. The battery is thus designed using organic materials such as cellulose, carbon paper, and beeswax that can be fabricated by affordable methods with low energy consumption and layered to form an integrated device. Energy is stored in the form of water-soluble organic redox species inside the pad, representing two dormant electrochemical half-cells. The battery is activated by the addition of a liquid sample that dissolves the reactants and carries them to the electrodes by capillary flow. After electrochemical discharge of power, the device can be disposed of together with organic waste or even discarded on the ground for natural decomposition, as it comprises exclusively biodegradable materials and does not contain any metals, plastics, or harmful substances. In summary, the proposed battery function comprises three simple steps: (1) add water; (2) extract power; and (3) dispose of.

More specifically, the proposed biodegradable battery is designed as a vertical capillary flow cell. As shown in Figure 1, the device structure is composed of several patterned cellulose layers that when stacked together define the microfluidic paths of the cell and the compartments that house the electrodes and reactant compounds. In order to render the structural parts rigid and impermeable, the cellulose is impregnated with natural beeswax, which allows creating hydrophobic areas in a selective manner. The top structural cellulose layer hosts a central inlet pad able to receive an external liquid sample.

Underneath this pad, two separated small reservoirs contain the positive and negative redox species and the supporting

electrolytes originally stored in the solid state. The two electrodes made of hydrophilic porous carbon paper are placed below the respective reactant reservoirs and sandwiched between two thin layers of cellulose in order to ensure reliable capillary flow of reactants through the electrodes and into the large cellulose absorbent pad at the bottom. The outward facing surfaces of the device are sealed with a beeswax-covered cellulose layer in order to prevent liquid leakages. The electrodes are accessed via the positive and negative terminals on the top surface of the device in order to connect a load. The proposed battery is conceived as a single use power source that is activated by the addition of a small sample of liquid, such as water, urine, or saliva, on the inlet cellulose pad. When the inlet pad is saturated, water flows by capillarity to each of the reservoirs and dissolves the stored redox species and electrolytes. Once dissolved, the reactant species flow through the porous carbon electrodes toward the absorbent pad. The battery starts generating power when the two electrolytes get in contact at the absorbent pad. This pad has an important role in the device function as it establishes the capillary flow that makes the species flow through the electrodes while also providing electrolytic contact between the two electrochemical half-cells. Due to the colaminar flow established by capillarity in the paper sheets, the two reactant streams are effectively separated after activation of the battery and start mixing only by diffusion at their contact interface.^[15] Taking into account the diffusion coefficient of the redox species in aqueous media ($\approx 10^{-6} \text{ cm}^2 \text{ s}^{-1}$) and the distance between the electrodes (2 mm), no significant crossover of reactants is expected during the battery operation time, which ranges from minutes to a few hours. Furthermore, this time could even be extended by engineering capillary microfluidics to sustain a flow of reactants for longer times. Consequently, the proposed battery can operate effectively without an ion-conducting membrane otherwise used to separate the electrodes, which is particularly critical in the present case considering that most membranes are made from specialized polymer films that are not readily biodegradable. Furthermore, the capillary flow enables convenient integration of flow-through porous electrodes, which have been shown to deliver drastic performance improvements compared to flow-over and planar electrodes by means of high active surface area and internal mass transport rates.^[16] The provision of flow in the form of a redox capillary flow battery thus contributes three critical services that together enable the unique function of the PowerPAD: (1) activation; (2) membrane elimination; and (3) high-performing electrodes. Finally, it is noteworthy that the passive capillary flow facilitated by the device eliminates the need for an external pump otherwise required to drive the flow of electrolyte, and hence does not add any overhead or parasitic power consumption.

2.2. Chemistry Selection

In order to meet the PowerPAD requirements, the redox species used as reactants in the positive and negative half-cells should be biodegradable (preferably organic) and exist in solid form in the desired redox state at ambient conditions. They should also be soluble in water or other desired electrolytes in order to be dissolved and delivered to the electrodes during

device operation. Their electrochemical reactions should also be compatible with catalyst-free porous carbon electrodes and have fast kinetics.

Organic quinone redox species have recently captured the attention of the flow battery research community, owing to their eco-friendly, nature-inspired redox reactions with fast kinetics and low cost.^[17] These quinone compounds match the majority of the requirements for the proposed battery. However, the quinone species available commercially are not in the desired redox state for discharge, which means that an initial charging step would be required to meet the current application requirements. In order to circumvent this issue, the strategy of mixed-media electrolyte conditions is deployed, wherein an acidic positive half-cell can be combined with an alkaline negative half-cell. This operational scheme is uniquely enabled by membrane-less devices such as colaminar flow cells,^[18] in which reactant separation is “virtually” enabled by a colaminar flow interface, and the choice of media is not dictated by the membrane chemistry. In the present case, this facilitates the use of a broader range of commercially available redox chemistries for each half-cell. Furthermore, the proposed mixed-media condition with an acidic cathode and an alkaline anode offers two additional, significant benefits for the PowerPAD concept: (i) an increased Nernstian cell potential between the two electrodes,^[19] which boosts the cell performance; and (ii) an opportunity for neutralization of the electrolytes after complete mixing in the downstream absorbent pad, which supports safe disposal. Hence, a fully organic, catalyst- and membrane-free safely disposable cell chemistry can be developed by tuning the supporting electrolyte compositions in a stoichiometric balance for complete neutralization after discharge.

Oxalic acid ($C_2H_2O_4$) is accordingly selected as supporting electrolyte for the positive half-cell since it is a strong acid available in solid form that can be deposited and stored in the paper, and is an organic phytochemical present in plants and predicted to have ready biodegradability according to the US Environmental Protection Agency’s EPISuite.^[20] The solubility of $C_2H_2O_4$ in water is found to be 1 M, which is hence taken as the target concentration for the PowerPAD device. Similarly, potassium hydroxide (KOH) is selected as supporting electrolyte for the negative half-cell, as it is available in solid form for onboard storage and has high solubility and ready biodegradability prediction. A target KOH concentration of 2 M is used in order to match the 2 M protonic charge contributed by the diprotic oxalic acid for neutralization and safe disposal. As a screening approach, prospective quinone redox species that are stable in these media and available in the correct oxidation state are evaluated by linear sweep voltammetry in a conventional three-electrode electrochemical cell with various supporting electrolyte conditions. The express purpose of these measurements is to investigate the half-cell open circuit potential (OCP) and qualitatively assess the kinetics of the redox reactions on catalyst-free carbon electrodes and the effect of different supporting electrolytes.

The preliminary screening of redox chemistries identified a suitable pair of commercially available quinone species, comprising of *p*-benzoquinone (pBQ) at the positive side and hydroquinonesulfonic acid potassium salt (H_2BQS) at the negative side. These species are selected for the proof-of-concept

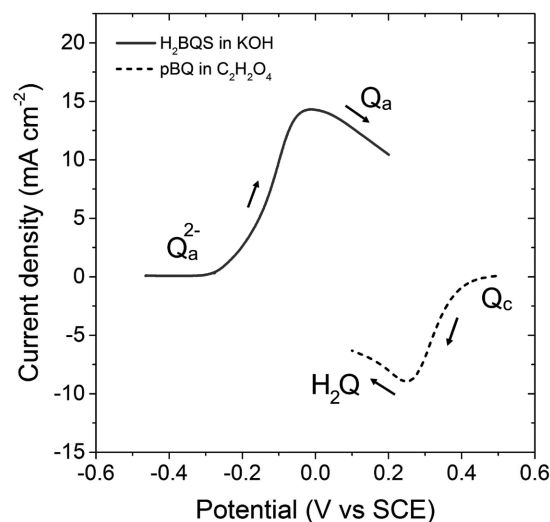


Figure 2. IR-compensated linear sweep voltammograms of the proposed all-organic redox chemistries representing oxidation of 0.2 M H_2BQS in 2 M KOH at the negative electrode and reduction of 0.2 M pBQ in 1 M $C_2H_2O_4$ at the positive electrode.

as they are the most convenient off-the-shelf forms of quinones/hydroquinones with two ketone/phenol groups. The simplicity of the compounds enables good solubility, which is desired for PowerPAD operation. In addition, benzoquinones are predicted to have ready biodegradability according to EPISuite^[20] and other published works.^[21] The electrochemical reactions of the quinone species used for this work were previously studied and shown to have reversible redox reactions.^[22] In acidic conditions, the redox reactions involve a single-step two electron two-proton process, while in alkaline conditions, the redox reactions involve two electrons process with no proton involved.^[19,23] A target concentration of 0.2 M is taken, close to the solubility limit of these species. The obtained IR-compensated voltammograms for the negative (0.2 M H_2BQS in 2 M KOH) and positive (0.2 M pBQ in 1 M $C_2H_2O_4$) half-cells are provided in **Figure 2**. The result shown is a representation of the intended discharge electrochemical reactions immediately following species dissolution during PowerPAD operation. These reactions correspond to the oxidation of deprotonated H_2BQS (BQS^{2-}) in KOH at the negative half-cell and the reduction of pBQ in $C_2H_2O_4$ at the positive half-cell. The OCPs are measured to be -0.46 and 0.49 V versus saturated calomel electrode (SCE) for the negative and positive half-cells, respectively, suggesting a possible discharge cell potential window up to ≈ 1 V for the combined cell reaction. The results also indicate rapid electrochemical kinetics for both half-cells on the pure carbon electrodes. The slightly lower peak observed for pBQ can be explained by the somewhat lower solubility found for pBQ compared to H_2BQS . Based on these findings, the proposed cell chemistry is deemed adequate for the PowerPAD application.

2.3. Battery Operation

As per the previously described PowerPAD design (Figure 1), the proposed biodegradable battery activates upon the addition

of a liquid that dissolves the reactants stored within the device in solid form. The dissolved reactants are carried by capillary flow through the electrodes, where the electrochemical reactions take place, and into an absorbent pad at the bottom of the device. The battery operation is thus a transient process that starts upon reactant dissolution and continues for a period of time until the reactants are consumed or mixed internally, thereby causing the output voltage to drop below a certain cut-off value. Provided the passive nature of the device operation once liquid is added, the flow characteristics are fundamentally controlled by the geometrical features and surface properties of the internal materials, while the reactant concentrations are controlled by the relative dissolution rates. In order to decouple these effects, the device is first characterized with reactants in premixed solutions at the defined target concentrations based on their solubility. This approach is used to demonstrate the overall flow battery operation and to evaluate the impact of the absorbent pad dimensions on the battery performance. This pad plays an important role, as it drives the capillary flow, defines the ion-exchange interface, and serves as storage of dissolved reactants. Four different absorbent pads with varying thickness (h) are tested (Figure S1, Supporting Information).

The total volumes of solutions added to the batteries for each measurement are 170, 390, 740, and 1440 μL for absorbent pad thicknesses of $h/2$, h , $2h$, and $4h$, respectively, in order to reach saturation of the internal components. The open circuit voltage (OCV) of the batteries is continuously measured after adding the solutions, reaching a pseudo-steady state value of 0.75 ± 0.05 V in all cases. Polarization curves for battery discharge are measured once the solutions are completely absorbed in the absorbent pad, with results shown in Figure 3. It is observed that the maximum power delivered by the battery increases with the absorbent pad thickness, reaching a maximum value of 1.7 ± 0.2 mW with the thickest pad ($4h$).

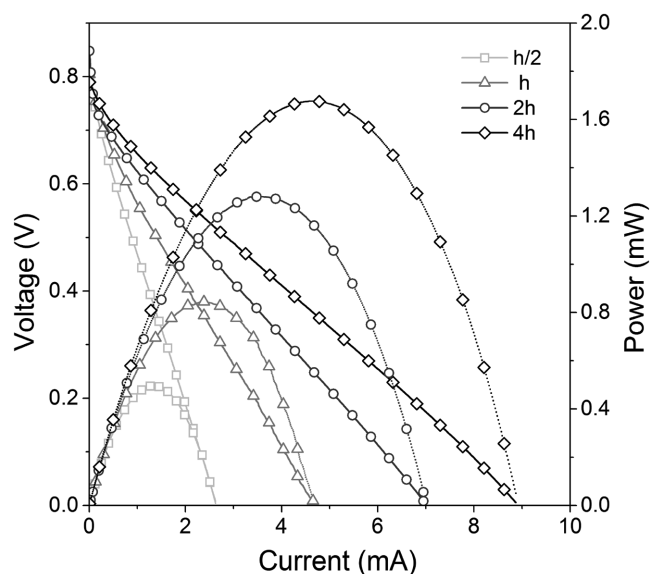


Figure 3. Discharge polarization curves of biodegradable redox capillary flow battery prototypes with four different absorbent pad thicknesses (as indicated; $n \geq 3$) supplied with premixed solutions of 0.2 M H_2BQS in 2 M KOH and 0.2 M pBQ in 1 M $\text{C}_2\text{H}_2\text{O}_4$ at the negative and positive electrodes, respectively, at room temperature.

Based on the geometrical electrode area of 0.25 cm^2 , the battery yields a maximum power density of $6.8 \pm 0.5 \text{ mW cm}^{-2}$ at a current density of 18.9 mA cm^{-2} , which is comparable to the power densities of large-scale redox flow batteries with all-quinone chemistry^[17a] and at least an order of magnitude higher than any biodegradable battery reported so far.^[7,8] The significant rise in power output obtained by increasing the absorbent pad thickness is primarily attributed to the reduced internal cell resistance associated with the increased cross-sectional area for ion conduction in the pad. This can be qualitatively observed by the changes in the linear slope of the polarization curves as the pad thickness is increased.

Next, continuous battery operation is characterized by measuring discharge curves for different external loads (0.5, 1, and 2 k Ω). The battery cut-off voltage is set to 0.5 V, representing two-thirds of the original OCV. Figure 4 shows the discharging curves obtained with the four different absorbent pad thicknesses. As expected, batteries operated at the lowest load (500 Ω) delivered higher power values (0.50–0.85 mW) but for shorter service times (2–13 min), while batteries working under the highest load (2 k Ω) delivered lower power outputs (0.12–0.25 mW) for longer operation times (15–85 min). For any given load, the batteries with thicker absorbent pad show better performance not only in terms of delivered power but also in operation times. The latter result is attributed to the larger amount of electroactive species stored in the pad, which enlarges the capacity of the device. The output capacity achieved with the batteries with absorbent pad thickness of $4h$ operated under 2 k Ω load reached 0.42 mAh (Figure 4), which considerably exceeds the measured capacities of the other battery designs.

The complete, integrated battery device is then tested with redox species and electrolytes stored internally in solid form and dissolved dynamically during operation upon the addition of water on the inlet pad. For comparative purposes, the amounts of liquid (volume) and stored reactants (moles) used in these experiments are identical to those used previously in the premixed solutions for each of the four different absorbent pad thicknesses. Given that the operational nature of the device is inherently transient, its performance is evaluated solely during continuous operation in the form of complete discharge runs until the cut-off voltage is reached. The obtained discharging curves under a fixed external load of 2 k Ω are provided in Figure 5.

Overall, the results indicate that the batteries with internally stored reactants have a similar response to those operated with premixed solutions. In most cases, the batteries with internal storage initially deliver lower voltages but sustain the power output for longer times (up to 100 min). This is reasonable considering the dynamic dissolution of reactants, which is not instantaneous and rather leads to a gradual ramp in concentration of reactants flowing through the porous electrodes as a function of time. The close proximity of storage and reaction sites allowed a gradual release that counteracted the diffusive mass transport limitations during battery discharge and improved the performance at high run-times.

The high-capacity pad configuration combined with internal reactant storage provides a particularly effective solution with performance and capacity that exceed those of the premixed

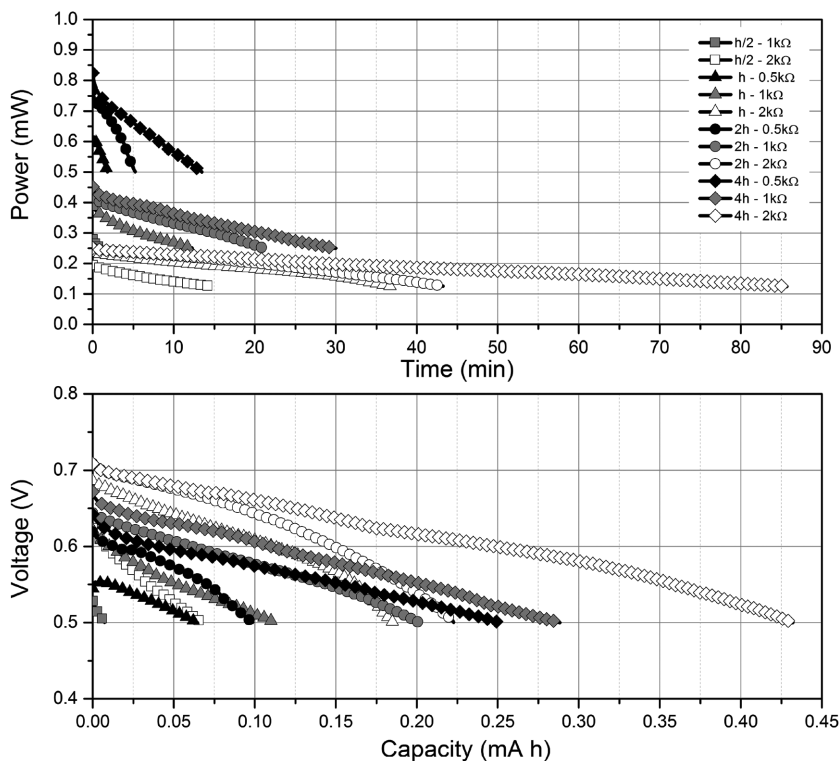


Figure 4. Continuously measured discharge curves of the biodegradable primary battery prototypes with four different absorbent pad thicknesses subjected to fixed external loads (as indicated; $n = 3$) and a cut-off voltage of 0.5 V, using premixed solutions of 0.2 M H_2BQS in 2 M KOH and 0.2 M pBQ in 1 M $\text{C}_2\text{H}_2\text{O}_4$ at the negative and positive electrodes, respectively, at room temperature.

reactant experiment. The operational energy density of the prototype device, based on the electrical energy generated from the discharge data in Figure 5 normalized by the mass of the stored reactants, is estimated to be 32 Wh kg^{-1} . This value compares favorably to other recently reported biodegradable batteries,^[7,8] albeit further improvements are needed to reach the level of conventional primary batteries such as Li-ion batteries. An important advantage of the present device configuration, in terms of energy density, is that the reactants are stored in the dry, solid state. Compared to an equivalent redox flow battery with the same reactants stored in liquid electrolytes, the operational energy density is $\approx 7\times$ higher. This feature is particularly important for the portable applications intended for the battery.

Figure S2 (Supporting Information) shows the Coulombic electroactive material utilization calculated from the discharge curves of the battery prototypes in Figure 5 as the fraction of active species converted by the battery during discharge until the cut-off voltage (in this case 0.5 V) is reached. The batteries with an intermediate absorbent pad thickness operated under a high load show the highest active material utilization among the tested conditions. Interestingly, under these conditions, the device with internally stored reactants achieves a higher utilization (13.3%) than the corresponding device supplied with premixed reactant solutions (8.9%), which could be due to reactions already taking place in the dissolved active species before coming into the battery. This indicates yet another advantage of the proposed PowerPAD flow battery configuration with

onboard reactant storage in terms of reactant utilization, although further optimization is required to fully exploit its potential in this regard.

2.4. Voltage Scalability

Most commonly used electronic applications require power delivery at higher voltage ($\approx 2.0\text{--}3.0 \text{ V}$) than that produced by a single-cell battery such as the PowerPAD cell reported above. One of the strategies to obtain a higher output voltage from a battery is to stack several cells in series, which is the strategy selected here in order to demonstrate scalability. For the present PowerPAD device configuration, it is necessary to reduce the width of the absorbent pad (w) in order to increase the number of cells within the same device footprint (Figure S1, Supporting Information). In addition, by splitting the absorbent pads, the cells within the stack are isolated electrolytically, which is practical in order to minimize internal shunt currents and losses occurring in serial stacks with electrolytic connection.^[24] Single cells with different absorbent pad widths are hence analyzed as a first step in order to explore the scalability of the PowerPAD concept. Figure S3 (Supporting Information) shows the internal layers of the batteries and

Figure S4 (Supporting Information) depicts the electrode configurations in more detail. For comparative purposes, the absorbent pad volume is kept constant by increasing the thickness of the pad proportionally to the reduction in width (Figure S5, Supporting Information). Figure S6 (Supporting Information) shows the average polarization curves obtained for single cell batteries with $1h\text{-}1w$, $2h\text{-}w/2$, and $4h\text{-}w/4$ absorbent pad dimensions of fixed volume supplied with premixed reactant solutions. All devices show good performance with similar overall characteristics. Interestingly, however, the devices with the lowest absorbent pad width achieve the highest performance ($1.2 \pm 0.1 \text{ mW}$ peak power), which is attributed to the greater absorbent pad thickness.

Next, batteries with absorbent pad dimensions of $2h\text{-}w/2$ are used to assemble a 2-cell stack with a nominal output voltage of 1.5 V. In addition, a 4-cell stack with absorbent pad dimensions of $4h\text{-}w/4$ is developed to provide a nominal output voltage of 3.0 V. The multicell stacks use the same footprint as the single cell device ($26 \text{ mm} \times 26 \text{ mm}$). Each stack features two or four pairs of reactant compartments placed above the corresponding electrodes. The individual cells are connected internally in series and share a single inlet pad such that they can be simultaneously activated by a single shot of water, but use separate absorbent pads for voltage scalability. The assembled battery stack prototypes are shown in Figure 6a along with measured polarization curves in Figure 6b. The 2-cell and 4-cell stacks are observed to reach 1.5 ± 0.2 and $3.0 \pm 0.2 \text{ V}$ open circuit

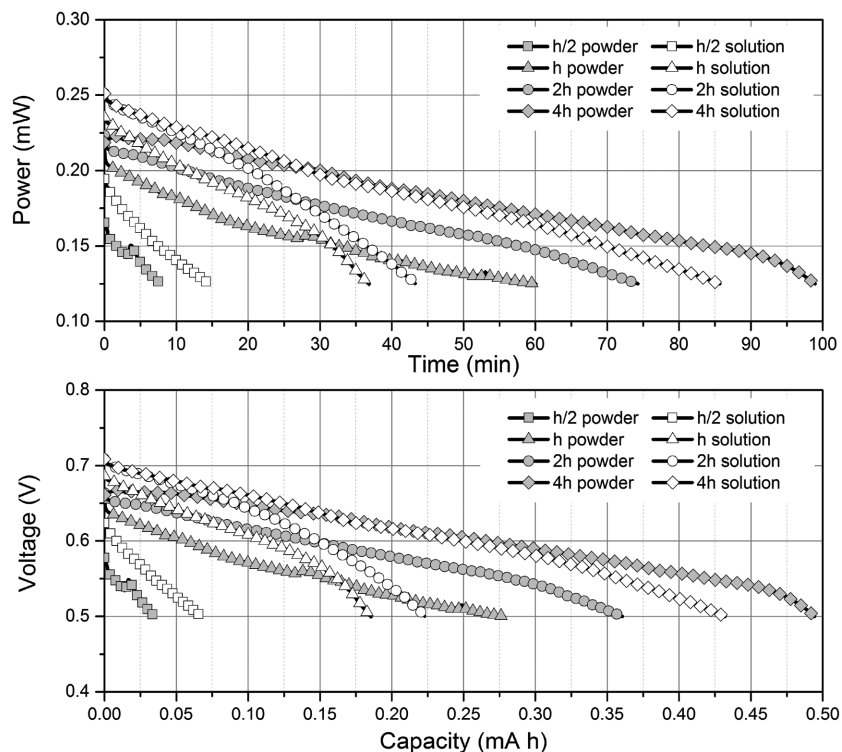


Figure 5. Discharge curves of integrated biodegradable primary batteries activated with water measured at room temperature for various absorbent pad thicknesses and external loads with a cut-off voltage of 0.5 V (as indicated; $n = 3$). The battery prototypes contained internal storage of redox species and electrolytes in the solid state that dissolved and flowed by capillarity upon the addition of water at the inlet pad.

voltage, respectively, as intended by design. Similarly, the two stacks produce a maximum power output of 1.5 ± 0.1 and 2.8 ± 0.1 mW, respectively, close to the optimal doubling and quadrupling of the single cell performance.

2.5. Practical Application

As a proof-of-concept of the utility of the PowerPAD for practical, real-world applications, the 4-cell stack is demonstrated

as the sole power source for a portable water-monitoring instrument that usually runs with a 3 V Li-ion coin cell battery, which is now removed. The instrument measures temperature, conductivity, and total dissolved solids (TDS) in a water sample, which are typically relevant parameters in water sensing. For this experiment, two different samples are used: a sample of laboratory grade deionized water and a sample of natural water collected from a local river in Barcelona, Spain. The water analyzer is connected to the PowerPAD device and the detector is inserted into a beaker containing the water sample. A small volume of the same water sample to be analyzed is then added to the battery inlet pad for activation. An image of the water analyzer powered directly by the 4-cell PowerPAD stack, without any ancillary power conversion systems or components, is shown in Figure 7a. The current drawn by the water analyzer and the battery output voltage obtained for the two different water samples during the experiment are depicted in Figure 7b. It can be seen that the battery activated with the river sample yields a fairly similar open circuit than the one activated with deionized water. The measurement is successfully carried out after 30 s of battery activation. The analyzer requires an average current of ≈ 0.2 mA to continuously measure the sample and display the result on its LCD

display. Once the measurement is taken (results yielding 6 ppm TDS and $12 \mu\text{S cm}^{-1}$ for the deionized water and 424 ppm TDS and $958 \mu\text{S cm}^{-1}$ for the river water), the reading is stored by pushing a button of the instrument, which halts the sensing function and freezes the information in the display. During this phase, the current required by the analyzer decreases to $\approx 20 \mu\text{A}$. After activation, the battery voltage decreases up to 300 mV during the high current demand phase when the analyzer measures and displays the results, after which the voltage increases again to a value close to its open circuit during the

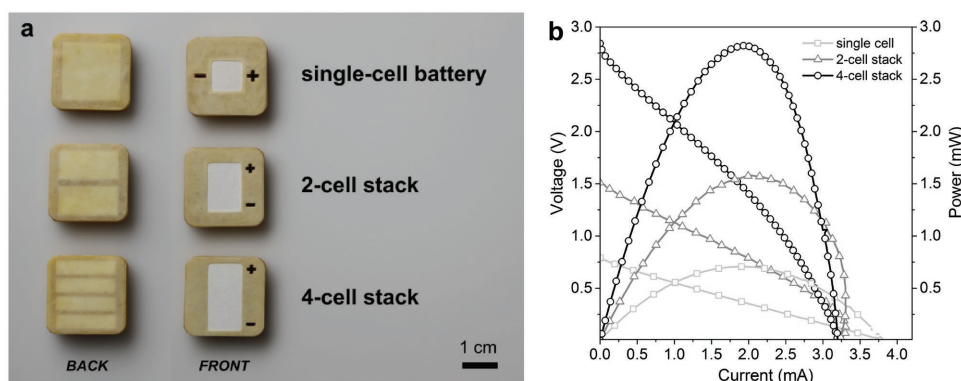


Figure 6. Scalability of the biodegradable redox capillary flow battery demonstrated by integration of one, two, and four cells within the same device footprint. a) Image of the assembled single cell, 2-cell stack, and 4-cell stack prototypes. b) Average polarization curves ($n \geq 3$) measured with premixed reactant solutions of 0.2 M H_2BQS in 2 M KOH and 0.2 M pBQ in 1 M $\text{C}_2\text{H}_2\text{O}_4$.

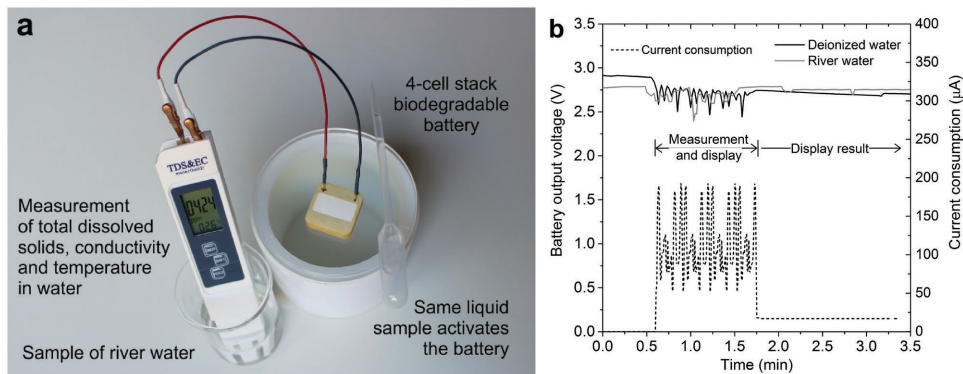


Figure 7. Practical utility of the biodegradable redox capillary flow battery demonstrated by powering a portable water monitoring instrument. a) Image of a portable water monitoring device powered directly by a biodegradable battery. The device analyzes a river water sample that is also used to activate the battery. b) Electric current drawn by the water monitoring device and output voltage of the battery during the measurement process.

secondary phase when the result is stored and displayed. Throughout this experiment, the PowerPAD unit is shown to reliably deliver the required levels of voltage and current for both operational phases of the measurement in the complete absence of supplementary electronics.

2.6. Biodegradability

The biodegradability of the PowerPAD battery, expressed as primary degradation (Dp), is determined following the guideline of the OECD Test 311^[25] that comprises recommendations of other normalized tests (ISO,^[26] ASTM,^[27] US-EPA,^[28]) and is widely used as standard test. Biodegradation is defined as a process where a material breaks down into simple compounds, such as CO₂, CH₄, H₂O, and N₂, as a result of the action of microorganisms. The assay simulates the biodegradation process under biotic anaerobic conditions of disposable devices taking into account a specific WEEE management practice. Furthermore, the low concentration of the evaluated materials in the performed test ensures that the biodegradation kinetics reflect those expected in the environment being simulated. The selection of an anaerobic test represents the worst-case scenario for the biodegradation of the batteries, as the biodegradation of cellulose-based materials is slower than that in aerobic conditions.^[29] Only 5%–10% of cellulose degrades in natural environment anaerobic conditions because in the case of landfills, water-logged soils or aquatic sediments where anaerobic or anoxic environments are expected, lower rates and longer times for biodegradation are expected because the local population of microorganisms in these natural environments may be smaller than that in the biodegradability assay with an artificially induced high population.^[30] The test monitors the inherent biodegradability in anaerobic conditions, expressed as the percentage of the initial total carbon mass of the material that is transformed into C-CO₂ and C-CH₄ after a minimum period of 60 d. The initial total carbon (TC) content that is biodegraded is calculated from periodic measurements of gas products and its evolution is plotted in a curve. **Figure 8** shows the evolution of the obtained biodegradation curves of the complete and blank batteries (with and without internally stored chemical

reactants), as well as the reference material (cellulose acetate). A clear plateau, indicating maximal degradation, is attained from day 40 for the batteries and from day 63 for the cellulose reference. It is noteworthy that the degradation rate of the batteries is even greater than that of pure cellulose, despite their larger particle size. All tested materials reach similar levels of biodegradation after 60 d, with values of 54% ± 4%, 46% ± 2%, and 52% ± 2% for the complete battery, blank battery, and cellulose, respectively, indicating that primary biodegradation of the studied materials occurred. These values are coherent with those reached in cellulose acetate based material biodegradation tests, with values between 40% and 60% TC under anaerobic conditions. Based on these results, the batteries can be considered biodegradable, and no toxic effects may be expected from the use of the present quinone-based redox chemistry. Therefore, according to the norm, these devices can be considered nonpersistent and assumed to degrade by microorganisms present in soils or water bodies in the medium to long term or in simple waste treatment plants or other environmental compartments in the short term.

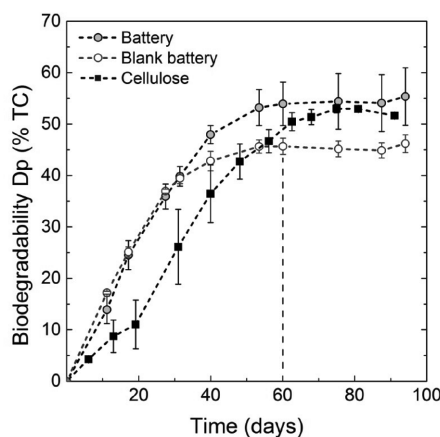


Figure 8. Battery biodegradability. Primary degradation (Dp) or biodegradability of complete batteries, blank batteries (without internally stored reactants), and reference material (cellulose acetate) in terms of initial total carbon content (%TC) that is biodegraded.

3. Discussion

The biodegradable battery prototypes presented here can operate for up to 100 min with an output voltage that can be scaled to match the voltage needs of portable electronic devices (1.5–3.0 V). Despite its working principle based on the well-known redox flow batteries, it is the first time that this principle has been explored to develop a single-use portable format with clear environmental advantages. Moreover, the technology allows further increases of both operation time and output power. It is noteworthy that even at the present laboratory stage, the prototypes have proven to readily substitute a coin cell battery in a real application, with cost of materials in the range of tens of euro/dollar cents (see Bill of Materials in Table S1 in the Supporting Information).

This new class of biodegradable, portable redox capillary flow batteries is ideally suited to provide power for a new generation of green electronic devices, and could further be explored in terms of operative design, structural materials, and chemistry. For instance, the battery half-life can be extended by engineering the absorbent pad to sustain a capillary flow of species for a longer duration. Moreover, the present battery is designed to work once and its operation is intrinsically transient. Several relevant parameters affecting its performance are time-dependent and start changing after the liquid is added; for example, the rate of dissolution of species/electrolytes, the concentration of species/electrolytes, and the flow rate of reactants. These aspects offer a rich set of parameters to further optimize in future studies.

For this proof-of-concept, beeswax was used as structural material because it is abundant, organic, inexpensive, moldable, impermeable, and mechanically robust. Furthermore, its properties can be customized for hardness and melting temperature. However, other materials such as biopolymers—olylactic acid (PLA) or polyhydroxyalkanoate (PHA)^[31]—are potential alternatives to substitute beeswax. These materials, already used in the industry as biodegradable paper coatings, would confer the device a compostable characteristic and an industrially scalable fabrication process.

The redox chemistry proved for this first development was based on suitable quinone species available off-the-shelf with good kinetics on carbon. However, the device is not restricted to these species, and other commercially available candidates could be considered. Caffeic acid, a hydroquinone and antioxidant found in coffee, and water-soluble vitamin K₃, a naphthoquinone, are examples of other commercially available quinone species that are available in the desired redox state for discharge. Moreover, other research groups are working on modeling the effect of functional groups on quinones.^[32] For example, hydroxyl functional groups were shown to enhance solubility and reduce standard potential, which would benefit the battery anode, while sulfonic acid functional groups were shown to enhance solubility and increase standard potential, which would be beneficial for the cathode. By in-house synthesis of quinone species with custom functional groups, the number of candidates meeting the requirements of this approach could be increased and the performance of the device may be further enhanced. This would enable tailored solubility, rate of dissolution, and standard potential difference as well as

reduce the cost of chemical compounds. Furthermore, besides using quinone species, inorganic redox couples can also be suitable for this approach, while maintaining a similar or even higher cell voltage. Some of these inorganic salts may form hydroxide precipitates in alkaline media, yet are compatible for the cathode by utilizing mixed-media operation. For example, nitrates, sulfates, or phosphates are known to benefit the soils, which if combined with cheap and abundant metal redox ions, may lead to a battery that could even be compostable, adding value to the soil or water in which it is disposed of.

The biodegradability study of the PowerPAD batteries was carried out at biotic anaerobic conditions which proved their primary biodegradation. Upcoming work will include long-term biodegradability tests at aerobic conditions that could even meet the certification of home compostability.^[33] Additional biodegradation tests without previous conditioning steps would be of interest such as simulation tests of regulated disposal in landfill conditions as well as unregulated disposal in soils or aquatic systems.

4. Conclusion

This work introduced the PowerPAD concept, a fully biodegradable battery for portable and disposable single-use applications that follows the sustainability guidelines of the circular economy. The battery was prepared using exclusively organic materials and low-energy consuming fabrication techniques. According to the results obtained in the biodegradability test, it can be disposed of in soils and waters and thus eliminate the need for recycling and the associated cost and energy consumption. Ultimately, this disposable power source concept holds great promise to radically change the portable battery paradigm; from considering it a harmful waste to a source of materials that nurture the environment, enrich soil, or remove toxins from water, far beyond the traditional life cycle of a battery.

5. Experimental Section

Materials: The chemical compounds used in this work consisted of H₂BQS (H18402), pBQ (B10358), oxalic acid dihydrate (C₂H₂O₄, O0376), KOH (P1767) (all from Sigma-Aldrich, St Louis, Missouri, USA). For the experiments using predissolved reagents, redox electrolytes were prepared at concentrations of 0.2 M H₂BQS in 2.0 M KOH and 0.2 M pBQ in 1.0 M C₂H₂O₄. During the storage of redox species in solid form within the device, an amount equivalent to the maximum solubility concentrations of the redox species was added to the compartments: H₂BQS (0.023 g), pBQ (0.011 g), KOH (0.056 g), and C₂H₂O₄ (0.063 g). Each species was dissolved in 500 μL of water.

Electrochemical Measurements: The linear sweep voltammetry measurements were performed in a conventional three-electrode electrochemical cell. Glassy carbon electrode (0.07 cm²), platinum wire electrode, and SCE (CH instruments Inc., TX, USA) were used as working electrode, counter electrode, and reference electrode, respectively. All polarization measurements were recorded with a potentiostat (Gamry Reference 3000) at a scan rate of 5 mV s⁻¹. The OCP of each half-cell was measured before polarization. The potential was swept from OCV in the direction of the intended discharge reaction of the measured half-cell. The solution resistance was measured at OCP using the same potentiostat and was used to perform postmeasurement IR-compensation. All chemicals were purchased from Sigma-Aldrich

(Oakville, ON, Canada) and used as received unless otherwise stated. The solutions were prepared by consecutively dissolving the supporting electrolytes and quinone species in 10 mL deionized water to the desired concentrations. The solutions were bubbled with nitrogen to minimize solution oxidation due to dissolved oxygen or ambient air.

Device Fabrication: The device components were designed in a CAD program (CorelDRAW, Corel, Ottawa, ON, Canada). Cellulose membranes were cut using a CO₂ laser cutter (Mini 24, Epilog Laser, Golden, CO, USA). Most of the device assembly was done layer by layer using alignment jigs. The structural cellulose components (238, 320, 601, CFSP223000, from Ahlstrom, Helsinki, Finland) were impregnated with melted natural beeswax (Iberceras, Madrid, Spain), which provided an impermeable coating and was also used to bond the layers. An inlet cellulose pad (238, Ahlstrom) was used to receive the liquid sample into the device. Different absorbent pad configurations were tested. A single layer of cellulose membrane 222 (Ahlstrom) with a thickness of 0.83 mm was taken as baseline material, labeled *h*. The absorbent pads *2h* and *4h* consisted of two or four layers of cellulose 222 to obtain pad thicknesses of 1.66 and 3.32 mm, respectively. In order to test a thinner pad configuration, the pad labeled as *h/2* consisted of one layer of cellulose 238 (0.34 mm thick). The electrodes consisted of porous carbon paper (TGP-120, Toray, Japan). This material has 78% porosity, with an average pore diameter around 30 μm and is 0.37 mm thick. Further details about the electrodes material and its structure and morphology may be found elsewhere.^[34] The electrodes were thermally pretreated to ensure capillary flow.

Battery Testing: The cell voltage/current was recorded using a DropSens μStat400 bipotentiostat/galvanostat and DropView 8400 Software (DropSens S.L., Asturias, Spain). The polarization and power curves for the single cell and battery stacks were generated using linear sweep voltammetry, sweeping from the OCV to 0 V at a scan rate of 50 mV s⁻¹. The discharging curves were recorded under different external loads of 0.5, 1.0, or 2.0 kΩ. All tests were performed at room temperature.

Biodegradability Testing: The assay was performed to determine the inherent biodegradability of the battery devices in anaerobic conditions. Although the main aspects were based on the OECD Test 311, the methodology also included recommendations described by Holliger et al.^[35] and Angelidaki et al.^[36] for anaerobic degradation tests. The test was carried out on the same type of single-cell batteries used for the electrochemical characterization, which contained H₂BQS (0.023 g), pBQ (0.011 g), KOH (0.056 g), and C₂H₂O₄ (0.063 g) as stored reactants. For comparison, identical batteries without reactants were also tested, labeled as blank battery. A reference material consisting of cellulose acetate powder (CAS number 9004-35-7) was also included in the study. Prior to physicochemical characterization, four specimens of each device were shredded to a particle size of <0.5 mm in a cryogenic grinder (Freezer/Mill 6850, SPEX, Metuchen, NJ, USA). The minced devices were used for the biodegradability test in order to avoid abiotic degradation or disintegration. The materials were evaluated after being characterized by their total solids, total chemical oxygen demand, and TC content, shown in Table S2 (Supporting Information). The assay was prepared in duplicate, using glass vessels that contained 50 mL of liquid media and 70 mL of headspace. A greater headspace volume than in the OECD Test 311 was fixed in order to avoid excess overpressure inside the vessels. The initial concentration of device per vessel is given in Table S3 (Supporting Information). An anaerobic digested sludge from an urban wastewater treatment plant was used as inoculum, which was filtered to eliminate coarse materials and was kept for 7 d at 35 °C to diminish residual organic matter. The inoculum to material ratio was selected based on the OECD Test 311 recommendations (10 g_{TS}-inoculum g_{TC}-material⁻¹), but a higher inoculum concentration per vessel was fixed (14.5 g_{TS} L⁻¹) that allowed shortening the start-up time and duration of the test. Once filled, all vessels were bubbled with nitrogen to remove oxygen and closed with gastight seals (crimp cap and septum). The assay was performed at 35 ± 2 °C for 94 d. The biodegradation was monitored through the evolution of CO₂ and CH₄ content in the gas space of the vessels as determined by gas

chromatography (Varian GC 3800, Agilent Technologies, Santa Clara, CA, USA), instead of using a pressure-measuring device and signal transducer as described in OECD Test 311. The biodegradation extent was calculated as primary degradation (D_p) after 60 d and was expressed as the percentage of the initial carbon mass of the material that was transformed into C-CO₂ and C-CH₄.

Supporting Information

Supporting Information is available from the Wiley Online Library or from the author.

Acknowledgements

The funding for this research provided through the Science for Solving Society's Problems Challenge by the Electrochemical Society and the Bill & Melinda Gates Foundation powerPAD is highly appreciated. J.P.E. thanks support from the Marie Curie International Outgoing Fellowship (APPOCS – GA.328144) within the 7th European Community Framework. Additional support from the Natural Sciences and Engineering Research Council of Canada (NSERC), the Canada Foundation for Innovation (CFI), and the British Columbia Knowledge Development Fund (BCKDF) is also acknowledged. E.K. acknowledges support from the Canada Research Chairs program. N.S. would like to thank financial support received from the European Research Council (BE) Grant (SUPERCCELL – GA.648518). L. Tey from the GIRO Research Unit is thanked for her support in the biodegradation tests. The authors thank Iberceras for beeswax customization.

Conflict of Interest

The authors declare no conflict of interest.

Keywords

biodegradable batteries, green electronics, paper microfluidics, redox flow batteries

Received: January 30, 2017

Revised: March 10, 2017

Published online: May 16, 2017

- [1] R. Widmer, H. Oswald-Krapf, D. Sinha-Khetriwal, M. Schnellmann, H. Böni, *Environ. Impact Assess. Rev.* **2005**, *25*, 436.
- [2] L. Moreno-Merino, M. E. Jiménez-Hernández, A. de la Losa, V. Huerta-Muñoz, *Sci. Total Environ.* **2015**, *526*, 187.
- [3] T. C. Wanger, *Conserv. Lett.* **2011**, *4*, 202.
- [4] D. Larcher, J. M. Tarascon, *Nat. Chem.* **2015**, *7*, 19.
- [5] F. O. Ongondo, I. D. Williams, T. J. Cherrett, *Nucl. Chem. Waste Manage.* **2011**, *31*, 714.
- [6] M. Irimia-Vladu, *Chem. Soc. Rev.* **2014**, *43*, 588.
- [7] Y. J. Kim, W. Wu, S.-E. Chun, J. F. Whitacre, C. J. Bettinger, *Proc. Natl. Acad. Sci. USA* **2013**, *110*, 20912.
- [8] L. Yin, X. Huang, H. Xu, Y. Zhang, J. Lam, J. Cheng, J. A. Rogers, *Adv. Mater.* **2014**, *26*, 3879.
- [9] Y. Ding, G. Yu, *Angew. Chem., Int. Ed.* **2016**, *55*, 4772.
- [10] K. Fu, Z. Wang, C. Yan, Z. Liu, Y. Yao, J. Dai, E. Hitz, Y. Wang, W. Luo, Y. Chen, M. Kim, L. Hu, *Adv. Energy Mater.* **2016**, *6*, 1502496.

- [11] a) F. Sharifi, S. Ghobadian, F. R. Cavalcanti, N. Hashemi, *Renewable Sustainable Energy Rev.* **2015**, *52*, 1453; b) J. Winfield, L. D. Chambers, J. Rossiter, J. Greenman, I. Ieropoulos, *J. Mater. Chem. A* **2015**, *3*, 7058; c) C. W. Narvaez Villarrubia, F. Soavi, C. Santoro, C. Arbizzani, A. Serov, S. Rojas-Carbonell, G. Gupta, P. Atanassov, *Biosens. Bioelectron.* **2016**, *86*, 459; d) M. J. González-Guerrero, F. J. del Campo, J. P. Esquivel, D. Leech, N. Sabaté, *Biosens. Bioelectron.* **2017**, *90*, 475.
- [12] L. Nyholm, G. Nyström, A. Mhraryan, M. Strømme, *Adv. Mater.* **2011**, *23*, 3751.
- [13] a) C. Chen, Y. Zhang, Y. Li, J. Dai, J. Song, Y. Yao, Y. Gong, I. Kierzewski, J. Xie, L. Hu, *Energy Environ. Sci.* **2017**, *10*, 538; b) L. Hu, J. W. Choi, Y. Yang, S. Jeong, F. La Mantia, L.-F. Cui, Y. Cui, *Proc. Natl. Acad. Sci. USA* **2009**, *106*, 21490.
- [14] J. P. Esquivel, N. Sabaté, P. Alday, E. Kjeang, O. Ibrahim, *ES Patent EP15200865* **2015**.
- [15] a) J. L. Osborn, B. Lutz, E. Fu, P. Kauffman, D. Y. Stevens, P. Yager, *Lab Chip* **2010**, *10*, 2659; b) J. P. Esquivel, F. J. Del Campo, J. L. Gomez de la Fuente, S. Rojas, N. Sabate, *Energy Environ. Sci.* **2014**, *7*, 1744.
- [16] E. Kjeang, R. Michel, D. A. Harrington, N. Djilali, D. Sinton, *J. Am. Chem. Soc.* **2008**, *130*, 4000.
- [17] a) B. Yang, L. Hooper-Burkhardt, F. Wang, G. K. Surya Prakash, S. R. Narayanan, *J. Electrochem. Soc.* **2014**, *161*, A1371; b) B. Huskinson, M. P. Marshak, C. Suh, S. Er, M. R. Gerhardt, C. J. Galvin, X. Chen, A. Aspuru-Guzik, R. G. Gordon, M. J. Aziz, *Nature* **2014**, *505*, 195; c) K. Lin, Q. Chen, M. R. Gerhardt, L. Tong, S. B. Kim, L. Eisenach, A. W. Valle, D. Hardee, R. G. Gordon, M. J. Aziz, M. P. Marshak, *Science* **2015**, *349*, 1529.
- [18] a) E. Kjeang, N. Djilali, D. Sinton, *J. Power Sources* **2009**, *186*, 353; b) E. R. Choban, J. S. Spendelow, L. Gancs, A. Wiecekowsky, P. J. A. Kenis, *Electrochim. Acta* **2005**, *50*, 5390; c) R. Ferrigno, A. D. Stroock, T. D. Clark, M. Mayer, G. M. Whitesides, *J. Am. Chem. Soc.* **2002**, *124*, 12930.
- [19] M. Quan, D. Sanchez, M. F. Wasylkiw, D. K. Smith, *J. Am. Chem. Soc.* **2007**, *129*, 12847.
- [20] Environmental Protection Agency, Estimation Programs Interface Suite for Microsoft Windows, v 4.11, **2016**.
- [21] a) F. J. Enguita, A. L. Leito, *BioMed. Res. Int.* **2013**, *2013*, 14; b) K. G. Harbison, R. T. Belly, *Environ. Toxicol. Chem.* **1982**, *1*, 9.
- [22] a) M. Rafiee, D. Nematollahi, *Electroanalysis* **2007**, *19*, 1382; b) R. Gulaboski, I. Bogeski, V. Mirčeski, S. Saul, B. Pasięka, H. H. Haeri, M. Stefova, J. P. Stanoeva, S. Mitrev, M. Hoth, R. Kappl, *Sci. Rep.* **2013**, *3*, 1865; c) Y. Xu, Y. Wen, J. Cheng, Y. Yanga, Z. Xie, G. Cao, presented at *2009 World Non-Grid-Connected Wind Power and Energy Conf.*, Nanjing, China, September **2009**; d) B. Yang, L. Hooper-Burkhardt, S. Krishnamoorthy, A. Murali, G. K. S. Prakash, S. R. Narayanan, *J. Electrochem. Soc.* **2016**, *163*, A1442; e) Y. Zhao, Y. Ding, Y. Li, L. Peng, H. R. Byon, J. B. Goodenough, G. Yu, *Chem. Soc. Rev.* **2015**, *44*, 7968; f) Y. Ding, Y. Li, G. Yu, *Chem* **2016**, *1*, 790.
- [23] P. S. Guin, S. Das, P. C. Mandal, *Int. J. Electrochem.* **2011**, *2011*, 22.
- [24] a) O. A. Ibrahim, M.-A. Goulet, E. Kjeang, *J. Electrochem. Soc.* **2015**, *162*, F639; b) B. Ho, E. Kjeang, *J. Fluids Eng.* **2013**, *135*, 021304; c) O. A. Ibrahim, M.-A. Goulet, E. Kjeang, *Electrochim. Acta* **2016**, *187*, 277.
- [25] Organization of Economic Cooperation and Development, OECD311. *Anaerobic Biodegradability of Organic Compounds in Digested Sludge: by Measurement of Gas Production*, **2006**.
- [26] International Organization for Standardization, ISO 11734. *Water Quality: Evaluation of the ultimate anaerobic biodegradation of organic compounds in digested sludge*, **1995**.
- [27] American Society of the International Association for Testing and Materials, *E1192-92 Standard Test Method for Determining the Anaerobic Biodegradation Potential of Organic Chemicals*, **1992**.
- [28] United States Environmental Protection Agency, *Fate, Transport and Transformation Test Guidelines OPPTS 835.3400 Anaerobic Biodegradability of Organic Chemicals*, **1998**.
- [29] a) J.-D. Gu, D. Eberiel, S. P. McCarthy, R. A. Gross, *J. Environ. Polym. Degrad.* **1993**, *1*, 281; b) J. Puls, S. A. Wilson, D. Hölter, *J. Polym. Environ.* **2011**, *19*, 152.
- [30] J. Pérez, J. Muñoz-Dorado, T. de la Rubia, J. Martínez, *Int. Microbiol.* **2002**, *5*, 53.
- [31] *Metabolix*, Vol. 2016, Lowell, MA, USA **2016**.
- [32] S. Er, C. Suh, M. P. Marshak, A. Aspuru-Guzik, *Chem. Sci.* **2015**, *6*, 885.
- [33] Vinçotte, OK Compost EN 13432, **1995**.
- [34] F. C. Store, Vol. 2017, Fuel Cells Store, **2017**, Toray Carbon Paper 120.
- [35] C. Holliger, M. Alves, D. Andrade, I. Angelidaki, S. Astals, U. Baier, C. Bougrier, P. Buffière, M. Carballa, V. de Wilde, F. Ebertseder, B. Fernández, E. Ficara, I. Fotidis, J. C. Frigon, H. Fruteau de Lacroix, D. S. M. Ghasimi, G. Hack, M. Hartel, J. Heerenklage, I. Sarvari Horvath, P. Jenicek, K. Koch, J. Krautwald, J. Lizasoain, J. Liu, L. Mosberger, M. Nistor, H. Oechsner, J. Vitor Oliveira, M. Paterson, A. Pauss, S. Pommier, I. Porqueddu, F. Raposo, T. Ribeiro, F. Rüsç Pfund, S. Strömberg, M. Torrijos, M. van Eekert, J. van Lier, H. Wedwitschka, I. Wierinck, *Water Sci. Technol.* **2016**, *75*, DOI: 10.2166/wst.2016.336.
- [36] I. Angelidaki, M. Alves, D. Bolzonella, L. Borzacconi, J. L. Campos, A. J. Guwy, S. Kalyuzhnyi, P. Jenicek, J. B. van Lier, *Water Sci. Technol.* **2009**, *59*, 927.

ADVANCED ENERGY MATERIALS

Supporting Information

for *Adv. Energy Mater.*, DOI: 10.1002/aenm.201700275

A Metal-Free and Biotically Degradable Battery for Portable Single-Use Applications

Juan Pablo Esquivel, Perla Alday, Omar A. Ibrahim, Belén Fernández, Erik Kjeang, and Neus Sabaté*

Supporting Information

A metal-free and biotically degradable battery for portable single-use applications

*Juan Pablo Esquivel**, *Perla Alday*, *Omar A. Ibrahim*, *Belén Fernández*, *Erik Kjeang* and *Neus Sabaté*

Dr. J. P. Esquivel, P. Alday, Prof. N. Sabaté
Instituto de Microelectrónica de Barcelona, IMB-CNM (CSIC)
C/ del Tí·lers. Campus Universitat Autònoma de Barcelona (UAB)
08193 Bellaterra, Barcelona, SPAIN
E-mail: juanpablo.esquivel@csic.es

Dr. J. P. Esquivel
Department of Bioengineering
University of Washington
98195, Seattle, WA, USA

O. A. Ibrahim, Prof. E. Kjeang
Fuel Cell Research Lab (FCReL), School of Mechatronic Systems Engineering
Simon Fraser University, V3T 0A3 Surrey, BC, Canada

Dr. B. Fernández
GIRO Joint Research Unit IRTA-UPC, Torre Marimon
08140 Caldes de Montbui, Barcelona, Spain

Prof. N. Sabaté
Catalan Institution for Research and Advanced Studies (ICREA)
Passeig Lluís Companys 23, 08010 Barcelona, Spain

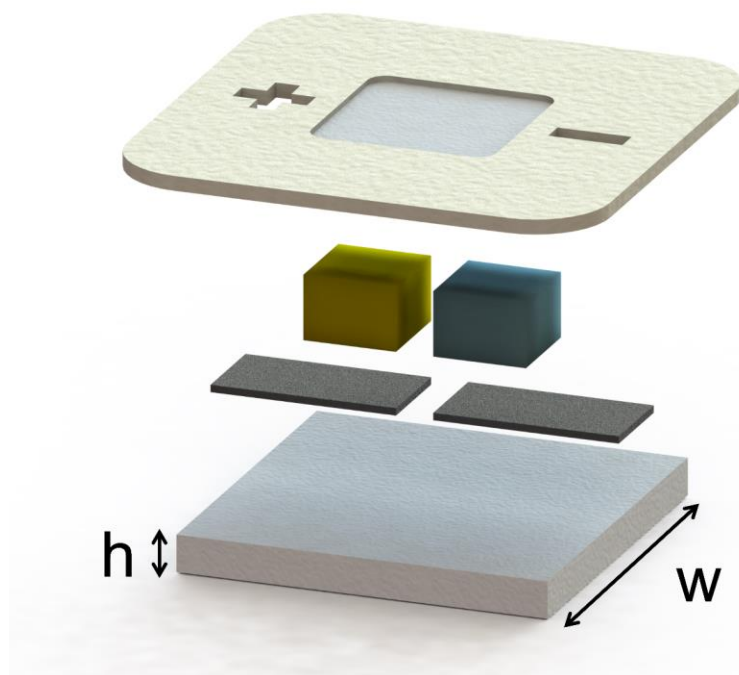


Figure S1. PowerPAD conceptual schematic of the proposed biodegradable battery showing the geometrical parameters evaluated for the characterization of the battery performance: absorbent pad width (w) and thickness (h).

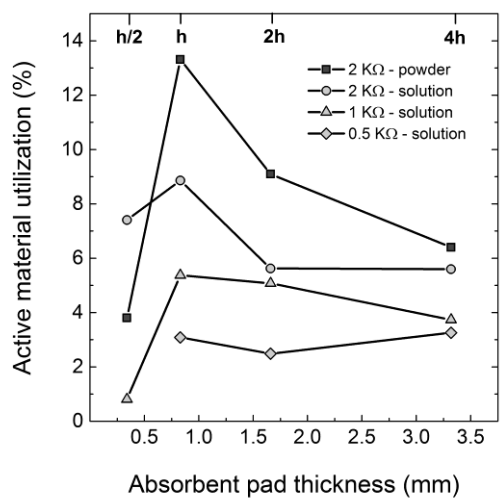


Figure S2. Electroactive material utilization of the biodegradable redox battery prototypes calculated from the discharging curves.

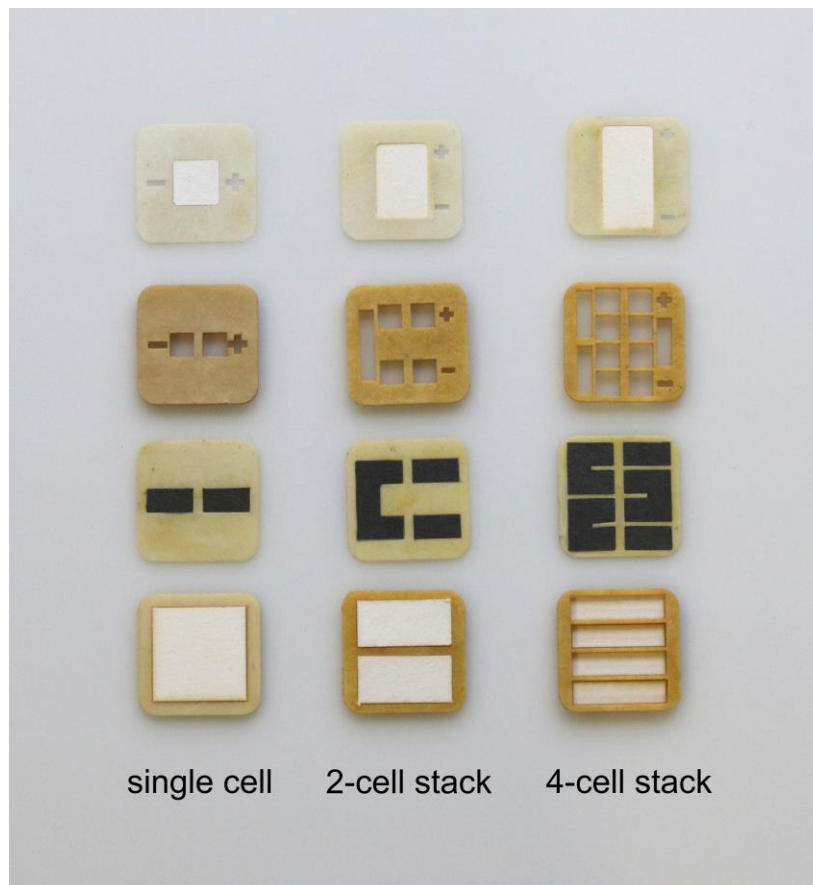


Figure S3. Photograph of relevant internal layer of biodegradable batteries.

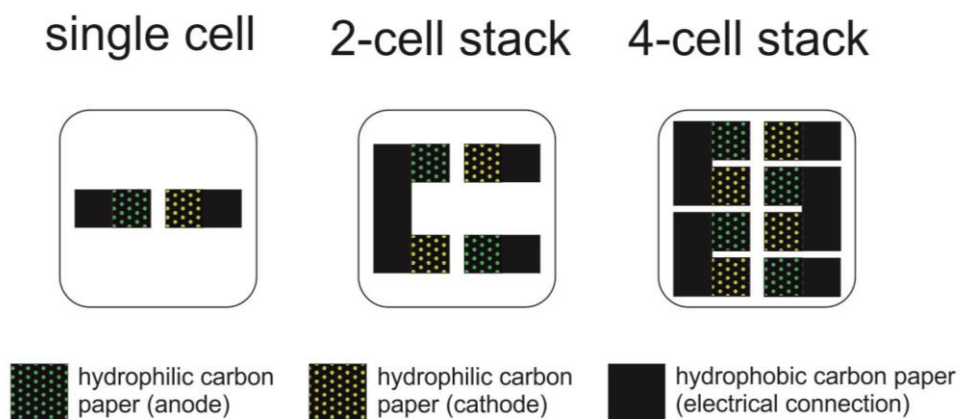


Figure S4. Diagram showing the conductive and reactive regions of the porous carbon electrodes for the single cell, 2-cell and 4-cell stacks.

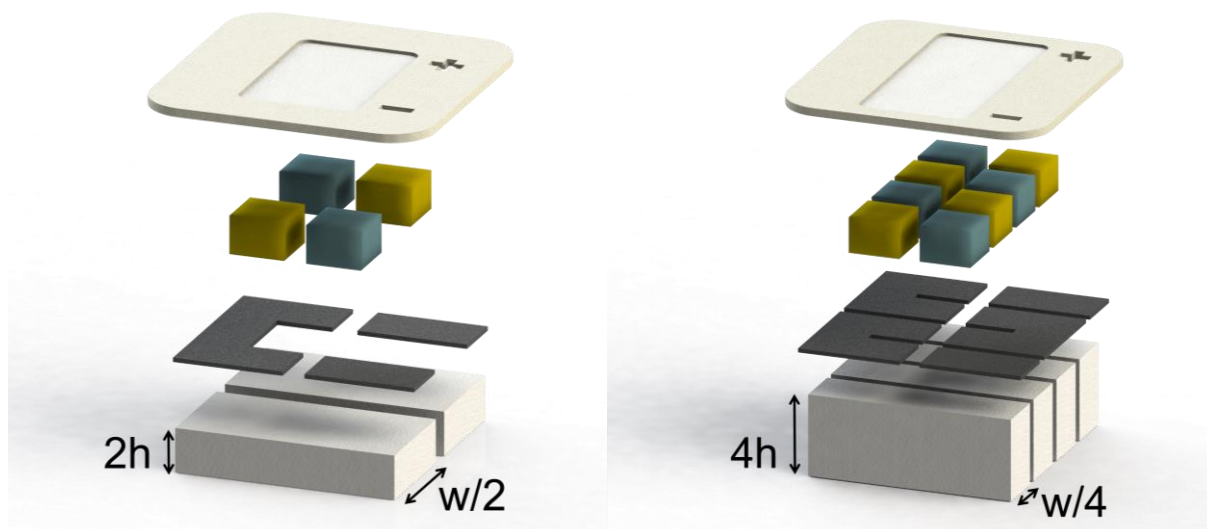


Figure S5. Schematic representation of 2-cell stack and 4-cell stack of the proposed biodegradable batteries.

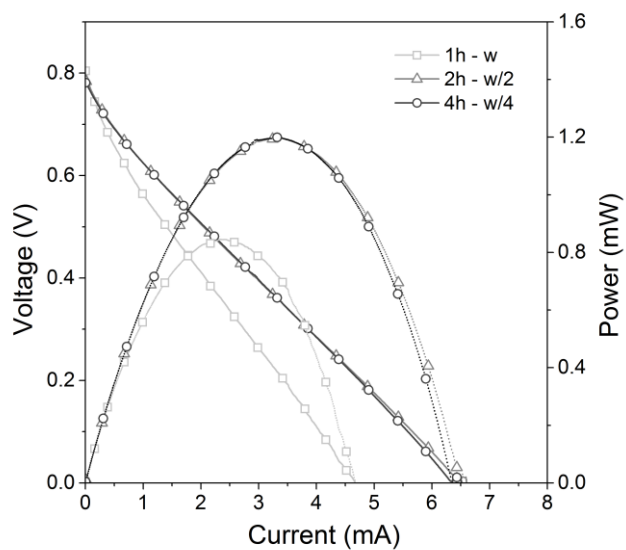


Figure S6. Polarization curves of biodegradable redox flow batteries with three different absorbent pad widths. Shown are the average polarization curves ($n \geq 3$) of batteries supplied with pre-mixed solutions of 0.2 M H_2BQS in 2 M KOH and 0.2 M pBQ in 1 M $\text{C}_2\text{H}_2\text{O}_4$.

Table S1. PowerPAD biodegradable battery - Bill of Materials.

	Single cell		2-cell stack		4-cell stack	
	QUANTITY	COST (€)	QUANTITY	COST (€)	QUANTITY	COST (€)
CELLULOSE						
Cellulose 601 (Ahlstrom)	13.52 cm ²	0.033	13.52 cm ²	0.033	13.52 cm ²	0.033
Cellulose 222 (Ahlstrom)	4 cm ²	0.009	8 cm ²	0.018	16 cm ²	0.037
Cellulose 238 (Ahlstrom)	21.78 cm ²	0.027	23.28 cm ²	0.029	26.28 cm ²	0.033
Cellulose 320 (Ahlstrom)	13.52 cm ²	0.053	13.52 cm ²	0.053	13.52 cm ²	0.053
Cellulose 270 (Ahlstrom)	6.76 cm ²	0.026	6.76 cm ²	0.026	6.76 cm ²	0.026
CARBON ELECTRODES						
Carbon paper TGP-H-120	1 cm ²	0.115	2.35 cm ²	0.270	3.3 cm ²	0.380
WAX						
Beeswax sheets	2 g	0.052	2 g	0.052	2 g	0.052
CHEMICAL REAGENTS						
H ₂ BQS (H18402, Sigma Aldrich)	0.0089 g	0.004	0.0178 g	0.008	0.0356 g	0.015
pBQ (B10358, Sigma Aldrich)	0.0046 g	0.001	0.0092 g	0.002	0.0184 g	0.005
KOH (P1767, Sigma Aldrich)	0.023 g	0.001	0.046 g	0.003	0.092 g	0.005
C ₂ H ₂ O ₄ (247537, Sigma Aldrich)	0.026 g	0.007	0.052 g	0.015	0.104 g	0.029
TOTAL		0.33 €		0.51 €		0.67 €

Price references from:

<https://us.vwr.com/store/product/12610321/thick-chromatography-paper-grade-222-ahlstrom>

<http://fuelcellstore.com/toray-carbon-paper-120>

<http://www.iberceras.es/>

<http://www.sigmaaldrich.com/catalog/product/fluka/p1767>

<http://www.sigmaaldrich.com/catalog/product/sial/247537>

<http://www.sigmaaldrich.com/catalog/product/sial/b10358>

<http://www.sigmaaldrich.com/catalog/product/aldrich/h18402>

Biodegradability study

The OECD-Test 311, for anaerobic biodegradability of organic compounds in digested sludge, is a guideline that included ISO 11734 (ISO, 1995) besides others, as the Shelton and Tiedje method (Shelton et al., 1984). This test has become the American standards (ASTM, 1992; US-EPA, 1998) for biodegradability, although problems related to the differing solubility of CO₂ and CH₄ in the test medium or to the calculation of the theoretical gas production of a test substance were not resolved. The ECETOC report (Birch et al., 1989) recommended the additional measurement of the dissolved inorganic carbon content of the supernatant liquid, which made the technique more widely applicable. After an international calibration exercise (or ring test), the ECETOC method became the ISO Standard ISO 11734 (ISO, 1995).

It is a screening method under a specific condition of an anaerobic digester, at a given time and range of concentration of microorganisms. The conditions of the test do not necessarily correspond to the conditions in all anaerobic digesters nor it is applicable for the assessment of anaerobic biodegradability under different environmental conditions, because (i) a diluted sludge is used with a relatively high concentration of test substance; and (ii) the duration of the test is typically longer than the retention time in anaerobic digesters. Nevertheless, this test provides the “inherent biodegradability” that refers to a classification of materials for which there is unequivocal evidence of biodegradation (primary or ultimate) in any test of biodegradability. Since inherent biodegradability is considered as a specific characteristic of a material, it is not necessary to define or limit the biodegradation rate. Biodegradation above 20% of theoretical (measured as %TC) may be regarded as evidence of primary biodegradability, whereas biodegradation above 70% of theoretical (measured as %TC) may be regarded as evidence of ultimate biodegradability. When results of other biodegradability tests, such as “ready biodegradation assays”, indicate that the pass level criterion is almost fulfilled (i.e. slightly below 60-70%), such results can be used to indicate inherent biodegradability.

Table S2. Characterization of batteries for biodegradability

Material	Description	Total solids (gTS kg ⁻¹)	TCOD (gO ₂ kg ⁻¹)	TC (gC kg ⁻¹)
Battery	Battery with H ₂ BQS-KOH & pBQ-C ₂ H ₂ O ₄	965.6 ± 3.5	2204.0 ± 68.3	610.9 ± 9.7
Blank battery	Battery without reactants	974.1 ± 3.5	2112.9 ± 228.4	653.4 ± 0.6
Cellulose	Acetate flakes	980.5 ± 1.1	1278.9 ± 0.0	461.6 ± 2.5

Table S3. Initial test conditions for biodegradability study.

Material	Vessel	Material	Material	Inoculum
	Liquid medium (mL)	TCOD (gO ₂ L ⁻¹)	Initial TC (mgC L ⁻¹)	Total solids (gTS L ⁻¹)
Battery	50.10 ± 0.07	7.60 ± 4.17	2.19 ± 1.20	14.50 ± 0.01
Blank battery	50.05 ± 0.06	5.16 ± 0.01	1.57 ± 0.00	14.50 ± 0.01
Cellulose	50.03 ± 0.04	5.50 ± 0.18	1.98 ± 0.07	14.49 ± 0.01

Supplementary references:

ISO 11734. Water Quality: Evaluation of the ultimate anaerobic biodegradation of organic compounds in digested sludge. Method by measurement of the biogas production. International Organization for Standardization. 1995.

Shelton D.R. and Tiedje, J.M. 1984. General method for determining anaerobic biodegradation potential. Appl. Environ. Microbiology, 47, 850-857.

ASTM .1992. E1192-92 Standard Test Method for Determining the Anaerobic Biodegradation Potential of Organic Chemicals. ASTM, Philadelphia.

US-EPA. 1998. Fate, Transport and Transformation Test Guidelines OPPTS 835.3400 Anaerobic Biodegradability of Organic Chemicals.

Birch, R. R., Biver, C., Campagna, R., Gledhill, W.E., Pagga, U., Steber, J., Reust, H., Bontinck, 1989. W.J. Screening of chemicals for anaerobic biodegradation. Chemosphere 19, 1527-1550. (Also published as ECETOC Technical Report No. 28, June 1988).